

TOP CROSS SECTION RATIOS AS  
A TEST OF LEPTON UNIVERSALITY  
IN CHARGED WEAK DECAYS IN  
PROTON-PROTON COLLISIONS AT  
 $\sqrt{s} = 7$  TEV  
WITH THE ATLAS DETECTOR

**Jody David Palmer**

*Thesis submitted to the University of Birmingham  
for the degree of Doctor of Philosophy*



Particle Physics Group,  
School of Physics and Astronomy,  
University of Birmingham.

*September 26, 2013*

UNIVERSITY OF  
BIRMINGHAM

**University of Birmingham Research Archive**

**e-theses repository**

This unpublished thesis/dissertation is copyright of the author and/or third parties. The intellectual property rights of the author or third parties in respect of this work are as defined by The Copyright Designs and Patents Act 1988 or as modified by any successor legislation.

Any use made of information contained in this thesis/dissertation must be in accordance with that legislation and must be properly acknowledged. Further distribution or reproduction in any format is prohibited without the permission of the copyright holder.

# Abstract

In this thesis partial production cross sections of  $t\bar{t}$  events are measured in four channels, defined by the final state leptons from the decay of the  $W$  bosons and the triggering lepton, using  $\sim 5.6 \text{ fb}^{-1}$  of data taken with the ATLAS detector at  $\sqrt{s} = 7 \text{ TeV}$ . The di-lepton channel is defined as having one electron and one muon in the final state. The lepton plus tau channels are defined as having a final state electron or muon and one hadronically decaying tau. Partial cross sections for these channels are estimated, and ratios of partial cross sections, defined with the same triggering lepton, are calculated. The di-lepton events are divided into two non-exclusive channels defined by the presence of a trigger matched lepton.

The production cross-sections of  $t\bar{t}$  events with final states including an electron and a hadronically decaying tau, or an electron and a muon, were measured and used to calculate their ratio  $\mathcal{R}_{e\tau} = 0.65_{-0.10}^{+0.12}(\text{stat.}) \pm 0.18(\text{syst.})$ . The cross section ratio  $\mathcal{R}_{e\tau}$  measured in data is compared to that inferred from the world average  $W$  and tau branching fractions,  $\mathcal{R}_{e\tau}^{\text{Data}}/\mathcal{R}_{e\tau}^{\text{PDG}} = 1.1_{-0.17}^{+0.21}(\text{stat.}) \pm 0.31(\text{syst.})$  and is found to be consistent with unity.

# Acknowledgements

First and foremost I'd especially like to thank my supervisor Chris Hawkes for his continued support, patience, and guidance over the years: I really could not have done this without him. Another big thank you to Simon Head who has provided invaluable technical help, and encouragement in the latter part of my PhD

I'm also very grateful to the Science and Technology Funding Council for the generous funding for this PhD, and to the University of Birmingham in general for their support.

A special thanks to the charged Higgs working group whose work provided the basis for the cut selection used in this analysis, and to the top cross section working group (and the lepton plus tau sub-group) for providing invaluable guidance on the measurement of the lepton fake rate. I'd like to also thank the ATLAS top working group who provided or validated many of the systematic tools, and MC samples, and for providing much of supporting work referenced in this thesis. I also highly appreciate the work of the particle physics theoretical community in producing the MC generators, and the other numerous ATLAS members involved in producing the MC samples used in this analysis.

I'm very grateful for all the hard work of the ATLAS combined performance groups and the wider ATLAS community for ensuring the detector is so well understood and that event reconstruction works so well, and whose work was invaluable in helping me to understand the ATLAS detector. Additionally, thanks to the LHC team who exceeded the high expectations and delivered an exceptionally high integrated luminosity in the first full year of running.

Thanks also needs to go to John Wilson who helped me a lot in the early years of my PhD working on the SCT, and for his continued support. Thanks to also to Pat Ward and the rest of the SCT Off-line group who helped me in my understanding of the Inner Detector and tracking, and to Bilge whose thesis helped fill the gaps in my understanding of SCT and the ATLAS detector.

A special thank you to all the lecturers and tutors of the 2009 UK HEP Summer School whose lectures and notes helped my understanding of particle physics, and helped form the foundation of my theory chapter.

To Pete Watkins and Paul Newman, thank you for giving me a chance in first place, and for providing invaluable support over the last few years. More thanks to Miriam Watson, Mark Slater, Paul Thomson, the Birmingham ATLAS group, and the Birmingham HEP group, for your tutoring, technical help, advice, and support over the years. I'd also like to thank Lawrie for keeping the computers working at all costs, and Maria for her help navigating the bureaucracy.

To all of the Birmingham students, in particular Tim, Dave, Arvinder, Patrick and Tom, thank you for the late night beers, beds, and for your coding help. A special mention goes to Mark Stockton for being a great friend too. It almost goes without saying that without all of my friends from my LTA at CERN to talk, drink or snowboard through problems with, the last few years would have been much duller and less productive. Thank you for maintaining my sanity. To all my new climbing buddies, thank you for being there for those few precious hours every week, listening when I needed it, and climbing when I didn't.

And finally, thank you to my Mum and Dad. Its impossible to completely express how important you've been in getting me here. You've always encouraged me to learn and expand my horizons, believed in me, trusted my personal drive, and shown almost inexhaustible patience. I have gone my further than I ever really imagined (and to who knows where next) and for that I'll always be grateful

# Author's Contribution

As well my own original work, this thesis outlines the operation of the Large Hadron Collider (LHC) and details on the design and performance of the A Toroidal LHC ApparatuS (ATLAS) detector. The operation of both the LHC and the ATLAS detector relied on the continued effort of thousands of scientists and engineers.

As part of my official service task for the ATLAS collaboration I looked at the tracking performance of the Semi-Conductor Tracker (SCT) detector using cosmic ray data. I was able to show that in some cases SCT strips which correctly gave a positive signal for the presence of a track were excluded from the track reconstruction routine. The details of this analysis are not included as part of this thesis.

While at European Organisation for Nuclear Research (CERN) I was involved in several ATLAS top groups. The object pre-selection is from the work the ATLAS Top Analysis Group. My only small contribution to this was a Monte Carlo (MC) study which aimed to optimise the electron and muon isolation requirements for a  $t\bar{t}$  cross-section measurement.

As part of the ATLAS  $t\bar{t}$  lepton plus tau cross section group I validated an initial lepton fake rate measurement in the signal region [1]. This included re-measuring lepton real efficiencies and fake rates. While part of the top sub-group measuring the tau cross-section, I initially performed a cross-check of the di-lepton fake rate estimate using the matrix method described in this chapter.

The above matrix method for estimating lepton fake yields was modified to use the event selection of the ATLAS charged Higgs group to provide an alternative measurement to that used in their final analysis [2]. The overlap removal and event selection described in this thesis are from my work with this group. Consequently I re-measured the electron and muon efficiencies and fake rates.

The measurements of the rates that jets fake taus are my own, as are the estimates of the number of jets faking taus in the  $t\bar{t}$  control and signal regions.

The analysis code is written by myself using a framework (set-up by Simon Head) common to some Birmingham top group analyses, which included some standard object pre-selection.

# Plain English Summary

Electrons are fundamental particles. They orbit atomic nuclei to form atoms and conduct electricity because they are negatively charged particles. In what is known as the Standard Model the negatively charged electron (symbol  $e$ ), and its positively charged anti-particle the positron, are in the first of three lepton ‘generations’ (which group related particles). The muon (symbol  $\mu$ ) and tau (symbol  $\tau$ ) (in the second and third generation respectively) are almost identical to the electron except they have masses  $\sim 200$  and  $\sim 3500$  times larger than it. Each lepton in a generation also has an uncharged partner with a tiny mass known as a neutrino and which barely interact with matter (they pass through the Earth as if it were a window).

Protons and neutrons are heavy particles,  $\sim 2000$  times heavier than the electron, and are the constituents of atomic nuclei. While electrons are bound to atomic nuclei because of the electro-magnetic force, which acts on electric charge, protons and neutrons in nuclei are bound together due a force known as the strong force.

Unlike electrons, protons and neutrons are not fundamental particles and are actually made of smaller fundamental particles called quarks. The force that holds nuclei together also binds quarks together to form protons and neutrons. The proton and neutron are made of different combinations of two particles, the *up* and *down* quarks.

Similarly to the leptons, there are three generations of quarks, of which the up and down quark form the first. The second generation has the *strange* and *charm* quarks, and the third generation the *bottom* and *top* quarks. Similarly to the lepton generations, the quarks get heavier from one generation to the next. The top quark is the heaviest with a mass  $\sim 200$  times that of the proton (and  $\sim 300,000$  that of the electron).

Each of the fundamental forces that leptons and quarks interact with is carried by a particle: these are called gauge (or force) bosons. The electro-magnetic force is carried by the massless photons between charged particles, the strong force is carried by massless particles known as gluons between the quarks. A third force, the weak force is carried by two particles that have mass: the  $W$  and  $Z$  bosons.

The weak force is much weaker than the electro-magnetic and strong forces because its force carrying bosons have mass and cannot travel long distances. The heavy

quarks decay into lighter quarks via the charged  $W$ . This is responsible for one type of radioactive decay, beta decay, in which electrons are emitted from certain radioactive nuclei.

One final particle, the Higgs boson, completes the Standard Model (SM). Recently discovered at the LHC, it gives the  $W$  and  $Z$  their masses. The fundamental particles, and their interactions, are collectively known as the Standard Model of particle physics. It is one of the most successful theories in modern science, with many of its values predicted and confirmed by experiment to extremely high levels of precision.

The  $W$  itself also decays to electrons, muons and taus because it is much heavier than them. This occurs in almost exactly equal amounts to each lepton generation, which is known as lepton universality.

In the LHC ring, huge numbers of protons are circulated in opposite directions to nearly the speed of light. They are forced to collide using magnets at points in the centre of four detectors. When the protons collide new particles are produced because of their high energies. One of these detectors is ATLAS which is a general purpose detector. It shares many properties with digital cameras, and in essence takes high resolution 3D pictures each time protons collide. ATLAS can measure the path that charged particles take, and measure the energies and direction of almost all the particles produced in the interaction. It can also distinguish each type of lepton from one another accurately.

In the LHC top quarks are produced in pairs in some of these collisions. To measure how often this occurs in proton-proton collisions, a quantity known as a cross-section (with symbol  $\sigma$ ) is measured which has a unit of area. This quantity is directly proportional to the number of top quark pairs produced.

Top quarks are never directly seen in the detector, they almost always decay to a bottom quark and a  $W$  and the decay products of these can be seen by the ATLAS detector. The  $W$  can decay either to other quarks, which then go on to form hadrons (these are particles formed from quarks, like the proton), or one of the three leptons (and the associated lepton neutrino). When the  $W$  decays to a lepton and its neutrino, the lepton type can be identified by the ATLAS detector. This allows the cross section to be divided into types. For example, some top quark pairs decay to an electron and muon, and some to an electron and a tau. The *partial* cross sections  $\sigma^{e\mu}$  and  $\sigma^{e\tau}$  correspond to the number of top quark pairs produced in proton-proton collisions that respectively subsequently decay to an electron and a muon, or an electron and a tau respectively.

The ATLAS detector is used to reconstruct events that appear to be a top quark pair decaying to two leptons (a candidate event). However, these can sometimes be what is known as a background event. The true number of top quark pairs is calculated by taking an estimate for these backgrounds from the total number of top quark pair candidates seen in ATLAS.

These backgrounds can be broadly classified into two types. The first is where the final state particles seen in the detector are identified correctly, but the intermediate particles are different. For example a pair of  $W$  bosons decaying to leptons can look identical to a top quark pair. These events are well described by mathematical models, which are relied upon to tell us how often these are produced instead of top quark pairs. The other type of background is where the particle is a *fake*. These can come from several sources including mis-identifying similar particles, different collisions overlapping, or even electrical noise. Data driven methods are used in this thesis to estimate the number of events with fake electrons, muons and taus in them from all possible sources.

Once backgrounds have been subtracted, the number of top quark pairs with an electron and muon, or an electron and tau can be calculated. As previously mentioned, we expect  $W$  bosons produced in the decay of top quark pairs to decay almost equally to all types of lepton. Dividing the two cross sections yields a cross section ratio  $\mathcal{R}_{e\tau} = \sigma^{e\tau} / \sigma^{e\mu}$ .

The value measured in data is compared to that predicted by theoretical physics, and if  $W$  bosons decay to all leptons equally, the ratio of these will be 1. The ratio measured in data divided by that predicted by theory is measured to be  $\mathcal{R}_{e\tau}^{Data} / \mathcal{R}_{e\tau}^{theory} = 1.1$ . One source of error, the statistical uncertainty indicates this value will be within 0.93 and 1.31 with a probability of  $\sim 2/3$ <sup>1</sup>. Both indicate that the true value is close to one, and consistent with what we know about the Standard Model of particle physics.

---

<sup>1</sup>This statement is subtly imprecise because of how probabilities are defined. Technically, if the value measured was that of the true value, and the experiment was repeated multiple times, it would lie within these ranges 68% of the time.

*“I love deadlines. I like the whooshing sound they make as they fly by.”* - Douglas Adams

# Contents

<b>Acronyms</b>	<b>vii</b>
<b>List of Figures</b>	<b>xi</b>
<b>List of Tables</b>	<b>xviii</b>
<b>1 Introduction</b>	<b>1</b>
<b>2 The ATLAS experiment at the LHC</b>	<b>5</b>
2.1 Inner Detector . . . . .	7
2.1.1 Pixel Detector . . . . .	11
2.1.2 Semi-Conductor Tracker . . . . .	12
2.1.3 Transition Radiation Tracker . . . . .	13
2.1.4 Solenoid Magnet . . . . .	14
2.1.4.1 Tracking Performance . . . . .	14
2.2 Calorimeters . . . . .	16
2.2.1 Liquid Argon Electromagnetic Barrel Calorimeter . . . . .	19
2.2.2 LAr Electromagnetic End-cap Calorimeter . . . . .	21
2.2.3 Hadronic Tile Calorimeter . . . . .	21
2.2.4 Liquid Argon HEC . . . . .	23
2.2.5 Forward Calorimeter . . . . .	23

2.3	Muon Spectrometer . . . . .	24
2.3.1	Muon Drift Tube chamber . . . . .	25
2.3.2	Cathode Strip Chamber . . . . .	26
2.3.3	Muon Trigger Chambers . . . . .	26
2.3.4	Resistive Plate Chamber . . . . .	27
2.3.5	Thin Gap Chamber . . . . .	28
2.3.6	Toroid Magnets . . . . .	28
2.3.7	Forward Detectors . . . . .	28
2.4	Triggers and Data Acquisition . . . . .	29
2.4.1	Electron Triggers . . . . .	30
2.4.2	Muon Triggers . . . . .	31
2.5	Summary . . . . .	32
<b>3</b>	<b>The Standard Model and Top Physics</b>	<b>33</b>
3.1	The Standard Model of Particle Physics . . . . .	34
3.1.1	Tau Physics . . . . .	38
3.2	Electro-weak Theory . . . . .	39
3.2.1	Yukawa Couplings . . . . .	39
3.3	Quantum Chromo-Dynamics . . . . .	40
3.3.1	Strong Coupling . . . . .	41
3.4	Perturbation Theory . . . . .	42
3.5	Top Cross sections and Ratios . . . . .	43
3.5.1	Production and decay of $t\bar{t}$ events . . . . .	43
3.5.2	Lepton Universality . . . . .	47
3.6	Other Top Quark Physics . . . . .	49
3.6.1	Top Mass . . . . .	49

3.6.2	Top Properties . . . . .	49
3.7	Physics Beyond the SM . . . . .	51
3.7.1	Supersymmetry . . . . .	52
3.8	Summary . . . . .	54
<b>4</b>	<b>Event Selection of <math>t\bar{t}</math> Events</b>	<b>58</b>
4.1	Object Reconstruction and Identification . . . . .	58
4.1.1	Electrons . . . . .	59
4.1.2	Muons . . . . .	60
4.1.3	Jets . . . . .	61
4.1.3.1	Jet Energy Scale . . . . .	61
4.1.3.2	Jet Energy Resolution . . . . .	62
4.1.3.3	Jet Reconstruction Efficiency . . . . .	63
4.1.4	B-Jets . . . . .	63
4.1.5	Hadronically Decaying Taus . . . . .	64
4.1.6	Missing Transverse Energy . . . . .	67
4.1.7	Sum of the Transverse Momentum of ID Tracks . . . . .	68
4.2	Object Pre-selection . . . . .	68
4.2.1	Hadronic Jets . . . . .	68
4.2.2	Leptonic Cuts . . . . .	68
4.2.2.1	Electrons . . . . .	68
4.2.2.2	Muons . . . . .	69
4.2.2.3	Hadronically Decaying Tau Leptons . . . . .	69
4.3	Overlap Removal . . . . .	70
4.4	Event selection . . . . .	71
4.4.1	Data Periods . . . . .	72

4.4.2	Event Quality Cuts . . . . .	73
4.4.3	Lepton Triggers . . . . .	74
4.4.4	Leptonic Cuts . . . . .	74
4.4.5	Hadronic Jet Selection . . . . .	76
4.4.5.1	Selecting b-jets . . . . .	76
4.4.6	Missing Transverse Energy . . . . .	76
4.4.7	Sum of the Transverse Momentum of ID Tracks . . . . .	76
4.5	Selecting $t\bar{t}$ Events . . . . .	76
4.6	Monte Carlo Samples . . . . .	77
4.6.1	$t\bar{t}$ Monte Carlo Samples for Estimating Generator Systematic Uncertainties . . . . .	79
4.6.2	Classifying $t\bar{t}$ truth events . . . . .	80
4.7	Alternative $t\bar{t}$ Selection Strategies . . . . .	80
4.8	Summary . . . . .	82
<b>5</b>	<b>Lepton Fake Rate Estimation</b>	<b>83</b>
5.1	Electron and Muon Fake Rate Estimation . . . . .	83
5.1.1	The Matrix Method for data driven background estimation . . . . .	85
5.1.2	Real Lepton Efficiency Measurement . . . . .	88
5.1.2.1	Making pure $Z \rightarrow e^+e^-$ and $Z \rightarrow \mu^+\mu^-$ samples . . . . .	89
5.1.2.2	Real Lepton Efficiencies . . . . .	90
5.1.3	Lepton fake rate in a Quantum Chromo-Dynamics (QCD) en- riched region . . . . .	94
5.1.3.1	Lepton Fake Rates . . . . .	107
5.2	Electron and Muon Fakes in the Di-lepton Control Region . . . . .	112
5.3	Hadronic Tau Fake Rates . . . . .	116
5.3.1	Measuring $jet \rightarrow \tau$ fake rate using $Z \rightarrow e^+e^-/Z \rightarrow \mu^+\mu^- + jets$	118

5.3.1.1	Tau fake rates . . . . .	124
5.3.2	Measuring the $jet \rightarrow \tau$ fake rate using $W \rightarrow e + jets$ and $W \rightarrow \mu + jets$ events . . . . .	129
5.3.3	Tau fake rates measured in $W$ events . . . . .	130
5.3.4	Tau fake rates comparison . . . . .	139
5.4	Lepton and Tau Fake Yields in the Lepton Plus Tau Control Region .	140
5.5	Future Strategies for Measuring Fake Rates . . . . .	150
5.6	Summary of the Fake Rate Measurements . . . . .	151
<b>6</b>	<b>Top Candidates, Cross sections and Their Ratios</b>	<b>154</b>
6.1	Control Region for $t\bar{t}$ Events . . . . .	155
6.1.1	Control Region Event Selection . . . . .	155
6.1.2	Selected Event in a $t\bar{t}$ Control Region . . . . .	159
6.1.3	Control Region Yields . . . . .	162
6.2	Signal Region Event Selection . . . . .	162
6.2.1	Signal Region Yield . . . . .	165
6.2.2	Selected $t\bar{t}$ Events . . . . .	166
6.3	Cross section and Ratio Measurements . . . . .	166
6.3.1	Cross Sections . . . . .	168
6.3.2	Top Signal Efficiency Measurement using MC . . . . .	169
6.4	Systematic Uncertainties . . . . .	171
6.4.1	Systematic Tools . . . . .	174
6.4.1.1	Systematic Uncertainties from $t\bar{t}$ Modelling . . . . .	176
6.4.2	Measuring the Systematic Uncertainties on the Partial Cross-Sections . . . . .	177
6.5	Top Cross Section Ratio Measurement . . . . .	179
6.6	Future Analysis Extensions . . . . .	182

6.7 Summary of Results . . . . .	184
<b>Bibliography</b>	<b>186</b>

# Acronyms

**ADC** Analogue to Digital Conversion

**ALFA** Absolute Luminosity for ATLAS

**ALICE** A Large Ion Collider Experiment

**AOD** Analysis Object Data

**ATLAS** A Toroidal LHC ApparatuS

**BDT** Boosted Decision Tree

**BSM** Beyond Standard Model

**CB** Combined Algorithm

**CDF** Collider Detector at Fermilab

**cMSSM** Constrained MSSM

**CERN** European Organisation for Nuclear Research

**CIS** Charge Injection System

**CKM** Cabibbo–Kobayashi–Maskawa

**CMB** Cosmic Microwave Background

**CMBR** Cosmic Microwave Background Radiation

**CMS** Compact Muon Solenoid

**CPV** Charge-Parity Violation

**CSC** Cathode Strip Chamber

**CTP** Central Trigger Processor

**DAQ** Data Acquisition System

**DQ** Data Quality

**EM** Electromagnetic  
**EMEC** Electromagnetic End-cap Calorimeter  
**EF** Event Filter  
**ESD** Event Summary Data  
**FCal** Forward Calorimeter  
**FCal1** Forward Calorimeter 1  
**FCal2** Forward Calorimeter 2  
**FCal3** Forward Calorimeter 3  
**FEB** Front End Board  
**FSR** Final State Radiation  
**GRL** Good Runs List  
**GUT** Grand Unifying Theory  
**HCal** Hadronic Calorimeter  
**HEC** Hadronic End-cap Calorimeter  
**HEC1** Hadronic End-cap Calorimeter 1  
**HEC2** Hadronic End-cap Calorimeter 2  
**HEP** High Energy Physics  
**HLT** High Level Trigger  
**ID** Inner Detector  
**IP** Interaction Point  
**ISR** Initial State Radiation  
**ITC** Intermediate Tile Calorimeter  
**JES** Jet Energy Scale  
**JER** Jet Energy Resolution  
**JRE** Jet Reconstruction Efficiency  
**L1** Level 1  
**L1A** Level-1 Accept  
**L2** Level 2

**L3** Level 3

**LAr** Liquid Argon

**LEP** Large Electron–Positron Collider

**LHC** Large Hadron Collider

**LHCb** Large Hadron Collider – Beauty

**Linac 2** Linear Accelerator 2

**LSP** Lightest Stable SUSY Particle

**LUCID** LUminosity measurement using Čerenkov Integrating Detector

**MBTS** minimum bias trigger scintillator

**MC** Monte Carlo

**MCFM** Monte Carlo for FeMtobarn processes

**MDT** Muon Drift Tube chamber

**MIP** Minimum Ionising Particle

**MLE** Maximum Likelihood Estimator

**MS** Muon Spectrometer

**MSSM** Minimally Supersymmetric Standard Model

**MuID** Inner Detector Reconstructed Muons

**MWPC** Multi-wire Proportional Chamber

**ND** Non-Diffractive

**NIM** Nuclear Instrumentation Module

**NIEL** Non Ionising Energy Loss

**NLO** Next-to-Leading Order

**NNLO** Next-to-next-to-Leading Order

**PID** Particle Identification

**PDF** Parton Distribution Function

**PDG** Particle Data Group

**PMT** Photo Multiplier Tube

**PS** Proton Synchrotron

**PSB** Proton Synchrotron Booster  
**PV** Primary Vertex  
**QCD** Quantum Chromo-Dynamics  
**QED** Quantum Electro-Dynamics  
**QFT** Quantum Field Theory  
**QGP** Quark-Gluon Plasma  
**RF** Radio Frequency  
**RoI** Region of Interest  
**RPC** Resistive Plate Chamber  
**RPC1** Resistive Plate Chamber 1  
**RPC2** Resistive Plate Chamber 2  
**RPC3** Resistive Plate Chamber 3  
**SA** Standalone Algorithm  
**SCT** Semi-Conductor Tracker  
**SPS** Super Proton Synchrotron  
**SM** Standard Model  
**SUSY** Supersymmetry  
**TGC** Thin Gap Chamber  
**ToT** Time over Threshold  
**TOTEM** TOTal cross section, Elastic scattering and diffraction dissociation Measurement at the LHC  
**TRT** Transition Radiation Tracker  
**UV** Ultra Violet  
**UE** Underlying Event  
**VEV** Vacuum Expectation Value  
**ZDC** Zero Degree Calorimeter

# List of Figures

1.1	The LHC is a 27 km particle accelerator and accelerates protons and heavy ion beams up to a nominal 7 TeV in opposing directions around the ring [5]. . . . .	2
2.1	The ATLAS detector. The inner detector has a low total thickness in radiation lengths and good transverse momentum resolution. The solenoid has a magnetic field of 2T. The energy resolutions of the electromagnetic and hadronic calorimeters contribute to particle identification, $p_T$ measurements and $E_T^{\text{miss}}$ measurements. The muon chambers provide muon Particle Identification (PID) and triggering. The superconducting air-core toroids have 0.5T and 1T magnetic fields in the barrel and end-caps respectively, and bend the muon tracks so that their $p_T$ can be measured [10]. . . . .	6
2.2	Plan view of a quarter of the Inner Detector giving the dimensions of detector barrels and disks, and services [11]. . . . .	7
2.3	Relative momentum resolution as a function of $p_T$ for Inner Detector (ID) tracks, Muon Spectrometer (MS) tracks, and combined muons [12] (see section 4.1.2 for details on the different muon definitions). Momentum resolution increases with increasing $p_T$ due to stiffer tracks making the measurement of the sagitta more difficult. Adding the Transition Radiation Tracker (TRT) hits to tracks improves the resolution by increasing the lever arm. . . . .	10
2.4	The Inner Detector material distribution in radiation lengths as a function of $\eta$ divided down into the detectors and combined services [11]. . . . .	11
2.5	Number of pixel clusters vs. the number of reconstructed primary vertices per bunch crossing. Pixel clustering is stable for an increasing amount of pile-up, and is well modelled by PYTHIA 8 MC in all regions of the Pixel detector [16]. . . . .	12

2.6	Bi-dimensional distribution of $dE/dx$ vs. charge times momentum for high quality tracks with 4 or more good pixel clusters. Superimposed on the distributions are fitted probability distributions of pions (black, inner pair), kaons (gray, middle pair) and protons (blue, outer pair), showing the quality of PID, see [17] for further details. . . . .	13
2.7	The number of pixel, SCT and TRT hits and missing SCT hits (SCT holes) for tracks that meet the robust requirements (outlined in [19]), normalised to the same number of tracks. . . . .	15
2.8	Average number of reconstructed primary vertices as a function of the average number of interactions per bunch crossing ( $\mu$ ) in 2011 data [19]. . . . .	16
2.9	Cutaway showing the electromagnetic and hadronic liquid Argon calorimeters, the hadronic tile calorimeters, and forward calorimeters [11]. . .	17
2.10	Estimate for the interaction lengths of ATLAS calorimetry as a function of pseudo-rapidity [21]. . . . .	18
2.11	The invariant mass distribution of $Z \rightarrow e^+e^-$ events for electrons with $ \eta  < 2.47$ in $40 \text{ pb}^{-1}$ of data taken at $\sqrt{s} = 7 \text{ TeV}$ in 2010 with ATLAS [22]. . . . .	18
2.12	Electromagnetic calorimeter barrel section showing its accordion shape. [11]. . . . .	20
2.13	Timing resolution of electrons in the middle layer of the Electromagnetic (EM) barrel calorimeter taken from $W \rightarrow e\nu_e$ candidate events as a function of energy deposited in the cell in data in 2011 $\sqrt{s} = 7 \text{ TeV}$ proton-proton collisions [24]. . . . .	21
2.14	Structure of the HEC between plates. [11]. . . . .	24
2.15	The ATLAS detector with the four muon spectrometer sub-detectors highlighted [11]. . . . .	25
2.16	Cross section through a Resistive Plate Chamber [11]. . . . .	27
2.17	The efficiency of e22vh_medium1 relative to offline medium++ electrons (see section 4.1.1 for more details on electrons) was measured using a $Z \rightarrow e^+e^-$ tag and probe study as a function of the number of primary vertices in the event for Level 1 (L1), Level 2 (L2) and Event Filter (EF) triggers [30]. . . . .	31
3.1	The fundamental particles of the SM: the three generations of leptons and quarks, the gauge bosons and the Higgs scalar boson [42]. . . . .	35

3.2	The tau branching fractions calculated by the Particle Data Group (PDG) [9]. . . . .	38
3.3	The four leading order strong interaction production modes of $t\bar{t}$ pairs. Diagram a) is from $q\bar{q}$ annihilation, b) from gluon-gluon fusion, c) and d) via top quark exchange. . . . .	43
3.4	In the decay of the top quark there are three leptonic decay modes, and two quark decay modes each with three possible strong colour charges each. The top quarks depicted here decay to b-quarks: decays to the lower mass quarks are very rare. . . . .	45
3.5	The Feynman diagram of a top quark decaying to a b-quark, and a charged Higgs boson which decays to a tau and a tau neutrino. . . . .	53
3.6	ATLAS mass exclusions for various Supersymmetry (SUSY) particles and other exotic processes as published in [96]. . . . .	57
4.1	The b-tag efficiency using at function of $p_T$ the MV1 b-tagging algorithm at the nominal 70% efficiency. [119] . . . . .	64
4.2	Templates for light-flavour jets, b-jets and c-tagged jets were created in data as a function $p_T^{rel}$ (the momentum of a muon transverse to a muon plus jet axis) fitted to data before and after the application of the MV1 algorithm with a 70% efficiency [119]. . . . .	65
4.3	Tau BDT score for QCD di-jets from data reconstructed as taus, and taus from MC. A higher score indicates a higher probability of having a real single-pronged tau instead of a jet [120]. . . . .	66
4.4	Efficiencies as functions of the off-line $p_T$ (a)) and $\eta$ (b)) for lowest unpre-scaled triggers (e20_medium, e22_medium and e22vh_medium1 triggers respectively) in periods B-H, I-K and L-M as measured in [30].	75
4.5	Trigger efficiency for the mu18_medium trigger for $ \eta  < 1.05$ as measured in [32]. . . . .	75
5.1	Di-lepton invariant mass plots in $Z \rightarrow e^+e^-$ (a)) and $Z \rightarrow \mu^+\mu^-$ (b)) events for data and MC for samples used for tag and probe studies of lepton efficiencies. . . . .	91
5.2	Real electron efficiencies for data and MC, no scale-factors have been applied to the MC samples to correct for detector effects. . . . .	92
5.3	Real muon efficiencies for data and MC, no scale-factors have been applied to the MC samples to correct for detector effects. . . . .	93

5.4	Lepton efficiency as a function of run period for electrons (a)) and muons (b)). . . . .	95
5.5	Electron efficiency as a function of $\eta$ measured using $Z \rightarrow ee$ events in data and MC using $40 \text{ pb}^{-1}$ of data in 2010, as measured in [22]. . .	96
5.6	Muon efficiency as a function of $p_T$ for data and MC measured using $40 \text{ pb}^{-1}$ of data taken in 2010. The efficiency was measured using the tag-and-probe method using a selection of $Z \rightarrow \mu\mu$ events for Inner Detector Reconstructed Muons (MuID) combined muons in [146] using similar muon definitions and overlap removal to that defined in 4.1.2 and 4.3 respectively. . . . .	96
5.7	$E_T^{\text{miss}}$ distribution for events with a single electron (a) and muon (b). . . . .	100
5.8	$m_T$ distribution for events with a single electron (a) and muon (b). . . . .	101
5.9	$\Delta R$ between probe lepton and the nearest jet for data and MC after the cuts in table 5.3 have been applied. An increase of low $\Delta R$ leptons data is apparent. . . . .	102
5.10	Number of jets in events with secondary electrons associated with hadronic jets for data and MC. . . . .	103
5.11	Number of jets in events with secondary muons associated with hadronic jets for data and MC. . . . .	104
5.12	Jet $p_T$ of reconstructed jet with smallest $\Delta R$ of a reconstructed electron for data and MC. . . . .	105
5.13	Jet $p_T$ of jets within $\Delta R < 0.6$ of a reconstructed muon for data and MC. . . . .	106
5.14	Electron fake rates in events with secondary electrons associated with hadronic jets. The error bands indicate the statistical uncertainty. . .	108
5.15	Muon fake rates in events with secondary muons associated with hadronic jets. The error bands indicate the statistical uncertainty. . .	109
5.16	The lepton fake rates per period. . . . .	111
5.17	Number of b-jets ((a) and (b)) and jets ((c) and (d)) in the electron channel and the muon channel respectively in events with $E_T^{\text{miss}} < 40 \text{ GeV}$ . . . . .	113
5.18	Lepton $p_T$ distributions in the electron triggered channel ((a) and (b)) and the muon triggered channel ((c) and (d)) in events with $E_T^{\text{miss}} < 40 \text{ GeV}$ . . . . .	114

5.19	The $E_T^{\text{miss}}$ distributions in the di-lepton control region before the $E_T^{\text{miss}}$ cut. . . . .	115
5.20	Two events are represented with five hadronic objects. The event on the left contains one fake hadronic tau, and the event on the right does not. . . . .	117
5.21	Di-lepton invariant mass plots for $Z$ events used to measure tau fake rates. . . . .	120
5.22	The distributions of the numbers of jets ((a) and (c)) and b-jets ((b) and (d)) in $Z \rightarrow e^+e^- + \text{jets}$ events (a) and b)) and $Z \rightarrow \mu^+\mu^- + \text{jets}$ events (c) and d)) before any tau selection has been applied comparing data and MC. . . . .	121
5.23	Lead jet $p_T$ in $Z \rightarrow e^+e^-$ (a))and (b)) $Z \rightarrow \mu^+\mu^-$ events before any tau selection has been applied comparing data and MC. . . . .	122
5.24	Tau lepton $p_T$ distributions in $Z \rightarrow e^+e^- + \text{jets}$ events and $Z \rightarrow \mu^+\mu^- + \text{jets}$ events comparing data and MC. . . . .	123
5.25	Total number of jets before and after a cut on the number of hadronic taus in $Z \rightarrow e^+e^- + \text{jets}$ events ((a) and (b)) and $Z \rightarrow \mu^+\mu^- + \text{jets}$ events ((c) and (d)) comparing data and MC. . . . .	124
5.26	Tau fake rate as a function of number of jets in the event shown for $Z \rightarrow e^+e^- + \text{jets}$ (a)) and $Z \rightarrow \mu^+\mu^- + \text{jets}$ (b)). . . . .	126
5.27	The yield of events for $Z \rightarrow e^+e^- + \text{jets}$ (a) and $Z \rightarrow \mu^+\mu^- + \text{jets}$ (b) with fake positively and negatively charged reconstructed tau leptons. 127	127
5.28	Tau fake rate as a function of number of jets in the event combining the electron and muon channels, separating the fake rates for positive taus and negative taus. . . . .	128
5.29	The $m_T$ distribution in $W \rightarrow e\nu$ (a)) and $W \rightarrow \mu\nu$ (b)) events comparing data and MC. . . . .	131
5.30	The $E_T^{\text{miss}}$ distribution in $W \rightarrow e\nu$ (a)) and $W \rightarrow \mu\nu$ (b)) events comparing data and MC. . . . .	132
5.31	Jet and b-jet distributions in $W \rightarrow e\nu$ events before any hadronic tau selection has been applied, comparing data and MC. . . . .	133
5.32	Jet and b-jet distributions in $W \rightarrow \mu\nu$ events before any hadronic tau selection has been applied, comparing data and MC. . . . .	134

5.33	Total number of jets before (a) and after (b) a cut on the number of hadronic taus in $W \rightarrow e + \text{jets}$ events comparing data and MC. . . . .	135
5.34	Total number of jets before (a) and after (b) a cut on the number of hadronic taus in $W \rightarrow \mu + \text{jets}$ events comparing data and MC. . . . .	136
5.35	Tau fake rate as a function of number of jets in the event for electron channel (a)) and muon channel (b)) events comparing data and MC. . . . .	137
5.36	Tau fake rate as a function of number of jets in the event with the electron and muon channels combined comparing data and MC. . . . .	138
5.37	Tau fake rates measured using $Z$ and $W$ tagged events respectively. For each the electron and muon trigger channels have been combined for both samples. . . . .	139
5.38	Lead lepton $p_T$ for the electron channel (a) and muon channel (b) in the lepton plus tau control region, comparing data and the predicted background distributions. . . . .	142
5.39	The number of jets in the electron and muon trigger channels in the lepton plus tau control region, comparing data and the predicted signal plus background distributions. . . . .	144
5.40	Number of b-jets in the electron and muon trigger channels in the lepton plus tau control region, comparing data and the predicted signal plus background distributions. . . . .	145
5.41	The lead jet $p_T$ distributions for the electron and muon trigger channels in the lepton plus tau control region, comparing data and the predicted signal plus background distributions. . . . .	147
5.42	The $E_T^{\text{miss}}$ distributions for the electron and muon trigger channels before any $E_T^{\text{miss}}$ cut. A band indicates the effect of a systematic shift in the tau fake rate, but does not include other systematic errors. . . . .	148
5.43	The $\Sigma p_T$ distributions for the electron and muon trigger channels before any $E_T^{\text{miss}}$ cut. A band indicates the effect of a systematic shift in the tau fake rate, but does not include other systematic errors. . . . .	149
6.1	Number of b-jets in the control region for the electron triggered channels ( $e\mu$ (a), $e\tau$ (b)) and the muon triggered channels ( $\mu e$ (c), $\mu\tau$ (d)) before any cut on $\Sigma p_T$ or $E_T^{\text{miss}}$ . The di-lepton channel figures (a) and (b) were previously seen in figure 5.17, and the lepton plus channel figures (c) and (d) are repeated from 5.40. They depicted again for comparison purposes. . . . .	156

6.2	The $\Sigma p_T$ of all tracks in the control region for the electron triggered channels ( $e\mu$ a), $e\tau$ b)) and the muon triggered channels ( $\mu e$ c), $\mu\tau$ d) before any cut on $\Sigma p_T$ or $E_T^{\text{miss}}$ . The lepton plus channel figures (c) and (d) are repeated from 5.43. They depicted again for comparison purposes. . . . .	157
6.3	The $E_T^{\text{miss}}$ distributions in the control region for the electron triggered channels ( $e\mu$ a), $e\tau$ b)) and the muon triggered channels ( $\mu e$ c), $\mu\tau$ d) after the $\Sigma p_T$ cut. The lepton plus channel figures (c) and (d) are repeated from 5.42. They depicted again for comparison purposes. . .	158
6.4	The $p_T$ of the triggered electron (a)) and muon (b)) in the low $E_T^{\text{miss}}$ region with no b-jet requirements. . . . .	159
6.5	The number of jets in the events for electron (a)) and muon (b)) triggered events in the low $E_T^{\text{miss}}$ region with no b-jet requirements. .	160
6.6	The number of b-jets in the events for electron (a)) and muon (b)) triggered events in the low $E_T^{\text{miss}}$ region. . . . .	161
6.7	The $\Sigma p_T$ of all tracks in the signal region for the electron triggered channels ( $e\mu$ a), $e\tau$ b)) and the muon triggered channels ( $\mu e$ lower left, $\mu\tau$ lower right) before any cut on $\Sigma p_T$ or $E_T^{\text{miss}}$ . . . . .	163
6.8	The $E_T^{\text{miss}}$ of all tracks in the signal region for the electron triggered channels ( $e\mu$ a), $e\tau$ b)) and the muon triggered channels ( $\mu e$ c), $\mu\tau$ d) before the $E_T^{\text{miss}}$ cut. . . . .	164
6.9	The number of jets in the events for electron (a)) and muon (b)) triggered events in the signal region. . . . .	167
6.10	The $p_T$ of the triggered electron (a)) and muon (b)) in the signal region.	168
6.11	The $E_T$ of the lead jet for the electron (a)) and muon (b)) triggered events in the signal region. . . . .	169
6.12	The $\Sigma E_T$ of all selected objects for the electron (a)) and muon (b)) triggered events in the signal region. . . . .	170

# List of Tables

2.1	TRT parameters for both sides of the barrel and an individual end-cap [6]. . . . .	9
3.1	The masses, charges and spins of the three charged leptons and their uncharged neutrino partners [9]. . . . .	36
3.2	The masses, charges and spins of the six quarks. The b-quark mass is quoted in the $\overline{MS}$ scheme and the top from direct measurements [9].	36
3.3	The masses, charges and spins of the three charged leptons and their uncharged neutrino partners [9]. . . . .	37
3.4	The branching fractions for all final state channels calculating using the PDG values of the single particle branching fractions of the $W$ and tau. . . . .	46
3.5	The branching fractions of the final state leptons broken down into the contributions from the initial decay products of the $W$ , calculated using the PDG values [9]. All values and errors are absolute. . . . .	47
3.6	The ratios of branching fractions as calculated using PDG branching fractions for the $W$ for various branching fractions of the top to a charged Higgs. The efficiency of such events would not be expected to be the same and measurements looking for this signal would need to include this correction. All uncertainties are absolute and only include those propagated from the PDG branching fraction measurements [9].	56
4.1	Summary of the $t\bar{t}$ signal region selection cuts explained in detail in section 4.4 for electron triggered events. The cuts are identical except for the number of leptons selected. . . . .	77
4.2	Summary of the $t\bar{t}$ signal region selection cuts explained in detail in section 4.4 for muon triggered events. The cuts are identical except for the number of leptons selected. . . . .	78

4.3	Proportion of each channel in the non-fully-hadronic $t\bar{t}$ MC samples based on the final state of the leptons in the event, including those from the decay of a tau. Only hadronically decaying taus are included in the tau channels. Values derived from PDG $W$ decay branching fractions are included [9]. The errors for PDG derived values are from combining the experimental errors quoted in the PDG. For the branching fractions, only the statistical error from the total number of events is included, a complete estimate would include errors similar to those quoted for the PDG value. . . . .	81
5.1	Event selection for a high purity sample of $Z \rightarrow e^+e^-$ and $Z \rightarrow \mu^+\mu^-$ events with one randomly selected loose lepton used to probe the real lepton efficiencies. . . . .	89
5.2	The absolute systematic errors on the electron and muon efficiencies.	94
5.3	Cuts to select events with a single lepton while cutting out $W$ decays to leave a majority of QCD events. . . . .	98
5.4	The absolute systematic error on the electron and muon fake rates. .	110
5.5	Cut flow to select $Z \rightarrow e^+e^-$ events and $Z \rightarrow \mu^+\mu^-$ events to measure the $jet \rightarrow \tau$ fake rate. . . . .	119
5.6	Cut flow selection of $W \rightarrow e\nu$ and $W \rightarrow \mu\nu$ events used to measure the $jet \rightarrow \tau$ fake rate. . . . .	129
5.7	Data yields and predicted signal and background yields for each $t\bar{t}$ channel measured in a low $E_T^{\text{miss}}$ region with no b-tag requirements. .	150
6.1	Data yields and predicted signal and background yields for each $t\bar{t}$ channel in the signal region with 2 b-tagged jets and $E_T^{\text{miss}} > 40$ GeV.	166
6.2	Signal $t\bar{t}$ efficiencies, relative to the previous cut, measured using MC inclusive of the detector acceptance for leptons, hadronic taus and jets.	171
6.3	Signal $t\bar{t}$ efficiencies, relative to the previous cut, measured using MC inclusive of the detector acceptance for leptons, hadronic taus and jets.	172
6.4	The calculated cross-sections, and the POWHEG systematic uncertainty from the comparison between an MC@NLO and a POWHEG $t\bar{t}$ samples, the ALPGEN systematic uncertainty from the comparison between an MC@NLO and a ALPGEN $t\bar{t}$ samples. The average generator systematic uncertainty is included in the total systematic uncertainty. All uncertainties are absolute. . . . .	178

6.5	The calculated cross-sections, their respective individual systematic uncertainties, the statistical uncertainty, the total systematic uncertainty, and the luminosity uncertainty. All uncertainties are absolute.	179
6.6	Comparison of the partial cross sections predicted using the Compact Muon Solenoid (CMS) $t\bar{t}$ production cross section result [56] and the branching ratios inferred from the PDG, with the calculated cross-sections.	180
6.7	The calculated ratios, their respective individual systematic uncertainties, the total statistical uncertainty, and the statistical uncertainty. All uncertainties are absolute.	181
6.8	The calculated ratios compared to those calculated from MC and PDG branching fractions. All uncertainties are absolute.	182
6.9	Partial cross section ratio estimates using the charged Higgs MC with branching fractions given in the table. Because the MC is treated like $t\bar{t}$ signal MC, this takes into account the difference between the charged Higgs and top reconstruction efficiencies. The $t\bar{t}$ branching fractions were reduced to ensure the total branching fraction was unity in each case. The uncertainties only include the MC statistical errors.	182
6.10	The ratio of the measured cross-section ratios to values inferred from the PDG calculated in section 3.5.2 (see [9]).	183

# Chapter 1

## Introduction

The Large Hadron Collider (LHC) is a 27 km circular proton-proton collider at the European Organisation for Nuclear Research (CERN) laboratory. It began operation in November 2009, and at the end of 2011 had reached a centre of mass energy of  $\sqrt{s} = 7$  TeV and an instantaneous luminosity of  $0.36 \times 10^{34} \text{cm}^{-2} \text{s}^{-1}$ . Up to the end of the 2011 data taking period  $\sim 5.6 \text{fb}^{-1}$  of integrated luminosity was delivered to two of the experiments, A Toroidal LHC ApparatuS (ATLAS) and the Compact Muon Solenoid (CMS).

In 2012, the proton-proton ( $p-p$ ) centre of mass energy increased to  $\sqrt{s} = 8$  TeV and the LHC delivered  $23.3 \text{fb}^{-1}$  of integrated luminosity. They initially produced by ionising an  $\text{H}_2$  source and accelerated to increasing energies in the Linear Accelerator 2 (Linac 2), Proton Synchrotron Booster (PSB), Proton Synchrotron (PS) and finally the Super Proton Synchrotron (SPS) accelerates the protons to 450 GeV before injection into the LHC [3]. Each filling sequence is repeated 12 times for each LHC ring before being accelerated to the nominal energy.

Protons are injected and accelerated in bunches containing typically  $1.2 \times 10^{11}$  protons [4]. They are focused by LHC magnets and collided in ATLAS at a small crossing angle of around a few milli-radians. The small volume in which these interactions occur is known as the Interaction Point (IP), and the vertex formed by tracks origi-

nating from this is known as the Primary Vertex. Proton bunches are injected as part of bunch trains, with spacings of 50 ns between bunches.

The four large experiments are situated at collision points around the ring (see figure 1.1). A Large Ion Collider Experiment (ALICE) is designed to look at Pb-Pb collisions (as well as proton-proton collisions) for studying properties of the Quark-Gluon Plasma (QGP), ATLAS is a general purpose experiment designed for discovery of new physics, CMS is another general purpose experiment, and Large Hadron Collider – Beauty (LHCb) is an experiment designed to make precision measurements of bottom physics and Charge-Parity Violation (CPV).

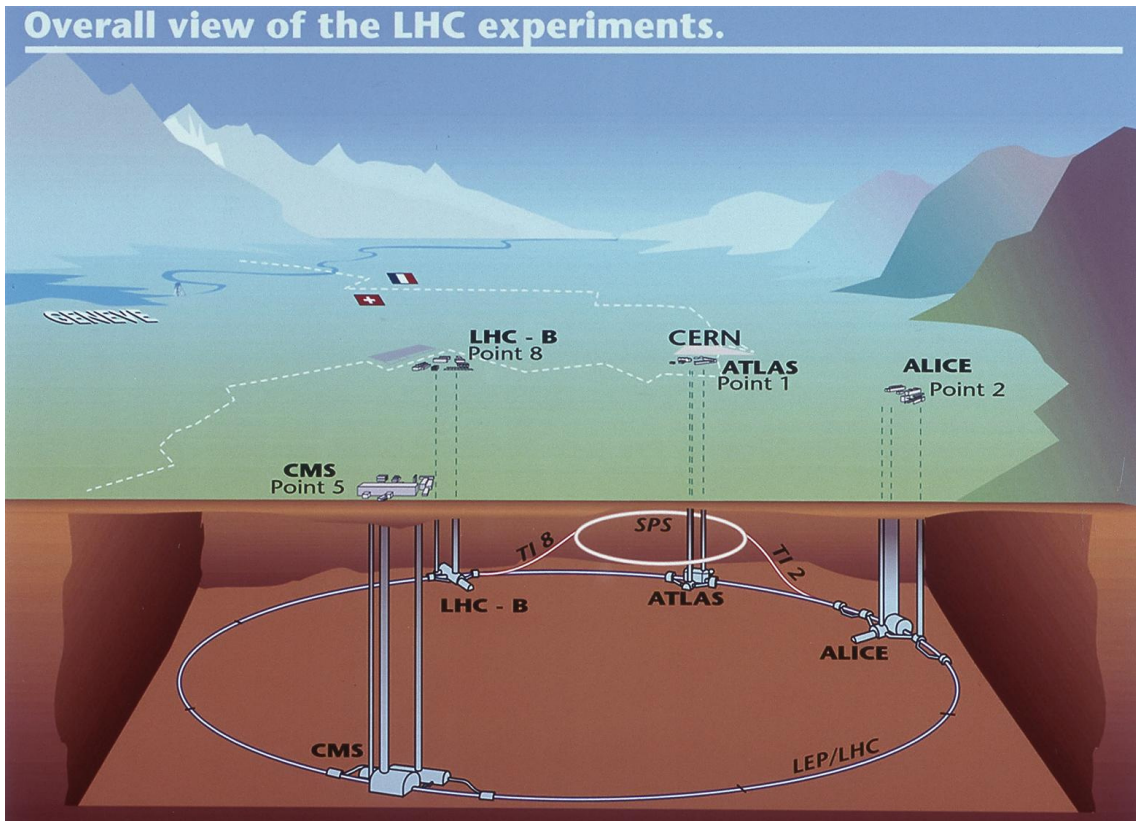


Figure 1.1: The LHC is a 27 km particle accelerator and accelerates protons and heavy ion beams up to a nominal 7 TeV in opposing directions around the ring [5].

Searching for new physics requires several general strategies. This includes precision measurements of cross sections and particle masses, well understood physics processes, that can be studied for deviations from Standard Model (SM) expectations. A complementary strategy is to search for Beyond Standard Model (BSM)

physics that might be directly observable at the TeV scale such as the Minimally Supersymmetric Standard Model (MSSM). Open searches, that look for theoretically unexpected signatures, attempt to ensure that a lack of a pre-existing theoretical model does not prevent new discoveries. All of these strategies require a versatile detector.

Only long lived particles can be directly observed in the detector. These include charged leptons such as the electron, and the heavier muon and tau, which are described in section 3.1. The proton and neutron are both stable hadrons which can be directly observed from the energy deposits they leave. They are both composed of two types of quark, the up and down quark. Other hadrons, such as pions, can be composed of other quark combinations and can also live long enough to interact directly with the detector. It is also possible to infer the presence of neutrinos, uncharged partners of the leptons, from missing transverse energy ( $E_T^{\text{miss}}$ , see section 4.1.6). See section 3.1 for a longer discussion on the SM particles.

The ATLAS detector was designed to meet certain specifications. It has a high efficiency and purity for detection of stable leptons and hadron decay products, and has a good transverse momentum ( $p_T$ , the momentum transverse to the direction of the beam in the  $x$ - $y$  plane)<sup>1</sup> and energy resolution to allow reconstruction of different particle. Good energy resolution and high angular segmentation give a precise measurement of missing transverse energy and direction. It also is hermetic to allow studies of processes that occur at very high and very low pseudo-rapidity<sup>2</sup>. Finally, it has an efficient and versatile trigger system that can identify processes of interest, and that can discriminate between events from the high rate of hadronic events from a Quantum Chromo-Dynamics (QCD) background.

---

<sup>1</sup>ATLAS uses a right-handed coordinate system with its origin defined as the nominal IP for proton-proton collisions. The positive  $x$ -direction is from the interaction point to the centre of the LHC ring, and the positive  $y$  direction is vertically up, while the beam-line defines the  $z$ -axis. The A-side of the detector is defined as the positive  $z$  direction, and C is the opposite side. The azimuthal angle  $\phi$  is around the beam axis, and the polar angle  $\theta$  is the angle from the beam axis [6].

<sup>2</sup>Rapidity for a massive particle is defined as  $y = 1/2 \ln [(E + p_z)/(E - p_z)]$  and is useful because particles are produced roughly uniformly as a function of rapidity. In the ultra-relativistic limit rapidity can be approximated by pseudo-rapidity which is defined as  $\eta = -\log \tan(\theta/2)$  and is independent of the incoming particle kinematics.

Because of the high instantaneous luminosity, the maximum number of collisions per bunch crossing were  $\sim 20$  [4]. When a hard scattering interaction occurs, this is amongst a background of soft, minimum bias, QCD events that have low transverse momentum, and have a high track multiplicity. These background events are known as pile-up. Because of the large size of the detectors, particles produced from the proton-proton collisions can still be traversing the detector when the next collision occurs. These are known as out-of-time pile-up. While the Radio Frequency (RF) cavities which accelerate the protons have a period of 2.5 ns a much shorter bunch spacing that 50 ns would make it too difficult to ascertain which collision event a particle originated from.

Because of the high level of pile-up the ATLAS detector must be radiation hard and be able to trigger and reconstruct hard scattering events in this environment. The various ATLAS sub-detectors minimise the effect of pile-up on the recorded data including minimising charge collection times, and introducing a minimum period a several bunch crossings before reading more data from the detector.

In 2012 the two general purpose LHC experiments, ATLAS and CMS, reported independent  $\sim 5\sigma$  excesses in various channels consistent with a SM Higgs boson (see [7] and [8]). The high specifications of the detectors proved their worth in pushing the boundaries of particle physics.

The ATLAS detector, explained in detail in chapter 2, collected the data from which the  $t\bar{t}$  events discussed in this thesis are reconstructed. Chapter 3 has an overview of particle physics theory and current experimental observations. In chapter 5 the matrix method for measuring the electron and muon fake rates in the signal region is explained; the tau fake rates in the signal region are also measured. In chapter 4 the method for selecting top quark pair ( $t\bar{t}$ ) events is explained in detail and the cross section ratios measured in data.

# Chapter 2

## The ATLAS experiment at the LHC

The ATLAS detector (see figure 2.1) has nearly  $4\pi$  of angular coverage (close to a hermetic detector), is capable of high resolution charged particle tracking, and has good electro-magnetic and hadronic jet energy resolution. ATLAS' tracking detector, the Inner Detector, is composed of three detector systems with a low thickness in number of radiation lengths<sup>1</sup>. The innermost detector is the Pixel detector which provides good resolution tracking from silicon pixels. Outside this is the Semi-Conductor Tracker (SCT) providing additional space points via pairs of semi-conducting strips. The outermost detector, the Transition Radiation Tracker (TRT), provides additional tracking and Particle Identification (PID). Surrounding the ID is the solenoid magnet producing a 2T axial field that bends the tracks of charged particles in the x-y plane and allows a measurement of their transverse momentum ( $p_T$ ). Outside the solenoid are the liquid Argon calorimeters. The innermost calorimeter is the Electromagnetic (EM) barrel calorimeter designed to collect and measure the energy of light electromagnetically interacting particles such as electrons and photons. Outside this is the Hadronic Calorimeter (HCal) which measures the energy of hadronic jets. Beyond the calorimeters are the muon chambers and the barrel and

---

<sup>1</sup>Radiation length is a property of a material which characterises the amount of matter traversed by electromagnetically interacting particles (usually measured in  $g\text{ cm}^{-2}$ ). For electrons, which lose energy via Bremsstrahlung the radiation length is the distance over which their energy is reduced by  $1/e$ . For photons, which lose energy through producing  $e^+e^-$  pairs, a radiation length is  $7/9$  of the mean free path for pair production [9].

end-cap toroidal magnets. The air-core superconducting barrel and end-cap toroids produce a toroidal magnetic field of 0.5 T and 1 T respectively. The muon system is instrumented with trigger and precision tracking chambers. There are four types of muon spectrometer in use, the Muon Drift Tube chambers (MDTs), the Cathode Strip Chambers (CSCs), the Resistive Plate Chambers (RPCs), and the Thin Gap Chambers (TGCs). A full review of the ATLAS detector design can be found in [6], which formed the basis for the information contained in this chapter.

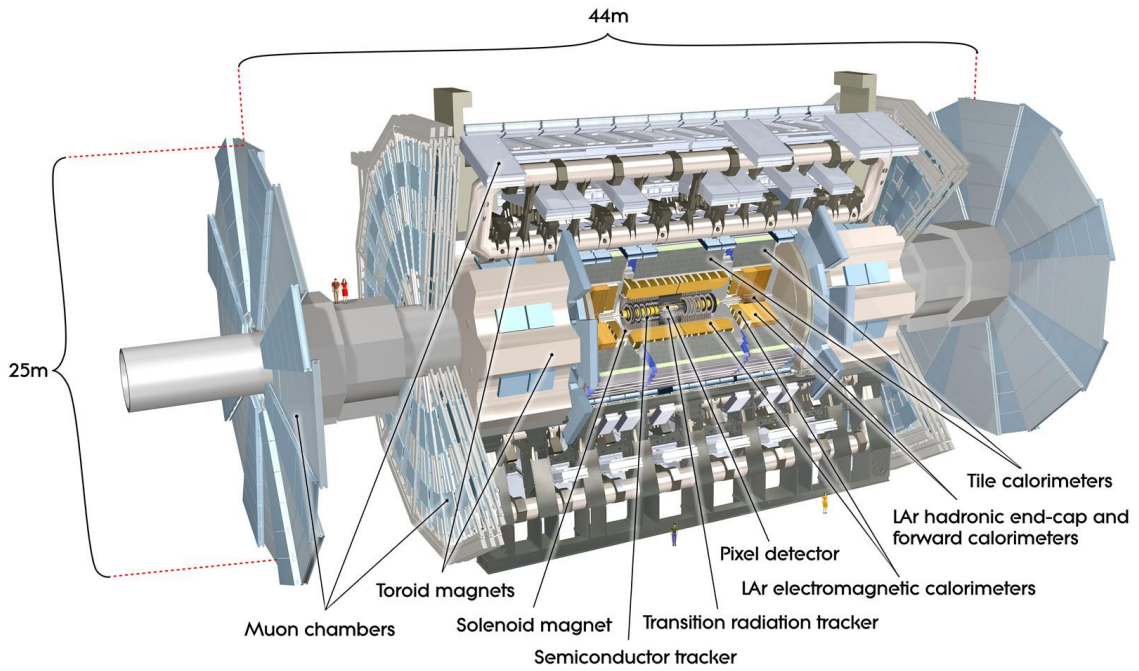


Figure 2.1: The ATLAS detector. The inner detector has a low total thickness in radiation lengths and good transverse momentum resolution. The solenoid has a magnetic field of 2T. The energy resolutions of the electromagnetic and hadronic calorimeters contribute to particle identification,  $p_T$  measurements and  $E_T^{\text{miss}}$  measurements. The muon chambers provide muon PID and triggering. The superconducting air-core toroids have 0.5T and 1T magnetic fields in the barrel and end-caps respectively, and bend the muon tracks so that their  $p_T$  can be measured [10].

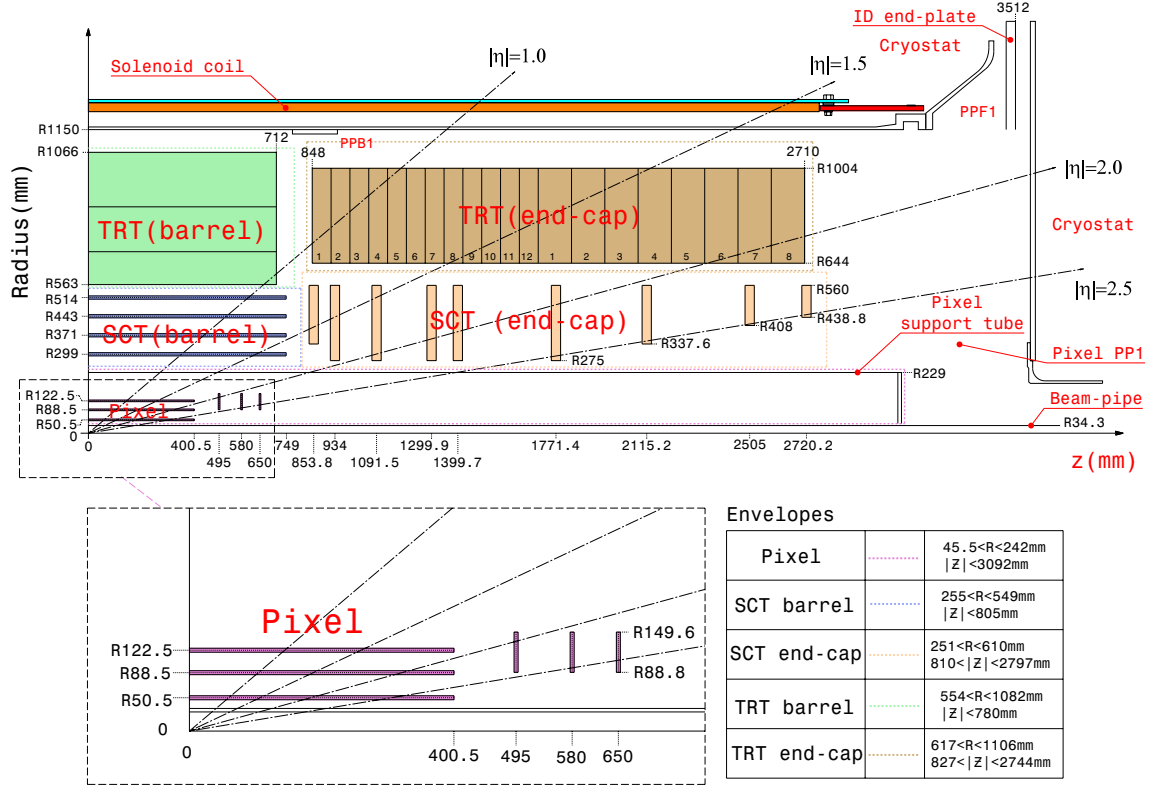


Figure 2.2: Plan view of a quarter of the Inner Detector giving the dimensions of detector barrels and disks, and services [11].

## 2.1 Inner Detector

The Inner Detector is designed to provide high resolution tracking of charged particles in the x-y plane with coverage of  $|\eta| < 2.5$ . The length of the Inner Detector (ID) is 3512 mm and it has a radius of 1150 mm. The solenoid magnet outside of the ID allows a  $p_T$  measurement for charged particle tracks in the range  $0.5 \text{ GeV} < p_T < 100 \text{ GeV}$  in the inner detector. The radius of the detector, its magnetic field, and its angular granularity places the upper limit of  $p_T$  that can be measured.

Three sub-detectors constitute the ID as shown in figure 2.2. Two silicon tracking detectors, the Pixel and SCT, provide very good resolution tracking and fast readout times. The low material distribution of the TRT means it has a low thickness in radiation lengths and provides tracking and PID information at a radius where the

cost of a silicon detector would be prohibitive.

The Pixel detector has 1744 sensors, and each sensor has 47232 pixels. In the barrel each pixel is  $50 \times 400 \mu\text{m}^2$ , and  $50 \times 600 \mu\text{m}^2$  in the end-cap, orientated along  $\phi - z$ . The SCT has 4088 modules in four coaxial cylindrical layers in the barrel region, and two end-caps with 9 disks each. The barrel region consists of 2112 modules, and the end-caps consist of 988 modules each. Each module has four sensors in stereo pairs that are 12 cm long. Each sensor has 768 strips with an  $80 \mu\text{m}$  pitch and a 20 mrad stereo rotation between each sensor pair to provide space-points. The TRT straws have a radius of 4 mm, and a mean spacing between the straws of 7 mm. These are filled with a radiation hard gas mixture composed of 70% Xenon, 27%  $\text{CO}_2$  and 3%  $\text{O}_2$ . The number of straws in each section of the TRT is listed in table 2.1. The anodes of the straws are  $31 \mu\text{m}$  thick tungsten wires under tension. The straw walls are two  $35 \mu\text{m}$  thin multi-layer films each composed of  $25 \mu\text{m}$  polyimide film, coated with a  $0.2 \mu\text{m}$  Al film and a 5–6  $\mu\text{m}$  graphite-polyimide film, and a  $5 \mu\text{m}$  polyurethane layer seals these films together. The fractional  $p_{\text{T}}$  resolution as a function of inner detector track  $p_{\text{T}}$  is shown in figure 2.3 and shows the high resolution for tracks in the ID over a large  $p_{\text{T}}$  range. The fine segmentation of the detector, and accuracy of the magnetic field measurements mean that the momentum resolution is only begins to dominate for transverse momenta greater than  $\sim 100 \text{ GeV}$ . The tracking algorithms take account for the energy loss of particles and multiple scattering with the material in the detector volume, the modelling of these energy losses becomes the limiting factor on the resolution at low momenta [12].

Comparing the rate of energy loss and the momentum of tracks as measured in the ID gives good PID. Reconstruction of decay vertices is used to infer the lifetimes of unstable particles, allowing particles which decay before entering the ID volume to be identified (such as b-hadrons). As the ID is designed for tracking, momentum measurement, and PID of charged particles, but it is not designed to measure the energy of particles, the material budget must be kept as low as is feasible to minimise the energy deposited before the calorimeters, as shown in figure 2.4. Using materials with a low atomic mass like silicon in the pixel and SCT, and gas filled tubes in the

Module Type	$ z _{min}$ /mm	$ z _{max}$ /mm	$R_{min}$ /mm	$R_{max}$ /mm	Number of modules	Number of layers	Straws per module
<b>Barrel</b>	0	780	554	1082	96	73	52544
Type-1 (inner)	400	712.1	563	624	32	9	329
(outer)	7.5	712.1	625	694		10	
Type-2	7.5	712.1	697	860	32	24	530
Type-3	7.5	712.1	863	1066	32	30	793
<b>End-cap</b>	827	2744	615	1106	20	160	122880
Wheels							
Type-A	848	1705	644	1004	12	8	6144
Type-B	1740	2710	644	1004	8	8	6144

Table 2.1: TRT parameters for both sides of the barrel and an individual end-cap [6].

TRT, keeps the material budget low. In addition to the material in active parts of the sub-detectors, materials from services such as cabling and cooling are also present in the ID and need to be measured accurately to correct the energy and momentum of particles for losses in this un-instrumented material. The material of the ID has been measured in collision data by reconstructing the vertices from secondary hadronic interactions [13] against which the modelling of the material is then be directly calibrated. This improves the momentum resolution of tracks with  $p_T < \sim 100$  GeV which is limited by the modelling of multiple particle scattering.

The Pixel and SCT detectors are cooled by the same system with liquid nitrogen to keep the temperature of the silicon sensors at around  $-5^\circ C$  to  $-10^\circ C$ , which minimises radiation damage and keeps the silicon below the temperature needed to be conducting. The TRT is kept at room temperature by heater pads between the TRT and SCT to prevent condensation. The sub-detector was designed to have an operating lifetime of ten years, and the inner pixel layer will be replaced after three years of operation.

The semi-conductor silicon is the active material in the Pixel and SCT sub-detectors. In semi-conductors at low temperatures, electrons are in a low energy state around individual silicon atoms and are unable to conduct electricity. An energy barrier exists which electrons must overcome before they are free charge carriers, this gives

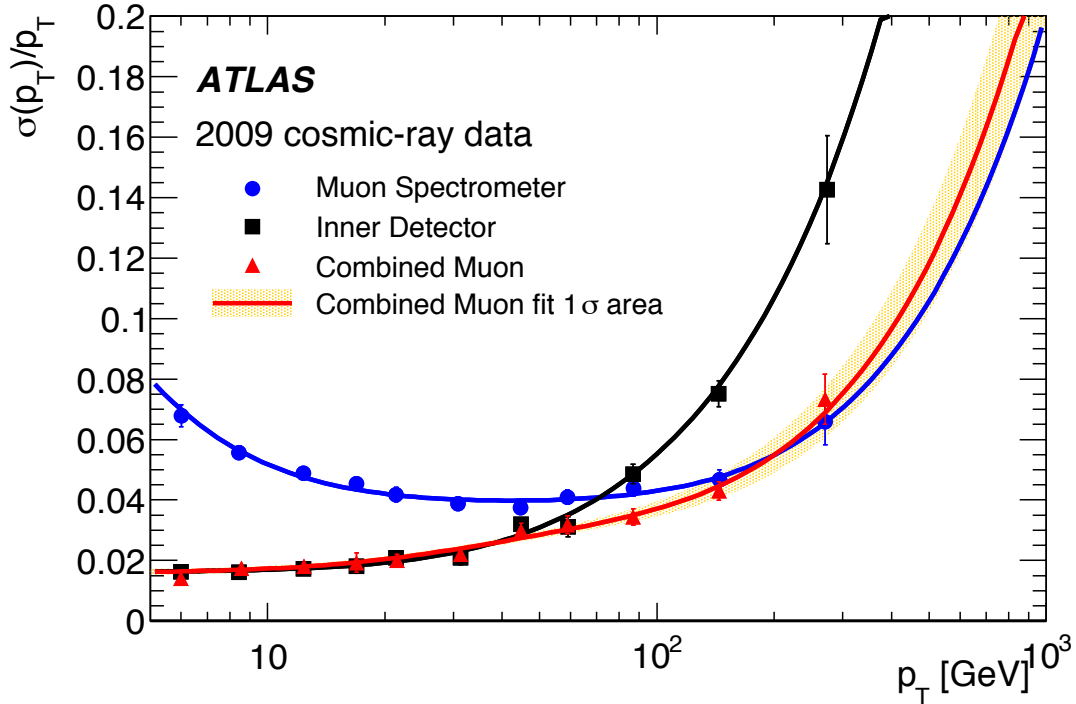


Figure 2.3: Relative momentum resolution as a function of  $p_T$  for ID tracks, MS tracks, and combined muons [12] (see section 4.1.2 for details on the different muon definitions). Momentum resolution increases with increasing  $p_T$  due to stiffer tracks making the measurement of the sagitta more difficult. Adding the TRT hits to tracks improves the resolution by increasing the lever arm.

them their semi-conducting properties. At high enough temperatures most electrons have energies above the barrier and can conduct, while at low temperatures the electrons have to be excited by ionising radiation to produce charge carrying pairs of electrons and holes (an unfilled energy level). The silicon in the ID is semi-conducting below  $-5^\circ C$  and has a low level of thermal noise at this temperature. Doping silicon with different elements allows the type of charge carrier to be chosen. N-type semi-conductors have impurities which form 4 covalent bonds with the silicon but leave an extra valence electron. P-type semi-conductors form only three covalent bonds leaving an electron ‘hole’. Electrons can move from one bond to another, which is mathematically equivalent to a positive charge carrier moving in the opposite direction (i.e. a hole). The Pixel detector sensors are constructed from an n-type wafer on which  $n^+$ -type readout pixels are placed ( $n^+$ -type and  $p^+$ -type indicates

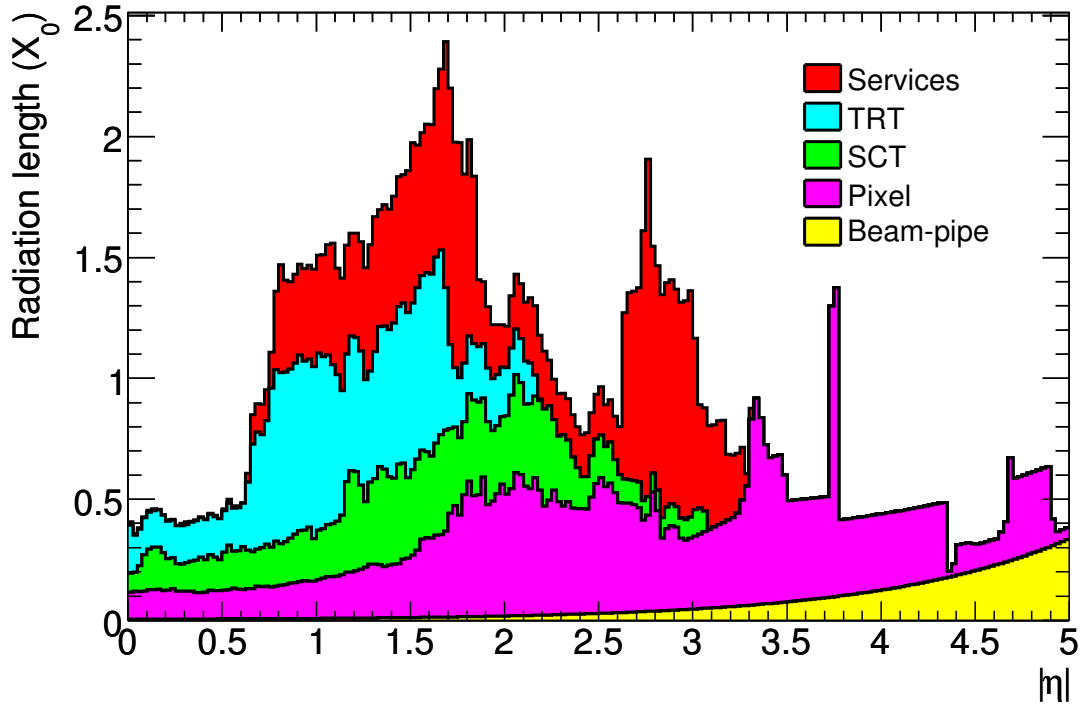


Figure 2.4: The Inner Detector material distribution in radiation lengths as a function of  $\eta$  divided down into the detectors and combined services [11].

there is a high concentration of dopants).

### 2.1.1 Pixel Detector

The Pixel detector has been shown to perform well under high pile-up conditions, with the number of pixel clusters on a reconstructed track increases close to linearly with the number of primary vertices as show in figure 2.5. Figure 2.6 shows that the Pixel detector can also be used to provide additional PID for tracks with 4 or more pixel clusters on a track.

The Pixel detector has been designed for an integrated neutron flux equivalent<sup>2</sup>,  $F_{neq} = 8 \times 10^{14} \text{ n cm}^{-2}$  ( $F_{neq}$  allows comparison of material irradiation properties).

<sup>2</sup>To allow the comparison of irradiation levels the Non Ionising Energy Loss (NIEL) per equivalent fluence ( $F_{neq}$ ) is defined. This is expressed in terms of the equivalent displacement damage caused by a flux of 1 MeV neutrons in  $\text{n cm}^{-2}$ . [14]

Radiation damage will cause leakage current to increase linearly [15]. After a flux  $F_{neq} = 2 \times 10^{13} \text{ cm}^{-2}$  the n-type silicon will undergo a type inversion to p-type silicon, but the detector is designed to still operate with minimal current leakage. To increase radiation tolerance the silicon is highly oxygenated.

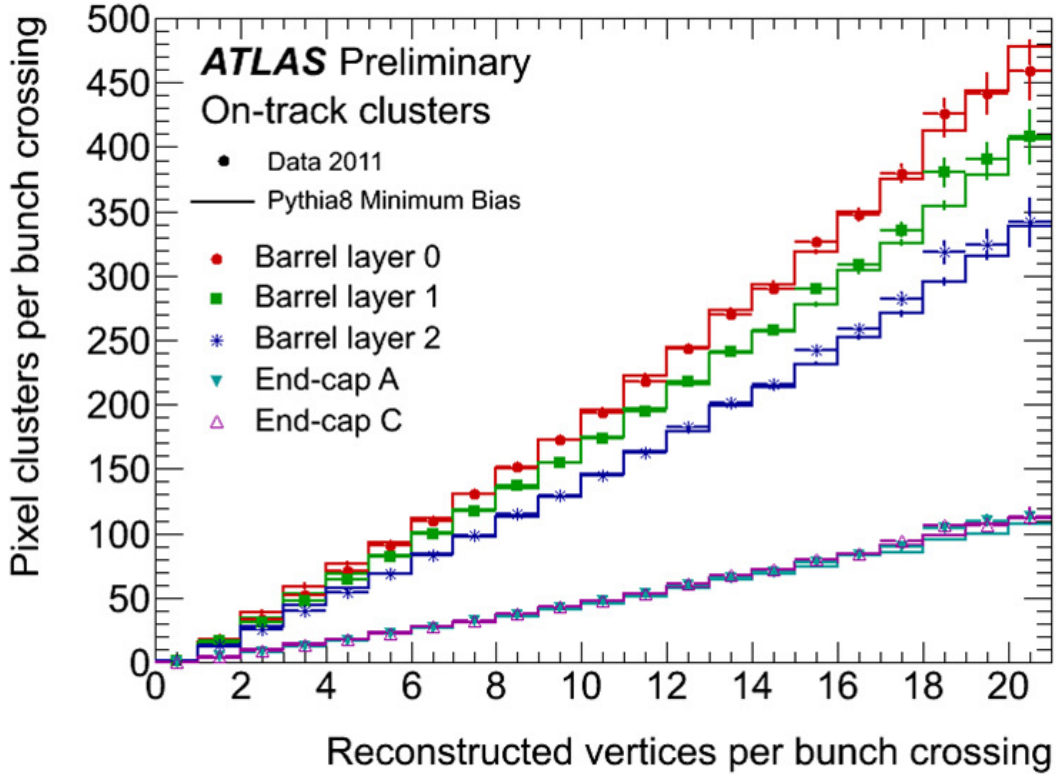


Figure 2.5: Number of pixel clusters vs. the number of reconstructed primary vertices per bunch crossing. Pixel clustering is stable for an increasing amount of pile-up, and is well modelled by PYTHIA 8 MC in all regions of the Pixel detector [16].

### 2.1.2 Semi-Conductor Tracker

There are 2112 SCT modules in 4 barrels, and 1976 modules in the 18 end- cap disks (see figure 2.2). Barrel modules are made of 4 single-sided silicon sensors, a baseboard to provide rigidity and thermal transfer, and 12 hybrid chips. The silicon sensors are  $285 \mu\text{m}$  thick n-type silicon, with an  $\text{n}^+$ -type layer on one side, and 768 strips of p-type silicon with a pitch (the distance between the centre of strips) of  $80 \mu\text{m}$ ; each is overlaid with  $22 \mu\text{m}$  wide Aluminium strips. A voltage of up

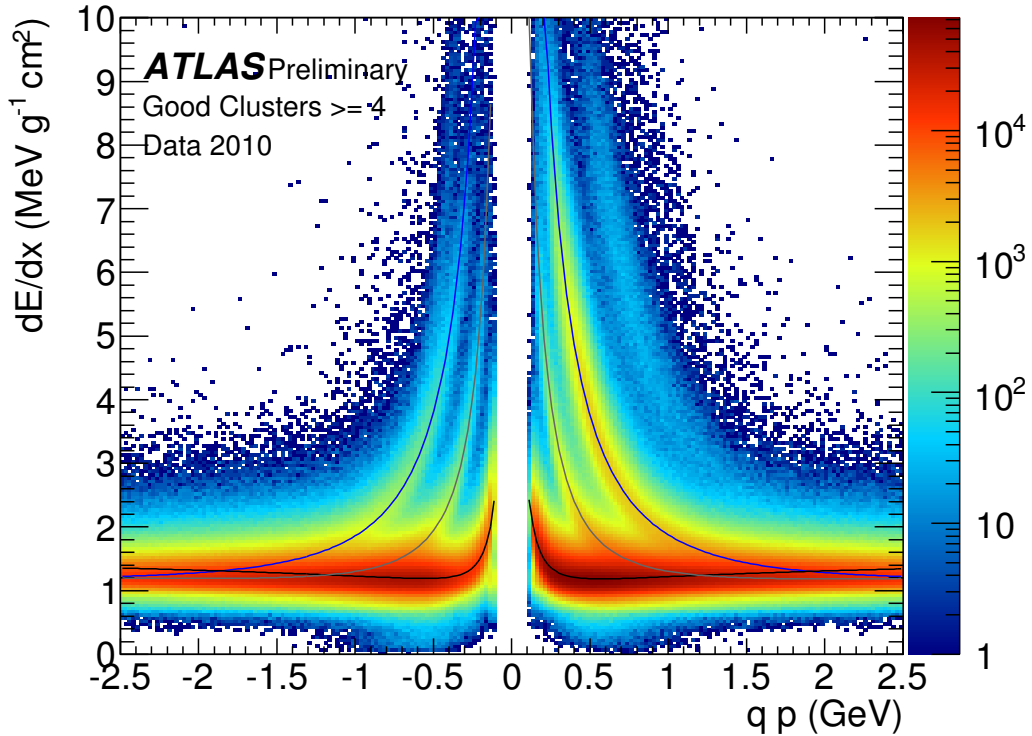


Figure 2.6: Bi-dimensional distribution of  $dE/dx$  vs. charge times momentum for high quality tracks with 4 or more good pixel clusters. Superimposed on the distributions are fitted probability distributions of pions (black, inner pair), kaons (gray, middle pair) and protons (blue, outer pair), showing the quality of PID, see [17] for further details.

to 150V is applied across each sensor to fully deplete the bulk of the material from charge carriers. The 12 hybrid chips (ABCD3TA ASICs) digitise the analogue signal received from each strip that is then read-out by the Data Acquisition System (DAQ). The charge threshold can be set per chip and so is common to all 128 channels (between 0 fC and 12.8 fC in 0.5 fC steps). There is a pipeline for each channel that stores 132 bunch crossings of data, around  $3.2 \mu\text{s}$ , to give time for the  $\sim 2.5 \mu\text{s}$  Level 1 (L1) trigger decision [18], see section 2.4 for more details.

### 2.1.3 Transition Radiation Tracker

The TRT provides a complementary low cost addition to the ID at large radii and as well as providing additional tracking information, good PID measurements are provided by  $dE/dx$ . Transition radiation occurs when a relativistic charged particle

traverses a region with different refractive indices [9]. In the TRT this occurs when charged particles cross between the polyimide tubes and the Xenon gas mixture. The low energy transition radiation photons ionise the Xenon gas to produce electrons which are collected at the cathode. The mean electron collection time is 48 ns, and the propagation time of the signal along the cathode gives a 130  $\mu\text{m}$   $z$ -resolution. The charge collected from each incident particle can be related indirectly to the energy of the particle. The continuous nature of the TRT also allows precision measurement of the  $dE/dx$ , providing good particle discrimination. The amplitude is not read out directly, but rather the Time over Threshold (ToT) is digitised. Up to momenta of  $\sim 100$  GeV there is good separation between electrons and pions from the TRT alone.

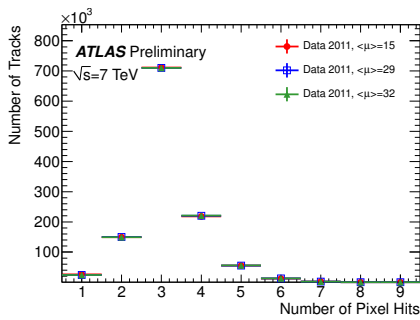
## 2.1.4 Solenoid Magnet

The central solenoid provides an axial field of 2T, while keeping the material thickness in front of the calorimeters low ( $\sim 0.66$  radiation lengths). A single coil of 12 mm thick superconducting Al-stabilised Niobium-Titanium creates the magnetic field, when temperatures are below 4.5 K. The steel of the hadronic calorimeter and its girder structure provide a flux return yoke. To save on material the solenoid magnet shares a vacuum chamber with the TRT, eliminating two vacuum walls. Deviations from a constant axial field were found not to have a significant impact on reconstruction, and so are not included in detector simulations [6].

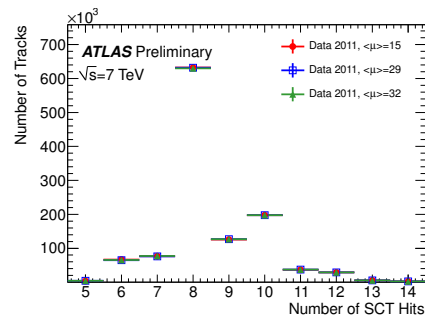
### 2.1.4.1 Tracking Performance

The performance of the ID and track reconstruction routines has been measured in data taken in early 2011. The periods shown in figure 2.7 had 5-15 interactions per bunch crossing and show the numbers of hits for each ID sub-detector for these relatively high pile-up condition and each distribution has very consistent performance. Figure 2.8 shows the stability of the robust tracking algorithms with high pile-up

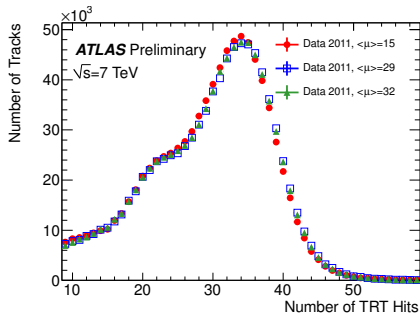
conditions when the detector occupancy is high. This indicates that the tracking reconstruction routines rarely reconstruct fake tracks when occupancy is high, and that they have a reasonable efficiency at reconstructing real tracks. A vertex reconstruction routine with an efficiency below one, as shown here, is not dominated by fake vertices (which were not the result tracks reconstructed from charged particles produced in a collision). There is a decrease in the efficiency for a high number of primary vertices, the number of fake tracks being reconstructed was shown to be low using MC [19]. While this is not sufficient to ensure that the reconstruction of particles has a high efficiency and purity, it is necessary to have a stable, linear response [19].



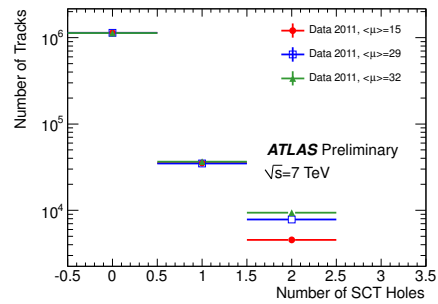
(a) pixel hits



(b) SCT hits



(c) TRT hits



(d) SCT holes

Figure 2.7: The number of pixel, SCT and TRT hits and missing SCT hits (SCT holes) for tracks that meet the robust requirements (outlined in [19]), normalised to the same number of tracks.

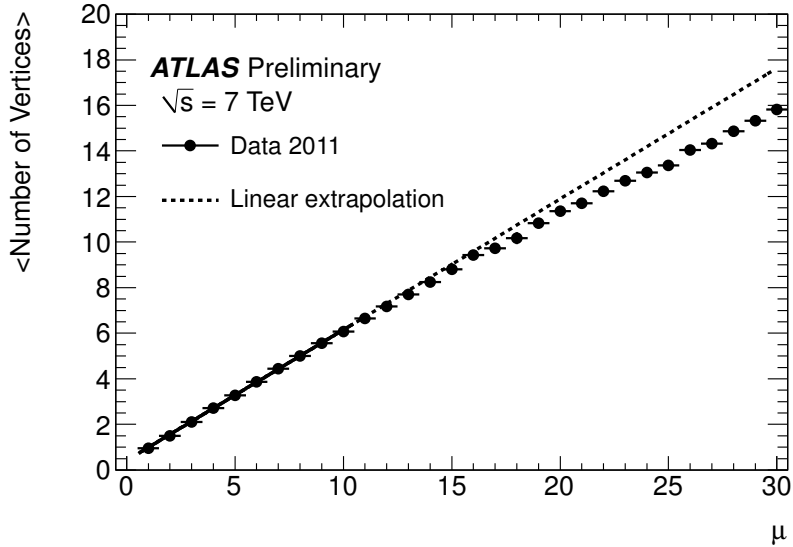


Figure 2.8: Average number of reconstructed primary vertices as a function of the average number of interactions per bunch crossing ( $\mu$ ) in 2011 data [19].

## 2.2 Calorimeters

The calorimeters have fine segmentation and a linear response to energy deposition over an energy range from  $\sim 10$  GeV to several TeV [20]. The EM barrel calorimeter, Electromagnetic End-cap Calorimeter (EMEC), Hadronic End-cap Calorimeter (HEC), and the Forward Calorimeter (FCal) all use liquid argon as the active medium (see figure 2.9) because it has linear behaviour, radiation hardness and has a stability of its response over time. The tile barrel calorimeter and the tile extended barrel use scintillating polystyrene as the active medium and measure hadronic energy deposition. Three cryostats house the Liquid Argon (LAr) calorimeters; one cryostat in the barrel houses the EM barrel calorimeter, and each end-cap cryostat houses an EMEC, an HEC and, in the forward region, an FCal. The hadronic calorimeters cover the range  $|\eta| < 4.9$ .

The hadronic calorimeters must have a large thickness in both radiation and interaction lengths to contain all electromagnetic and hadronic showers in the calorimeters. Only non-interacting particles and minimum ionising particles (e.g. muons) get through to the muon chambers. An estimate for the thickness of the calorimeter

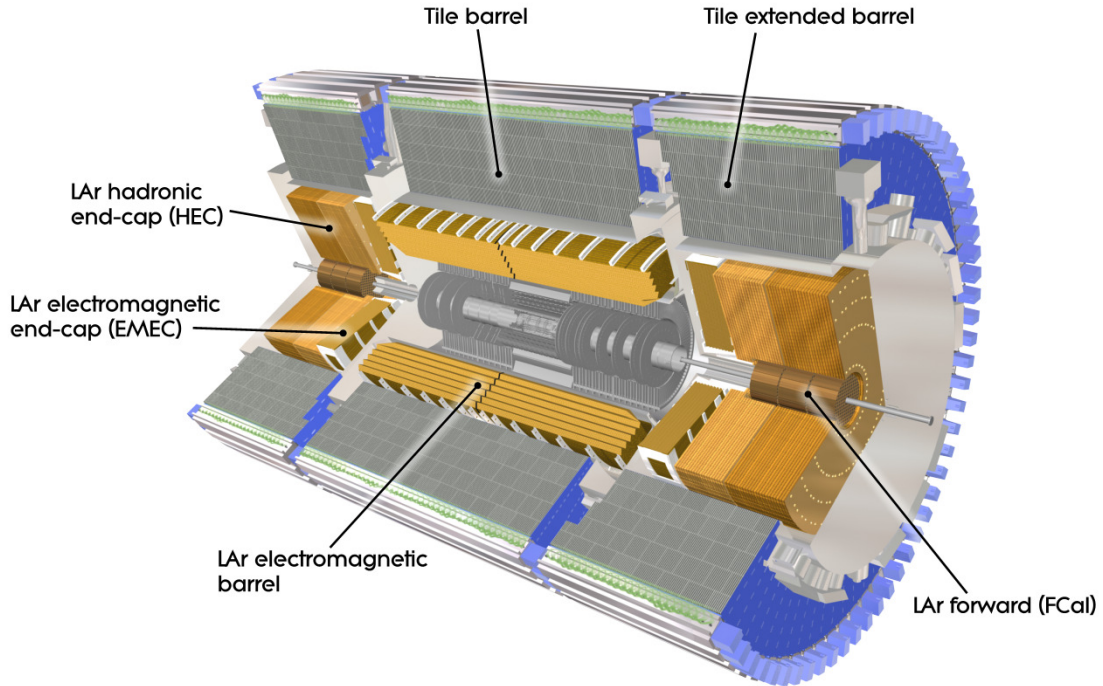


Figure 2.9: Cutaway showing the electromagnetic and hadronic liquid Argon calorimeters, the hadronic tile calorimeters, and forward calorimeters [11].

in interaction lengths<sup>3</sup> is shown in figure 2.10.

The energy resolution of electrons reconstructed in the EM calorimeters is compared with MC for data taken during 2010. Figure 2.11 shows the invariant mass distribution of  $Z \rightarrow e^+e^-$  events. The width of the distribution is sensitive to the energy resolution of electrons: the discrepancy seen in between data and MC necessitates measuring the resolution using data. Due to limited statistics, only the dominant constant energy resolution parameters were measured in [22]. To account for any further discrepancies in the electron energy resolution between data and MC, corrections are applied to MC, see section 4.1.1.

---

<sup>3</sup>The interaction length is the characteristic length at which a particle that interacts with the atomic nuclei of the material reduces in energy by  $1/e$ .

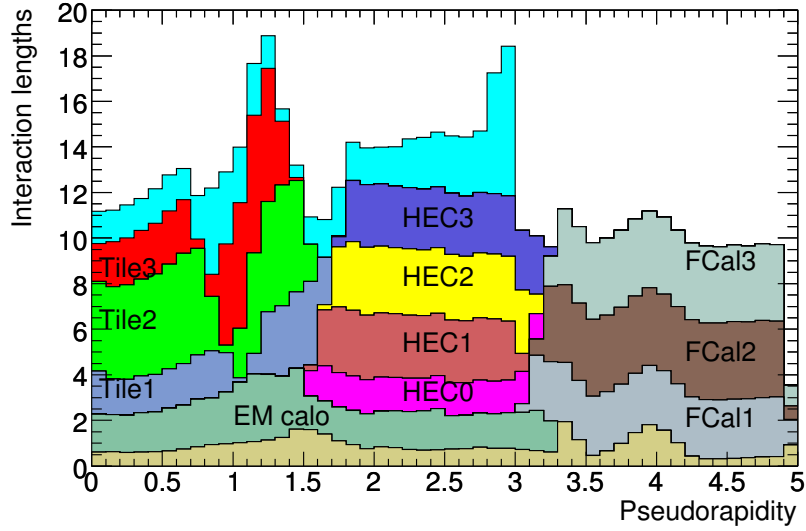


Figure 2.10: Estimate for the interaction lengths of ATLAS calorimetry as a function of pseudo-rapidity [21].

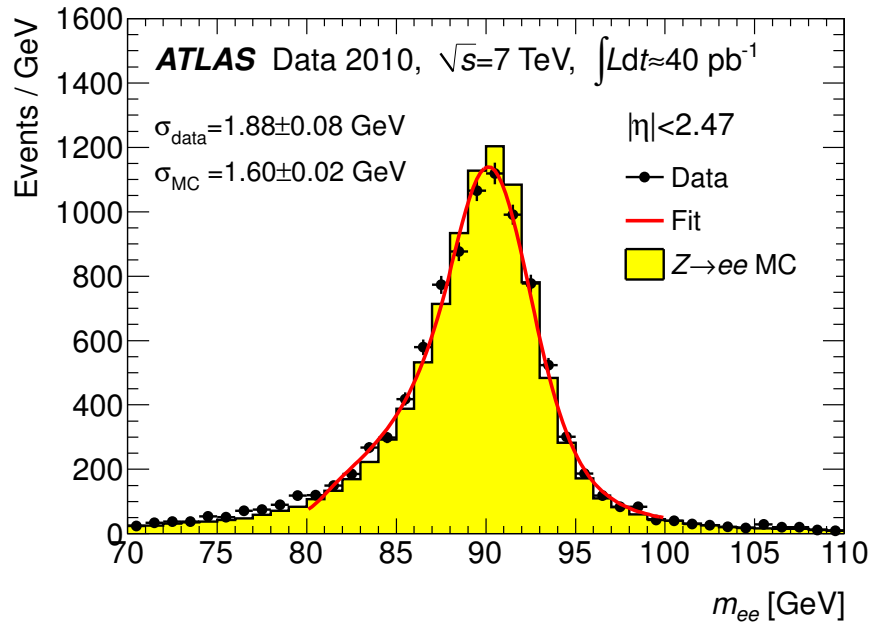


Figure 2.11: The invariant mass distribution of  $Z \rightarrow e^+e^-$  events for electrons with  $|\eta| < 2.47$  in  $40 \text{ pb}^{-1}$  of data taken at  $\sqrt{s} = 7 \text{ TeV}$  in 2010 with ATLAS [22].

## 2.2.1 Liquid Argon Electromagnetic Barrel Calorimeter

The EM barrel calorimeter, covering the pseudo-rapidity region  $|\eta| < 1.475$ , is designed for energy measurement of electrons and photons, along with good PID from the shower shapes to distinguish them from  $\pi^0$ 's. The calorimeter modules have an accordion shape ensuring that each overlaps to leave no gaps in  $\phi$  (see figure 2.12). The folding angles of the accordion shaped modules vary with radius to maintain a constant liquid-argon gap, leading to a linear energy response and energy resolution at increasing distance from the IP. The showers produced by light electromagnetically interacting particles, such as the electron and the photon, are contained within the EM calorimeter.

The ionisation material of the EM barrel calorimeter is liquid Argon which has a high density compared to gas calorimeters so no signal amplification is needed. The signal propagates slowly through the high density liquid and to maintain a reasonable drift time the size of the LAr gap is kept small. In the pre-sampler, in front of the ID solenoid, the gap size is  $\sim 2$  mm and has a drift time of 400 ns [23]. The timing performance of the EM calorimeter is shown in figure 2.13. A high resolution is achieved during high pile-up conditions with long pulse lengths by using the leading edge of the pulse.

Absorbers are made from 1.53 mm thick lead plates sandwiched between 0.2 mm thick steel plates for stability. Between the plates are the readout electrodes which consist of three copper conducting layers sandwiched between two polyimide sheets. The outer layers are at a high voltage, and the inner layer is used for signal readout.

An electromagnetic pre-sampler before the solenoid and the Inner Detector services provides calibration sampling in non-instrumented material including material from the barrel cryostat. It consists of 64 azimuthal modules with 11 mm LAr gaps, with a minimum  $\eta$  granularity of  $\Delta\eta = 0.2$  [11].

Electrons radiate when they encounter the absorbers, producing electron-positron pairs causing an electromagnetic cascade. Photons will cause similar cascades by



Figure 2.12: Electromagnetic calorimeter barrel section showing its accordion shape. [11].

producing electron-positron pairs. Differences in the shapes of the electro-magnetic showers are resolved by the fine segmentation of the calorimeter, providing good discrimination between different particle types which interact electro-magnetically.

The calorimeter is calibrated in several ways. Charge can be directly injected into the detector; the response of the detector and the resulting digital signal read out allows calibration of the full Analogue to Digital Conversion (ADC) chain. Testing modules with a test beam before assembly of ATLAS allows calibration of the detector to GeV energy scales.

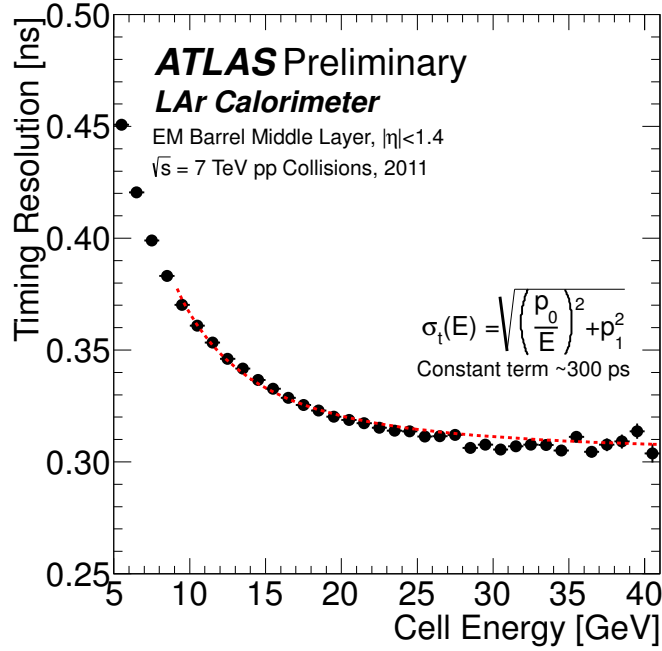


Figure 2.13: Timing resolution of electrons in the middle layer of the EM barrel calorimeter taken from  $W \rightarrow e\nu_e$  candidate events as a function of energy deposited in the cell in data in 2011  $\sqrt{s} = 7$  TeV proton-proton collisions [24].

## 2.2.2 LAr Electromagnetic End-cap Calorimeter

The EMEC uses the same LAr module technology as the EM barrel calorimeter. Covering  $1.375 < |\eta| < 3.2$ , the end-caps' accordion waves are parallel to the radial direction and run axially; the LAr gap increases with radius as the wave amplitude and folding angles vary with radius. Each end-cap consists of two co-axial wheels each constructed of 8 modules with no discontinuity in  $\phi$  due to the accordion geometry.

## 2.2.3 Hadronic Tile Calorimeter

The hadronic tile calorimeter, covering  $|\eta| < 1.7$ , consisting of a central 5.8 m long barrel, and two 2.6 m long extended barrels over a radial range of  $2.28m < R < 4.25m$ . The tile modules consist of steel absorber plates, with polystyrene scintillator

as the active medium. Wavelength shifting fibres shift the Ultra Violet (UV) scintillation to visible wavelengths which Photo Multiplier Tubes (PMTs) convert into an electronic signal. At  $\eta = 0$  the tile calorimeter has a thickness of  $\sim 11$  interaction lengths, which is enough to contain hadronic jets and reduce punch-through to the muon chambers. It provides a high resolution energy measurement for hadronic jets and the shower shape discriminates against electromagnetic particles that punch through the EM barrel calorimeter. The Intermediate Tile Calorimeter (ITC) instruments a service gap providing energy correction [11].

The aim of the tile calorimeter calibration is to:

- measure its EM scale and its uncertainties,
- minimise cell-to-cell variations in EM scale,
- measure and correct non-linearity of response,
- measure the energy resolution,
- measure the timing offset between collisions and signal collection,
- monitor stability of corrections over time,
- measure the effect of the magnetic field on measurements.

Three calibrations, obtained by independent systems, are used at various points in the readout chain:

- a movable  $^{137}\text{Cs}$   $\gamma$  source allows the digital readout from PMTs to be calibrated; performed in-between data taking periods, every few weeks to few months;
- a laser is used to measure the gain of each PMT photo-cathode, and monitor its stability and the change over time (performed twice per week) ;
- a Charge Injection System (CIS) allows measurement and monitoring of the gain of the PMTs (this is performed twice per year in dedicated runs [25]).

As well as these calibration methods, before installation into ATLAS, data was taken with a test beam for calibration purposes. Timing calibration performed with the lasers was supplemented with cosmic muon and beam splash events.

## 2.2.4 Liquid Argon HEC

The HEC consists of a front wheel (Hadronic End-cap Calorimeter 1 (HEC1)) and rear wheel (Hadronic End-cap Calorimeter 2 (HEC2)) in each end-cap. Each wheel has 32 wedge-shaped modules in each end-cap that share a cryostat with the EM barrel calorimeter and the FCal and cover the range  $1.5 < |\eta| < 3.2$ . They have parallel copper absorbing plates to withstand the high radiation doses, and a LAr active medium (see figure 2.14). Each module in HEC1 is composed of 24 copper plates each 25 mm thick and a 12.5 mm thick front plate, while HEC2 has 16 copper plates each with a 50 mm thickness and a 25 mm front plate.

## 2.2.5 Forward Calorimeter

The FCal is located in the same cryostats as the end-cap calorimeters with coverage of  $3.1 < |\eta| < 4.9$ . Three FCals are located in each end-cap. FCal1 is an electromagnetic calorimeter, with copper absorbing plates. FCal2 and FCal3 are hadronic calorimeters with Tungsten absorption plates. Each rod shaped module is 45 cm long and orientated axially. Due to the high particle fluxes at high  $\eta$ , smaller LAr gaps of  $0.269\text{ mm}$ ,  $0.376\text{ mm}$  and  $0.508\text{ mm}$  are used for Forward Calorimeter 1 (FCal1)-Forward Calorimeter 3 (FCal3) respectively avoiding ion build-up problems and giving faster signal readout times. A shielding plug of copper mounted behind FCal3 gives better containment for the high particle flux at high  $\eta$  reducing backgrounds in the end-cap muon system [11].

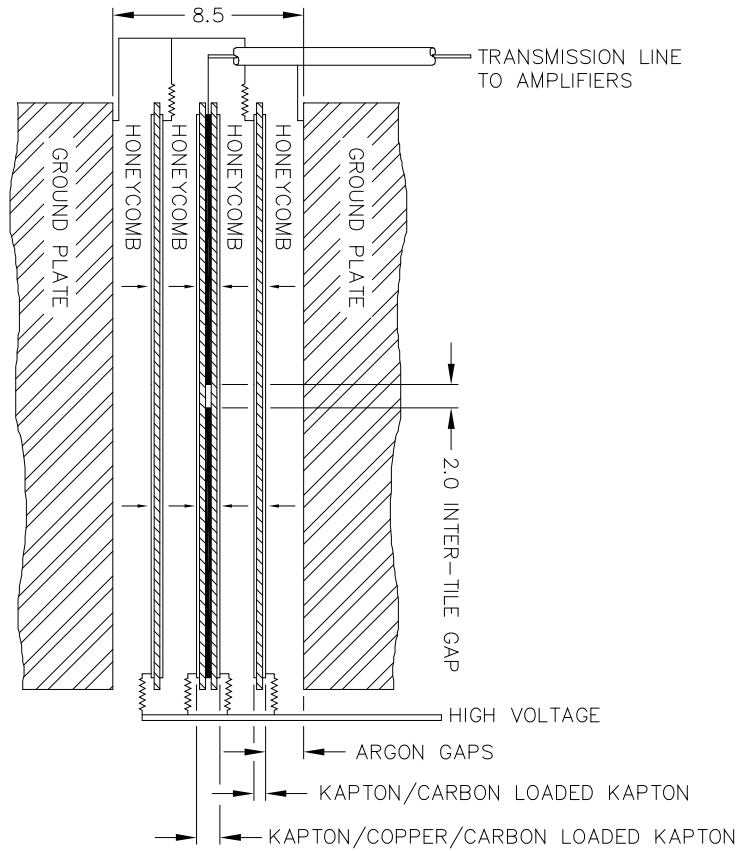


Figure 2.14: Structure of the HEC between plates. [11].

## 2.3 Muon Spectrometer

The muon spectrometer is composed of four sub-systems (see figure 2.15) that measure the momenta, and provide L1 trigger information, for muons that exit the barrel and end-cap calorimeters. There are two precision measurement tracking chambers: the MDT, covering  $|\eta| < 2.7$  ( $|\eta| < 2.0$  for the innermost barrel layer); and the CSC, covering  $2.0 < |\eta| < 2.7$ . Two trigger chambers cover different pseudo-rapidity regions: the RPC covering  $|\eta| < 1.05$ , and the TGC covering  $1.05 < |\eta| < 2.7$  ( $|\eta| < 2.4$  for triggering). The air core toroids provide a  $0.5\text{--}1T$  magnetic field,

orthogonal to the axial field produced by the solenoid magnetic, providing an independent  $p_T$  measurement by deflecting the muon tracks in the  $r$ - $\eta$  plane.

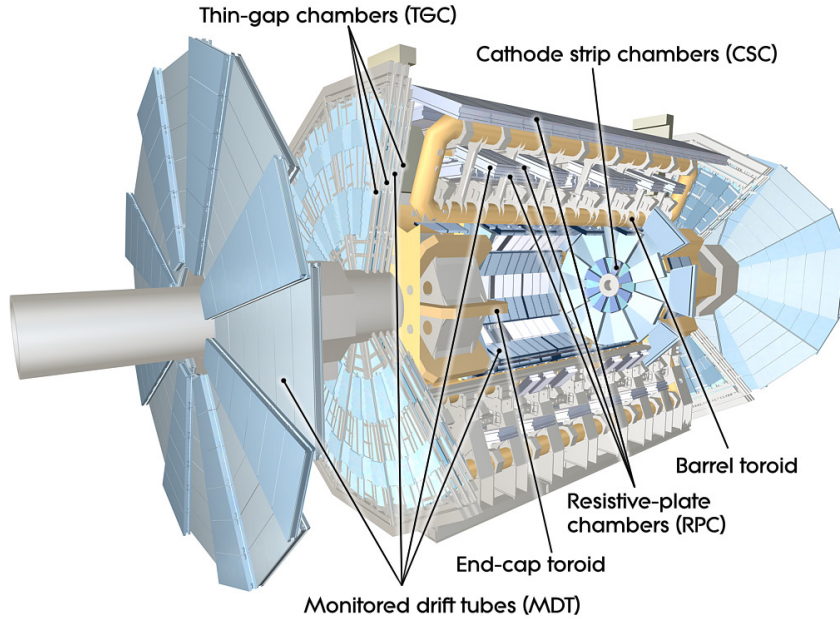


Figure 2.15: The ATLAS detector with the four muon spectrometer sub-detectors highlighted [11].

### 2.3.1 Muon Drift Tube chamber

The MDTs provide the precision muon tracking measurements covering the pseudo-rapidity range  $|\eta| < 2.7$ , except for the inner layer which covers  $|\eta| < 2.0$ . Each chamber consists of 3–8 layers of drift tubes achieving a resolution of  $\sim 80 \mu\text{m}$  per tube. The shape of the chambers has been optimised to reduce acceptance losses around the magnet coils and support structures. Each 29.970 mm tube is pressurised at 3 bar with an Ar (97%)/  $\text{CO}_2$  (3%) mixture which is radiation hard. The ionisation produced by charged particles is collected at Tungsten-Rhodium wires. The maximum drift time of the ionisation pulse is 700 ns, as only the leading edge of a pulse is used to indicate a hit.

### 2.3.2 Cathode Strip Chamber

The CSCs are precision tracking chambers covering the pseudo-rapidity range  $2.0 < |\eta| < 2.7$  on the inner layer of the muon chambers, arranged in two discs of 8 large and 8 small chambers each side. Due to the high particle flux at high rapidity instead of MDTs, the CSCs are Multi-wire Proportional Chambers (MWPCs) with segmented cathodes with radially orientated wires. The CSCs are radiation hard and have larger maximum counting rates than MDTs. Each chamber contains four CSC planes, each with 205 and 402 wires per plane in the small and large chambers respectively, with a resolution of  $60\mu\text{m}$ . The electron drift time is  $40\text{ns}$ , giving a timing resolution of  $7\text{ns}$  per plane.

### 2.3.3 Muon Trigger Chambers

Two sub-systems provide fast muon triggering information, allowing L1 trigger logic to recognise their multiplicity and approximate momentum.

The muon triggering system is required to discriminate approximately on transverse momentum, identify the bunch crossing, and provide coarse tracking information, and additional co-ordinate measurements supplementing the MDT and CSC measurements.

At high  $|\eta|$  the  $p_{\text{T}}$  of muons is lower which is accompanied by a decrease in integrated bending power. This necessitates an increase in  $\eta$  dependent granularity in the end-cap system to match the  $p_{\text{T}}$ -resolution of the barrel. Also levels of radiation in the end-cap region are  $\sim 10$  times that of the barrel. In the region  $1.3 \leq |\eta| \leq 1.65$  the end-cap and barrel toroid magnets overlap, leading to a complex superposition of magnetic fields with large inhomogeneities. In two regions in the  $\eta - \phi$  plane the field falls close to zero leading to straight tracks which are difficult to distinguish from high  $p_{\text{T}}$  tracks; measures to avoid an artificially high trigger rate include masking this region (requiring a high granularity trigger).

Two muon triggering technologies are used: in the barrel region ( $|\eta| \leq 1.05$ ) the RPCs, and in the end-cap region ( $1.05 \leq |\eta| \leq 2.4$ ) the TGCs.

### 2.3.4 Resistive Plate Chamber

The RPC consists of three concentric layers in the barrel region. Each RPC is a gaseous ( $\text{C}_2\text{H}_2\text{F}_4/\text{Iso-C}_4\text{H}_{10}/\text{SF}_6$  with a mix of 94.7%/5%/0.3%) parallel electrode-plate detector, with a separation of 2 mm. The resulting pulse produced by incident muons is around 2 ns in length, and gives good timing resolution. Each unit is made of two pairs of plates enclosing a gaseous volume. The gas volumes are divided by spacers 100 mm apart. Readout strips above and below the gas volumes are respectively orientated in the  $\eta$  and  $\phi$  directions, see figure 2.16.

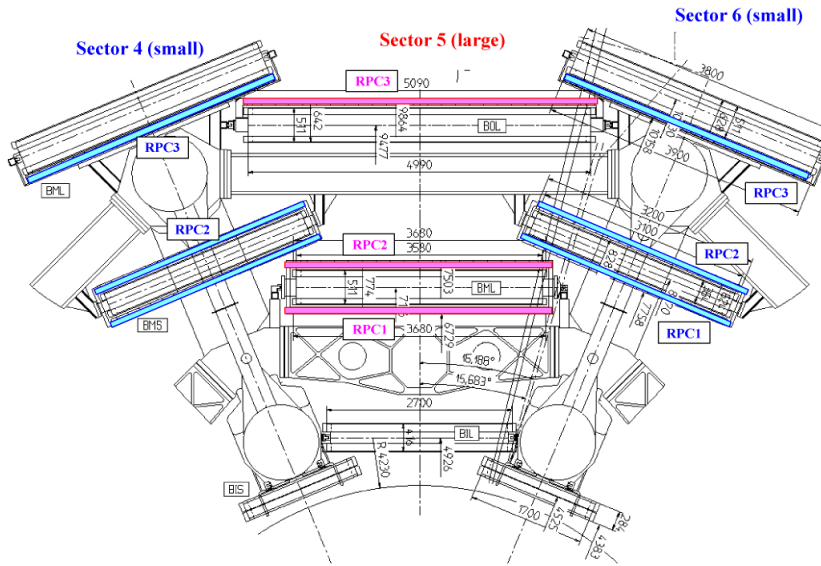


Figure 2.16: Cross section through a Resistive Plate Chamber [11].

The RPC readout electronics have a maximum frequency response of 100 MHz. Co-incidences in the same sector and tower are compared between Resistive Plate Chamber 1 (RPC1) and Resistive Plate Chamber 2 (RPC2) to form a low- $p_T$  trigger. To form a high  $p_T$  trigger an additional signal from Resistive Plate Chamber 3 (RPC3) is required.

### 2.3.5 Thin Gap Chamber

The TGCs provide triggering capability for the end-cap of the muon spectrometer and provide tracking information in addition to that from the MDT end-caps. The middle layer of the MDT is accompanied by seven TGC layers, and the inner MDT layer by two TGC layers, segmented into two non-overlapping layers.

Each TGC uses MWPC technology. A single layer of wire anodes is positioned 1.8 mm apart, at a distance of 1.4 mm from the graphite cathode layers. However, the spatial resolution is determined by the ganging of the readout. A time resolution of 4 ns means the correct bunch crossing can be identified for each trigger.

### 2.3.6 Toroid Magnets

The air-core superconducting toroid magnets produce an average field strength of around 0.5T and 1T in the barrel toroid (which is 23 m in length) and the end-cap toroids respectively. The fields have an 8-fold structure in  $\phi$  and curve charged particles in the  $r$ - $\eta$  plane to provide momentum information. When the coils are cooled to 4.6 K the resistance drops to zero and they become superconducting, the large currents that can be maintained when resistance is zero allows the large magnetic fields to be generated. The cooling process takes 5 weeks starting from ambient temperature [11]. The toroids are deflected by significant Lorentz forces, the toroids' weight of 830 tonnes, 400 tonnes of muon chambers, and temperature changes that cause deformation. 3D Hall probes are used to measure accurately the strength and direction of the magnetic field.

### 2.3.7 Forward Detectors

Two detectors in the very forward region, LUMinosity measurement using Čerenkov Integrating Detector (LUCID) at  $\pm 17$ m, and ALFA (Absolute Luminosity For ATLAS)

at  $\pm 240$  m, provide luminosity measurements. The Zero Degree Calorimeters (ZDCs) are located at  $\pm 140$  m from the interaction point and are designed to detect neutrons from heavy ion collisions, and provide information about minimum bias events. All are designed to withstand the high radiation flux of  $F_{neq} \sim 10^{15}$ . [11]

## 2.4 Triggers and Data Acquisition

During 2011 the LHC time between proton bunch crossings was  $50$  ns at  $\sqrt{s} = 7$  TeV, with up to 30 collisions per bunch crossing. Each event readout contains around 1.3MB of data and the design recording capacity limits the final event rate to 200–400 Hz which requires accepting around 1 in  $10^7$  events (though this was sometimes exceeded during data taking). In order to satisfy the physics aims of ATLAS it is necessary to have a high efficiency for rare events, while recording enough data for precision studies of known processes. To achieve this three trigger levels are used.

Physics analyses may depend on different triggers or combinations of triggers. Rare events, like an SM Higgs to four muons ( $H \rightarrow ZZ \rightarrow \mu^+ \mu^- \mu^+ \mu^-$ ), require high  $p_T$  muon triggers with an efficiency near 100%. However, common minimum bias events require triggers in the forward region, but do not need a high efficiency to perform their precision studies. With a fixed readout rate the triggers and their sensitivities must be balanced between different physics channels. When collision conditions change such that a trigger channel fires too often, the trigger is pre-scaled to reduce its rate. Accounting for such changes is complex and un-prescaled triggers are preferred in many analyses.

The L1 trigger is composed of purpose-built hardware and uses reduced granularity information from the muon chambers and calorimeters to identify particles or jets with a high  $p_T$  and large  $E_T^{\text{miss}}$ . A time of  $\sim 2.5$   $\mu\text{s}$  is required to get event information to the Central Trigger Processor (CTP). The L1 trigger must therefore make the decision within  $\approx 1$   $\mu\text{s}$  as to whether to pass the event onto the Level 2 (L2) trigger. This should reduce the event rate to 75kHz [26].

The L2 trigger is software based and runs on commercially available computing hardware. It looks at specific detector regions identified by the L1 trigger using full granularity information from all the sub-detectors in this region (including ID information). With better information on energy deposition and track reconstruction giving particle identification, an event rate of 1-3kHz is produced. [26]

Finally the Level 3 (L3) trigger, or Event Filter (EF), uses fully reconstructed events and produces an output of  $\sim 200\text{Hz}$ . [26]

### 2.4.1 Electron Triggers

Triggers for electrons and photons use shower shape information from the calorimeters to distinguish them from low momentum hadronic jets. The fine segmentation of the first layer of the EM calorimeter, as described in sections 2.2.1 and 2.2.2, allows photons to be distinguished from  $\pi^0 \rightarrow \gamma\gamma$  decays. Distinguishing photons from electrons in the L1 trigger is not possible as tracking information is not available. The  $e/\gamma$  clusters seen at L1 are reconstructed with a fast algorithm (seeded by the highest energy cell). At L2 the clusters are reconstructed using a sliding window algorithm [6], and a fast reconstruction of ID tracking information is used to distinguish electrons from photons. Corrections to calorimeter cell energies are not applied at the trigger level, only at the reconstruction stage. Triggers with increasing electron  $p_T$  thresholds are defined. If a low  $p_T$  trigger has a large pre-scale to reduce its rate to levels that can be recorded, a higher  $p_T$  threshold trigger will ensure events with high  $p_T$  electrons are not missed. An example of this is shown in figure 2.17 which measures a measurement of the trigger efficiency of the e22vh\_medium1 trigger at L1, L2 and EF relative to electron definitions defined later in section 4.1.1. A more detailed discussion can be found in [27], [28], [29], [30], and [31].

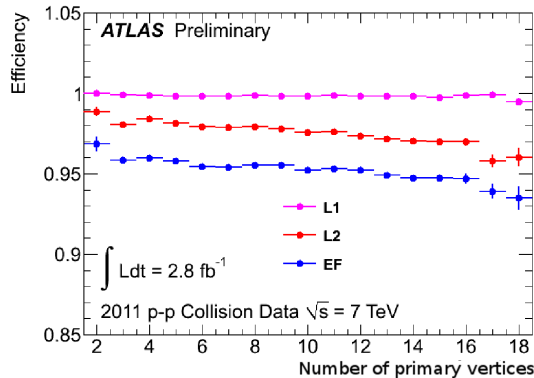


Figure 2.17: The efficiency of e22vh\_medium1 relative to offline medium++ electrons (see section 4.1.1 for more details on electrons) was measured using a  $Z \rightarrow e^+e^-$  tag and probe study as a function of the number of primary vertices in the event for L1, L2 and EF triggers [30].

## 2.4.2 Muon Triggers

The MDT and RPC are specifically designed to provide L1 trigger information in the barrel and end-cap regions respectively. There are three trigger algorithms available at L2: the Standalone Algorithm (SA), the Combined Algorithm (CB), and the isolated trigger algorithm. The SA reconstructs muon tracks using hits in the MS in Regions of Interest (RoIs) defined by the L1 seed. The CB uses ID hit information, in addition to track information provided by the SA, to provide improved track reconstruction. Combining the CB with calorimeter information, and the sum of  $p_T$  of ID tracks in a cone around the muon, the isolated muon trigger algorithm is formed.

At the EF level muons are reconstructed using the full event information using two algorithms seeded by the ID and MS to form three EF trigger algorithms. The MS seeded muons provide the EF SA triggers. Combining these with ID track information forms EF CB triggers. The “inside-out” EF trigger algorithm is seeded by ID tracks that are extrapolated to the MS which are then combined with overlapping MS triggers. Using all three trigger algorithms proved to be complementary during early data taking as they provided a redundancy. Several triggers are defined with increasing  $p_T$  thresholds so a muon trigger always exists which has no pre-scale

applied, see [32] and [33] for full details.

## 2.5 Summary

The ATLAS detector is a near hermetic detector, with high precision tracking of charged particles, and high resolution calorimetry for EM particles and hadrons providing good PID, and high precision muon spectrometry and triggering from the four muon sub-detectors surrounded by a 0.5–1  $T$  toroidal magnetic field. The high resolution and hermeticity, allow precision estimates for  $E_T^{\text{miss}}$  for identifying the presence of neutrinos in an event. Three trigger levels provide fast readout and high efficiency for events of interest.

The triggered events are recorded for reconstruction off-line into physical objects and event level information, which is described in chapter 4. The intermediate particles such as the  $Z$ , and events with a complicated topology, such as  $t\bar{t}$  events, can then be reconstructed and analysed.

# Chapter 3

## The Standard Model and Top Physics

In this chapter the Standard Model of particle physics is introduced. The material found here is partly based on that found in [34] and should be considered the source for any general information that has not been referenced.

While the SM is one of the most complete theories in physics, there are observations inside and outside of High Energy Physics (HEP) that cannot be explained by the SM alone:

- The excess of matter over anti-matter observed in the universe cannot be explained by the small amount of CPV seen in SM physics, see [9] for a brief introduction and [35, 36] for an overview of experimental results.
- Gravity cannot be quantised without introducing theories such as loop quantum gravity or string theory. The weakest of the four forces, its relative weakness is not fully understood. While theoretical progress continues to be made, such models are difficult to test experimentally [37, 38].
- Neutrino oscillations imply they have a small mass, but the electroweak force only interacts with left-handed neutrinos  $\nu_L$  and their CP-conjugate right

handed anti-neutrinos  $\bar{\nu}_R$ , two facts that can be resolved if neutrinos are their own anti-particles (Majorana particles) [39].

- Cosmological inflation, as an explanation for the uniformity of the Cosmic Microwave Background Radiation (CMBR), implies the volume of the universe increased by  $10^{78}$  soon after the big bang [40].
- Dark matter accounts for around 22.8% of the observable energy density of the universe [41] and is required to explain galactic rotations, the movement of galaxies, and larger cosmological structures, but cannot be directly observed.
- Dark energy makes  $\sim 72.6\%$  of the universe's energy density [41], and appears in models as the cosmological constant. As it stands, few theories of dark energy exist that can be tested at HEP experiments with today's technology and understanding.

### 3.1 The Standard Model of Particle Physics

The Standard Model describes the interactions between the known fundamental particles, see figure 3.1. The particles are divided into the fermionic (spin-1/2) leptons and quarks, and the bosonic (integer spin) particles, which mediate the fundamental forces (gauge bosons) excluding gravity, and the Higgs boson. Tables 3.1, 3.2, and 3.3 list the masses, charge and spin for the leptons, quarks and boson respectively. See [9] for up-to-date listings of the fundamental particles and their properties, and a review current particle physics measurements. For a more in depth introduction to the SM see [42].

The leptons are divided into three generations of lepton pairs. Each pair contains a charged, massive lepton and an un-charged and near-massless lepton-neutrino. The leptons in each generation have an intrinsic quantum number, the lepton number, which is conserved in the SM. The lepton number and the mass of each lepton is the only difference between each generation; the rest energy of the lightest charged

lepton, the electron, is  $m_e = 0.510998928 \pm 0.00000001$  MeV and the heaviest lepton, the tau, has a mass  $m_\tau = 1776.82 \pm 0.16$  MeV [9].

	quarks			gauge bosons	
charge	2/3	2/3	2/3	1	0
spin	1/2	1/2	1/2	1	0
	<b>u</b> up	<b>c</b> charm	<b>t</b> top	<b>γ</b> photon	<b>H</b> Higgs boson
	-1/3	-1/3	-1/3	0	
	1/2	1/2	1/2	1	
	<b>d</b> down	<b>s</b> strange	<b>b</b> bottom	<b>g</b> gluon	
	-1/3	-1/3	-1/3	0	
	1/2	1/2	1/2	1	
	<b>e</b> electron	<b>μ</b> muon	<b>τ</b> tau	<b>Z</b> Z boson	
	0	0	0	±1	
	1/2	1/2	1/2	1	
	<b>ν<sub>e</sub></b> electron neutrino	<b>ν<sub>μ</sub></b> muon neutrino	<b>ν<sub>τ</sub></b> tau neutrino	<b>W</b> W boson	
	leptons				

Figure 3.1: The fundamental particles of the SM: the three generations of leptons and quarks, the gauge bosons and the Higgs scalar boson [42].

The remaining six fermions, the quarks, are similarly arranged into three generations with one quark in each pair possessing fractional charge  $+2/3e$  and the other  $-1/3e$  (where the charge of the electron is  $e$ ). In the first generation the up quark has a quantum number, iso-spin,  $I_3 = +1/2$  and the down quark has  $I_3 = -1/2$  similarly to the lepton generations. The remaining quarks have similar flavour charges, charm ( $C = +1$ ), strangeness ( $S = -1$ ), beauty ( $\tilde{B} = -1$ ) and truth ( $T = +1$ ) for the charm, strange, bottom and top quarks respectively (note that the difference in the flavour charges from the first generation is essentially notational and does not represent a difference in the physics). Hyper-charge ( $Y$ ) relates these

Lepton	Mass / MeV	Charge / e	Spin
$e$	$0.510998928 \pm 0.00000001$	-1	1/2
$\mu$	$105.6583715 \pm 0.0000035$	-1	1/2
$\tau$	$1776.82 \pm 0.16$	-1	1/2
$\nu_e$	$< 2 \times 10^{-6}$	0	1/2
$\nu_\mu$	$< 0.19$	0	1/2
$\nu_\tau$	$< 18.2$	0	1/2

Table 3.1: The masses, charges and spins of the three charged leptons and their uncharged neutrino partners [9].

Quark	Mass / GeV	Charge / e	Spin
$u$	$2.2_{-0.5}^{+0.7} \times 10^{-3}$	2/3	1/2
$d$	$4.8_{-0.3}^{+0.5} \times 10^{-3}$	-1/3	1/2
$c$	$1.25 \pm 0.025$	2/3	1/2
$s$	$95 \pm 5$	-1/3	1/2
$t$	$173 \pm 0.5 \pm 0.7$	2/3	1/2
$b$	$4.18 \pm 0.03$	-1/3	1/2

Table 3.2: The masses, charges and spins of the six quarks. The b-quark mass is quoted in the  $\overline{MS}$  scheme and the top from direct measurements [9].

quantum numbers and the baryon number (B) [42]:

$$Y \equiv B + S + C + \tilde{B} + T \quad (3.1)$$

and is conserved in all strong interactions, while iso-spin relates to the quark charge (Q) [42] :

$$I_3 \equiv Q - Y/2 \quad (3.2)$$

Hyper-charge (Y) is the charge with which the group  $U(1)_Y$  interacts before symmetry breaking is introduced. These quantum numbers are conserved in strong interactions, however in charged weak interactions (via the  $W$ ) the quarks can change flavour at tree level (though not in neutral weak interactions via the  $Z$ ) [9, 42–44].

Boson	Mass / MeV	Charge / e	Spin
$\gamma$	0	1	1
g	0	0	1
Z	$91.2 \pm 0.0021$	0	1
W	$80.4 - 0.015$	$\pm 1$	1
H	$125.6 \pm 0.3$	0	0

Table 3.3: The masses, charges and spins of the three charged leptons and their uncharged neutrino partners [9].

The gauge bosons (with spin 1) mediate the fundamental forces. The electromagnetic force is mediated by the photon between charged particles, the weak force by the  $Z$  and  $W^\pm$  between weakly interacting particles, and the gluons mediate the strong force between colour charged particles (colour charge is expanded upon in section 3.3). The other boson is the spin-0 Higgs boson which was introduced to give the  $W$  and  $Z$  mass [42].

The electro-magnetic force is governed by the interaction of the photon with charged particles. In Quantum Field Theory (QFT) the electro-magnetic force is the result of the invariance of the Lagrangian under local phase transformations ( $U(1)$ ). In the SM, before symmetry breaking, the electro-weak symmetry group is  $SU(2) \times U(1)_Y$ . When the Higgs field is added to give the  $W$  and  $Z$  mass, electro-magnetism arises which interacts instead with particles with charge [42].

Almost every measurement performed to date has been consistent with the SM expectation. One constant that has been measured to high precision is the muon magnetic dipole moment for which a  $3.6\sigma$  deviation between the value measured and that predicted by the SM has been observed [9]. If confirmed it would indicate a contribution from new physics.

### 3.1.1 Tau Physics

The tau lepton is the heaviest lepton with a mass of  $1776.82 \pm 0.16$  MeV [9] and consequently, in addition to decaying leptonically to a muon and electron and their associated neutrinos, it decays to the first and second generations of quarks that are kinematically available. The majority of hadronic tau decays are to the lowest mass quarks and their hadrons; decays with one or three charged pions are common, and are referred to as one and three prong tau decays. The tau branching fractions are depicted in figure 3.2, including rarer decays into kaons containing a strange quark. The lifetime of the tau is  $(290.6 \pm 1.0) \times 10^{-15}$ s [9], and so in the ATLAS detector a tau generally decays before reaching the inner layers of the ID. While a small displacement of the tau decay vertex could be reconstructed for particles originating from a tau decay, the biggest indicator of a leptonically decaying tau would be additional  $E_T^{\text{miss}}$  in an event.

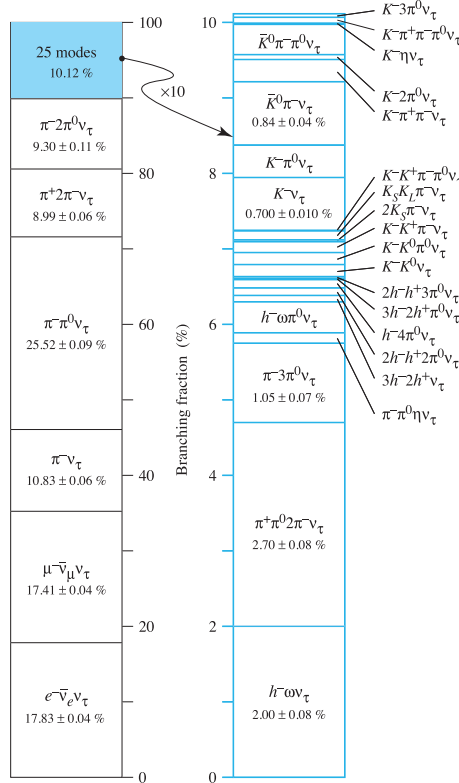


Figure 3.2: The tau branching fractions calculated by the PDG [9].

## 3.2 Electro-weak Theory

Electro-weak interactions are obtained from the group  $SU(2)_L \times U(1)_Y$  where  $SU(2)_L$  is the special unitary group of helicity ( $L$ , the projection of the spin onto the direction of a particle's momentum) and  $L$  indicates that right handed particle operators are singlets under  $SU(2)$  and so operate only on left handed particles. The hypercharges of the quarks and leptons give the interactions between the initially massless particles. The  $W$  and  $Z$  are massive particles (resulting in their short range) which implies that  $SU(2)$  is a broken symmetry. Directly introducing a mass term breaks gauge symmetry so we introduce a Higgs field which is an  $SU(2)$  doublet. It is chosen such that the field,  $\Phi$ , itself is gauge invariant, but its form is chosen such that the field has a ground state away from  $\Phi = 0$  of the form in equation 3.3:

$$V(\Phi) = -\mu^2 \bar{\Phi}\Phi + \lambda |\bar{\Phi}\Phi|^2, \quad (3.3)$$

where  $\mu$  and  $\lambda$  are positive real constants.

Because the state  $\Phi = 0$  is unstable the symmetry is spontaneously broken and so the Higgs acquires a non-zero vacuum expectation value. Choosing an appropriate gauge we acquire our physical gauge bosons which are a combination of the fields which acted on  $Y$  and  $L$ , and through the symmetry breaking they acquire their masses. The strength of the Higgs interaction with a particle is directly proportional to the particle's mass.

### 3.2.1 Yukawa Couplings

As charged fermions have mass, this presents a difficulty as it is possible via a Lorentz boost to find a frame where the helicity switches. Introducing mass terms directly for the fermions (via  $m\bar{\psi}\psi$ ) breaks the gauge invariance and prevents it being re-normalisable, leading to UV divergences. UV divergences occur when high order

corrections are introduced into the calculation of observables, and only in renormalisable theories can these be removed. A more subtle approach is to introduce a Higgs  $SU(2)$  doublet scalar field: this introduces fermion mass terms without breaking re-normalisability. Introducing these Yukawa coupling terms, we add to the Lagrangian density of a free lepton:

$$\mathcal{L}_{Yukawa} = -Y_f \bar{l}_i^c \Phi_i f_R + \text{hermitian conjugate} \quad (3.4)$$

where  $\bar{l}_i^c$  is the first generation  $SU(2)$  left-handed fermion doublet and  $f_R$  is the right-handed fermion singlet. In the limit of the exact  $SU(2)$  symmetry charged leptons are massless, and only obtain mass through the Higgs interaction.

### 3.3 Quantum Chromo-Dynamics

Quark colours arise from the  $SU(3)$  symmetry group [9]. Unlike  $SU(2)$ , which is broken,  $SU(3)$  remains an exact symmetry and the three colour charges (red, green and blue) are conserved in all interactions in the SM. There are 8 gluons (which correspond to 8  $SU(3)$  generators) that are super-positions of the three colours and anti-colours. Like the weak force, the Lagrangian includes terms resulting in 3 and 4-point self interactions, but as the symmetry remains unbroken even at low energies the force is in principle long distance. The strong coupling runs with the energy scale, and becomes weaker at higher energies / shorter distances, while at large distances the force is extremely strong.

However, it has been repeatedly observed that all final states are colour singlets (i.e. no free quarks or gluons have been observed) due a process known as confinement [9, 45]. Quarks have only been observed in bound states of two and three quarks with no net colour charge; in a meson for example, a quark and anti-quark pair are bound together by the strong force (to within  $\sim 1$  fm). Inside the proton the quarks are essentially free, which is known as asymptotic freedom.

In a hadron collider like the LHC the quarks in colliding protons are given enough energy to overcome the binding energy of the strong interaction. The scattered quarks are separated until the potential energy from the strong interaction exceeds the energy required for a quark–anti-quark pair to condense out of the vacuum. The original quarks then form new, colourless, hadronic states. The exact nature of these processes, which necessarily also involve colour reconnection to ensure all hadrons are colour neutral, is the subject of ongoing research [46–48]. A phenomenon related to colour reconnection is the underlying event, often defined as all the particles in a proton-proton collision except those from the hard scattering process of interest. Systematic uncertainties, that arise from the different ways in which colour reconnection and the Underlying Event (UE) are modelled, are evaluated using  $t\bar{t}$  samples with different model parameters: these samples are discussed in section 4.6.

[49, 50]

### 3.3.1 Strong Coupling

The coupling strength of an interaction is constant to leading order, but including higher order Feynman diagrams leads to UV divergences; these can be removed using re-normalisation up to some scale,  $\mu$ . [51] However, this introduces a scale dependence, and the couplings now change with energy. For the strong force, as the energy increases the couplings actually decrease so the use of perturbation theory is valid if the interactions are of sufficiently high energy. The effective strong coupling at some momentum scale  $Q$  (and introducing a re-normalisation scale  $\mu \ll Q$ ) is expanded as:

$$\alpha_s(Q^2) = \frac{\alpha_s(\mu^2)}{1 + \alpha_s(\mu^2) \frac{11N_c - 2n_f}{12\pi} \ln(Q^2/\mu^2)} \quad (3.5)$$

where the number of colours is  $N_c = 3$  and  $n_f$  is the number of energetically accessible flavours. Calculated production cross sections have a re-normalisation scale dependence because the strong coupling decreases with increasing energy.

## 3.4 Perturbation Theory

Using perturbation theory we consider the interaction Lagrangian,  $\mathcal{L}_{int}$ , choosing a regime where the coupling terms are small and fields can be expanded as small perturbations. For the electro-weak interactions at low energies and distances this approximation is valid. As the strong coupling constant decreases with increasing energies and decreasing distances, perturbation theory is sufficient to calculate matrix elements of the hard interactions such as  $t\bar{t}$  production at the LHC. So called leading-order diagrams contain no internal loops, diagrams with two additional internal vertices are referred to as Next-to-Leading Order (NLO). In lower energy processes such as gluon splitting, and quark and gluon hadronisation, perturbation theory is not sufficient. Processes must either be calculated to very high order and/or simplified models are tuned to measurements of low energy processes. For example, the HERWIG generator is used in parton shower and fragmentation in MC samples discussed in section 4.6 must be tuned to data.

Initial State Radiation (ISR) and Final State Radiation (FSR) refer to the radiation produced by incoming or outgoing quarks, gluons or leptons. Gluons and quarks, which have colour, generally radiate gluons through the strong interaction, and the charged leptons radiate photons. For the strong interaction, introducing higher order and lower energy corrections necessitates the use of non-perturbative QCD. This can affect the initial production cross sections, the  $p_T$  of selected jets, and the number of reconstructed jets (affecting the calculated selection efficiencies). To take account of uncertainties from the modelling of ISR and FSR, samples of  $t\bar{t}$  events were produced with differing amounts of radiation.

## 3.5 Top Cross sections and Ratios

### 3.5.1 Production and decay of $t\bar{t}$ events

Figure 3.3 shows the four leading order production mechanisms for  $t\bar{t}$  pairs in proton-proton collisions at the LHC that contribute to the cross section. Each Feynman diagram represents a time ordered matrix element calculation at leading order in quantum field theory. The proportion that each of these production mechanisms contributes depends on the quark and gluon Parton Distribution Functions (PDFs) of the proton; at  $\sqrt{s} = 7$  TeV gluon-gluon production was predicted to account for approximately 85% of  $t\bar{t}$  pairs [52, 53].

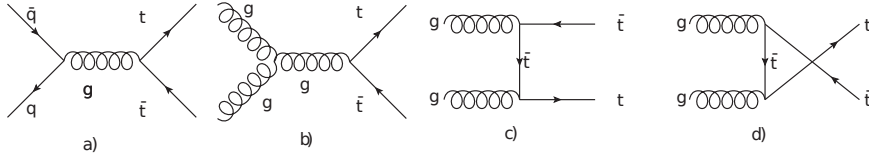


Figure 3.3: The four leading order strong interaction production modes of  $t\bar{t}$  pairs. Diagram a) is from  $q\bar{q}$  annihilation, b) from gluon-gluon fusion, c) and d) via top quark exchange.

It is possible to write the probability of producing a given final state from the scattering, or decay, of initial state particles in terms of the matrix elements for each contributing Feynman diagrams ( $\mathcal{M}_{fi}$ ) and the incoming particle four momenta. For example, for the scattering of two particles, of velocities  $\bar{v}_1$  and  $\bar{v}_2$ , and energies ( $E_1$  and  $E_2$ ), to produce up to  $N$  final state particles (each with momenta  $P_f$  and energy  $E_f$ ) the cross section can be written as:

$$\sigma = \frac{1}{|\bar{v}_1 - \bar{v}_2|} \frac{1}{E_1 E_2} \Sigma_{finalstates} \int |\mathcal{M}_{fi}|^2 \times LIPS(N), \quad (3.6)$$

where the Lorentz Invariant Phase Space (LIPS) is defined as:

$$LIPS(N) \equiv (2\pi)^3 \delta^4(P_f - P_i) \prod_{f=1}^N \frac{d^3\bar{k}}{(2\pi)^3 2E_f}.$$

where

This is a quantity that describes the number of possible final states available for  $N$  particles. The total cross section therefore depends on the incoming particle kinematics, the Feynman diagrams used to calculate  $\mathcal{M}_{fi}$ , and is independent of the outgoing particle kinematics.

To calculate the partial cross sections for di-lepton and lepton plus tau  $t\bar{t}$  final states from the decay of the top quarks, and the subsequent  $W$  decays, the branching ratios need to be included. As the Cabibbo–Kobayashi–Maskawa (CKM) matrix element  $|V_{tb}| = 0.999152_{-0.000045}^{+0.000030}$  [9] (assuming the CKM matrix is unitary), almost all top quarks decay to a  $W$  and a b-quark. Figure 3.4 shows the  $W$  decay modes into each of the three lepton generations, and the first and second generation quark pairs (which have three colour states each).

In the SM the branching ratios for each particle produced from the decay of a  $W$  are approximately equal as the weak coupling constants are the same for each lepton generation, and the first and second quark generations. There are corrections from off diagonal elements of the CKM matrix, but these are small.

Crucially, when considering cross section ratios the production mechanism, including the PDFs of the incoming partons and the incoming particle energies, cancel leaving only the branching ratios from the  $W$  decay. The assumption of lepton universality implies that the weak coupling constants are equal for each lepton generation.

The branching fractions of cross sections are the same as the ratio of the partial decay widths to the total decay width of the decaying particle. The Born approximation can be used to calculate a decay width assuming that a scattering potential is much

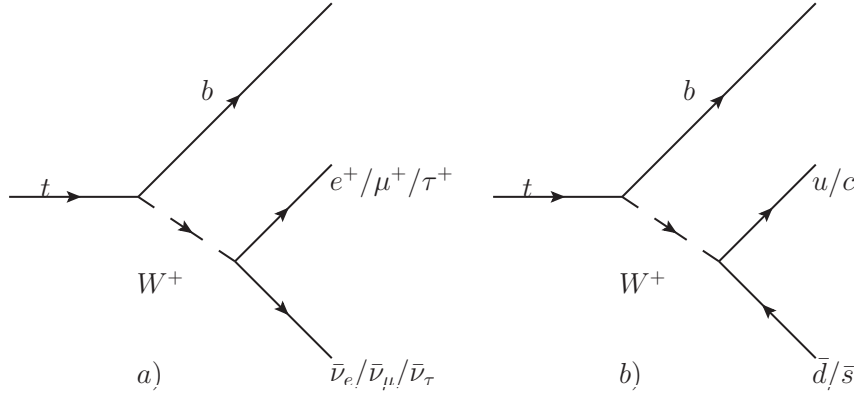


Figure 3.4: In the decay of the top quark there are three leptonic decay modes, and two quark decay modes each with three possible strong colour charges each. The top quarks depicted here decay to b-quarks: decays to the lower mass quarks are very rare.

smaller than the momenta of scattered leptons and setting  $m_{\nu_l} = 0$ . The decay width of the  $W$  becomes

$$\Gamma_{W_{l\nu}}^{Born} = \frac{\alpha_W^l M_W}{6 \cdot 2s_W^2} \left[ 1 - \frac{m_l^2}{2M_W^2} - \frac{m_l^4}{2M_W^4} \right] \left( 1 - \frac{m_l^2}{M_W^2} \right), \quad (3.7)$$

where  $M_W$  is the mass of the  $W$ ,  $l$  is the lepton flavour of mass  $m_l$ ,  $\alpha_W^l$  is the coupling strength of the  $W$  to the lepton  $l$ , and  $s_W$  is the sine of the weak mixing angle (see the [54] for more details).

Using equation 3.7 the corrections to the  $W$  branching fraction ratios are of order  $m_l^2/M_W^2$  and are less than 0.3% [54]. Here lepton universality defines  $\alpha_W^{l_i} = \alpha_W^{l_j}$  where  $l_i$  and  $l_j$  the final state fermions.

In data the definition of a cross section is :

$$\sigma = \frac{N^{data} - N^{bkg}}{\epsilon \mathcal{L}} \quad (3.8)$$

where  $N^{data}$  is the number of events observed in data,  $N^{bkg}$  is the expected number of background events,  $\epsilon$  is the selection efficiency (including detector acceptance), and  $\mathcal{L}$  is the integrated luminosity. The latest public results for the production cross

sections of  $t\bar{t}$  events in proton-proton collisions at  $\sqrt{s} = 7$  GeV were reported by the ATLAS and the CMS collaborations as  $\sigma_{t\bar{t}} = 177 \pm 3(stat.)_{-7}^{+8}(syst.) \pm 7(lumi.)$  pb [55] and  $\sigma_{t\bar{t}} = 165.8 \pm 2.2(stat.) \pm 10.6(syst.) \pm 7.8(lumi.)$  pb [56] respectively, assuming a top mass of 172.5 GeV, which were consistent with Next-to-next-to-Leading Order (NNLO) cross section predictions (165 $_{-16}^{+11}$  pb [57], 162 $_{-7}^{+9}(stat)_{-11}^{+12}(syst)$  pb [58], and NNLO cross sections as a function of the top mass [59]). Using two different PDF schemes, at a top mass of 172.3 GeV, the cross sections at 7 TeV were predicted to be 156 $_{-8}^{+7}(\text{perturbative})_{-9}^{+14}(\text{PDF} + \alpha_S)$  (MSTW2008 NNLO PDFs) and 154 $_{-8}^{+7}(\text{perturbative})_{-12}^{+13}(\text{PDF} + \alpha_S)$  (CTEQ6.6 PDFs), see [60].

The partial branching fractions of the  $t\bar{t}$  final states are listed in table 3.4 in section 4.6.2 using the values of the world average branching fractions of the  $W$  and the tau from the PDG [9]. For the channels being measured, the contributions to these final state branching fractions from each of the initial  $W$  decay is shown in table 3.5. A contribution events where a  $W$  decays to a tau which subsequently decays to a lepton is seen.

Channel	Branching fraction
$ee$	$0.016 \pm 0.00038$
$\mu\mu$	$0.016 \pm 0.0004$
$e\mu$	$0.032 \pm 0.00051$
$e\tau$	$0.018 \pm 0.0007$
$\mu\tau$	$0.018 \pm 0.00052$
$\tau\tau$	$0.0052 \pm 0.00031$
$e + jets$	$0.17 \pm 0.0019$
$\mu + jets$	$0.17 \pm 0.0022$
$\tau + jets$	$0.098 \pm 0.003$
$di-jets$	$0.46 \pm 0.0038$

Table 3.4: The branching fractions for all final state channels calculating using the PDG values of the single particle branching fractions of the  $W$  and tau.

Channel	Initial $W$ decay products			
	$e\mu$	$e\tau$	$\mu\tau$	$\tau\tau$
$e\mu$	$0.023 \pm 0.00042$	$0.0041 \pm 0.00014$	$0.0042 \pm 0.00014$	$0.00076 \pm 0.00021$
$e\tau$	0	$0.015 \pm 0.0005$	0	$0.0028 \pm 0.00049$
$\mu\tau$	0	0	$0.015 \pm 0.00051$	$0.0028 \pm 0.00012$

Table 3.5: The branching fractions of the final state leptons broken down into the contributions from the initial decay products of the  $W$ , calculated using the PDG values [9]. All values and errors are absolute.

### 3.5.2 Lepton Universality

The  $W$  coupling to the fermions, to left handed particles (represented by  $L$ ), is written as:

$$\frac{g}{\sqrt{2}} W_{\alpha}^{+} (\bar{\mathbf{U}}_L V_{CKM} \gamma^{\alpha} \mathbf{D}_L + \bar{e}_L \gamma^{\alpha} \nu_{eL} + \bar{\mu}_L \gamma^{\alpha} \nu_{\mu L} + \bar{\tau}_L \gamma^{\alpha} \nu_{\tau L}) + \text{hermitian conjugate} \quad (3.9)$$

where  $g$  is the weak coupling constant (and is implicitly assumed to equal for all weak charged interactions) [61]. Here  $\mathbf{U}^T = (u, c, t)$  and  $\mathbf{D}^T = (d, s, b)$  represent vectors of left handed quark spinors,  $W_{\alpha}^{+}$  represents the field of the  $W^{+}$ ,  $V_{CKM}$  the CKM mixing matrix (see [45] for more details), and  $\gamma^{\alpha}$  are the  $\gamma$ -matrices of QFT (see [61] for more details). A different value for  $g$  for any fermion interaction would be a violation of lepton universality.

Measurement of processes sensitive to neutral current interactions are entirely consistent with lepton universality [9]. For example the world average partial branching fractions of the  $Z$  to di-leptons from the PDG are

- $\Gamma(Z \rightarrow e^{+}e^{-}) = 83.91 \pm 0.12$  MeV,
- $\Gamma(Z \rightarrow \mu^{+}\mu^{-}) = 83.99 \pm 0.18$  MeV,
- and  $\Gamma(Z \rightarrow \tau^{+}\tau^{-}) = 84.08 \pm 0.22$  MeV [9].

A lower energy measurement performed by the CLEO experiment measured the ratio of  $\Upsilon \rightarrow \tau^+\tau^-$  to  $\Upsilon \rightarrow \mu^+\mu^-$  for  $\Upsilon(1S)$ ,  $\Upsilon(2S)$ , and  $\Upsilon(3S)$  for one prong tau decays as  $R^{\Upsilon(1S)} \equiv N(\Upsilon(1S) \rightarrow \tau^+\tau^-)/N(\Upsilon(1S) \rightarrow \mu^+\mu^-) = 1.06 \pm 0.02(stat.) \pm 0.03(syst.)$ ,  $R^{\Upsilon(2S)} = 1.00 \pm 0.03(stat.) \pm 0.12(bkgsyst.) \pm 0.03(syst.)$ , and  $R^{\Upsilon(3S)} = 1.05 \pm 0.07(stat.) \pm 0.05(bkgsyst.) \pm 0.03(syst.)$  [62], and a similar measurement performed at BaBar measured the ratio of the decay widths of the  $\Upsilon(1S)$  to  $\tau^+\tau^-$  and  $\mu^+\mu^-$  pairs as:  $\Gamma_{\Upsilon(1S) \rightarrow \tau^+\tau^-}/\Gamma_{\Upsilon(1S) \rightarrow \mu^+\mu^-} = 1.005 \pm 0.013(stat.) \pm 0.022(syst.)$  [63]. Both were consistent with the SM expectation.

Two low energy measurements sensitive to lepton violating processes in charged weak interaction found no significant deviations from SM expectations. The KLOE experiment measured the cross section ratio in  $K_S$  and  $K_L$  decays to leptons, via charged current interactions, as  $r_{\mu e} = 1.000 \pm 0.008$  [64], and the NA62 experiment measured decay rate ratio of  $K^+ \rightarrow e^+\nu$  to  $K^+ \rightarrow \mu^+\nu$  as  $R_K = (2.486 \pm 0.013) \times 10^5$  which is in agreement with the SM prediction  $R_K^{SM} = (2.486 \pm 0.013) \times 10^5$  [65].

A review of measurements at B-factories can be found in [66]; the measurements are consistent with SM expectations. The BaBar experiment measured the ratio of lepton weak couplings,  $|\frac{g_\tau}{g_\mu}| = 0.9856 \pm 0.0057$  and  $0.9827 \pm 0.0086$  using pions and kaons respectively. When these results were combined the ratio was measured to be  $|\frac{g_\tau}{g_\mu}| = 0.9850 \pm 0.0054$ , which is  $2.8 \sigma$  below the SM expectation of 1.0 [67].

Higher energy measurements were performed with the Large Electron–Positron Collider (LEP) experiments, ALEPH, DELPHI, L3, and OPAL. The ratio of  $W$  leptonic branching fractions were measured to be  $2B(W \rightarrow \tau\bar{\nu}_\tau)/(B(W \rightarrow e\bar{\nu}_e) + B(W \rightarrow \mu\bar{\nu}_\mu)) = 1.077 \pm 0.026$ ,  $2.8 \sigma$  above unity [68] (when assuming partial lepton universality between electrons and muons). The  $W$  branching ratios calculated to leading order, and taking account of the fermion masses, are  $B(W \rightarrow e\bar{\nu}_e) = 0.1083$ ,  $B(W \rightarrow \mu\bar{\nu}_\mu) = 0.1083$ , and  $B(W \rightarrow \tau\bar{\nu}_\tau) = 0.1082$  using the improved Born approximation [54]. Effects of fermion masses are of the order  $m_f^2/M_W^2$ , below 0.3%.

A measurement of the  $W \rightarrow \tau\nu$  partial cross section was performed at ATLAS [69],

but due to large systematic uncertainties no effect of the order observed at the LEP experiments were seen. This gives a motivation for studying decays where leptons are produced in weak charged currents. In  $t\bar{t}$  decays real  $W$  bosons are produced. By evaluating the cross section ratios as in equation 3.9 and comparing them to the SM expectations a channel can be studied that involves weak, charged currents.

## 3.6 Other Top Quark Physics

### 3.6.1 Top Mass

The top quark mass is a fundamental parameter of the SM. The measured top quark mass can be related to the re-normalised mass of the top quark in the SM Lagrangian (the re-normalised mass depends on the chosen re-normalisation scheme but these can be converted using perturbation theory). A review of top quark physics results from the LHC experiments ATLAS and CMS can be found in [70]. Tevatron results were combined to give a measured top mass  $m_t = 173.20 \pm 0.90$  GeV (quoted as the *pole* mass), see [71].

### 3.6.2 Top Properties

The top quark has a charge of  $+2/3e$  in the SM. As the top quark decays in around  $10^{-24}$ s [72–76], and does not form any stable hadrons, the charge of the top quark must be determined from its decay products. Previous Tevatron measurements excluded a charge  $Q = -4/3e$  at the 95% level [77]. Measurements at the ATLAS [78] and the CMS experiments [79] have excluded an exotically charged top quark at greater than  $5\sigma$  significance, and a measurement recently submitted for publication has measured the top quark charge as  $0.64 \pm 0.02(stat.) \pm 0.08(stat.)e$ , consistent with the SM [80].

Because of the short decay of the top quark it cannot form a stable hadron and

the spins of the top quark pairs can affect the angular correlations of their decay products.

Spin correlation measurements are possible in  $t\bar{t}$  events because the quarks decay before forming stable top hadrons. In a reference frame such as that defined by the decay products of one top quark, the angular distribution of the other top quark decay products can be reconstructed and reveal any angular correlations between them. The Tevatron reported measurements consistent with the SM expectation [81] and another measurement performed at ATLAS, which improved upon this result, was also consistent with the SM expectation [82] and excluded the zero spin correlation hypothesis at  $5.1\sigma$  significance.

A measurement sensitive to the existence of a fourth fermion generation is the ratio top decays  $R = B(t \rightarrow Wb)/B(t \rightarrow Wq)$ ; a deficit of  $2.5\sigma$  was observed in this ratio [83] by the *D0* Collaboration.

Charge asymmetry measurements, looking at the difference between  $t$  and  $\bar{t}$  rapidity distributions, are sensitive to BSM physics that could contribute to  $t\bar{t}$  production processes. Significant deviations from the SM expectation in these measurements from the Collider Detector at Fermilab (CDF) [84] and the *D0* experiments [85] have been observed in proton–anti-proton collisions at  $\sqrt{s} = 1.96$  TeV. Measurements from the ATLAS and the CMS experiments differ from those performed at the Tevatron  $p\bar{p}$  experiments as the proton-proton collisions of the LHC are inherently symmetric and so have a lower sensitivity. To date no measurements have been published with enough precision to see similar asymmetry levels at the LHC by the ATLAS [86] and the CMS collaborations [87]. The  $t\bar{t} \rightarrow b\bar{b}H^+W^-$ ,  $t\bar{t} \rightarrow b\bar{b}H^-W^+$ ,  $t\bar{t} \rightarrow b\bar{b}H^+H^-$  charged Higgs samples are produced PYTHIA 6.425 [88] where all charged Higgs decay to taus. The tau decay is simulated by TAUOLA 1.20 [89].

The first  $5\sigma$  observation of single top production was first presented by CDF [90] and *D0* [91] at the Tevatron collider and later confirmed by the ATLAS [92] and CMS [93] experiments, in agreement with SM expectations.

## 3.7 Physics Beyond the SM

Several observations imply that at some energy scale the SM must break down. Precise measurements of the dark matter content of the universe have been performed using WMAP2 [41]. The first direct evidence of dark matter was seen in the bullet cluster [41]. There are no particles in the SM that interact in the way dark matter has been inferred to do from astronomical observations. From the relative uniformity of the CMBR it is clear that the universe underwent a massive super-luminary expansion, known as inflation, in the first moments after the Big Bang. The hypothesised field particle responsible is known as the inflaton, though its properties are known only very generally. There are many theories as to the nature of this field and its associated particle; suffice to say that no SM particle could be responsible.

The other smoking gun is the excess of matter over anti-matter in the universe, inferred from estimates for the amount of matter compared the number of Cosmic Microwave Background (CMB) photons produced in matter-anti-matter annihilation before re-combination. While CPV has been observed in the SM, the size of these effects is orders of magnitude too small to account for the excess.

Beyond these observations theorists are working on models, including string theory, which seek to understand the existence of the universe and its genesis. Due to the energy scales involved, testing these theories is out of reach of any currently conceivable HEP experiment.

The last major piece of the SM, the observation of a Higgs boson, was independently confirmed by the ATLAS [7] and CMS [8] experiments in 2012 at the  $5\sigma$  significance level. While work is ongoing to understand the nature of this Higgs, so far all observations are consistent with a SM Higgs boson including its spin=0 nature [94]. Most popular extensions to the SM include a Higgs field of some type to break the  $SU(2)$  symmetry.

### 3.7.1 Supersymmetry

Supersymmetry (SUSY) is a set of theories that extend the SM by introducing a new symmetry between bosons and fermions. It posits that every SM fermion and boson has a super-partner boson and fermion respectively. When calculating the mass of a SM boson beyond tree-level, loop diagram corrections from the self-interacting nature of the Higgs are introduced which are quadratically divergent. These corrections are proportional to  $\Lambda_{BSM}$  which is the energy scale at which new physics processes start to contribute. Either there are new physics processes near the electro-weak scale that do not contribute to the processes observed at LEP and the LHC so far, or the Higgs mass is ‘fine tuned’ to exactly cancel the divergences exactly (for which there is no physical justification). Introducing SUSY allows us introduce a way that naturally solves much of the fine tuning problem. Additionally the running gauge couplings indicate that the strong, weak and electro-magnetic forces should unify at high energies. However high precision SM predictions for the gauge couplings near the unification scale predict that they do not become equal, and many attempts to extend the SM generally assume that the forces can exactly unify at some scale.

One prediction of SUSY is that the proton will have a very short lifetime ( $\sim 10^{-1}$  s [95]) which is obviously not the case. A new quantum number, R-parity is introduced

$$R = (-1)^{2S+3(B-L)}, \quad (3.10)$$

from the spin (S), baryon number (B) and lepton number (L) which is globally conserved and prevents the decay of the proton. The SM particles are R-parity even, and their super-partners are R-parity odd. This additionally allows a dark matter candidate to be introduced, the so-called Lightest Stable SUSY Particle (LSP). It is a stable particle that interacts very weakly via the strong and electro-weak forces, and has the necessary properties of a dark matter candidate inferred from astrophysical measurements. If R-parity is conserved all SUSY particles will decay to the LSP, which is stable and very weakly interacting. Note that there are other theories

that do not include SUSY that also have dark matter candidates such hypothetical particles called Axions [9].

As no super-partners to any of the SM particles have been observed the symmetry must be spontaneously broken. As this introduces  $\sim 125$  new free parameters compared to the 19 of the SM, constrained versions with fewer parameters have been introduced. One of the simplest is called Constrained MSSM (cMSSM). Many theories that extended the SM to unify all the forces (so called Grand Unified Theories (GUTs)) necessarily assume SUSY.

In SUSY models additional Higgs doublets are included with opposite hyper-charge leading to charged Higgs bosons. In the MSSM a charged Higgs would decay in a similar way to the  $W$  except for coupling more strongly to more massive particles. Interaction terms including Higgs couplings do not manifestly break lepton universality. However, introducing a charged Higgs that couples with leptons introduces Feynman diagrams that depend on the mass of the lepton. Figure 3.5 shows the decay of a top quark to a tau lepton via a charged Higgs. Measurements of the top cross section ratio from equation 3.13 could result in larger value than the SM expectation if this diagram contributed to the decay of the top quark.

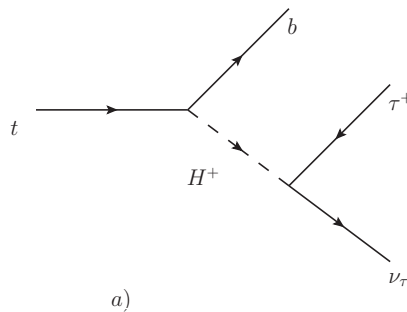


Figure 3.5: The Feynman diagram of a top quark decaying to a b-quark, and a charged Higgs boson which decays to a tau and a tau neutrino.

It is important to note that much of the parameter space for some of the most constrained SUSY models, such as MSSM, has now been excluded by numerous measurements at the LHC into and exceeding the TeV range (see [96], [97] and [98]) as illustrated in figure 3.6. However less constrained models could still be seen at the

LHC with increasing amounts of data and at higher collision energies.

### 3.8 Summary

The SM has proved to be one of the most successful theories of modern science, however we know from many observations beyond HEP that it must break down at some scale. Almost all measurements of SM parameters and assumptions have proved consistent, but some measurements have small deviations from SM expectations, such as the  $W$  branching ratios of tau and electron/muon final states, which could indicate a violation of lepton universality. The discovery of a Higgs boson, consistent with SM expectations, is necessary to some SUSY theories, which include additional charged Higgs bosons. While highly constrained SUSY models such as MSSM have had large amounts of their parameter space excluded, other less constrained theories have not. Measuring  $t\bar{t}$  cross section ratios with final states with a lepton and tau to di-lepton final states allows a comparison to SM expectations of the ratio which is sensitive to the weak couplings to leptons, and to the presence of charged Higgs bosons.

In section 4.1 reconstructed electrons and muons are defined irrespective of their parent particles and include those from tau decays. Two-particle branching ratios are defined based on the final states of  $t\bar{t}$  decay (e.g. the branching ratio of a  $t\bar{t}$  pair to a final state electron and muon is defined as  $B(t \rightarrow e) \cdot B(t \rightarrow \mu)$ , where the electron and muon originate from either top quark. The measured cross sections,  $\sigma_{l_1\tau}$  and  $\sigma_{l_1l_2}$ , ( $l_1 = e/\mu$ ,  $l_2 = \mu/e$ ) are defined in equations 3.11 and 3.12 respectively,

$$\begin{aligned} \sigma_{l_1\tau} \equiv \sigma_{t\bar{t}} [ & B(t \rightarrow \tau) \cdot B(t \rightarrow l_1) \cdot B(\tau \rightarrow h\nu_\tau) \\ & + B(t \rightarrow \tau) \cdot B(t \rightarrow \tau) \cdot B(\tau \rightarrow h\nu_\tau) \cdot B(\tau \rightarrow l_1\nu_{l_1}\nu_\tau) ] \end{aligned} \quad (3.11)$$

$$\begin{aligned}
\sigma_{l_1 l_2} \equiv \sigma_{t\bar{t}} & [B(t \rightarrow e) \cdot B(t \rightarrow \mu) + B(t \rightarrow \tau) \cdot B(t \rightarrow l_2) \cdot B(\tau \rightarrow l_1 \nu_{l_1} \nu_\tau) \quad (3.12) \\
& + B(t \rightarrow \tau) \cdot B(t \rightarrow l_1) \cdot B(\tau \rightarrow l_2 \nu_{l_2} \nu_\tau) \\
& + B(t \rightarrow \tau) \cdot B(t \rightarrow \tau) \cdot B(\tau \rightarrow l_1 \nu_{l_1} \nu_\tau) \cdot B(\tau \rightarrow l_2 \nu_{l_2} \nu_\tau)]
\end{aligned}$$

and the cross section ratios are defined by:

$$\mathcal{R}_{l_1 \tau} \equiv \frac{\sigma_{l_1 \tau}}{\sigma_{l_1 l_2}} \quad (3.13)$$

where lepton  $l_1$  is defined as the triggering lepton. Only hadronically decaying taus are counted in the numerator.

Using the branching fractions from [9] for the decay of the  $W$  and the tau the and equation 3.13, the expected SM cross section ratios are inferred to be  $\mathcal{R}_{e\tau} = 0.57 \pm 0.024$  and  $\mathcal{R}_{\mu\tau} = 0.56 \pm 0.019$ , assuming lepton universality.

A SUSY model with a charged Higgs boson which could be produced in the decay of the top quark and would dominantly decay to tau leptons. In table 3.6 the branching ratios have been calculated for several  $B(t \rightarrow H^+)$  values, simply by assuming  $B(H \rightarrow \tau) = 1$  and setting the branching ratio of of the top to the  $W$  to  $B(t \rightarrow bW) = 1 - B(t \rightarrow H^+)$ . This is not directly comparable to the cross-section ratios which are model independent, because it assumes that the efficiency of reconstructing an additional tau and its decay product has been corrected for. As seen in table 3.5 the di-lepton channel has contributions from tau decays which reduces such a measurements possible sensitivity.

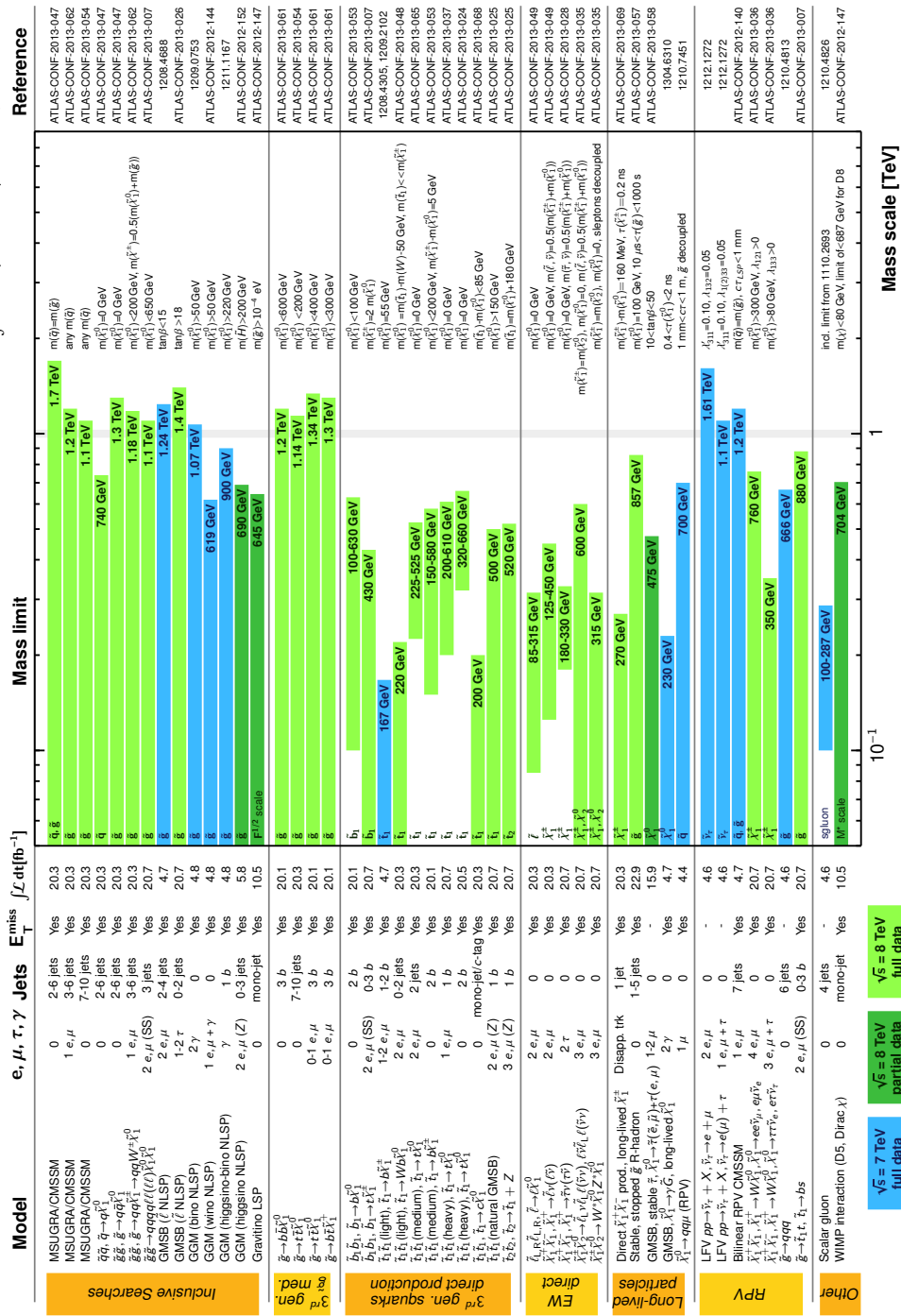
$B(t \rightarrow H^\pm)$	$\mathcal{R}_{e\tau}$	$\mathcal{R}_{\mu\tau}$
0.0	$0.57 \pm 0.024$	$0.56 \pm 0.019$
0.05	$0.64 \pm 0.026$	$0.63 \pm 0.021$
0.1	$0.72 \pm 0.029$	$0.71 \pm 0.023$
0.15	$0.80 \pm 0.032$	$0.79 \pm 0.025$
0.2	$0.89 \pm 0.035$	$0.88 \pm 0.028$

Table 3.6: The ratios of branching fractions as calculated using PDG branching fractions for the  $W$  for various branching fractions of the top to a charged Higgs. The efficiency of such events would not be expected to be the same and measurements looking for this signal would need to include this correction. All uncertainties are absolute and only include those propagated from the PDG branching fraction measurements [9].

# ATLAS SUSY Searches\* - 95% CL Lower Limits

Status: EPS 2013

ATLAS Preliminary  
 $\sqrt{s} = 7, 8 \text{ TeV}$   
 $\int \mathcal{L} dt = (4.4 - 22.9) \text{ fb}^{-1}$



\*Only a selection of the available mass limits on new states or phenomena is shown. All limits quoted are observed minus 1 $\sigma$  theoretical signal cross section uncertainty.

Figure 3.6: ATLAS mass exclusions for various SUSY particles and other exotic processes as published in [96].

# Chapter 4

## Event Selection of $t\bar{t}$ Events

In order to measure the properties of top decays in  $t\bar{t}$  events the raw data output from the ATLAS detector needs to be turned into physically meaningful information. In section 4.1 the basic reconstruction and identification of particles, and event level information is discussed. In section 4.2 these objects are pre-selected for the quality of their reconstruction and some minimal kinematic acceptance criteria. Overlap removal, after pre-selection, is discussed in section 4.3. The selection of  $t\bar{t}$  event candidates is discussed in section 4.4. The MC samples used to study the signal  $t\bar{t}$  and background yields and distributions are discussed in section 4.6.

### 4.1 Object Reconstruction and Identification

We want to know which particles are likely to have left ID space-points (to turn into tracks), calorimeter energy deposits (to turn into electromagnetic ‘clusters’ in the EM barrel calorimeter, or ‘jets’ in the hadronic calorimeter) and muon spectrometer information (to turn into muon tracks). Each reconstruction routine assigns the signatures left in each of the detectors to a candidate particle. There may be overlap, with some signatures being assigned to more than one reconstructed object.

Most objects are defined at several different working points allowing a choice in the trade off between highly efficient reconstruction, where most physical particles are reconstructed, and a high purity for those particles.

### 4.1.1 Electrons

There are several algorithms for reconstructing electromagnetic particles. For electrons the standard reconstruction routine is seeded by information from calorimeter clusters (identified as [author 1](#)), and an additional soft electron routine is seeded by reconstructed tracks (identified as [author 3](#)). Standard electron reconstruction starts with clusters formed with a sliding-window algorithm from cells in the EM barrel calorimeter. In the central region of the detector an electron is reconstructed if at least one ID track is matched to the cluster; the one with the smallest  $\Delta R = \sqrt{\Delta\eta^2 + \Delta\phi^2}$  distance to the seed cluster is used. The four-momentum is computed using information from the track and the final cluster, with the  $\eta$  and  $\phi$  positions determined by the track matched to the seed cluster, and the energy from the cluster energy [22].

Three different working points are used for electrons in the ATLAS reconstruction software in data taken in 2011: loose++, medium++, and tight++, which have increasing levels of background rejection. These were designed to have no more than one jet incorrectly reconstructed as an electron for approximately every 500, 5000 and 50,000 jets in MC simulation. Loose++ electrons use shower shape variables of the EM barrel calorimeter and hadronic leakage variables; medium++ electrons additionally use variables from the EM barrel calorimeter strip layer, track quality requirements and track cluster matching requirements; tight++ electrons use  $E/p$  and PID from the TRT and discriminate against photon conversions [22].

The energy scale of electrons is measured using  $Z \rightarrow e^+e^-$  events in data: scaling is applied to the data by default for all electrons with  $p_T > 7$  GeV ensuring the invariant mass peak in data matches MC [99–101]. Binned  $p_T$  and  $\eta$  dependent

corrections, with values of  $< 0.1\%$ – $\sim 5\%$ , are applied to the reconstructed electron cluster energy and  $p_T$ .

The difference between simulated and measured electron energy resolution is corrected by smearing MC electrons with  $p_T > 7$  GeV and applying a Gaussian shift to the electron energy and  $p_T$  to match the energy resolution measured from data [102]. The uncertainty in this smearing is a source of systematic uncertainty as explained in section 6.4.1.

No track or energy isolation requirements are placed on electrons at this stage. Because some small discrepancies were observed in the energy deposited by electrons data and MC [22]  $\eta$  dependent corrections were applied to the electron  $p_T$ , and expected energy deposit given the amount of pile-up in a cone of 0.2 or 0.3 radians around the electron. An isolation cut that is dependent on the electron  $p_T$  and  $\eta$  can be applied [22].

### 4.1.2 Muons

Several algorithms are used to reconstruct muons in the ATLAS detector, combining information from the two muon tracking detectors, ID and calorimeters. One collection of muons, the Inner Detector Reconstructed Muons (MuID) muon collection, combines inner detector and MS tracks using a global refit of the tracks to produce combined muons [29]. Combined muons produce the highest purity muons, and also have an efficiency measured in data of  $(0.991 \pm 0.001)$  [103].

Two measures of isolation can be used to define a set of very pure muons. The sum of the  $p_T$  of all tracks in a cone of size  $\Delta R = 0.3$  is defined as the variable *ptcone30* (where 30 represents the cone size of  $\Delta R = 0.3$ ). Similarly the sum of the energy from all the calorimeter cells,  $E_T$  in a cone of  $\Delta R = 0.2$  is defined as *etcone20*.

Muon smearing factors were calculated using tag and probe studies of  $Z \rightarrow \mu^+ \mu^-$  events so that the resolutions measured in data matched those simulated in MC.

They are applied by default to all MC muons before any object pre-selection using a standard software tool. The smearing factors are binned in  $p_T$  and  $\eta$ , and are dependent on the muon charge, and are applied separately for ID and MS muons as described in [104].

### 4.1.3 Jets

A stable jet reconstruction algorithm must satisfy three criteria: jets must be infrared safe so soft radiation does not affect reconstruction; and collinear safe where the jet reconstructed is independent of whether transverse momentum is carried by one particle, or two collinear tracks; and order independent, whereby the same jets are reconstructed from parton, particle or detector level information. While several algorithms fit these criteria, the anti- $k_\perp$  algorithm [105] reconstructs jets which have a conical shape, making detector level corrections and understanding of the jets more intuitive, see [29] for more details.

Particles leave energy deposits in the calorimeter cells, and the cells are calibrated to remove electronic and thermal noise before clustering nearby cells. Jets are reconstructed, using the anti- $k_\perp$  algorithm, from topological calorimeters to form jets with a cone radius  $R = 0.4$ . A baseline calibration is applied to the jet at the EM scale to account for deposits from electrons and photons see [6].

#### 4.1.3.1 Jet Energy Scale

The energy of each jet is subject to additional corrections according to its energy, its Jet Energy Scale (JES), depending on its position in the detector, its kinematic properties, the physics environment, the interactions of the different particles in the jet with the detector and the dead material, and corrections that relate the energy deposited. A summary of the full description in [106] and [107] can be found below.

The JES was measured using LHC collision data, test-beam data and MC simula-

tion [108–110], and is then applied to the jets. Data was compared to MC truth information, such that the kinematic variables including the energy and position of the true particle, correspond to those measured in the detector. This necessarily introduces MC modelling systematic uncertainties, including the simulations of interactions of particles with materials.

Corrections are applied to jets based on the  $\eta$  position in the detector. Larger corrections are applied to areas with limited instrumentation, correcting for the necessarily lower measured energies. Without this correction there would be a bias towards higher instrumented areas of the detector. Pile-up interactions result in extra energy deposition in the calorimeter, so a term is introduced to subtract the expected deposition. The reconstructed jet energies are also corrected according to the position of the primary vertex.

Uncertainties on these corrections have been measured using complementary means, including single-pion test beam measurements and single hadron response measurements, di-jet inter-calibration, di-jet balancing and  $\gamma - jet$  balancing. When measuring the systematic effect of these uncertainties on the measurements made in section 6.3, the uncertainties are combined into one set of systematic shifts of the JES while also propagating changes to the  $E_T^{\text{miss}}$  calculation.

#### 4.1.3.2 Jet Energy Resolution

The Jet Energy Resolution (JER) is measured in data using a di-jet balancing method by measuring the asymmetry of the jet  $p_T$ . As there is good agreement between the JER measured in data and that obtained from MC no smearing is performed by default. The error on the JER is obtained from data and is used by introducing smearing to the jet  $p_T$  by the corresponding amount [111, 112].

### 4.1.3.3 Jet Reconstruction Efficiency

The Jet Reconstruction Efficiency (JRE) has been measured in data and found to be very high for jets with  $p_T > 20$  GeV (an inefficiency of  $\sim 2$  jets per million for jets with  $20 \text{ GeV} < p_T < 30 \text{ GeV}$ ). There is good agreement between MC and data and no corrections are applied to MC. However, the measured efficiency has large errors for events with large numbers of jets due to limited statistics. The error on the measured JRE is treated as a systematic uncertainty; using a standard software tool jets are randomly dropped from events to achieve the desired jet inefficiency (see [113]) as described in section 6.4.1. In a previous study this systematic uncertainty was found to be 1% of the measured cross section [1].

### 4.1.4 B-Jets

To identify jets originating from a b-quark several b-tagging algorithms have been developed within ATLAS. Due to the relatively long lifetimes of b-hadrons they often have a displaced vertex. The SV1 algorithm uses the decay length significance ( $L_{3D} / \sigma_{L_{3D}}$ , the decay length over its uncertainty), the invariant mass of the tracks associated with the secondary vertex, and topological and kinematic information, which is combined using a likelihood ratio technique [114]. Two other techniques, the JetFitterCombNN and I3PD algorithms, are described in [115] and [116] respectively. Using the weights produced by I3PD, SV1 and JetFitterCombNN (which are all described in [116]) as inputs to a neural network algorithm, the MV1 b-tagging algorithm is created.

The b-tag efficiency for MV1 is defined at several working points. For a b-tagging efficiency of 70% the algorithm weight is  $MV1 > 0.601713$  as determined using MC samples. The efficiency as a function of the jet  $p_T$  measured in  $5 \text{ pb}^{-1}$  of data is shown in figure 4.1 and shows good agreement between data and MC. The b-tag efficiency has also been measured in data in a  $t\bar{t}$  sample [117] and found to have good agreement with MC. Mis-tag rates from light jets and c-jets have been measured

to be in the range 0.01-0.03 for the MV1 algorithm at the 70% efficiency working point, see [118] for more details.

Figure 4.2 show that applying the MV1 algorithm at the 70% efficiency working point selects a pure sample of b-tagged jets in data. Along with the very high rejection predicted in MC shown in figure 4.1 gives a high level of confidence that using this algorithm and working point will allow a high purity of events to be selected.

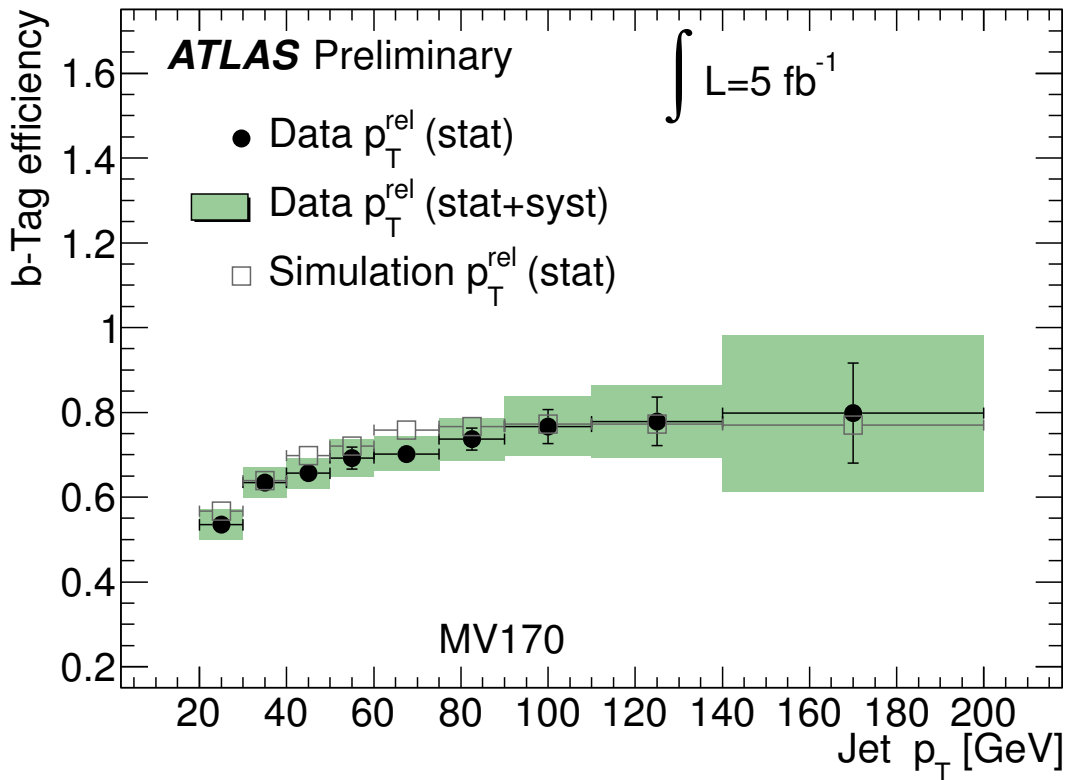


Figure 4.1: The b-tag efficiency using at function of  $p_T$  the MV1 b-tagging algorithm at the nominal 70% efficiency. [119]

#### 4.1.5 Hadronically Decaying Taus

Taus that decay hadronically must be distinguished from other hadronic jets. Anti- $k_\perp$  jets with a cone size of  $\Delta R = 0.4$  are taken as a seed for tau reconstruction.

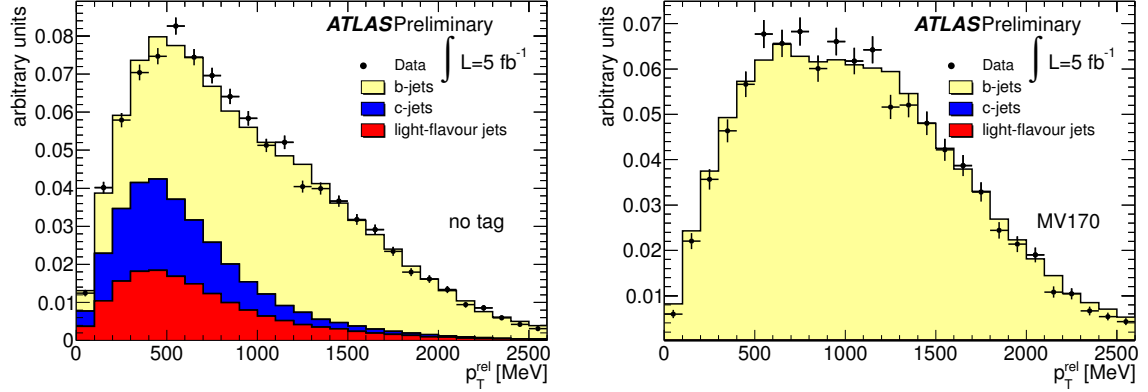


Figure 4.2: Templates for light-flavour jets, b-jets and c-tagged jets were created in data as a function  $p_T^{rel}$  (the momentum of a muon transverse to a muon plus jet axis) fitted to data before and after the application of the MV1 algorithm with a 70% efficiency [119].

Re-clustering is performed on the calorimeter cells, which are used to find associated tracks and to recalculate kinematic variables (including the calibration specific to taus). Variables calculated from the calorimeter and track information are used as inputs to a Boosted Decision Tree (BDT), which was trained to discriminate between hadronic taus and other hadronic jets using  $Z \rightarrow \tau\tau$ ,  $W \rightarrow \tau\nu$  and  $Z' \rightarrow \tau\tau$  MC samples as signal and a QCD jet background taken from data. The BDT produces a number varying from 0-1 with higher values designed to have increasing likelihood of being a tau lepton. Figure 4.3 shows this score for single pronged tau candidates [120]. The tight definition tau candidates have an efficiency around 30% and jet rejection factors of  $\sim 300$ .

While hadronic jets are more likely to fake a hadronically decaying tau, electrons can also deposit energy in the HCal. As the BDT is only trained using jets, it is necessary to introduce a way of discriminating between electrons and 1-pronged taus. Several properties allow electrons to be distinguished from taus. Compared to taus, electrons have a propensity to produce transition radiation (where particles changing between different media emit photons). They have wider and longer shower shapes, and deposit a higher proportion of their energy in the EM and pre-sample calorimeters, and a lower proportion in the HCal. The same variables that are used

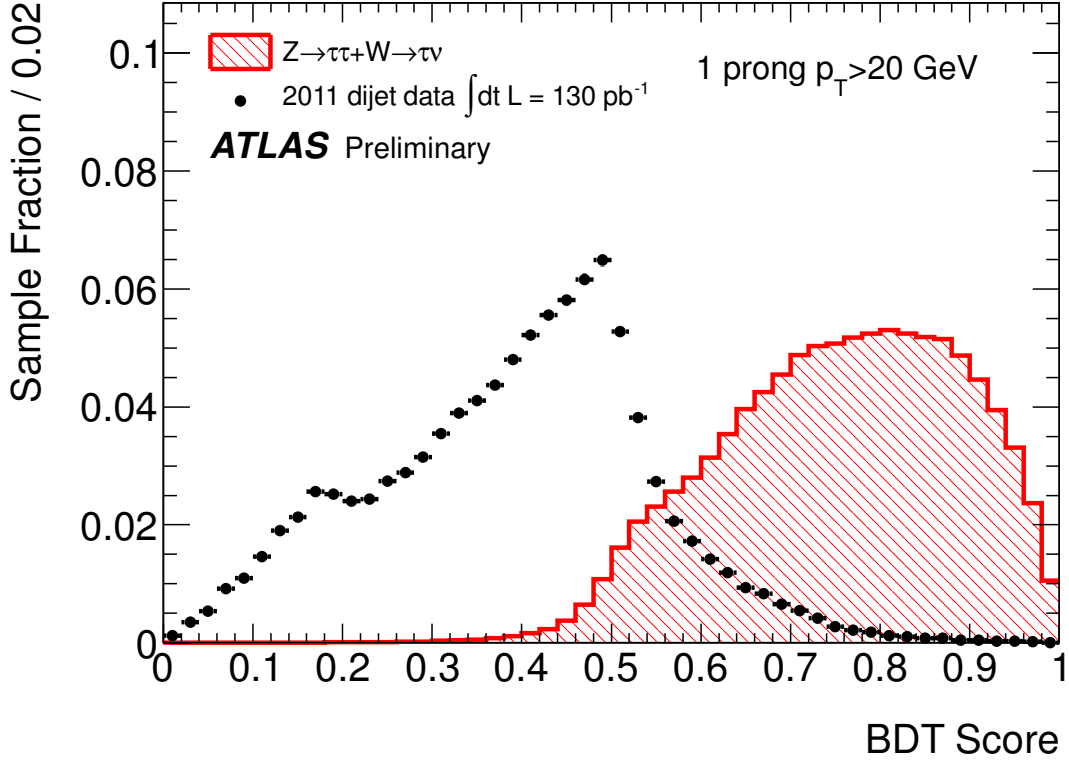


Figure 4.3: Tau BDT score for QCD di-jets from data reconstructed as taus, and taus from MC. A higher score indicates a higher probability of having a real single-pronged tau instead of a jet [120].

to create the tau BDT are used to train a BDT discriminant using  $Z \rightarrow e^+e^-$  and  $Z \rightarrow \tau\tau$  MC samples, and achieves electron rejection factors in the range 100-1000 for an efficiency of 50% [120].

Muons can also fake tau candidates, but have fake rates of the order  $1/1000$  for hadronic tau candidates [121]. Because of the low statistics, initial efforts to measure this rate were dropped. In its place a cut based veto can be applied which rejects  $\sim 50\%$  of muons reconstructed as tau candidates while maintaining a tau efficiency of 96% [122] after overlap removal. This leaves a very low muon fake rate which, as in other similar analyses [123], is not considered in this analysis.

## 4.1.6 Missing Transverse Energy

Because of momentum conservation, the total momentum of all particles produced in a proton-proton collision event in the  $x$ - $y$  plane, transverse to the beam direction, should be close to zero. The parameter  $E_{\text{T}}^{\text{miss}}$  is broadly defined as the vector sum of the  $E \sin \theta$  of all pre-selected objects in that event, plus remaining calorimeter information not associated to these objects. Because neutrinos do not interact with the ATLAS detector, any  $E_{\text{T}}^{\text{miss}}$  in an event can be attributed to the one or more neutrinos.

The performance of  $E_{\text{T}}^{\text{miss}}$  reconstruction in 7 TeV proton-proton collisions is described in [124]. The  $E_{\text{T}}^{\text{miss}}$  definition is dependent on the definition of objects used in each analysis, for example different jet algorithms can reconstruct differing jet energies. The definition of  $E_{\text{T}}^{\text{miss}}$  used in the analyses described here is calculated before any overlap removal and uses the following objects (see [125] for more details):

- all tight++ electrons with  $p_{\text{T}} > 10$  GeV
- all anti- $k_{\perp}$  jets as defined in section 4.1.3 with  $p_{\text{T}} > 20$  GeV
- soft anti- $k_{\perp}$  jets with  $7 \text{ GeV} < p_{\text{T}} < 20 \text{ GeV}$
- muons in the region  $|\eta| < 2.5$ , using their ID tracks to calculate their  $p_{\text{T}}$ , and muons with only muon spectrometer tracks (all muons are isolated from jets with  $\Delta R > 0.3$ )
- energy in the calorimeter, not associated with any objects defined above, is calibrated to the EM scale
- predictions for the amount of energy deposited in cells from pile-up events is subtracted from the  $E_{\text{T}}^{\text{miss}}$  calculation.

The systematic uncertainty on the  $E_{\text{T}}^{\text{miss}}$  measurement has been measured to be 6.6% which includes systematic uncertainties from the energy and position measurement

of soft-jets, jets and cell information. The systematic uncertainty associated with the subtraction of energy from cells predicted for the pile-up in a particular event is treated independently. A source of systematic uncertainty that has been neglected is that from correcting the energy of jets reconstructed as hadronically decaying taus, because measurements have indicated that it affects the acceptance by  $< 1\%$  [124].

### 4.1.7 Sum of the Transverse Momentum of ID Tracks

The parameter  $\sum p_T$  is defined as the scalar sum of the transverse momenta of all tracks with at least 1 pixel and 6 SCT hits, and with the longitudinal and transverse impact parameters  $|z_0|$  and  $|d_0| < 1.5 \text{ mm}$  to ensure they originate from the Primary Vertex (PV). The particles produced in hard scattering events such as  $t\bar{t}$  production have a high  $p_T$ , so a large  $\sum p_T$  indicates a hard scattering.

## 4.2 Object Pre-selection

### 4.2.1 Hadronic Jets

Anti- $k_\perp$  jets with a cone size of 0.4 are reconstructed off-line from deposits in the Liquid Argon Calorimeters. These jets are calibrated and the JES is applied to the reconstructed objects. Only jets with an energy greater than zero, after corrections, are used.

### 4.2.2 Leptonic Cuts

#### 4.2.2.1 Electrons

Electrons are defined as having an  $a_{\text{electron}}$  of 1 or 3 (see section 4.1.1),  $E_T > 20 \text{ GeV}$ , and passing the tight++ electron identification. Only electrons with a calorimeter

cluster deposit within the range  $|\eta| < 1.37$  or  $1.52 < |\eta| < 2.47$  are used, so electrons are central and outside the calorimeter crack regions. Good data quality was also required. Isolation criteria is additionally applied to tight++ electrons.

A standard software tool is used that calculate the additional  $E_T$  in cone of 0.2 (and 0.3) around the electron. This  $E_T$  is calculated by subtracting the  $p_T$  of the electron and the expected energy deposited given the number of primary vertices in the event from the total energy deposited in this cone. Both of these values subtracted from the  $E_T$  used in this calculation was recalculated using another standard ATLAS software tool to take into account small systematic differences observed between data and MC [22]. The actual isolation cut applied  $p_T$  and  $\eta$  dependent and is around  $\sim 3 - 5$  GeV.

#### 4.2.2.2 Muons

Muons are defined as being combined muons as described in section 4.1.2, with  $p_T > 15$  GeV and  $|\eta| < 2.5$ . Quality requirements are placed on the track associated with the muons as recommended by the Muon Combined performance group. The track is required to be isolated, with  $etcone20 < 3.5$  GeV and  $ptcone30 < 4$  GeV (see section 4.1.2).

#### 4.2.2.3 Hadronically Decaying Tau Leptons

Jet seeded taus are reconstructed using a BDT variable, see section 4.1.5. Taus are selected with  $p_T > 25$  GeV,  $|\eta| < 2.3$  and having 1 or 3 associated tracks. Before any electron or muon vetoes, the tight BDT has an efficiency of  $0.40 \pm 0.03 \pm 0.04$  [120].

### 4.3 Overlap Removal

Overlap removal is applied to the objects defined in section 4.2, before the event selection is applied. Only objects remaining after each step of the overlap removal are used subsequently. The overlap removal used here is based on that used in [2].

Particles are rarely produced in isolation in hadronic collisions. Leptons and hadrons can be produced either directly from a hard interaction, or from secondary interactions such as particle showers produced in jets. Both can produce particles that get reconstructed as objects that overlap in the detector, but the initially produced object is generally the one we want kept following overlap removal. Additionally one physical object can be reconstructed as multiple object candidates. Physical particles directly produced in a hard interaction can also overlap in the detector through chance. The method described here outlines a simple method for removing overlapping objects. In the simplest and most common scenarios, with highly pure objects such as muons overlap removal can make simple physical sense. For objects that are more difficult to reconstruct and distinguish, electrons and taus for example, overlap removal ensures events have a simple, well defined topology.

The overlap removal forms part of the definition of the selected objects. While no ideal method for overlap removal exists, it is most important to apply it consistently for all studies performed so the objects used have the same definitions.

Jets are formed from the hadronisation of quarks, where many stable and unstable particles are produced. Each particle can undergo further hadronisation, and decay to other particles including leptons. Neutral particles, such as a  $J/\psi(1S)$ , can decay to electron and muons pairs. If a muon pair is produced from a decay inside a jet and one of these muons is reconstructed within  $\Delta R < 0.4$  of a jet, this muon is removed. However as all electrons are seeded with jets, and the identification is optimised to distinguish jets from electrons, jets are removed if overlapping with an electron. Similarly, hadronic taus, which are seeded by jets, are kept if overlapping with a jet.

Combined muons are formed from ID and MS tracks, and will leave minimal energy deposits in the calorimeters. Electrons will shower electromagnetically in the EM calorimeter and will rarely punch through the hadronic calorimeter layers to leave tracks in the MS. So when an electron overlaps a muon, the electron is removed.

Hadronically decaying taus are seeded by jets and classified by a BDT variable. Similarly to electrons overlapping muons, when taus overlap with muons the tau is removed from the event. Reconstructed electrons and hadronically decaying taus are very similar objects; both are contained within the calorimeter. Electrons are generally contained within the EM layers of the calorimeter but can punch through to the hadronic layers. Electrons have a higher efficiency than hadronically decaying taus, and so taus are removed when overlapping an electron.

Overlap removal is performed in the following order :

- Muons within  $\Delta R < 0.4$  of a jet are removed
- Electrons within  $\Delta R < 0.2$  of a muon are removed
- Taus within  $\Delta R < 0.2$  of an electron are removed
- Taus within  $\Delta R < 0.2$  of a muon are removed
- Jets within  $\Delta R < 0.2$  of an electron are removed
- Jets within  $\Delta R < 0.2$  of a tau are removed

## 4.4 Event selection

The event selection is designed to increase the number of signal  $t\bar{t}$  events over background events, and is used to measure the partial cross sections and cross section ratios in chapter 6. The cuts detailed here are mostly based on previous selections in a charged Higgs search in ATLAS [2] and were fixed at an early stage of the analysis

before any yields were determined to avoid bias. Events with an electron trigger or a muon trigger define the trigger stream of the channels, and the selection of the second lepton leads to a definition of four channels. The electron triggered channels have one trigger matched electron as well as:

- one muon (the  $e\mu$  channel)
- one hadronically decaying tau (the  $e\tau$  channel).

The muon triggered channels have one trigger matched muon as well as

- one electron (the  $\mu e$  channel)
- one hadronically decaying tau (the  $\mu\tau$  channel).

The  $e\mu$  and  $\mu e$  channels are not exclusive and have a large overlap. Because of this, the muon triggered channels are only used as a cross check of the final measurements in the electron triggered channels. The overlap for  $t\bar{t}$  signal events is estimated using MC in section .

#### 4.4.1 Data Periods

A Good Runs List (GRL) includes all the periods, and runs in that period, with high quality data during stable proton-proton collisions. To decide which runs to include, each detector sub-system, trigger, and reconstructed object is given a Data Quality (DQ) flag determined by scrutiny of a standard set of distributions. By considering the relevant DQ flags, information on the magnetic field configuration, and the configuration of the beams in the LHC (number of bunches present, their energy etc.), a GRL is formed. Further discussion can be found in [126].

The GRL used in all the analyses presented here was approved by ATLAS and has an integrated luminosity of  $4710\text{pb}^{-1}$ . A systematic uncertainty from the measurement

of the luminosity delivered to atlas is given as 1.8% for all analyses performed on proton-proton collisions in the 2011 data taking period [4].

#### 4.4.2 Event Quality Cuts

As well as excluding particular luminosity blocks where the DQ was not good enough, individual collision events are also checked for quality. Backgrounds to proton-proton collision events include:

- beam gas collisions, where a proton in the beam collides with a gas molecule in the beam pipe,
- beam halo events (from long lived muons or pions travelling in the halo of the beam),
- cosmic ray muons coincident with a collision event.

Unlike collision events, few tracks in such background events will originate from the PV. Events are selected where the first vertex type is primary or pile-up and has at least 5 associated tracks (tracks are reconstructed when they have  $p_T > 1$  GeV).

In each collision event, jets not arising from proton-proton collision events can be reconstructed for several reasons. LHC beam conditions, cosmic ray showers, or hardware problems can all lead to these mis-reconstructed jets. Often these jets are not in time with a collision event, or the confidence on the energy measurements is low. Bad quality jets come from three main sources: single cells in the HEC where noise bursts occur; noise bursts in the EM calorimeter; out of time jets from cosmic ray events. Additionally there are jets seeded by in-time collisions in areas of the calorimeter where jet reconstruction is not accurate. A more complete discussion of data quality is found in [126]. Jets with these problems are labelled as *bad* jets. Events with one or more *bad* jets, before any pre-selection is applied, are vetoed.

### 4.4.3 Lepton Triggers

For each run in data taking, the lowest un-pre-scaled electron and muon triggers are used, see section 2.4. The electron triggers used for periods B-H, I-K and L-M; are e20\_medium, e22\_medium and e22vh\_medium1 respectively. The periods B-H, I-K and L-M correspond to  $1.098\text{fb}^{-1}$ ,  $1.124\text{fb}^{-1}$  and  $2.368\text{fb}^{-1}$  of integrated luminosity respectively.

The definitions for loose, medium and tight electron triggers can be found in [30]. Due to changing conditions in the LHC, several run periods are defined. In 2011 proton-proton data taking good quality data was taken in periods B-M. The changing conditions necessitated an increasing  $p_T$  threshold for the trigger from periods H to I. In later periods,  $\eta$  dependent thresholds and hadronic leakage requirements are used in triggers indicated with the suffix *vh* [30].

The muon triggers for periods B-H and I-M are mu18, and mu18\_medium respectively. The difference between these triggers is a change in the L1 trigger seeding the subsequent L2 triggers, from a 10 GeV to an 11 GeV threshold. The former had to be pre-scaled in runs after period H, as outlined in [32].

The electron trigger efficiencies can be seen in figure 4.4 and the muon trigger efficiency in 4.5. In the central region the electron trigger is more efficient than the muon trigger.

### 4.4.4 Leptonic Cuts

The lepton pre-selection is defined as explained in section 4.2, overlap removal is then applied to these pre-selected objects as described in section 4.3. A cut on the number of electrons, muons and taus is applied to both the pre-selected, and high  $p_T$ , objects. Each event must pass either the electron or muon trigger requirements and each EF trigger must be matched to a lepton. The electron trigger RoI must be within  $\Delta R < 0.15$  of the electron ID track. Similarly the muon trigger must be

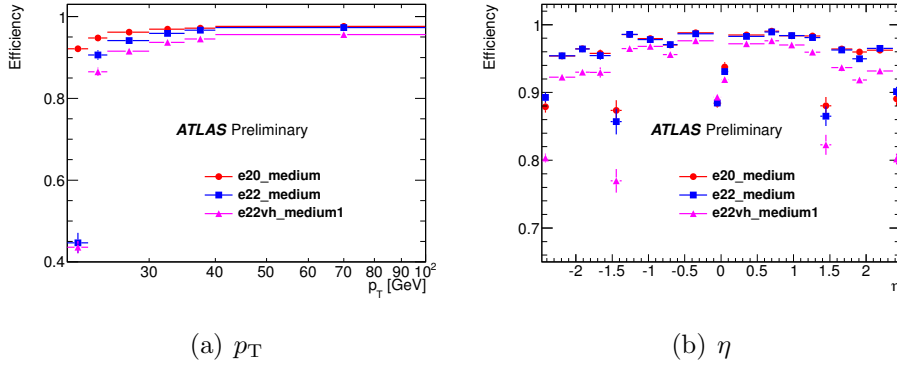


Figure 4.4: Efficiencies as functions of the off-line  $p_T$  (a) and  $\eta$  (b) for lowest un-pre-scaled triggers (e20\_medium, e22\_medium and e22vh\_medium1 triggers respectively) in periods B-H, I-K and L-M as measured in [30].

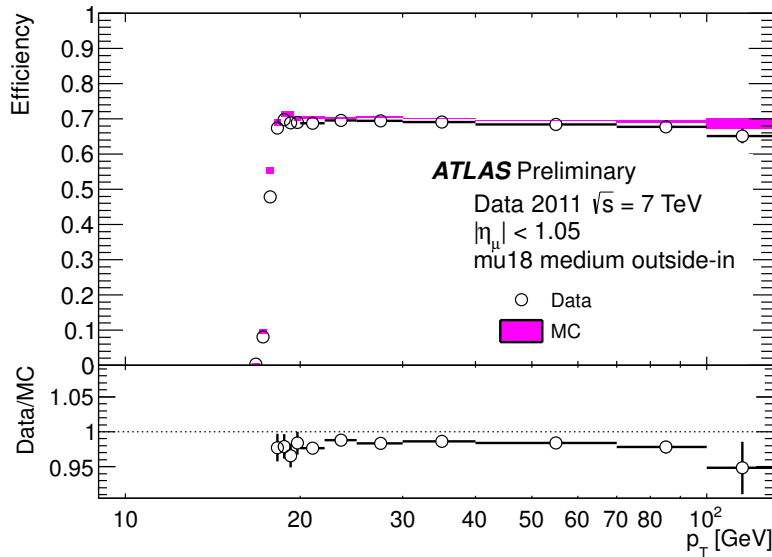


Figure 4.5: Trigger efficiency for the mu18\_medium trigger for  $|\eta| < 1.05$  as measured in [32].

within  $\Delta R < 0.15$  of the muon CB track. Electrons, muons and taus are additionally required to have  $p_T > 25$  GeV. Where a single electron or muon is selected, it is required that no additional electrons or muons are selected with  $15 \text{ GeV} \leq p_T < 25 \text{ GeV}$ .

## 4.4.5 Hadronic Jet Selection

After overlap removal of jets reconstructed as electrons and hadronically decaying tau candidates, events with 2 or more hadronic jets with  $p_T > 25$  GeV and within  $|\eta| < 2.4$  are selected.

### 4.4.5.1 Selecting b-jets

Events are selected with that exactly two b-jets candidates by requiring to satisfy  $MV1 > 0.601713$ , which has b-jet efficiency of 70%, see section 4.1.4 for more details.

## 4.4.6 Missing Transverse Energy

For  $t\bar{t}$  events where both top quarks decay to leptons, a high  $E_T^{\text{miss}}$  is expected from production of lepton neutrinos. Consequently the cut to select  $t\bar{t}$  events is  $E_T^{\text{miss}} > 40$  GeV.

## 4.4.7 Sum of the Transverse Momentum of ID Tracks

The parameter  $\sum p_T$  is defined in section 4.1.7. Hard scattering events will by their nature have large  $\sum p_T$ , and events with  $\sum p_T > 100$  GeV are selected.

## 4.5 Selecting $t\bar{t}$ Events

In this section the selection of  $t\bar{t}$  events is summarised. In section 4.1 the reconstruction and identification of electrons, muons, hadronic taus, jets, b-jets and the events  $E_T^{\text{miss}}$  are explained. In section 4.2 object pre-selection is discussed, where minimal object quality cuts are applied, objects are recalibrated, loose kinematic constraints

are applied and objects are required to be reconstructed within the detector acceptances for those objects. After this, overlap removal is applied, as explained in section 4.3 which, for example, removes jets overlapping with reconstructed electrons.

The analysis cuts explained in section 4.4 are applied, including the object selections. The electron and muon triggered channel event selections are listed in tables 4.1 and 4.2 respectively. Events are required to have two or more jets, and exactly 2 b-jets in each event. For each  $t\bar{t}$  channel two leptons with  $p_T > 25$  GeV are selected, which are required to have opposite charges. Selecting events with  $\Sigma p_T > 100$  GeV and  $E_T^{\text{miss}} > 40$  GeV ensures a higher proportion of  $t\bar{t}$  events.

Cut	$t\bar{t}$ electron triggered Channels	
	$e\mu$	$e\tau$
0 (data only)	passes the GRL	passes the GRL
1	Electron Trigger	Electron Trigger
2	5 or more primary vertex tracks	5 or more primary vertex tracks
3	No <i>bad</i> jets and no LAr errors	No <i>bad</i> jets and no LAr errors
4	1 trigger matched electron	1 trigger matched electron
5	2 or more jets	2 or more jets
6	exactly 2 b-jets	exactly 2 b-jets
7	1 muon	0 muons
8	0 taus	1 tau
9	Oppositely charged leptons	Oppositely charged leptons
10	$\Sigma p_T > 100$ GeV	$\Sigma p_T > 100$ GeV
11	$E_T^{\text{miss}} > 40$ GeV	$E_T^{\text{miss}} > 40$ GeV

Table 4.1: Summary of the  $t\bar{t}$  signal region selection cuts explained in detail in section 4.4 for electron triggered events. The cuts are identical except for the number of leptons selected.

## 4.6 Monte Carlo Samples

Measurements need to be compared to theoretical predictions that incorporate the extrapolation from particles produced in hard SM interactions to simulated detector signals. MC samples are made in three stages: event generation, where the proton-

Cut	$t\bar{t}$ muon triggered Channels	
	$\mu e$	$\mu\tau$
0 (data only)	passes the GRL	passes the GRL
1	Muon Trigger	Muon Trigger
2	5 or more primary vertex tracks	5 or more primary vertex tracks
3	No <i>bad</i> jets and no LAr errors	No <i>bad</i> jets and no LAr errors
4	1 trigger matched muon	1 trigger matched muon
5	2 or more jets	2 or more jets
6	exactly 2 b-jets	exactly 2 b-jets
7	1 electron	0 electrons
8	0 taus	1 tau
9	Oppositely charged leptons	Oppositely charged leptons
10	$\Sigma p_T > 100$ GeV	$\Sigma p_T > 100$ GeV
11	$E_T^{\text{miss}} > 40$ GeV	$E_T^{\text{miss}} > 40$ GeV

Table 4.2: Summary of the  $t\bar{t}$  signal region selection cuts explained in detail in section 4.4 for muon triggered events. The cuts are identical except for the number of leptons selected.

proton collision and production of particles is simulated and partons are hadronised to produce final state particles; detector simulation and digitisation, in which the interactions with the detector, including dead material, are simulated and the signals produced are turned into digital readouts; and finally, reconstruction which takes the digital readouts and converts them into the same reconstructed objects used in data. These three steps are collectively referred to as the ATLAS Full Simulation Chain.

Generation of  $t\bar{t}$  and single top quark events was performed using the NLO MC program MC@NLO [127–129] with the NLO parton density function set CTEQ6.6 PDF [130]. The  $t\bar{t}$  MC events are weighted with K-factors to normalise to the NNLO perturbative QCD cross section calculation from HATHOR [131] with a value of  $167^{\pm 17}$  pb (assuming a top quark mass of 172.5 GeV).  $Z + jets$  and  $W + jets$  events are generated using ALPGEN [132] with the CTEQ61 PDF set [133]. HERWIG is used to generate all di-boson events ( $WW/WZ/ZZ$ ) [134]. Parton hadronisation and the underlying event are modelled by HERWIG [134, 135] and JIMMY [136] respectively for all MC samples.

In time and out-of-time pileup events are simulated with PYTHIA 6 [137]. The amount of pileup is simulated to approximately match the pileup conditions during data taking; residual differences between MC and data due to effects such as decreasing luminosity during a run are accounted for by re-weighting each MC event.

The interactions of the final state particles with the dead material, and the responses of active parts of the detector, are simulated using GEANT4 [138], and then digitised to match the outputs of the ATLAS detector.

#### 4.6.1 $t\bar{t}$ Monte Carlo Samples for Estimating Generator Systematic Uncertainties

Several  $t\bar{t}$  samples were generated to evaluate systematic uncertainties associated with the modelling of  $t\bar{t}$  events. Differences between MC generators arise for several reasons including different treatment of non-perturbative effects, and the methods of removing interfering diagrams. A full discussion is outside of the scope of this thesis, and can be found in [52]. The following MC samples were produced using alternative modelling parameters that are used to assess the systematic uncertainty from modelling each effect.

The nominal  $t\bar{t}$  samples produced using MC@NLO can be compared to samples produced using two different generators: ALPGEN [132], and POWHEG [139]. All of these MC samples use the CTEQ6.6 PDF schemes and HERWIG for the parton shower model.

As discussed in section 3.4 the hadronisation of partons is non-perturbative in nature, and therefore difficult to model. An alternative generator, POWHEG, was used to produce two  $t\bar{t}$  samples with different parton shower and fragmentation schemes using PYTHIA 6 and HERWIG.

Samples of  $t\bar{t}$  events were generated with differing PYTHIA tune parameters that describe colour reconnection and the underlying event. The colour reconnection

systematic was estimated by comparing the Perugia 11 tune and Perugia 11 NOCR tune (with no colour reconnection), the underlying event systematic was estimate by comparing the Perugia 11 and Perugia 11 mpiHI tunes (where  $\Lambda_{QCD}$ , the QCD scale, is varied [9]). See for [140] details of the different tunes.

## 4.6.2 Classifying $t\bar{t}$ truth events

The  $t\bar{t}$  MC samples come in two datasets: one is composed only of fully hadronic  $W$  decays, and the other contains all other decays including semi-leptonic decays, and hadronic and leptonic tau decays. In later sections the contributions to the signal region from fake leptons and taus are estimated from data in chapter 5. To avoid double counting these events it is necessary to classify the events in the sample according to the MC generator truth information. Only final state particles are considered, such that leptons produced from tau decays are classified only according to the final state lepton. Table 4.3 lists the proportion of each type of  $t\bar{t}$  event according to the final state in the non-fully hadronic samples.

To validate the truth classification, the branching fractions for the  $W$  decay ( $B(W \rightarrow e\nu_e) = 0.1075 \pm 0.0013$  and  $B(W \rightarrow \mu\nu_\mu) = 0.1057 \pm 0.0015$ ), and the tau decay modes ( $B(\tau \rightarrow e) = 0.1782 \pm 0.0004$  and  $B(\tau \rightarrow \mu) = 0.1739 \pm 0.0004$ ) are taken from the PDG [9]. Using these and the  $W$  hadronic branching fraction ( $B(W \rightarrow q\bar{q}) = 0.6760 \pm 0.0027$  [9]) allows the proportions of  $t\bar{t}$  events to be estimated, while ensuring they sum to unity [9]. These values are listed in table 4.3 for comparison and have good agreement with the proportions in  $t\bar{t}$  MC.

## 4.7 Alternative $t\bar{t}$ Selection Strategies

The method of selecting  $t\bar{t}$  events presented in section 4.4 is a cut based method where events are either selected or rejected. The cut selection used in this analysis is based an early version to that used in [2] the selection is not optimised to

Channel	MC Branching fraction	PDG derived values
$ee$	$0.030 \pm 1.3\text{e-}10$	$0.030 \pm 0.00070$
$\mu\mu$	$0.030 \pm 1.3\text{e-}10$	$0.029 \pm 0.00074$
$e\mu$	$0.060 \pm 1.9\text{e-}10$	$0.058 \pm 0.00094$
$e\tau$	$0.033 \pm 1.4\text{e-}10$	$0.034 \pm 0.0013$
$\mu\tau$	$0.032 \pm 1.4\text{e-}10$	$0.033 \pm 0.00096$
$\tau\tau$	$0.0089 \pm 7.2\text{e-}11$	$0.0095 \pm 0.00057$
$e + jets$	$0.32 \pm 4.3\text{e-}10$	$0.32 \pm 0.0036$
$\mu + jets$	$0.32 \pm 4.3\text{e-}10$	$0.31 \pm 0.004$
$\tau + jets$	$0.17 \pm 3.2\text{e-}10$	$0.18 \pm 0.0054$

Table 4.3: Proportion of each channel in the non-fully-hadronic  $t\bar{t}$  MC samples based on the final state of the leptons in the event, including those from the decay of a tau. Only hadronically decaying taus are included in the tau channels. Values derived from PDG  $W$  decay branching fractions are included [9]. The errors for PDG derived values are from combining the experimental errors quoted in the PDG. For the branching fractions, only the statistical error from the total number of events is included, a complete estimate would include errors similar to those quoted for the PDG value.

decrease the statistical uncertainty of the final measurement. Most of the object selection strategies on which optimised individually by performance sub-groups, often to increase the statistical significance, to select a high purity of events [1, 2]. Additional variables could therefore be used and, using the MC, the cuts could be chosen based on where they increase the statistical sensitivity of the ratio measurement to expected deviations from the SM.

A review of methods to improve the sensitivity of analyses using machine learning techniques such as Neural Nets and BDTs, and other methods such as the Matrix Element method can be found in [141]. They are trained to discriminate signal MC from background MC events and data driven background estimates, the best of which are stable to the initial training datasets used. Many of the techniques are not based on sequential cuts, but can weight events or distributions on how signal-like they are. These techniques have been highly successful and often succeed in measuring parameters where a cut-based technique has failed, such as in the first observation of single-top quark production (see section 3.6.2). However they are inherently ‘black-box’, in that the properties of some of the more successful algorithms are not fully understood. Importantly, a good understanding of all the systematic uncertainties

is necessary to have full confidence in the results produced from these techniques. The success of these techniques means it would be prudent to explore their use in any future extension to this analysis.

## 4.8 Summary

In order to select  $t\bar{t}$  di-lepton and lepton plus tau events, first candidates for the physical final state particles must be reconstructed as described in section 4.1. This includes assigning a variable to hadronic jets optimised to select tau candidates as explained in section 4.1.5. Additionally reconstruction of event level objects, such as  $E_{\text{T}}^{\text{miss}}$ , which measures energy missing from the production of neutrinos, is covered in section 4.1.6. A basic pre-selection criteria are applied to these objects, explained in section 4.2 based on previous performance knowledge of the respective ATLAS groups. An overlap scheme is explained in section 4.2 which is used in all the analyses presented in chapters 5.

The final event selection is outlined in section 4.4 which is used from section 6.2. Similarly, orthogonal selections are used in chapter 5 to measure the lepton and tau fake rates. The details of the MC samples are outlined in section 4.6 which are used to verify the purity of the selections used in chapter 5 to measure the fake rates. The  $t\bar{t}$  truth filtering is also described, which is necessary for measuring the  $t\bar{t}$  selection efficiencies used to calculate the cross sections and cross section ratios in chapter 6.

# Chapter 5

## Lepton Fake Rate Estimation

Two important backgrounds to di-lepton and lepton plus tau  $t\bar{t}$  events are those in which the reconstructed electron, muon or tau is not produced directly from the interactions of a proton-proton collision. For reconstructed electron and muon candidates, these non-direct leptons are defined as fakes. The lepton fake rate is defined and measured in a multi-jet (QCD) enriched region in section 5.1. A matrix method (discussed in section 5.1.1) is used to predict the distributions and yields of electron and muon fakes in a di-lepton control region and used to validate the lepton fake rate method in section 6.4.1.

In section 5.3 a method of measuring the rate at which hadronic jets fake a reconstructed tau is discussed. To ensure the yields and distributions of variables on which cuts are placed are reasonable, a control region is used in section 5.4 to validate the methods for the lepton plus tau channel.

### 5.1 Electron and Muon Fake Rate Estimation

While MC has been shown in numerous ATLAS analyses to model hard processes well [142–144], modelling of soft processes is more difficult. Leptons that are produced

directly in a hard interaction are defined as real leptons, such as those produced from W decays, Z decays, and di-boson. These decays are well modelled in MC.

Leptons not produced in hard interactions (non-direct production), such as leptons produced in the decays inside hadronic jets, are defined as fake leptons. Some hadronic particles and their decay products, in particular neutral pions which decay to two photons, leave a significant portion of energy in the EM calorimeter. Combined with the high track multiplicity from multiple interactions in the high pile-up environment of the LHC, hadronic particles can overlap with tracks in the ID, which can then be mis-reconstructed as electrons.

Fake leptons can be reconstructed in softer multi-jet events (i.e. without a hard scattering, referred to QCD), but also in hard scattering processes such as  $W + jets$  events where leptons are produced in the hadronisation of jets. In MC the number of fakes produced is therefore highly dependent on MC modelling of QCD, detector simulations, and modelling of data taking conditions in the LHC.

While QCD MC samples are available, the underlying physics and the interactions of these events with the detector are difficult to model, additionally the MC samples available generally have too few events with high  $p_T$  leptons.

A simple method used in other analyses for estimating backgrounds is to use a side-band (using an orthogonal cut region) where the fake rate is assumed to be the same as for the signal region. Ideally this region should have a low contamination from signal events, which for  $t\bar{t}$  events is difficult, and sufficient statistics to provide a smooth variation of the fake rate as a function of event observables, and detector conditions.

However, as no region with a low contamination from signal could be found the number of fakes is estimated using the matrix method. By measuring the efficiency and fake rates of leptons selected from a looser definition (also to be selected by a tighter definition), an estimate can be made for the number of fake leptons in the signal region. To validate the method the fake rate is first measured in a region

orthogonal to the signal region.

A data driven fake rate estimate replaces MC events where a lepton has been faked. In the di-lepton channel MC events with a single electron or muon are not included in the final background estimate. Specifically this means  $W + \text{jets}$  events, and  $t\bar{t}$  events with one electron or muon, and single top events are excluded. In addition  $Z \rightarrow e^+e^-$  and  $Z \rightarrow \mu^+\mu^- + \text{jets}$  events are excluded to remove events where the inefficiency in lepton reconstruction has missed one lepton and another has been reconstructed from the decay products of a jet. Backgrounds from  $Z \rightarrow \tau\tau + \text{jets}$  events, and di-boson events are modelled by MC.

In the lepton plus tau channel  $Z \rightarrow e^+e^-$  and  $Z \rightarrow \mu^+\mu^- + \text{jets}$  events are not included as events where one lepton has not been reconstructed may contain a fake lepton or tau and so will be covered by the lepton and tau fake rate estimates. The MC samples for  $W + \text{jets}$ , single top events, and  $t\bar{t}$  events without a final state lepton and tau may include jets that fake a lepton or tau and one or fewer real leptons are also covered by these data driven estimates and are excluded. In the di-lepton channel, backgrounds from  $Z \rightarrow \tau\tau + \text{jets}$  events, and di-boson events are modelled by MC.

The MC backgrounds that are excluded are instead estimated using a Matrix method. The top event samples are not split into different lepton final states by default, and so to stop double counting of events the truth filtering described in section 4.6.2 is used to distinguish them.

### 5.1.1 The Matrix Method for data driven background estimation

Two definitions for each type of lepton, which will be called *loose* and *tight*, are constructed for which the *loose* selection has a higher number of fake leptons. Two exclusive selections are defined with high purities of real leptons and fake leptons,

respectively, which are used to measure the real and fake efficiencies: these measurements are discussed in sections 5.1.2 and 5.1.3.

The matrix method uses the real lepton efficiencies and fake lepton rates to determine the probabilities of being reconstructed as a *loose* but not *tight* lepton, or as a *tight* lepton in the final di-lepton event selection.

Using the two *loose* and *tight* definitions, we can construct four orthogonal populations of leptons in the final event selection ( $N^{tt}$ ,  $N^{tl}$ ,  $N^{lt}$  and  $N^{ll}$ ). Here the two super-scripts indicate whether the first (trigger) lepton and the second lepton are either *tight* ( $t$ ), or *loose* but not *tight* ( $l$ ). Note that in the efficiency and fake rate measurements *loose* leptons were inclusive of *tight* leptons, but now the loose population is all loose leptons not reconstructed as tight leptons. For each lepton in the event the expected efficiency and fake rate are calculated separately, so for di-lepton events two efficiencies and two fake rates are calculated.

Similarly four populations of real and fake leptons can be inferred ( $N_{rr}$ ,  $N_{rf}$ ,  $N_{fr}$ , and  $N_{ff}$ ) where the sub-scripts correspondingly refer to the primary (trigger) lepton and the non-triggering lepton and whether they are *real* ( $r$ ) or *fake* ( $f$ ) leptons. Hence  $N^{lt}$  refers to the total number of events with a *loose* (but not *tight*) triggering lepton, and *tight* non-triggering lepton regardless of origin. Also,  $N_{rf}$  refers to the total number of events where the triggering lepton is from a real source and the secondary from a fake source, regardless of their final reconstruction. These are related in equations 5.1 and 5.2 where  $r$  represents the efficiency of a *loose* real lepton being reconstructed as a *tight* lepton, and  $f$  represents the rate at which a *loose fake* lepton is reconstructed as *tight* lepton.

$$\begin{pmatrix} N^{tt} \\ N^{tl} \\ N^{lt} \\ N^{ll} \end{pmatrix} = M \begin{pmatrix} N_{rr} \\ N_{rf} \\ N_{fr} \\ N_{ff} \end{pmatrix}, \quad (5.1)$$

where

$$M \equiv \begin{pmatrix} r_1 r_2 & r_1 f_2 & f_1 r_2 & f_1 f_2 \\ r_1(1-r_2) & r_1(1-f_2) & f_1(1-r_2) & f_1(1-f_2) \\ (1-r_1)r_2 & (1-r_1)f_2 & (1-f_1)r_2 & (1-f_1)f_2 \\ (1-r_1)(1-r_2) & (1-r_1)(1-f_2) & (1-f_1)(1-r_2) & (1-f_1)(1-f_2) \end{pmatrix} \quad (5.2)$$

By inverting this matrix we obtain an expression that relates the number of fake lepton events passing our final di-lepton selection to the number of events reconstructed as each of the four combinations of *loose* and *tight* lepton definitions, see equation 5.3. Here, as in equation 5.1,  $N_{fr}^{tt}$  refers to the number of events where the triggering lepton is fake and is reconstructed as a *tight* lepton, and the secondary lepton is real and also is reconstructed as a *tight lepton*, and similarly for the other symbols.

The number of fakes in a signal  $t\bar{t}$  region with two reconstructed leptons is defined as the number of events where at least one of these leptons is fake. Using equation 5.1 and 5.2 this is written as:

$$\begin{aligned} N_{fakes}^{tt} &= N_{rf}^{tt} + N_{fr}^{tt} + N_{ff}^{tt} & (5.3) \\ &= r_1 f_2 N_{rf} + f_1 r_2 N_{fr} + f_1 f_2 N_{ff} \\ &= \alpha r_1 f_2 [(f_1 - 1)(1 - r_2) N^{tt} + (1 - f_1) r_2 N^{tl} + f_1(1 - r_2) N^{lt} - f_1 r_2 N^{ll}] \\ &\quad + \alpha f_1 r_2 [(r_1 - 1)(1 - f_2) N^{tt} + (1 - r_1) f_2 N^{tl} + r_1(1 - f_2) N^{lt} - r_1 f_2 N^{ll}] \\ &\quad + \alpha f_1 f_2 [(1 - r_1)(1 - r_2) N^{tt} + (r_1 - 1) r_2 N^{tl} + r_1(r_2 - 1) N^{lt} + r_1 r_2 N^{ll}] \end{aligned}$$

where

$$\alpha = \frac{1}{(r_1 - f_1)(r_2 - f_2)}.$$

In equation 5.3 there are four populations defined by their lepton content ( $N^{tt}$ ,  $N^{tl}$ ,  $N^{lt}$  and  $N^{ll}$ ), each of which has a coefficient which is a function of the two lepton efficiencies and fake rates. This co-efficient is used to weight each event reconstructed in data.

For single lepton events (with an electron or muon, and a hadronically decaying tau) a  $2 \times 2$  matrix is constructed that is similar to equation 5.2 which is then inverted to give a fake estimate analogous to equation 5.3.

### 5.1.2 Real Lepton Efficiency Measurement

The lepton efficiencies are measured independently from their respective trigger efficiencies using two definitions of leptons, the first *loose* definition inclusive of the second tighter definition. *Tight* leptons are the same as defined in section 4.2, while *loose* leptons have the following differences. *Loose* electrons are defined as the medium++ instead of the tight++ electron ID requirement (see section 4.1.1). *Loose* muons are defined in an identical way to *tight* muons, except that the track and calorimeter isolation requirements (*ptcone30* and *etcone20*) are dropped.

The reconstruction efficiency for real leptons is defined as

$$r = \epsilon_{real}^{e/\mu} = \frac{N_{real}^{tight}}{N_{real}^{loose}} \quad (5.4)$$

where the number of real leptons reconstructed as a *loose* lepton is  $N_{real}^{loose}$ , and a subset of these is also reconstructed as a *tight* lepton,  $N_{real}^{tight}$ .

### 5.1.2.1 Making pure $Z \rightarrow e^+e^-$ and $Z \rightarrow \mu^+\mu^-$ samples

Selected events must pass minimum data quality requirements as explained in section 4.4. For the lepton efficiency being measured, the *loose* selected objects are used in the overlap removal. Events are selected with exactly two oppositely charged *loose* leptons. The lepton pair must have a separation  $\Delta R > 0.4$  and an invariant mass within 10 GeV of the  $Z$  mass ( $m_Z = 91.2$  GeV [9]). This results in a high purity sample of real leptons from the decay of the  $Z$ . By randomly selecting one lepton as a tag and requiring it be *tight* and trigger matched, the other lepton is then the probe. The result of the probe passing or failing the *tight* lepton selection is recorded, and the efficiencies are independently measured as functions of the  $p_T$ ,  $\eta$ , and  $\phi$  of the probe lepton, the number of jets, the number of b-jets in the event, and the number of tracks associated with the primary vertex (which takes account of the amount of pileup in the event). The event selection cuts are shown in table 5.1.

Cut	Channel	
	$ee$	$\mu\mu$
0 (data only)	GRL	GRL
1	electron trigger	muon trigger
2	5 primary vertex tracks	5 primary vertex tracks
3	No loose bad jets	No loose bad jets
4	trigger matched electron	trigger matched muon
5	2 electrons ( $p_T > 25$ GeV)	0 electrons ( $p_T > 15$ GeV)
6	0 muons ( $p_T > 15$ GeV)	2 muons ( $p_T > 25$ GeV)
7	0 taus ( $p_T > 25$ GeV)	0 taus ( $p_T > 25$ GeV)
8	<i>tight</i> trigger matched tag	<i>tight</i> trigger matched tag
9	tag and probe $\Delta R > 0.4$	tag and probe $\Delta R > 0.4$
10	$ M_{ee} - M_Z  < 10$ GeV	$ M_{\mu\mu} - M_Z  < 10$ GeV
11	Oppositely charged leptons	Oppositely charged leptons
	Fill <i>loose</i> lepton histograms	
12	<i>tight</i> probe electron	<i>tight</i> probe muon
	Fill <i>tight</i> lepton histograms	

Table 5.1: Event selection for a high purity sample of  $Z \rightarrow e^+e^-$  and  $Z \rightarrow \mu^+\mu^-$  events with one randomly selected loose lepton used to probe the real lepton efficiencies.

Figure 5.1 shows the invariant masses of the di-lepton systems.  $W$  events,  $t\bar{t}$  events,

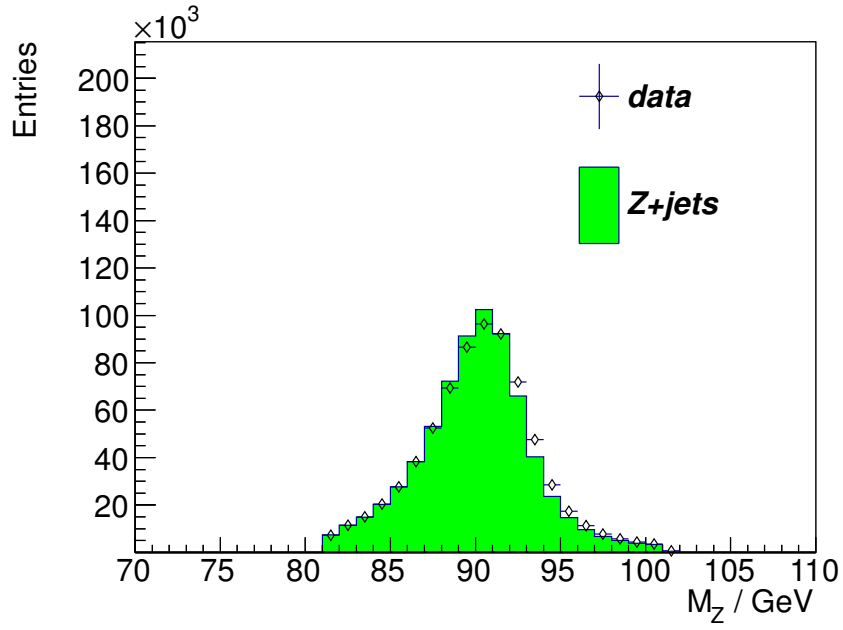
single top events, di-boson MC events are all included as backgrounds but only a insignificant number pass the selection cuts which confirms the purity of the selected events. In order to get a good agreement between to the MC and data the a bin-by-bin efficiency correction would have to be used to unfold the data for detector effects and Quantum Electro-Dynamics (QED) FSR, as was performed in [145]. The MC also does not include scale factors to account for differences in the resolution of the reconstructed leptons as was also performed in [145]. These could both account for the difference in the resolution seen in figure 5.1. As only the purity of the sample, and not the kinematic variables of a reconstructed  $Z$ , is important for measuring efficiencies in data these corrections were not applied.

### 5.1.2.2 Real Lepton Efficiencies

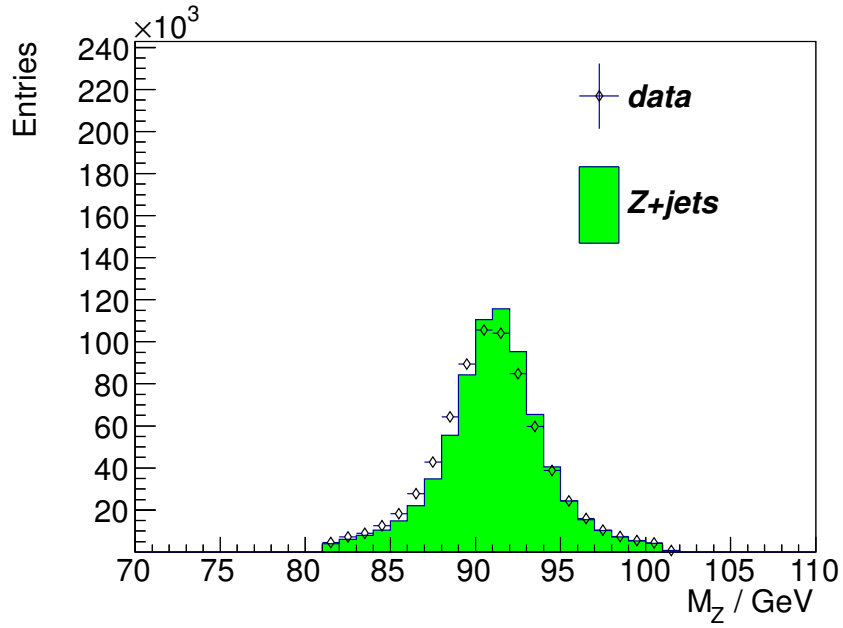
The lepton efficiencies are measured as a function of the lepton  $p_T$  and  $\eta$  as can be seen in figures 5.2 and 5.3. The efficiency as a function of lepton  $p_T$  is used to calculate the number lepton fake background as described in section 5.1.1. Note that  $p_T$  and  $\eta$  dependent scaling factors have not been applied to the MC samples which accounts for the statistically significant difference in the scale between them.

The lepton efficiencies were initially measured as a function of the lepton  $p_T$ ,  $\eta$  and  $\phi$ , the number of jets, and the number of b-jets. The lepton efficiencies showed a strong dependence on some of these variables and the limited statistics makes it un-feasible to measure the efficiencies in this multi-dimensional space. The electron and muon efficiencies as a function of  $\eta$  have a large variation as can be seen in figures 5.2 and 5.3.

For both the electron and muon efficiency as a function of  $\eta$  the highest and lower efficiency bins are used to estimate the systematic uncertainty. The difference between the upper uncertainty for the highest efficiency, and the lower uncertainty for the lowest efficiency is taken as the absolute systematic uncertainty. The absolute efficiencies are listed in table 5.2.

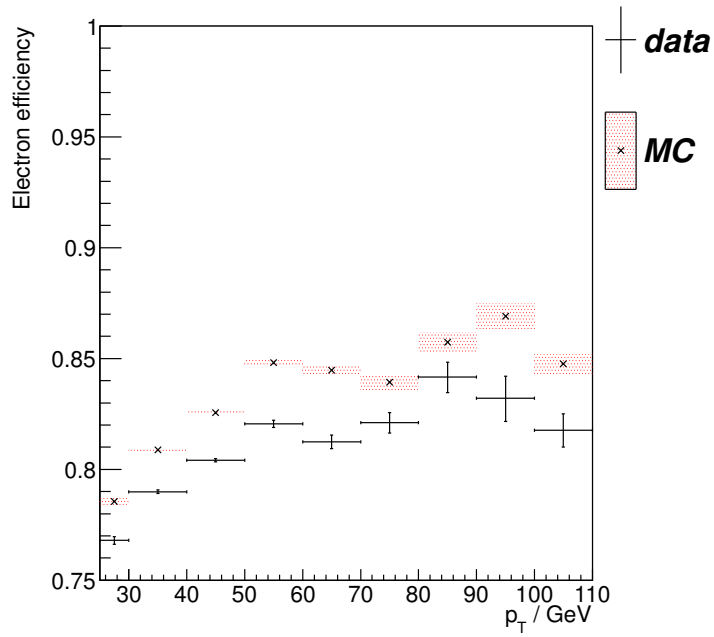


(a)  $Z \rightarrow e^+e^-$

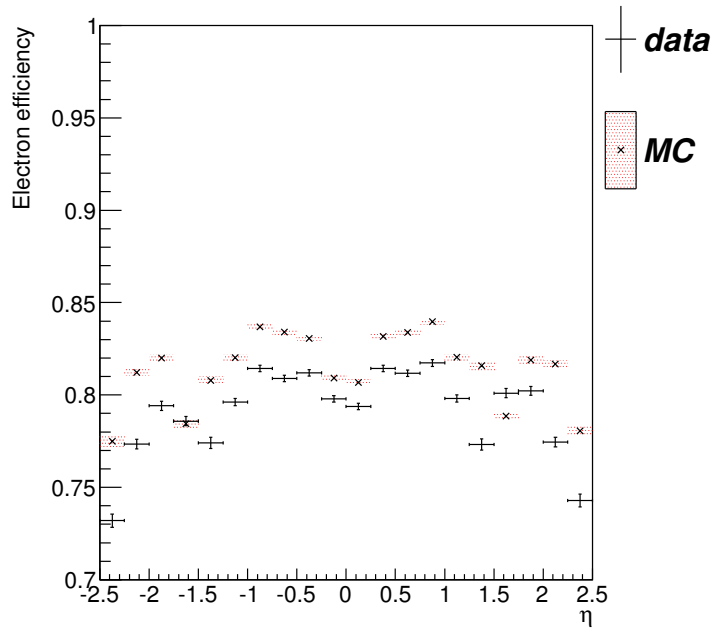


(b)  $Z \rightarrow \mu^+\mu^-$

Figure 5.1: Di-lepton invariant mass plots in  $Z \rightarrow e^+e^-$  (a) and  $Z \rightarrow \mu^+\mu^-$  (b) events for data and MC for samples used for tag and probe studies of lepton efficiencies.

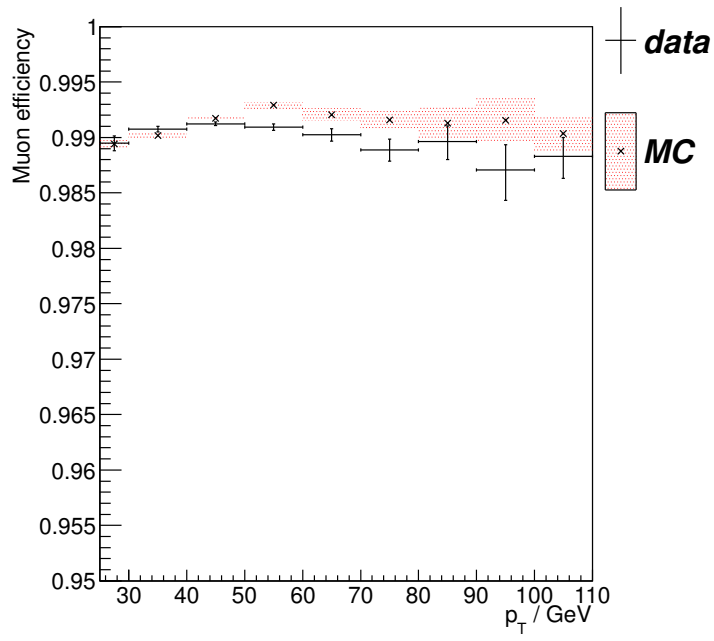


(a)  $\epsilon_{p_t}$

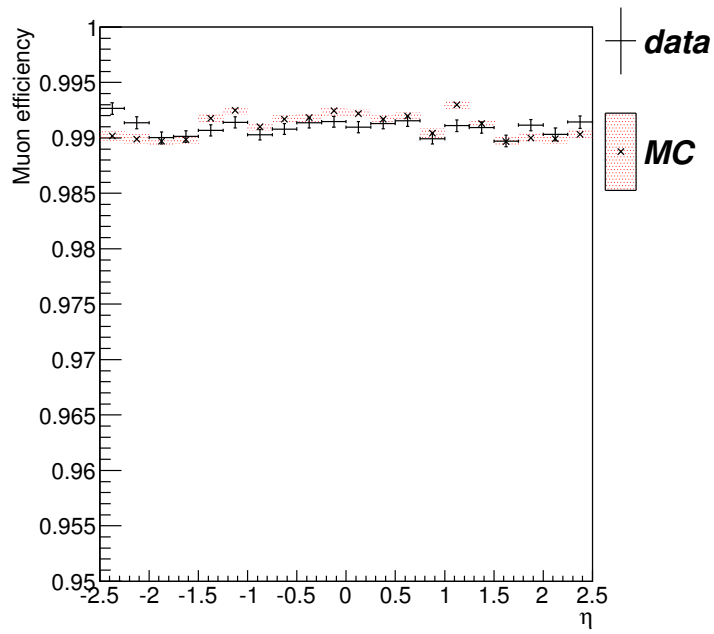


(b)  $\epsilon_{\eta}$

Figure 5.2: Real electron efficiencies for data and MC, no scale-factors have been applied to the MC samples to correct for detector effects.



(a)  $\epsilon_{p_t}$



(b)  $\epsilon_{\eta}$

Figure 5.3: Real muon efficiencies for data and MC, no scale-factors have been applied to the MC samples to correct for detector effects.

Lepton	Efficiency Systematic Error
e	$\pm 0.036$
$\mu$	$\pm 0.0019$

Table 5.2: The absolute systematic errors on the electron and muon efficiencies.

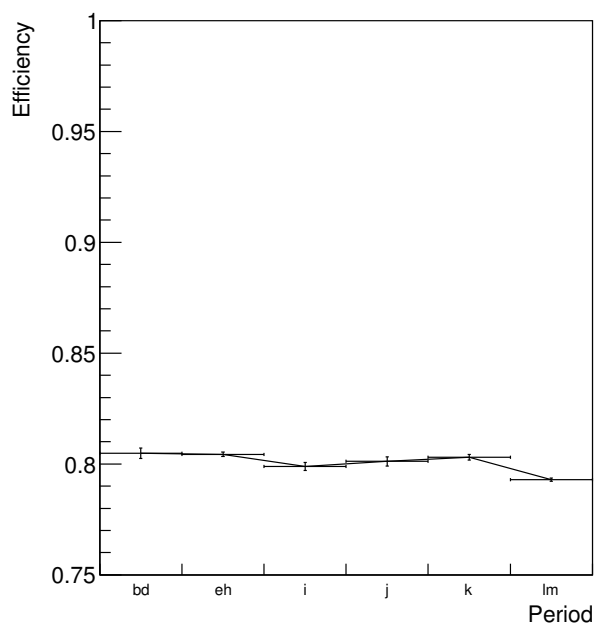
Increases in luminosity between different data taking periods result in increasing pile-up. Figure 5.4 shows the lepton efficiencies do show a small variation between periods. However, because the size of the variation is smaller than the systematic uncertainties listed in table 5.2 it will not result in a large systematic shift in the efficiencies.

The *tight* electron efficiency has been measured independently using a similar event selection in ATLAS data collected in 2010 proton-proton collisions, see figure 5.5. Though the object overlap removal, and event selection are not exactly the same, the results are compatible with those shown in figure 5.2. Similarly the muon efficiencies independently measured in data taken in 2010 [146](see figure 5.6) are compatible with those measured in figure 5.2.

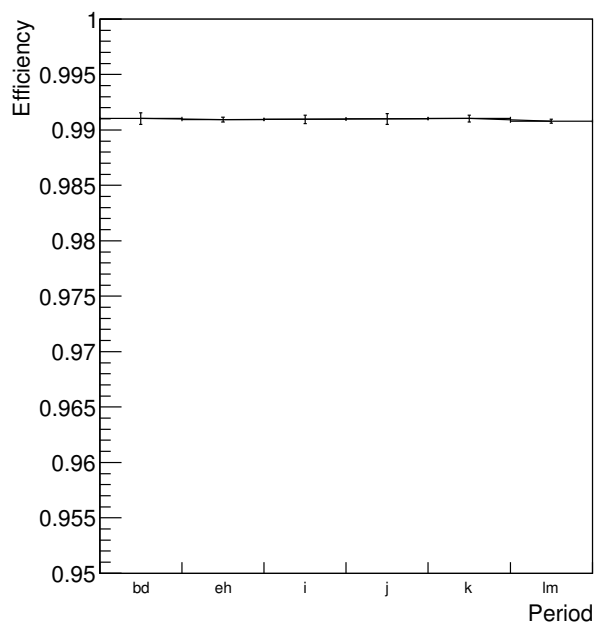
### 5.1.3 Lepton fake rate in a QCD enriched region

There are several ways to measure the lepton fake rates in data. To accurately predict the number of lepton fakes in the signal region the fake rate ideally needs to take account of the high numbers of jets and b-jets in the event. Selecting events with a single electron or muon results in a large number of real leptons from processes such as  $W + jets$  where only one direct lepton is expected, and a smaller number of  $Z \rightarrow ll$  events (where one lepton is outside the detector acceptance, or not well reconstructed). To measure the lepton fake rate a region with a higher proportion of fake leptons is selected from a sub-sample of single lepton events, in order to select a sample of QCD events.

Leptons produced as the decay products of particles inside jets with sufficient energy



(a)  $\epsilon^e$



(b)  $\epsilon^{\mu}$

Figure 5.4: Lepton efficiency as a function of run period for electrons (a) and muons (b)).

and separation from the jet can be reconstructed as separate objects and some will not be removed during overlap removal between leptons and jets. These non-prompt

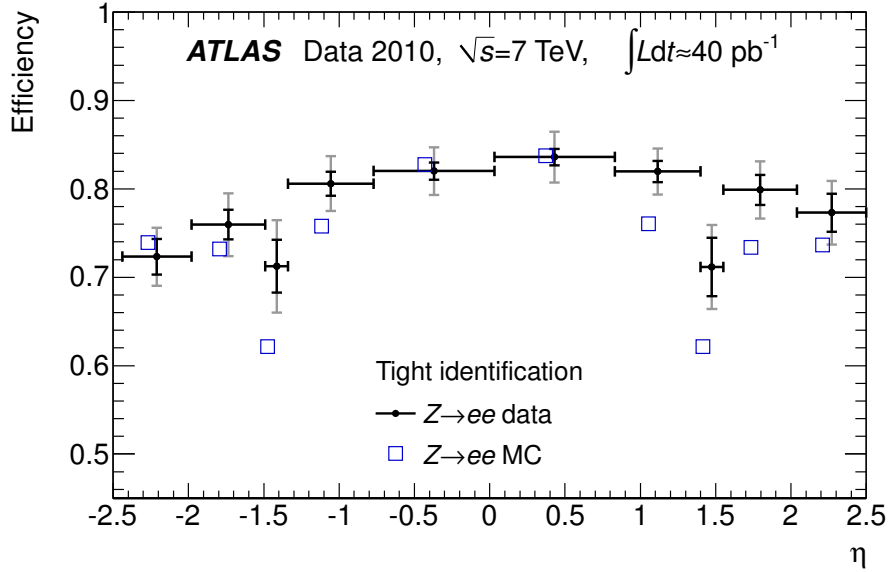


Figure 5.5: Electron efficiency as a function of  $\eta$  measured using  $Z \rightarrow ee$  events in data and MC using  $40 \text{ pb}^{-1}$  of data in 2010, as measured in [22].

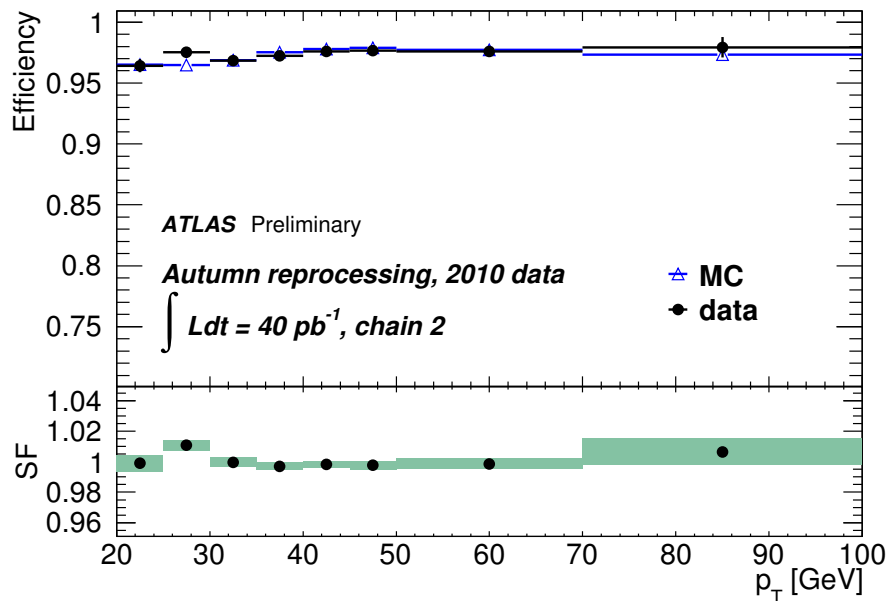


Figure 5.6: Muon efficiency as a function of  $p_T$  for data and MC measured using  $40 \text{ pb}^{-1}$  of data taken in 2010. The efficiency was measured using the tag-and-probe method using a selection of  $Z \rightarrow \mu\mu$  events for MuID combined muons in [146] using similar muon definitions and overlap removal to that defined in 4.1.2 and 4.3 respectively.

fake leptons will have a small  $\Delta R$  between themselves and the nearest reconstructed jet.

Fake electrons are also reconstructed from neutral hadronic particles and their decay products (such as pions which decay to two photons) which overlap with a track, but will not have this strong dependence on the  $\Delta R$  between themselves and the nearest reconstructed jet. By measuring fake rates as a function of the  $\Delta R$  between the lepton and the nearest jet, the different origins of fake leptons in data are partly accounted for.

The lepton fake rates are defined in an analogous way to lepton efficiencies with the use of *loose* and *tight* lepton definitions, where *tight* leptons are a subset of *loose*. Lepton fake rates are defined as:

$$f = \epsilon_{fake}^{e/\mu} = \frac{N_{fake}^{tight}}{N_{fake}^{loose}} \quad (5.5)$$

Lepton neutrinos with a large  $p_T$  are produced in the leptonic decay of  $W$  bosons in  $W + jets$  events: these will contribute to a large  $E_T^{\text{miss}}$ . QCD events will typically have a low  $E_T^{\text{miss}}$  as few high  $p_T$  neutrinos are produced.

$W + jets$  events contain a real, heavy, particle, unlike QCD events which by definition contain soft virtual particles. In the leptonic decay of a  $W$ , the momentum of the neutrino cannot be measured, only its  $p_T$  can be inferred from the  $E_T^{\text{miss}}$ .

The transverse mass ( $m_T$ ) for two particles of mass  $m_1$  and  $m_2$  with transverse energies  $E_{T,1}$  and  $E_{T,2}$ , and transverse momenta  $\vec{p}_{T,1}$  and  $\vec{p}_{T,2}$  respectively, is defined as:

$$m_T = \sqrt{m_1^2 + m_2^2 + 2(E_{T,1} \cdot E_{T,2} - \vec{p}_{T,1} \cdot \vec{p}_{T,2})}. \quad (5.6)$$

For a real  $W$  produced at the LHC, which decays to a lepton (mass  $m_l$  and transverse energy  $E_{T,l}$ ) and a neutrino (with negligible mass and transverse energy  $E_{T,\nu_l}$ , equivalent to the  $E_T^{\text{miss}}$ ), using the approximation  $m_l \ll E_l$  reduces this to:

$$m_T = \sqrt{2E_{T,l} \cdot E_{T,\nu_l}(1 - \cos \phi)}, \quad (5.7)$$

where  $\phi$  is the angle between the particles in the  $x$ - $y$  plane. There will be a peak in the  $m_T$  distribution from the reconstruction of the real  $W$  boson's transverse mass, unlike QCD which have no massive particles.

The cuts are listed in table 5.3 and are designed to increase the proportion of QCD events by selecting a low  $E_T^{\text{miss}}$  and a low  $m_T$  region by cutting out real  $W$  boson events.

Cut	Trigger Channel	
	electron	muon
0 (data only)	GRL	GRL
1	electron trigger	muon trigger
2	5 primary vertex tracks	5 primary vertex tracks
3	No loose bad jets	No loose bad jets
4	trigger matched electron	trigger matched muon
5	1 electron ( $p_T > 25$ GeV)	0 electrons ( $p_T > 15$ GeV)
6	0 muons ( $p_T > 15$ GeV)	1 muon ( $p_T > 25$ GeV)
7	0 taus ( $p_T > 25$ GeV)	0 taus ( $p_T > 25$ GeV)
8	electron is <i>loose</i> and trigger matched	muon is <i>loose</i> and trigger matched
9	$5 \text{ GeV} < E_T^{\text{miss}} < 20 \text{ GeV}$	$5 \text{ GeV} < E_T^{\text{miss}} < 20 \text{ GeV}$
10	$m_T < 50 \text{ GeV}$	$m_T < 50 \text{ GeV}$
11	1 jet ( $p_T > 25 \text{ GeV}$ )	1 jet ( $p_T > 25 \text{ GeV}$ )
	Fill <i>loose</i> lepton histograms	
12	1 <i>tight</i> electron	1 <i>tight</i> muon
	Fill <i>tight</i> lepton histograms	

Table 5.3: Cuts to select events with a single lepton while cutting out  $W$  decays to leave a majority of QCD events.

Using MC samples, with scale factors applied so detector effects are accounted for, real leptons are subtracted from the samples to ostensibly leave only fake leptons, which are referred to as probes. The lepton fake rates can then be measured by calculating the rate at which the loose lepton probes are reconstructed as tight leptons.

Figures 5.7 and 5.8 show the  $E_T^{\text{miss}}$  and  $m_T$  distributions before their respective cuts are applied. To increase the proportion of QCD events, only events with  $E_T^{\text{miss}} < 20 \text{ GeV}$ , and  $m_T < 50 \text{ GeV}$  are chosen. To check that the measured efficiencies were not strongly dependent on these cuts, the  $E_T^{\text{miss}}$  and  $m_T$  cuts were varied up

and down by 10 GeV independently. While this resulted in a large change in the number of events, the effect on the measured efficiencies was minimal and was found to be much smaller than the systematic uncertainties on the fake rates in section 5.1.3.1.

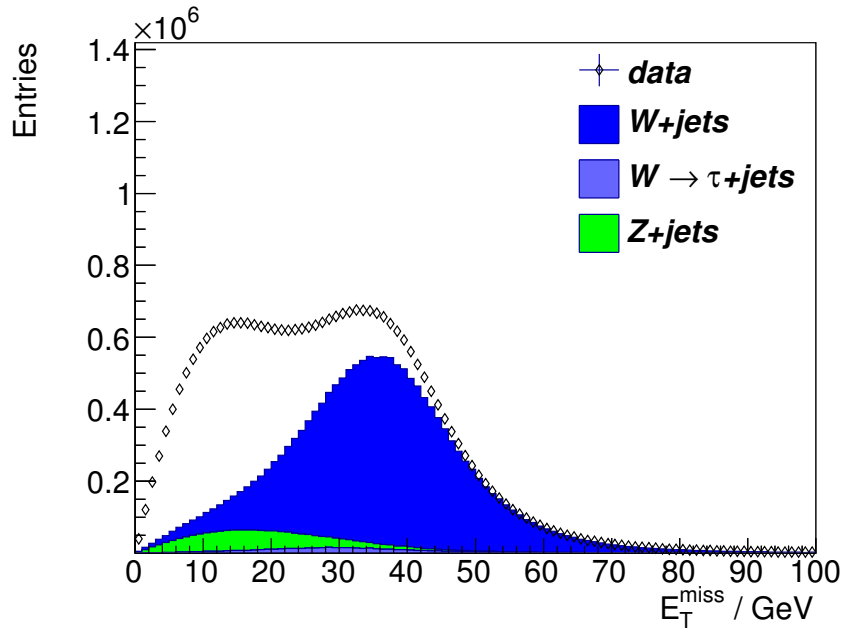
Figure 5.9 shows the  $\Delta R$  distribution between the probe lepton and the nearest jet before any *tight* requirements are placed on the probe lepton. An increase of events at  $\Delta R < 1.0$  in muon events is not observed in MC. The increase can be attributed to secondary leptons produced in the hadronisation and subsequent decay of particles in the jet. While most are contained within the jet cone and are not separately identified, some are produced outside this cone.

An excess also exists in the electron sample at all values of  $\Delta R$  which is attributable to pions that overlap with tracks. A structure at low  $\Delta R$  from indirectly produced electrons (similarly to that seen in the muon sample) is less apparent because of this additional source of fake electrons, but still exists.

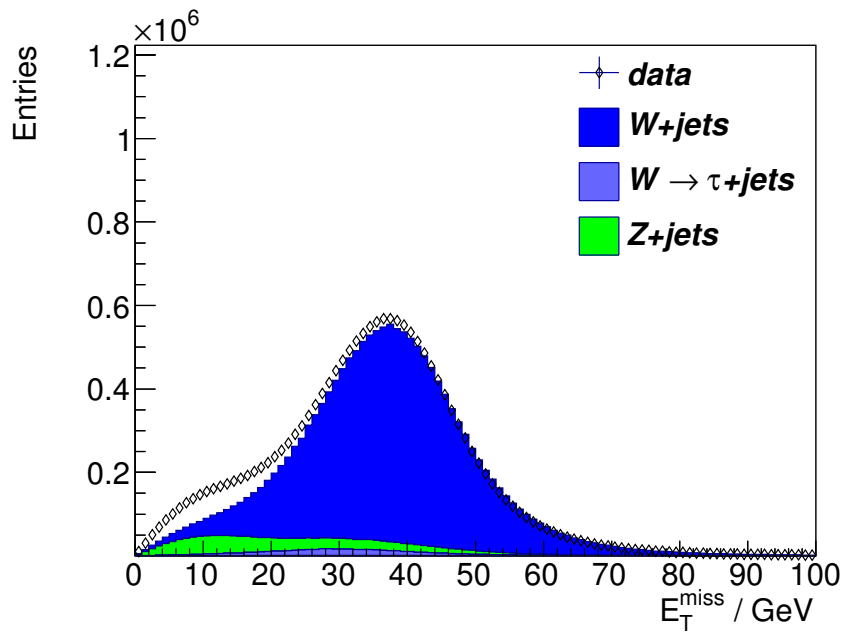
Figures 5.10 and 5.11 show numbers of jets in the selected events before and after the cut requiring a *tight* lepton. After subtracting the backgrounds from data, the ratio of the loose distribution to the tight distribution gives the fake rate as a function of number of jets. A similar procedure is used to calculate the lepton fake rates as a function of other variables.

The proportion of  $t\bar{t}$  events increases with increasing numbers of jets in the event, and dominates for more than 2 b-jets in an event. This means that the fake rate in the signal region is sensitive to the modelling of  $t\bar{t}$  events, and which results in a larger systematic uncertainty.

As many fake leptons are produced in the decay products of a jet, they are expected to have a lower  $p_T$  than directly produced leptons. In the muon channel the number of muons with  $p_T > 80$  GeV are low, particularly for *tight* leptons, and MC fluctuates above the data. Consequently without artificially re-binning the histograms and systematically shifting the muon fake rate, the muon fake rate cannot be calcu-



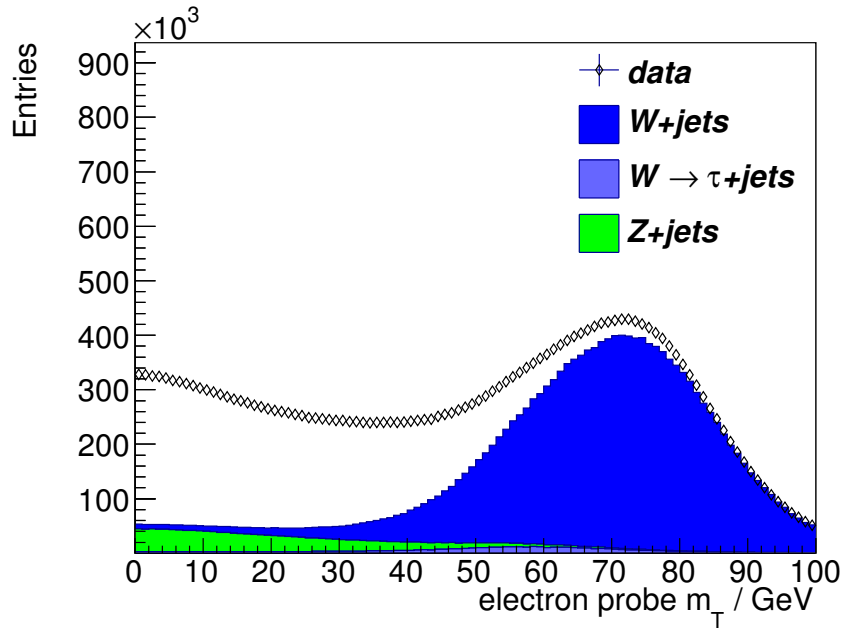
(a) electron channel



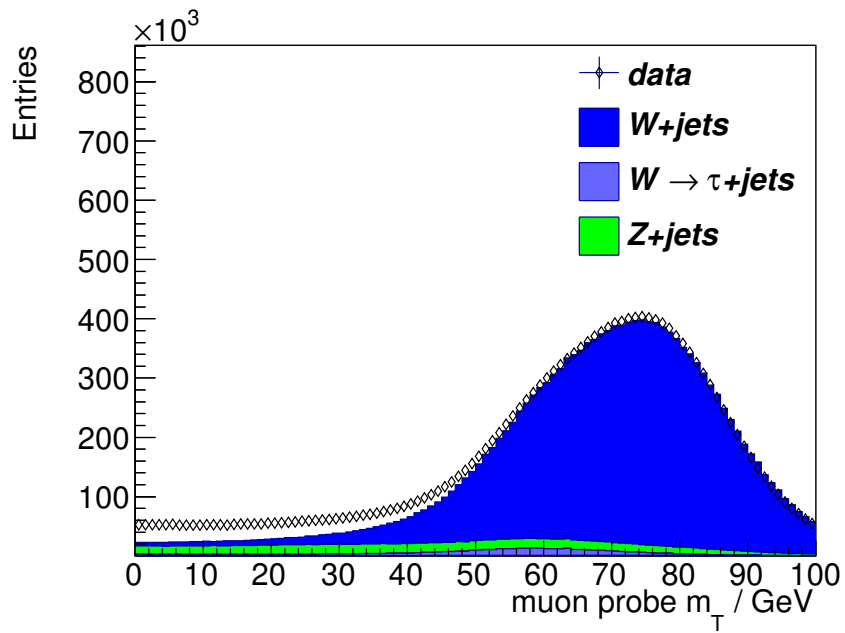
(b) muon channel

Figure 5.7:  $E_T^{\text{miss}}$  distribution for events with a single electron (a) and muon (b).

lated as a function of muon  $p_T$ . To compensate for this, the efficiency was evaluated as a function of the  $p_T$  of the nearest jet to the lepton. The lead jet distributions for



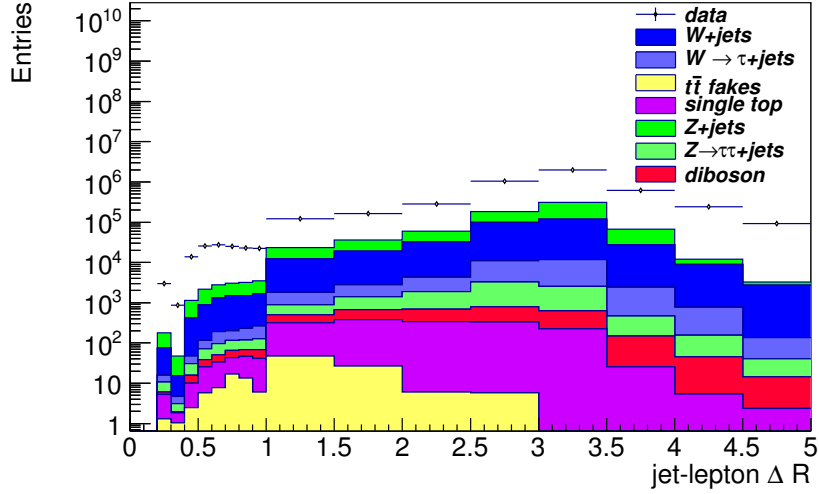
(a) electron channel



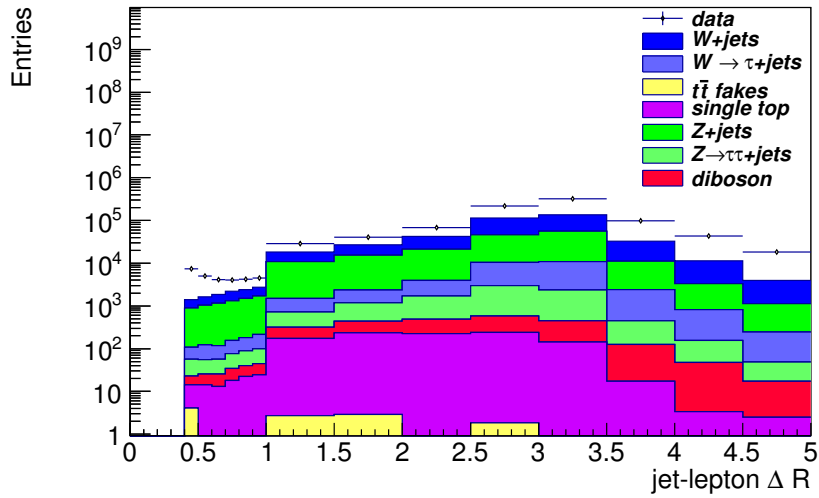
(b) muon channel

Figure 5.8:  $m_T$  distribution for events with a single electron (a) and muon (b).

loose and tight lepton probes used to calculate the fake rates are shown in figures 5.12 and 5.13 respectively.

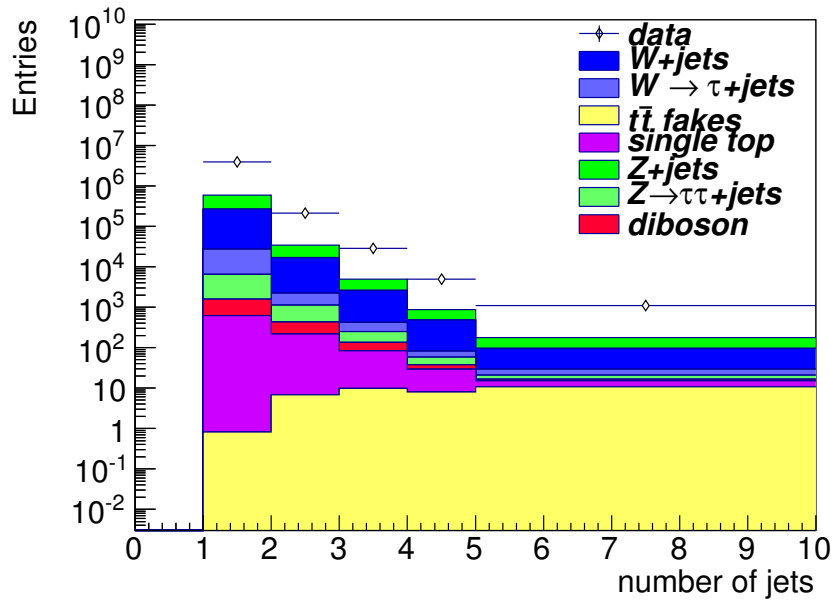


(a) electron channel

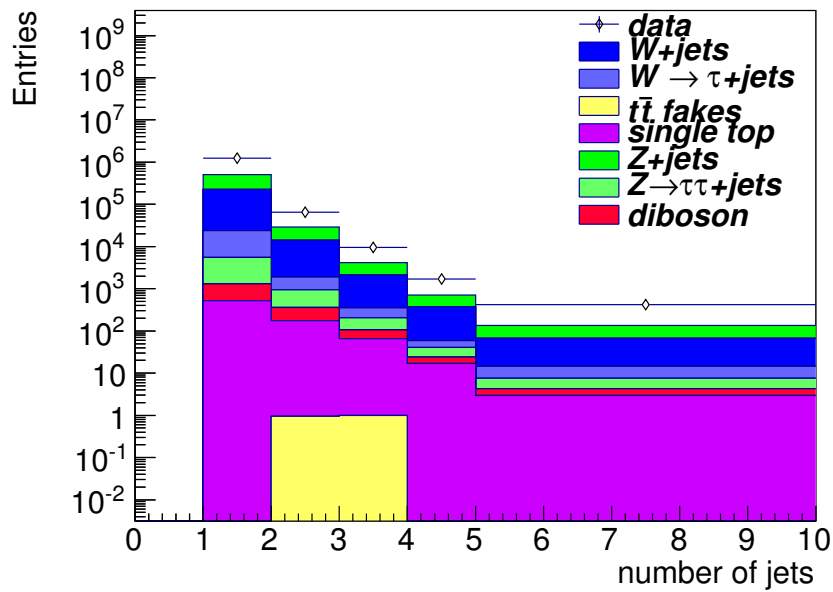


(b) muon channel

Figure 5.9:  $\Delta R$  between probe lepton and the nearest jet for data and MC after the cuts in table 5.3 have been applied. An increase of low  $\Delta R$  leptons data is apparent.

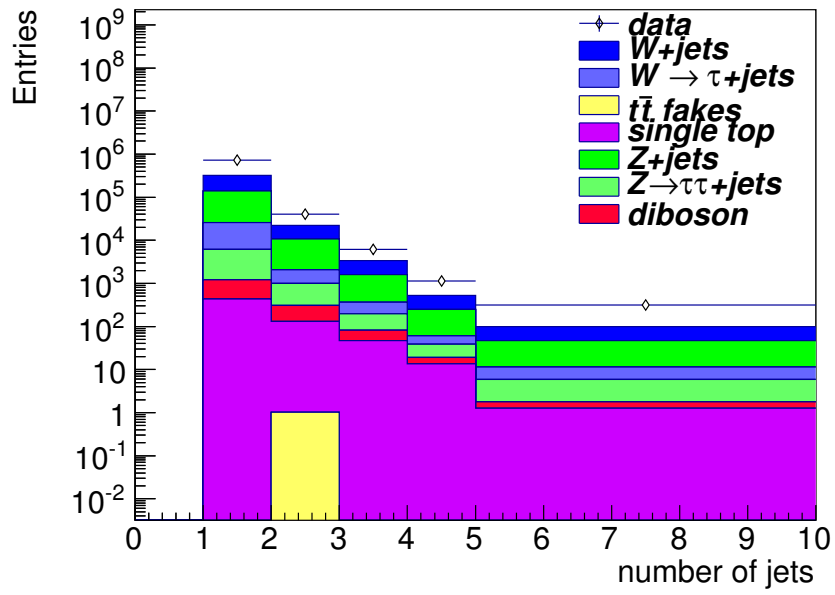


(a) Loose probe

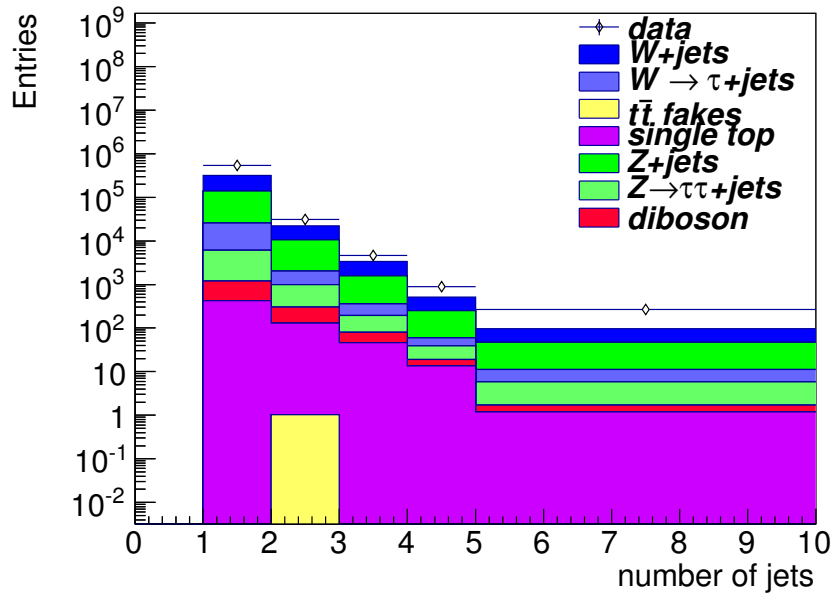


(b) Tight probe

Figure 5.10: Number of jets in events with secondary electrons associated with hadronic jets for data and MC.

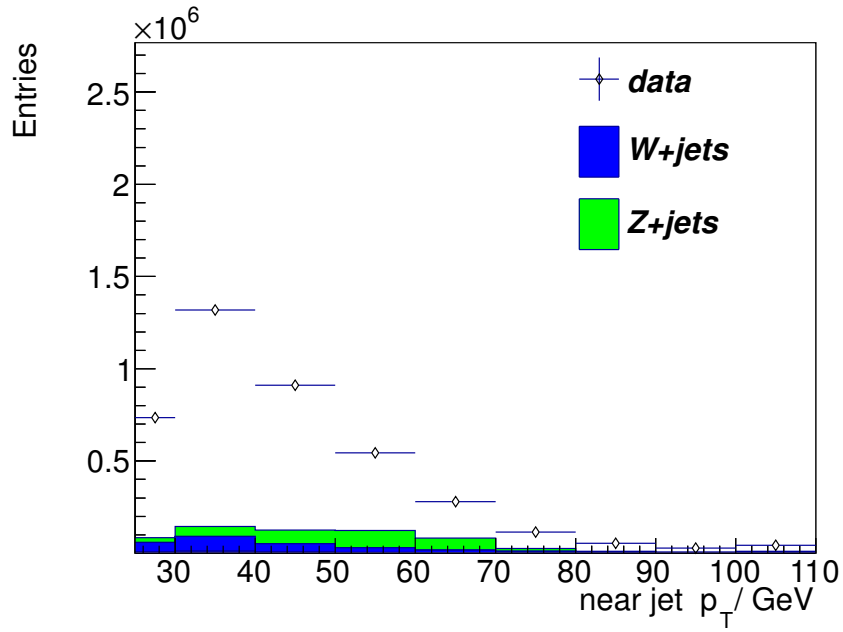


(a) Loose probe

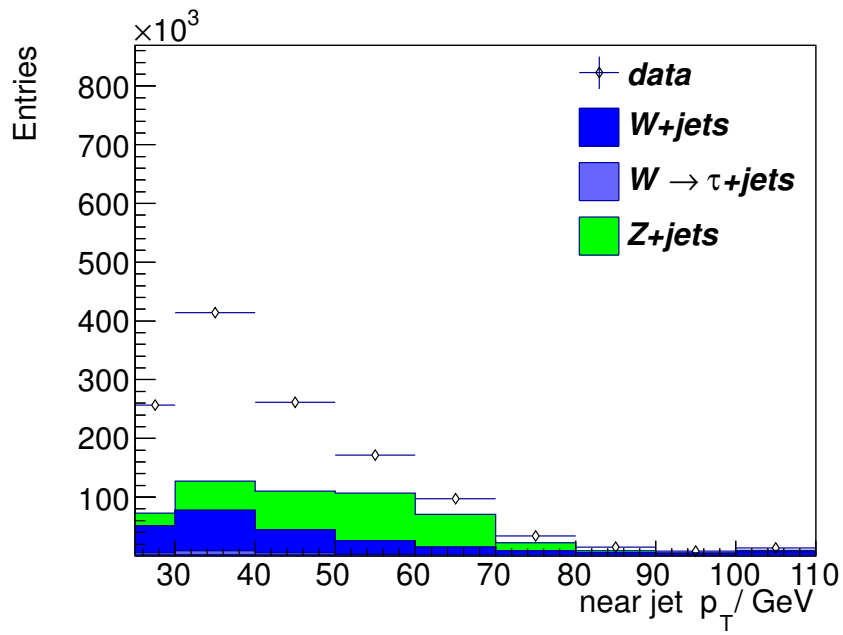


(b) Tight probe

Figure 5.11: Number of jets in events with secondary muons associated with hadronic jets for data and MC.

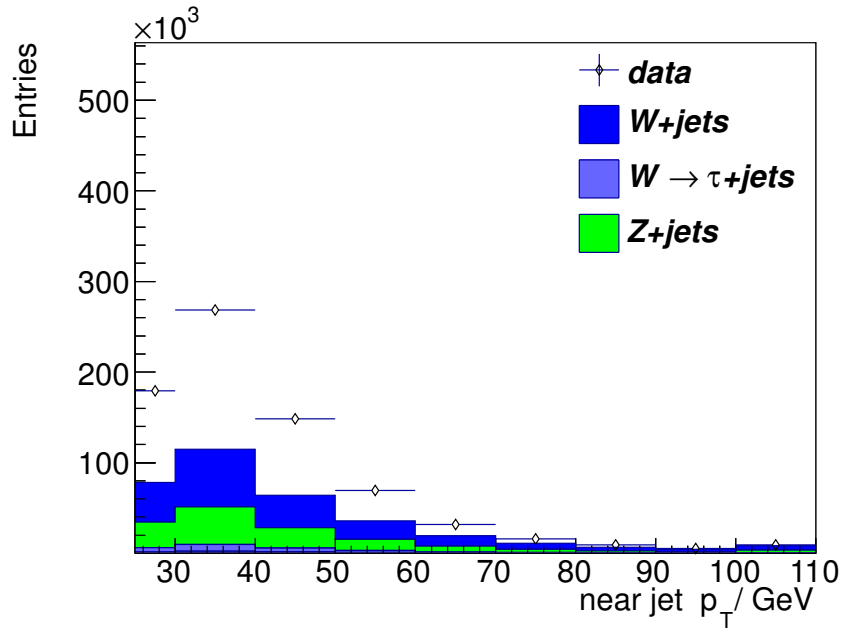


(a) Loose probe

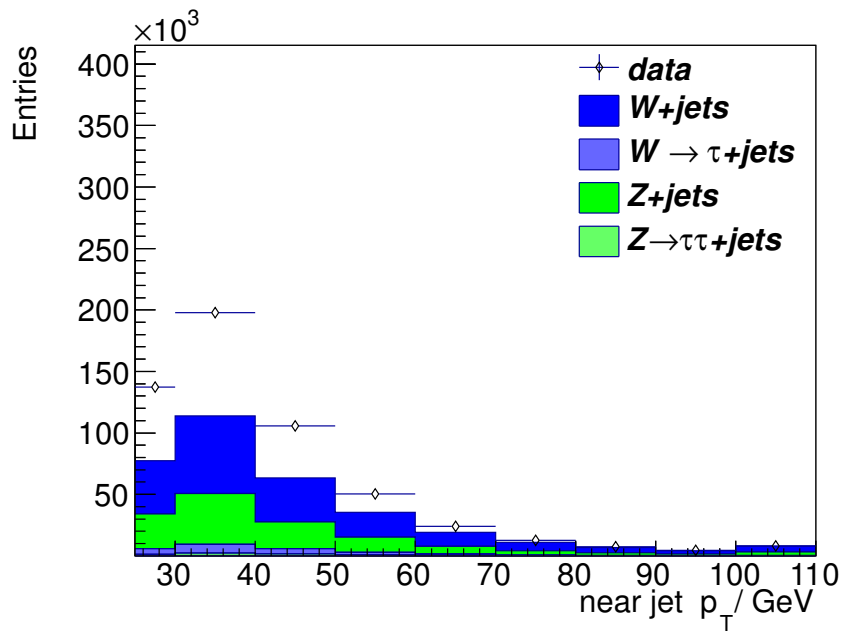


(b) Tight probe

Figure 5.12: Jet  $p_T$  of reconstructed jet with smallest  $\Delta R$  of a reconstructed electron for data and MC.



(a) Loose probe



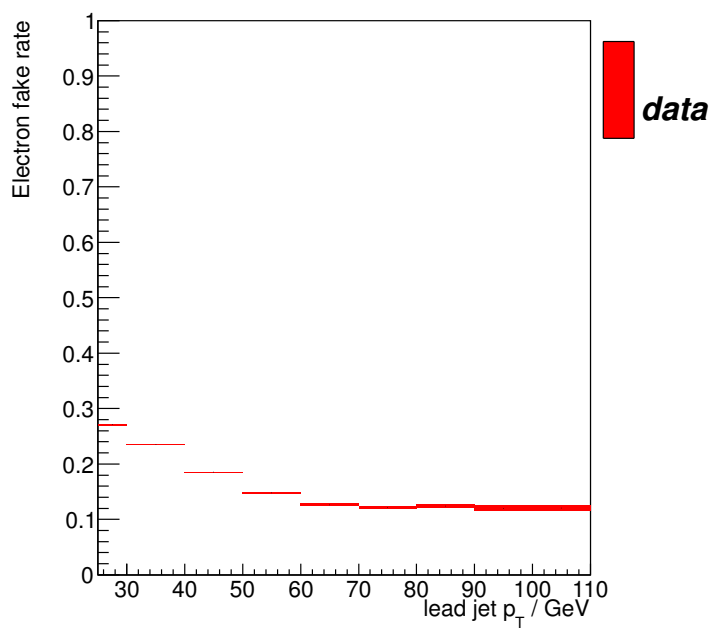
(b) Tight probe

Figure 5.13: Jet  $p_T$  of jets within  $\Delta R < 0.6$  of a reconstructed muon for data and MC.

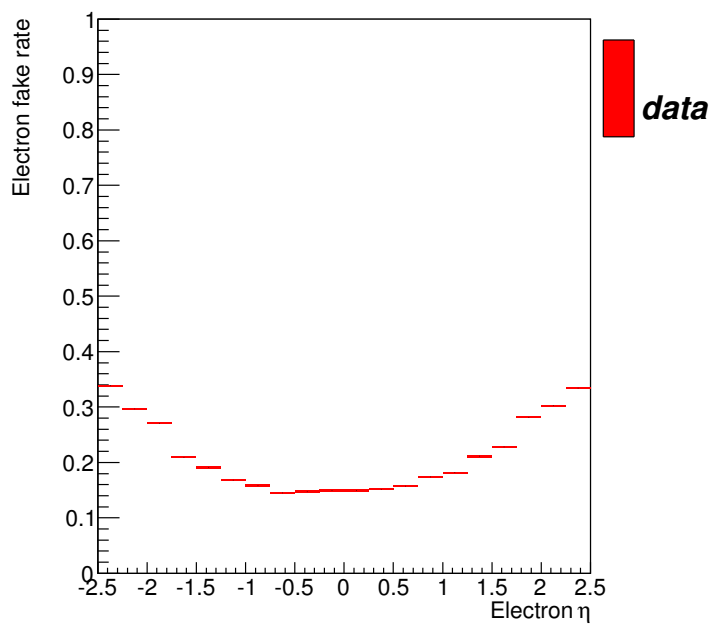
### 5.1.3.1 Lepton Fake Rates

The real lepton MC contributions are subtracted from the data in order to calculate the fake rates. The fake rate  $p_T$  of the nearest jet is chosen as the central value of the fake rate used in equation 5.3, these rates can be seen in figure 5.14. The electron and muon fake rates were initially evaluated as a function of near jet  $p_T$ ,  $\eta$ ,  $\phi$ , the number of jets, the number of b-jets, the number of primary vertices, and  $\Delta R$  between the lepton and the nearest jet. A large variation was seen in the fake rates for many of these, but due to insufficient statistics the fake rate could not be evaluated multi-dimensionally.

The fake rate as a function of electron  $\eta$ , and the number of jets in the muon channel both show a particularly large variation seen in figure 5.14. For both the electron and muon fake rates the highest and lower fake rate bins are used to estimate the systematic uncertainty. The difference between the upper uncertainty for the highest efficiency, and the lower uncertainty for the lowest efficiency is taken as the absolute systematic uncertainty. The absolute systematic on the fake rates are given in table 5.4. This will add a large systematic uncertainty to the lepton fake rates, it should take account for the large variation seen in other kinematic and topological variables.

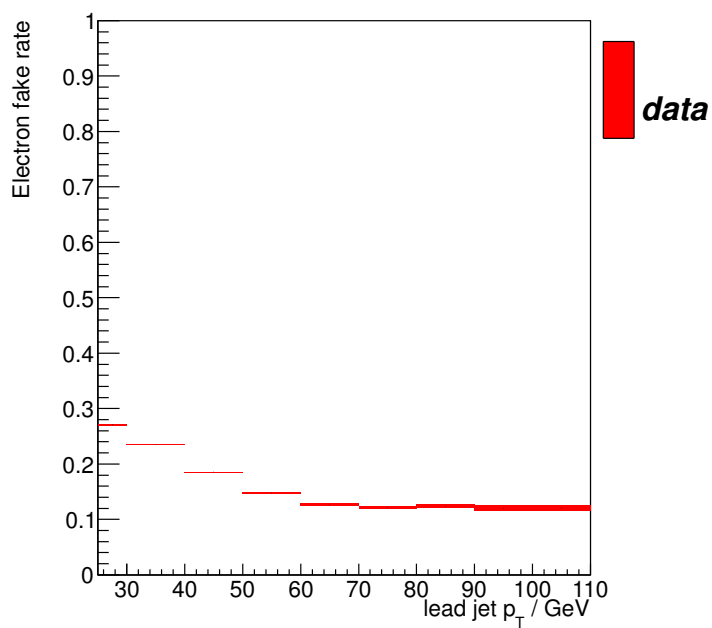


(a) lead jet  $p_T$

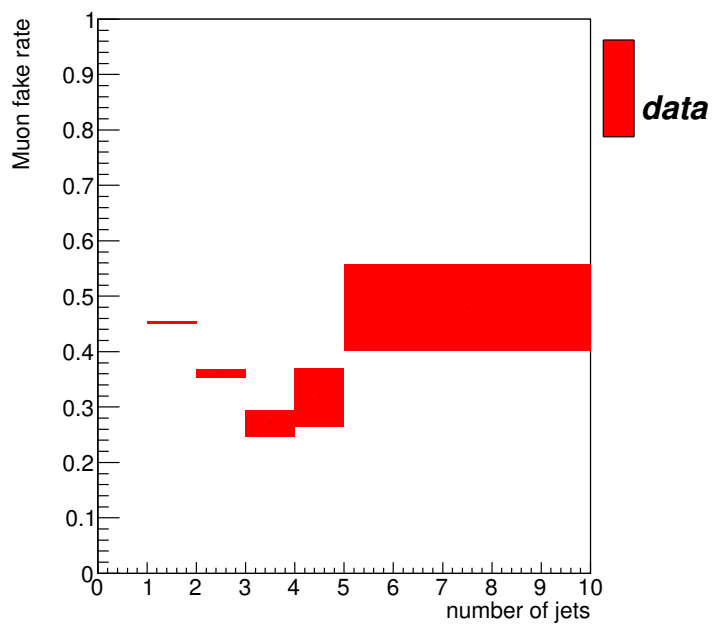


(b) electron  $\eta$

Figure 5.14: Electron fake rates in events with secondary electrons associated with hadronic jets. The error bands indicate the statistical uncertainty.



(a) lead jet  $p_T$



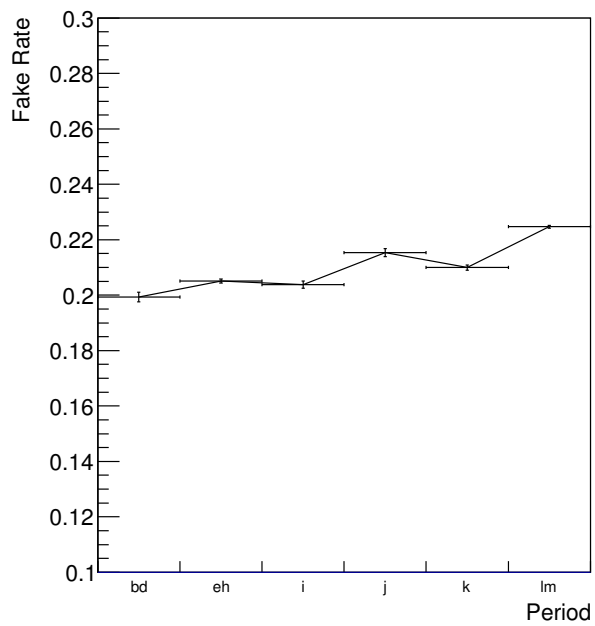
(b)  $N_{jets}$

Figure 5.15: Muon fake rates in events with secondary muons associated with hadronic jets. The error bands indicate the statistical uncertainty.

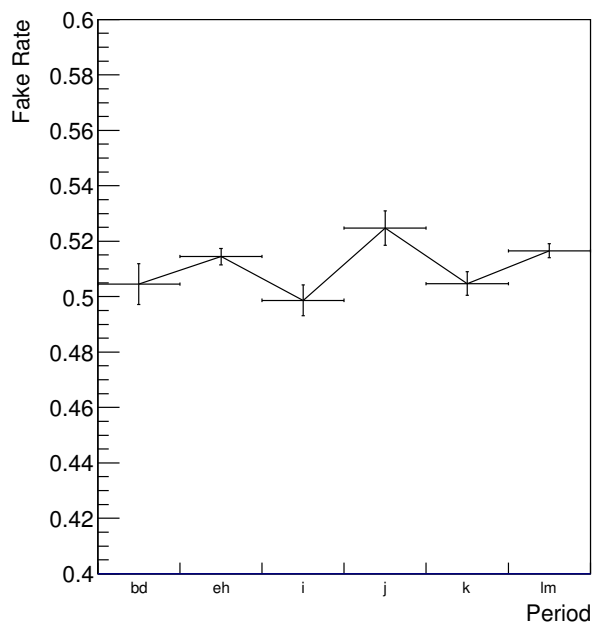
Lepton	Fake Rate Systematic Error
e	$\pm 0.10$
$\mu$	$\pm 0.15$

Table 5.4: The absolute systematic error on the electron and muon fake rates.

The fake rates are not highly stable for different run periods despite variations in data taking conditions, such as increasing pile-up, and changes in detector performance, as seen in figure 5.16. While an apparent increase in the electron fake rate can be seen, which may be due to different triggers in later runs, the difference is smaller than the systematic uncertainty shown in the table 5.4.



(a) electron channel



(b) muon channel

Figure 5.16: The lepton fake rates per period.

## 5.2 Electron and Muon Fakes in the Di-lepton Control Region

In order to check the matrix method a region orthogonal to the  $t\bar{t}$  di-lepton signal region given in section 4.4 is chosen by selecting low  $E_T^{\text{miss}}$  events ( $E_T^{\text{miss}} \leq 40$  GeV). As reversing the  $E_T^{\text{miss}}$  cut reduces the statistics of the sample, additionally the requirements on the number of b-jets in the event are dropped. This region is used to check the agreement between data, and the sum of  $t\bar{t}$  signal MC, MC backgrounds and lepton fakes.

Using the *loose* and *tight* lepton definitions given in section 5.1.2 four exclusive populations of events are constructed as explained in section 5.1.1, which differ only in the tightness of the lepton selections.

The efficiency (fake rate) for an individual lepton in an event is taken from the lepton  $p_T$  (lead jet  $p_T$ ) distributions in figures 5.2 and 5.3 (5.14 and 5.15). These are used as the likely efficiencies (or fake rates) of an individual lepton selected in one of the four loose/tight lepton populations in section 5.1.1.

Using these efficiencies, each event, defined by its loose and tight lepton content, is weighted using the coefficients for each population in equation 5.3. Note that events with two tight leptons or two loose leptons contribute a negative weight, and events with one loose and one tight lepton contribute a positive weight. As each event has the same topology as the signal region events, histograms can be filled as normal. However in regions of a histogram with a low expected contribution from *fakes* these can become negative. For this reason events are selected with no b-jet requirements to increase the numbers of events available to validate the fake rate method. The numbers of jets and b-jets in the  $t\bar{t}$  control region, including the fake lepton estimate, are shown in figure 5.17. Both indicate that the lepton fake rate will be low in the signal region, for high numbers of b-jets and jets. The lepton  $p_T$  distributions for the trigger lepton and the secondary leptons are shown in figure

5.18 shows good agreement between data and MC. An analogous method is used to predict the number of lepton fakes in the lepton plus tau  $t\bar{t}$  control and signal regions, this is presented with the tau fake estimates in sections 6.1 and 6.2.

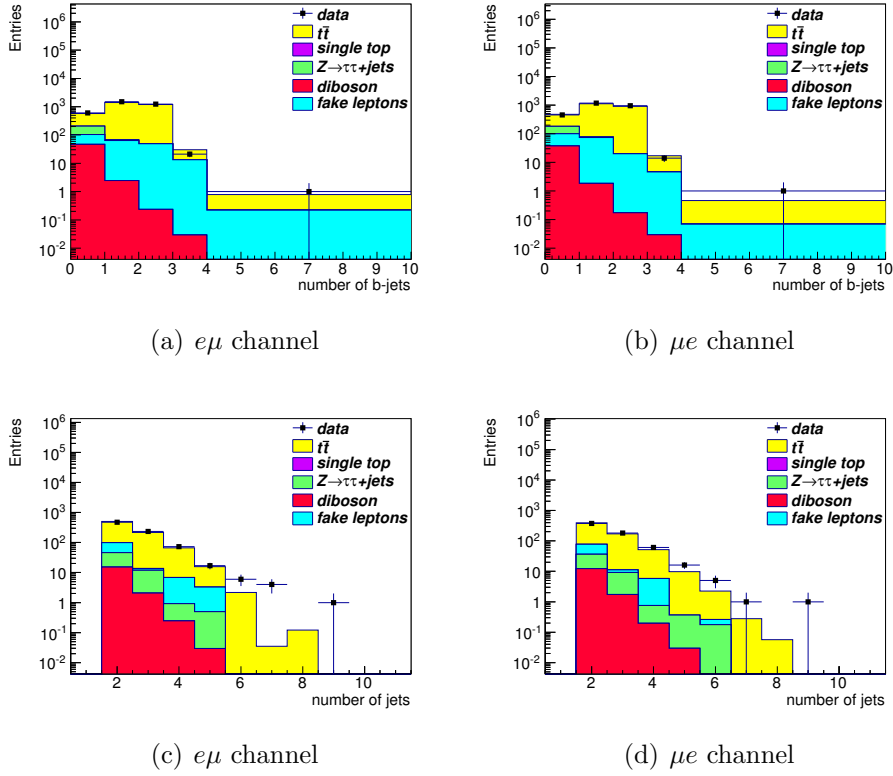
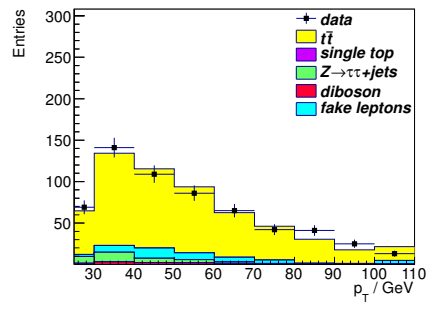
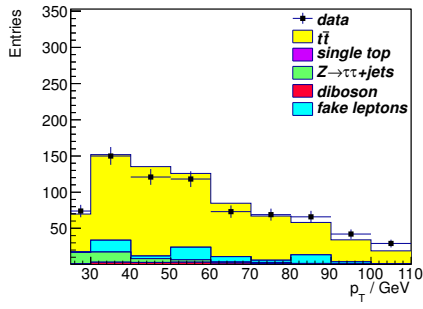
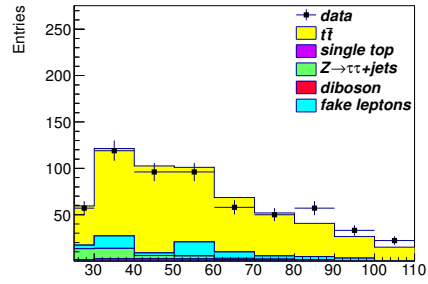
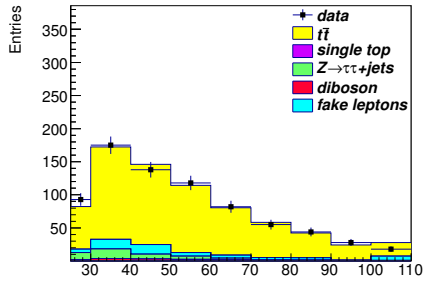


Figure 5.17: Number of b-jets ((a) and (b)) and jets ((c) and (d)) in the electron channel and the muon channel respectively in events with  $E_T^{\text{miss}} < 40$  GeV.



(a) trigger electron  $p_T$  in the  $e\mu$  channel (b) trigger muon  $p_T$  in the  $\mu e$  channel

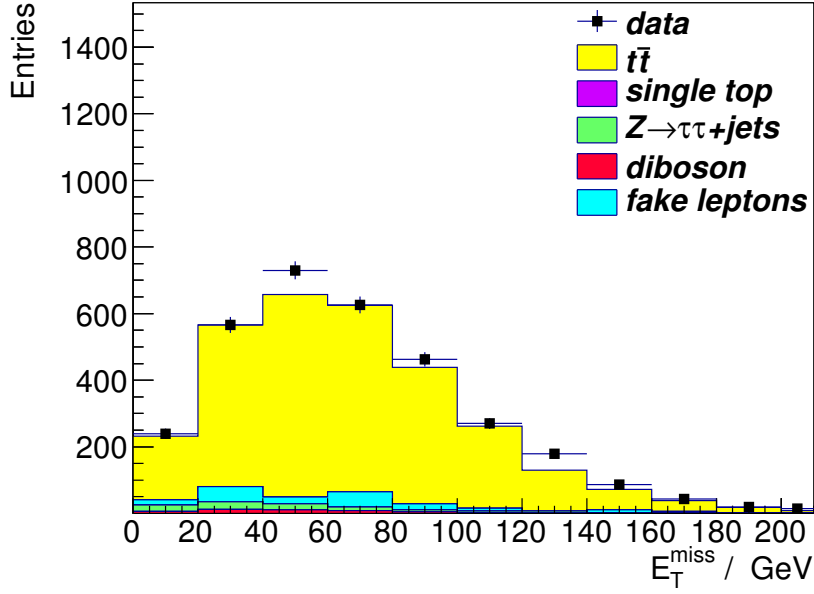


(c) muon  $p_T$  in the  $e\mu$  channel

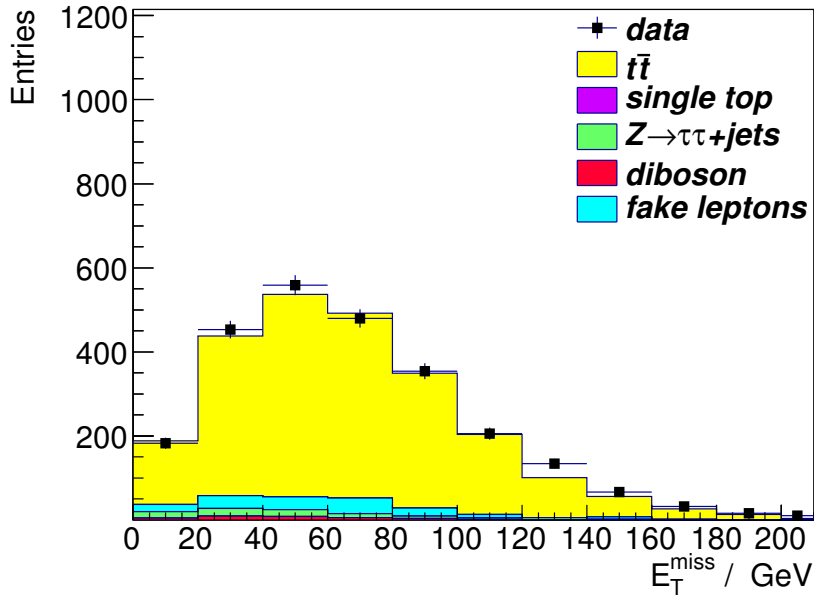
(d) electron  $p_T$  in the  $\mu e$  channel

Figure 5.18: Lepton  $p_T$  distributions in the electron triggered channel ((a) and (b)) and the muon triggered channel ((c) and (d)) in events with  $E_T^{\text{miss}} < 40$  GeV.

The  $E_T^{\text{miss}}$  distributions for events with no b-tag selection are shown in figure 5.19, no systematic uncertainties are included at this point.



(a) electron channel



(b) muon channel

Figure 5.19: The  $E_T^{\text{miss}}$  distributions in the di-lepton control region before the  $E_T^{\text{miss}}$  cut.

## 5.3 Hadronic Tau Fake Rates

As described in section 4.1.5, each hadronic jet is assigned a BDT variable which is optimised to accept hadronic tau jets over other hadronic jets, and for which different tau lepton efficiency working points are specified. Hadronically decaying tau leptons can be produced in the decay products in hadronic jets. *Fake* hadronic tau leptons are defined to be all reconstructed taus that are not produced directly in a hard interaction, inclusive of mis-identified jets and taus produced in the decay products of hadronic jets. As no tau triggers have been used at any stage in this physics analysis, fake taus are not simply defined in the same way as fake leptons.

To determine the tau fake rate it is necessary to construct a pure sample of hadronic jets with a low contamination of hadronic taus. Two independent channels are used to estimate the fake rate; one selects a pure sample of leptonically decaying  $Z$  bosons, and the other reconstructs  $W$  bosons which also decay leptonically. Using the reconstructed bosons as tags, the jets in the events are probed for reconstructed hadronically decaying taus. As will be shown in section 5.3.3, the  $W$  sample suffers from a high contamination from  $t\bar{t}$  events after selecting events with a hadronically decaying tau lepton. For this reason the  $W$  sample is used only as a cross check to the fake rate measured using the  $Z$  sample. This method assumes that the jet kinematic properties in  $Z$  and  $W$  events are similar to those of  $t\bar{t}$  events, comparisons are made in section 5.4 to ensure this is the case.

Using the event selection outlined in section 4.4 as a basis, events are selected that contain a single electron or muon and three or more jets. This selection will include  $t\bar{t}$  lepton plus jets events and leptonically decaying  $W$  events, both of which have the potential to be reconstructed as  $t\bar{t}$  lepton plus tau events, when one jet is reconstructed as a hadronic tau lepton. For a particular number of hadronic jets in an event ( $i$  jets) we can define a fake rate where exactly one of these jets is reconstructed as a hadronic tau (leaving  $i-1$  jets). For example, an event with three hadronic jets could be reconstructed as an event with two jets and one hadronic tau.

The fake rate for reconstructing one hadronic tau and  $i$ -jets from  $i + 1$  jets is defined as

$$\epsilon_{i+1 jets}^{\tau fake} \equiv \frac{N_{with \tau}^{i jets}}{N^{i+1 jets} + N_{with \tau}^{i jets}} \quad (5.8)$$

where  $N^{i+1 jets}$  is the number of events with  $i + 1$  jets and no reconstructed tau, and  $N_{with \tau}^{i jets}$  is the number of events with  $i$  jets and one hadronic tau. The denominator is defined such the events contain  $i + 1$  hadronic objects, inclusive of hadronic taus. Figure 5.20 shows a representation of two events with five hadronic objects. The number of events with one hadronic tau is the numerator for  $\epsilon_{5-jets}^{\tau fake}$  from equation 5.8, and the total number of events of both types is used in the denominator.

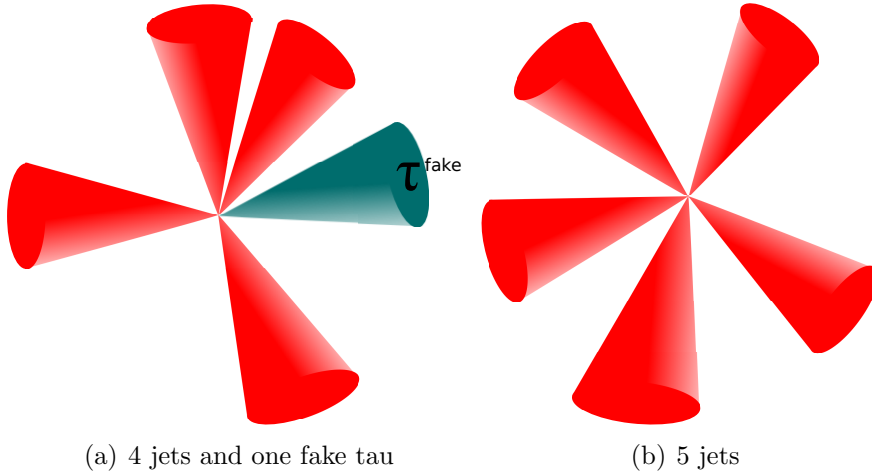


Figure 5.20: Two events are represented with five hadronic objects. The event on the left contains one fake hadronic tau, and the event on the right does not.

Re-arranging equation 5.8 gives the expected number of events with exactly one hadronic tau and  $i$ -jets in terms of this measured fake rate and the number of events with  $i + 1$  jets (and no reconstructed tau) as shown in equation 5.9.

$$N_{with \tau}^{i jets} = \frac{\epsilon_{i+1 jets}^{\tau fake}}{1 - \epsilon_{i+1 jets}^{\tau fake}} N^{i+1 jets}, \quad (5.9)$$

As noted in section 4.1.6, the effect of re-calibrating the calculated  $E_T^{\text{miss}}$  for the

presence of a hadronic tau is very small and is not applied in this analysis.

As the definition in equation 5.8 measures the number of events with  $i + 1$  jets to predict the number of tau fakes in events with  $i$ -jets the tau fake rate must be defined with its binning shifted, so that in the signal region, where the number of events with 5 or more jets is measured, the fake rate must be measured for 6 or more jets. The lepton plus jet events that are selected for the tau fake rate have the same selections as in tables 4.1 and 4.2, except only one electron or muon is selected and events must have 3 or more jets.

### 5.3.1 Measuring $jet \rightarrow \tau$ fake rate using $Z \rightarrow e^+e^-/Z \rightarrow \mu^+\mu^- + jets$

$Z \rightarrow e^+e^- + jets$  and  $Z \rightarrow \mu^+\mu^- + jets$  events are selected with a di-lepton invariant mass ( $M_{ll}$ ) within 10 GeV of the mass of the  $Z$  ( $M_Z$ ) using tight lepton definitions, with similar cuts to those that are used to measure the real lepton efficiencies. The numbers of jets and taus in the event are used to measure the fake rate as defined in equation 5.8.

For each respective electron / muon trigger channel, events are selected with two oppositely charged, *tight* electrons / muons that have  $p_T > 25$  GeV but no further electrons / muons with  $p_T > 15$  GeV in the same event, where at least one of these leptons is trigger matched.

Each lepton pair is required to have an invariant mass within 10 GeV of  $M_Z$ . The event is then probed for the presence of a tau lepton with  $p_T > 25$  GeV, and the number of jets before and after this cut is recorded. The event selection cuts are given in full in table 5.5. This event selection is run upon all the MC described in section 4.6. The purity of selected events can be seen in the invariant mass distribution of the  $Z$  in figure 5.21, before any cut on hadronic tau leptons is applied, as a very small number of background events pass the cuts. The numbers of jets and b-jets in

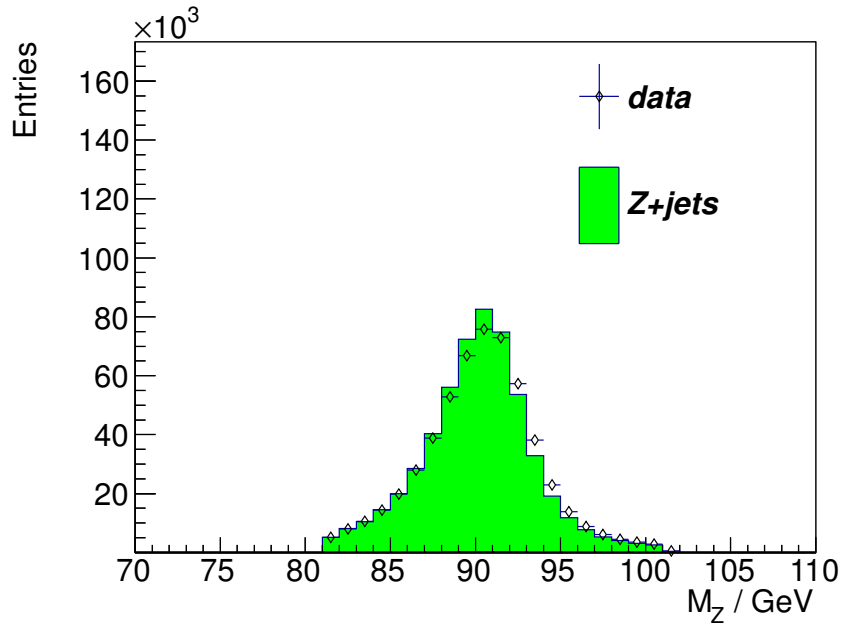
the events, before any tau selection is applied, are shown in figure 5.22. While the number of jets in the event seem relatively well modelled there is large disagreement between data and MC for number of b-jets in the event.

Cut	$Z \rightarrow e^+e^-$	$Z \rightarrow \mu^+\mu^-$
0 (data only)	passes the GRL	passes the GRL
1	Electron Trigger	Muon Trigger
2	5 or more primary vertex tracks	5 or more primary vertex tracks
3	No <i>bad</i> jets and no LAr errors	No <i>bad</i> jets and no LAr errors
4	2 electrons (one trigger matched)	2 muons (one trigger matched)
5	2 electron	0 electrons
6	0 muons	2 muons
7	1 <i>tight</i> trigger matched tag electron	1 <i>tight</i> trigger matched tag muon
8	$M_{ee} - M_Z < 10$ GeV	$M_{\mu\mu} - M_Z < 10$ GeV
9	Oppositely charged leptons	Oppositely charged leptons
10	fewer than 2 taus	fewer than 2 taus
	<i>Fill jet weight histograms with no tau requirement</i>	
11	1 tau	1 tau
	<i>Fill jet weight histograms</i>	

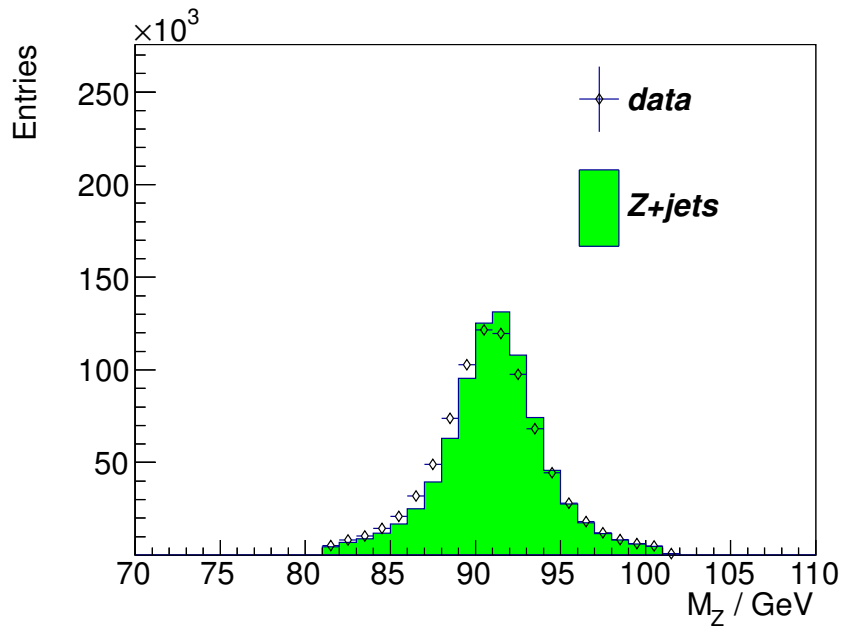
Table 5.5: Cut flow to select  $Z \rightarrow e^+e^-$  events and  $Z \rightarrow \mu^+\mu^-$  events to measure the  $jet \rightarrow \tau$  fake rate.

The lead jet  $p_T$  distributions are shown in figure 5.23, before any tau selection is applied, with good agreement between data and MC. As the tau fake rate definition does not correct for kinematic differences the lead jet  $p_T$  distributions needs to be well predicted in the  $t\bar{t}$  signal region.

The  $p_T$  distributions of selected taus are shown in figure 5.24. The  $p_T$  distribution from fake taus will depend on the  $p_T$  distribution of jets in the  $t\bar{t}$  signal region.

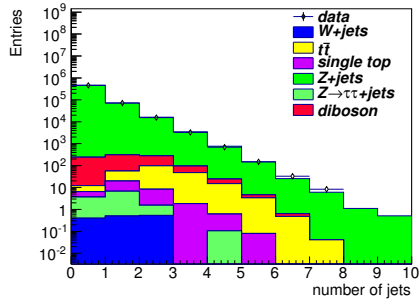


(a)  $Z \rightarrow e^+e^-$

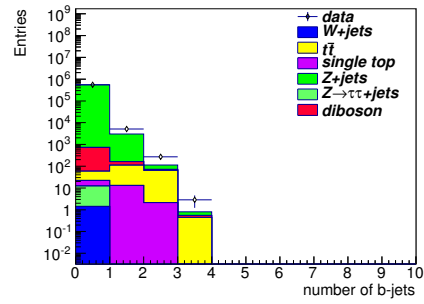


(b)  $Z \rightarrow \mu^+\mu^-$

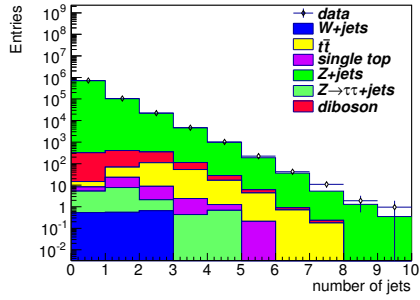
Figure 5.21: Di-lepton invariant mass plots for  $Z$  events used to measure tau fake rates.



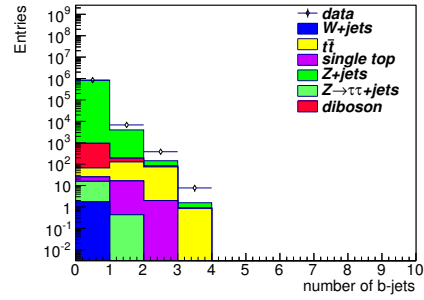
(a) Number of jets



(b) Number of b-jets

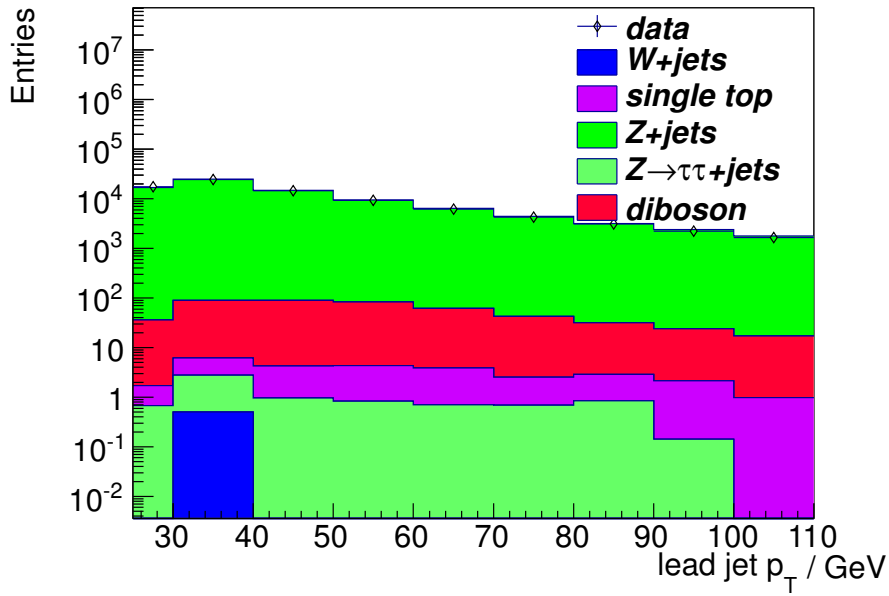


(c) Number of jets

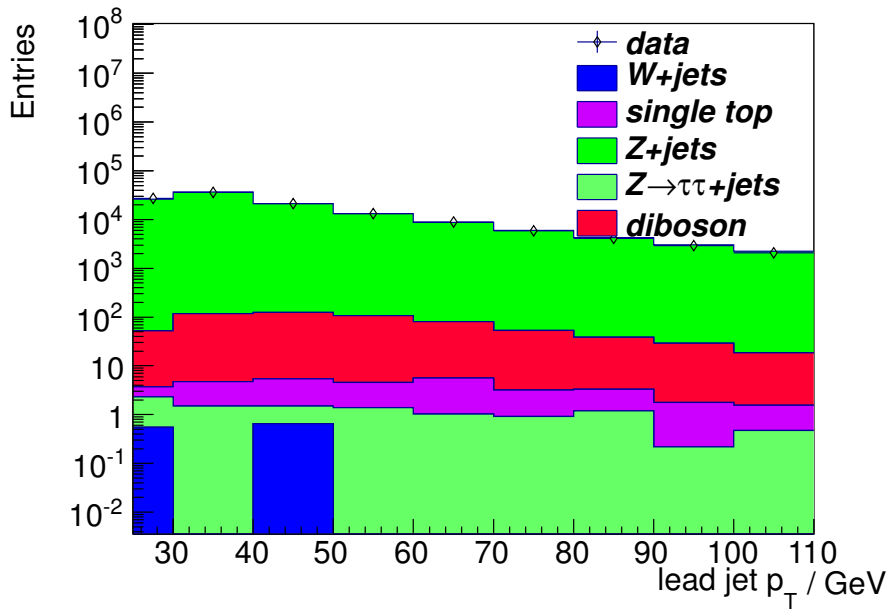


(d) Number of b-jets

Figure 5.22: The distributions of the numbers of jets ((a) and (c)) and b-jets ((b) and (d)) in  $Z \rightarrow e^+e^- + \text{jets}$  events (a) and b)) and  $Z \rightarrow \mu^+\mu^- + \text{jets}$  events (c) and d)) before any tau selection has been applied comparing data and MC.

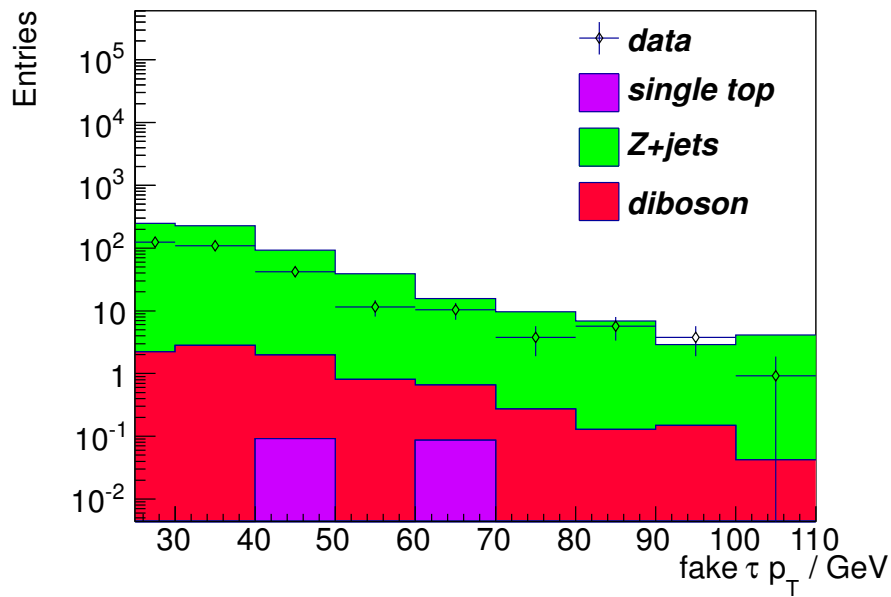


(a)  $Z \rightarrow e^+e^-$

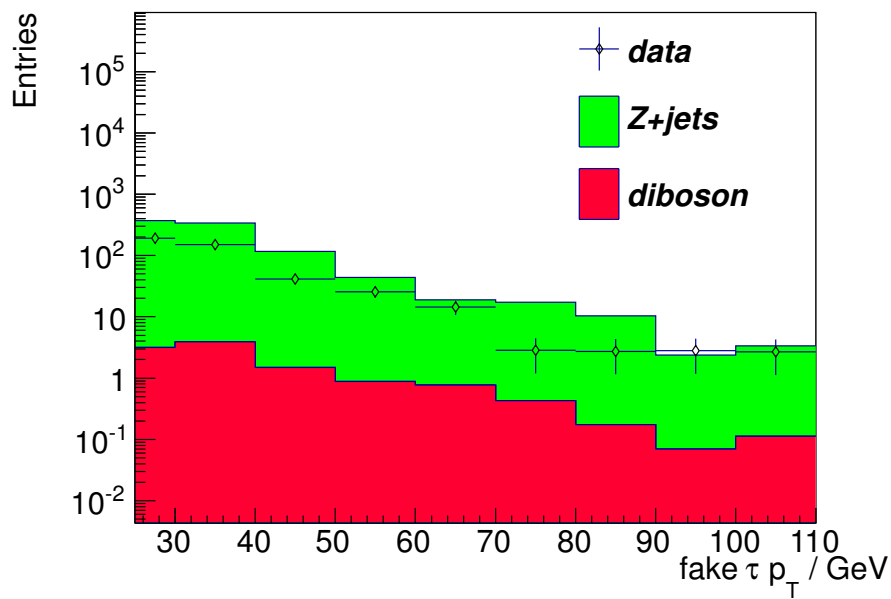


(b)  $Z \rightarrow \mu^+\mu^-$

Figure 5.23: Lead jet  $p_T$  in  $Z \rightarrow e^+e^-$  (a) and (b)  $Z \rightarrow \mu^+\mu^-$  events before any tau selection has been applied comparing data and MC.



(a) electron channel



(b) muon channel

Figure 5.24: Tau lepton  $p_T$  distributions in  $Z \rightarrow e^+e^- + \text{jets}$  events and  $Z \rightarrow \mu^+\mu^- + \text{jets}$  events comparing data and MC.

### 5.3.1.1 Tau fake rates

The jet and b-jet distributions before and after selecting a hadronically decaying tau are shown in figure 5.25. Note the binning here is chosen to give the same jet binning as the signal region (plus an additional bin as explained at the beginning of section 5.9). The shape of these distributions after selecting one hadronic tau is similar between data and MC, however the yield is higher in MC, and the fake rates calculated in data and MC can differ typically by  $\sim 200\%$  which justifies a data driven fake rate estimate.

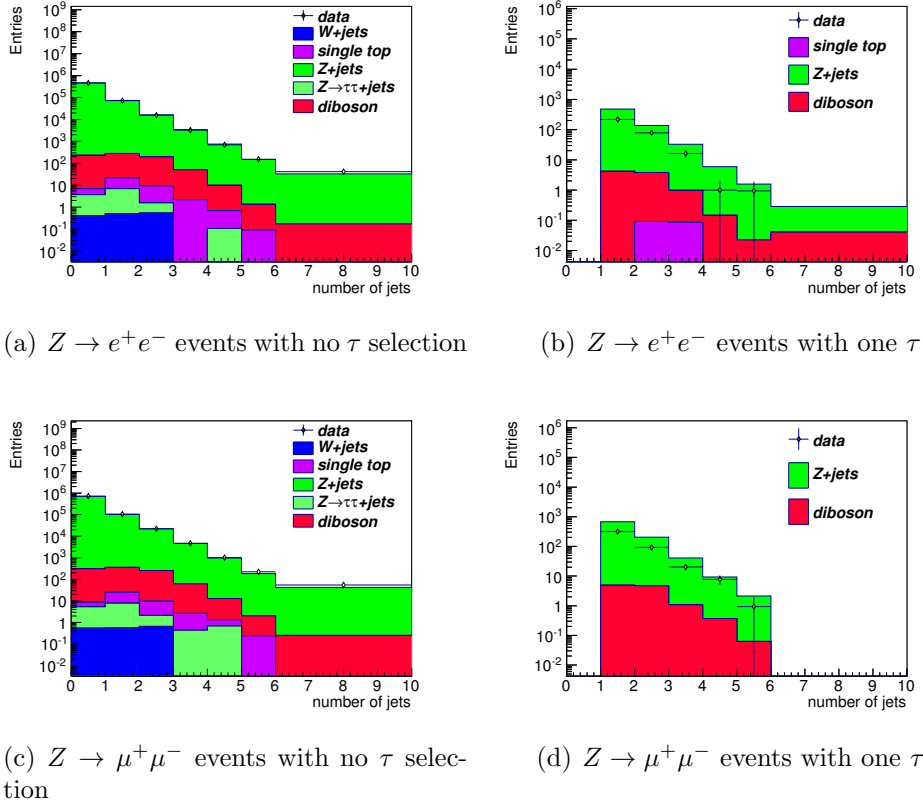
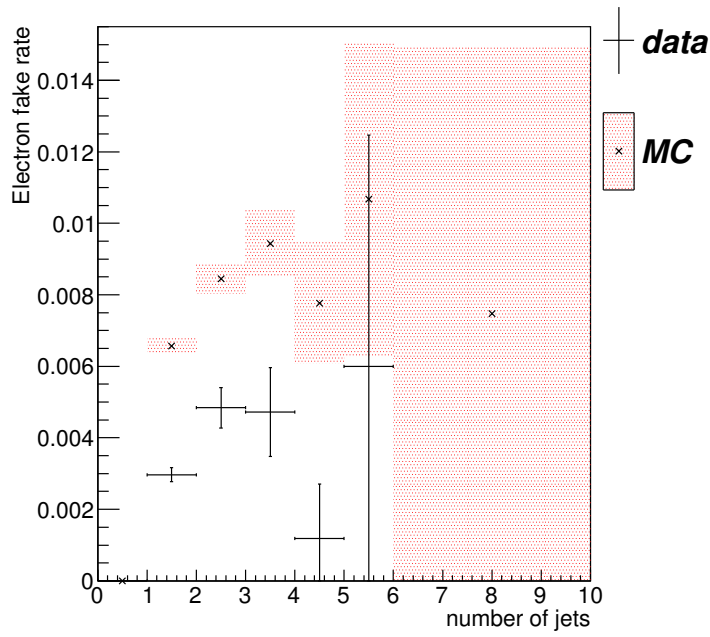


Figure 5.25: Total number of jets before and after a cut on the number of hadronic taus in  $Z \rightarrow e^+e^- + \text{jets}$  events ((a) and (b)) and  $Z \rightarrow \mu^+\mu^- + \text{jets}$  events ((c) and (d)) comparing data and MC.

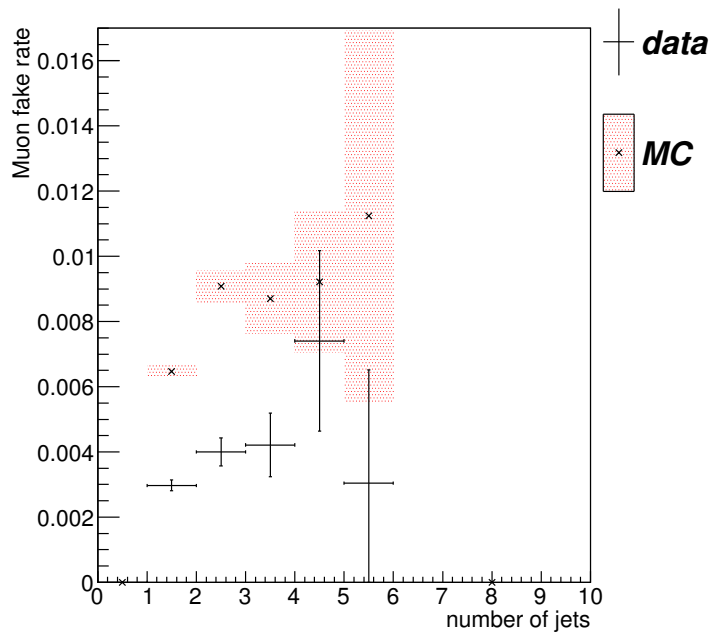
The tau fake rates are calculated by subtracting the number of MC events with real taus, consisting mostly of a small number of di-boson and  $t\bar{t}$  events, from the data distributions. The rates for jets faking taus as a function of the number of jets in

the event are shown in figure 5.26. As there are no significant differences in the fake rate between the electron and muon channels they are combined to improve the statistical error of the fake rate measurement for larger numbers of jets. The high purity, even for a large numbers of jets, makes this method suitable for predicting tau fake rates for  $t\bar{t}$  events without a heavy reliance on MC modelling of real taus.

An asymmetry in the yields between positive and negative fake tau leptons was observed in data and reproduced in MC in  $Z \rightarrow e^+e^-$  and  $Z \rightarrow \mu^+\mu^-$  events as seen in figure 5.27. To take account of this difference the combined fake rate was separated into events that yielded a positive and negative tau respectively and these are shown in figure 5.28 where a small systematic difference can be seen in the tau fake rates. This difference is  $\sim 15\%$  and is seen in both data and MC. A small effect is also seen in the  $t\bar{t}$  signal region in the yields in data and MC.

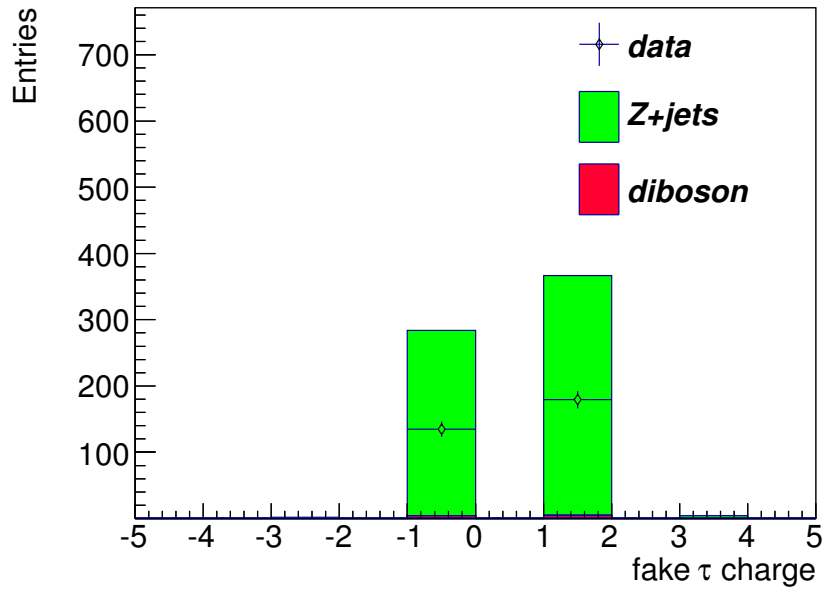


(a)  $Z \rightarrow e^+e^- + \text{jets}$

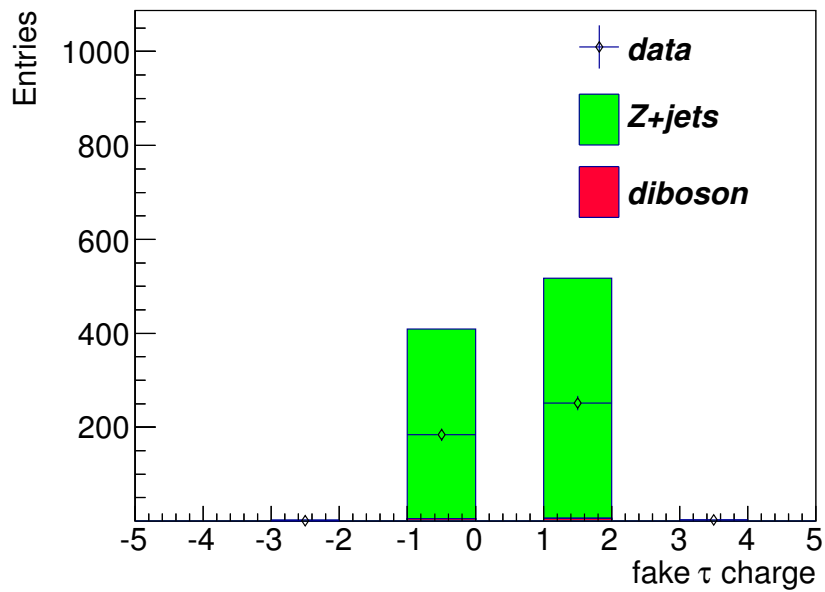


(b)  $Z \rightarrow \mu^+\mu^- + \text{jets}$

Figure 5.26: Tau fake rate as a function of number of jets in the event shown for  $Z \rightarrow e^+e^- + \text{jets}$  (a)) and  $Z \rightarrow \mu^+\mu^- + \text{jets}$  (b)).

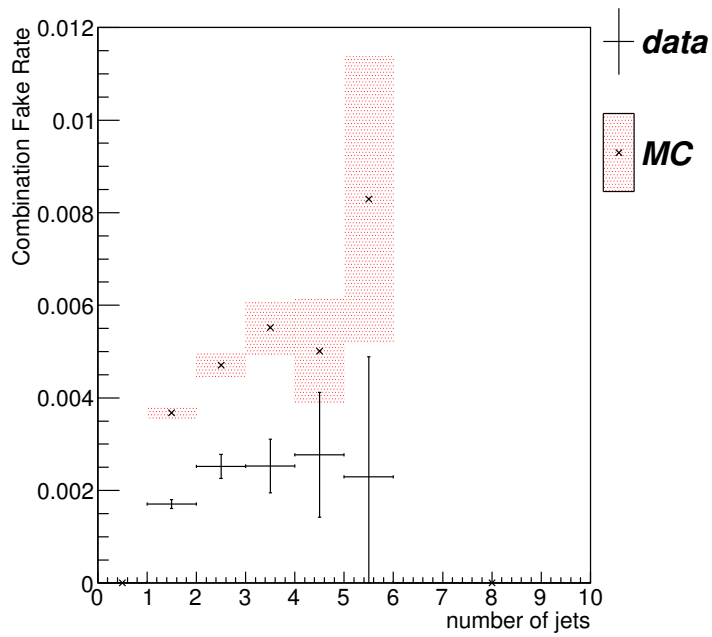


(a)  $Z \rightarrow e^+e^- + \text{jets}$

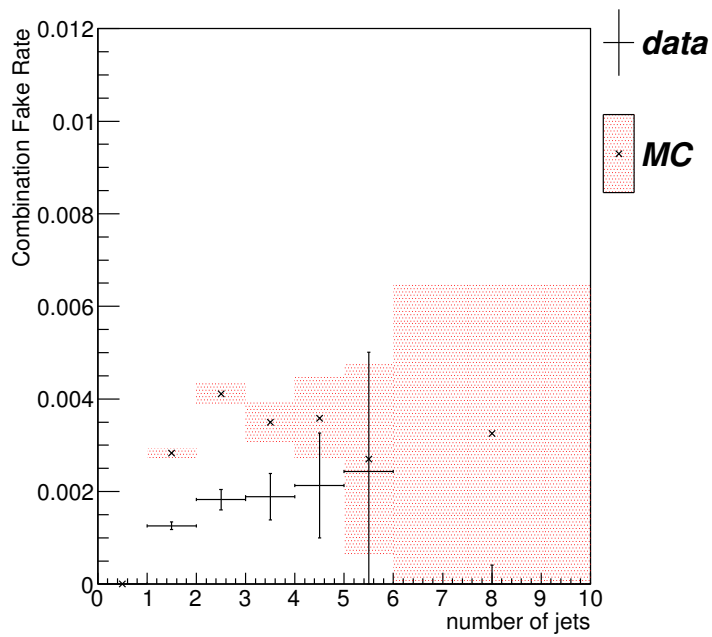


(b)  $Z \rightarrow \mu^+\mu^- + \text{jets}$

Figure 5.27: The yield of events for  $Z \rightarrow e^+e^- + \text{jets}$  (a) and  $Z \rightarrow \mu^+\mu^- + \text{jets}$  (b) with fake positively and negatively charged reconstructed tau leptons.



(a) The fake rate of  $\tau^+$  measured in  $Z + jets$  events



(b) The fake rate of  $\tau^-$  measured in  $Z + jets$  events

Figure 5.28: Tau fake rate as a function of number of jets in the event combining the electron and muon channels, separating the fake rates for positive taus and negative taus.

### 5.3.2 Measuring the $jet \rightarrow \tau$ fake rate using $W \rightarrow e + jets$ and $W \rightarrow \mu + jets$ events

In order to obtain an independent verification of the  $jet \rightarrow \tau$  fake rate,  $W \rightarrow e + jets$  and  $W \rightarrow \mu + jets$  events are selected. Note that this selection is not orthogonal to the lepton plus tau signal region and so it is only suitable as a cross-check of the tau fake rate estimate. Events are selected with a single *tight* electron / muon with  $p_T > 25$  GeV which is trigger matched, and no muons / electrons with  $p_T > 15$  GeV in the event. Reconstructing the  $W$  transverse mass ( $m_T$ ) distribution with the lepton  $p_T$  and  $E_T^{\text{miss}}$ , and selecting events with  $m_T > 50$  GeV and  $E_T^{\text{miss}} > 20$  GeV selects a high purity sample of  $W$  events. The jets are then used to probe the tau fake rate as defined in equation 5.8. The event selection cuts are given in full in table 5.6.

Cut	$W \rightarrow e\nu_e$	$W \rightarrow \mu\nu_\mu$
0 (data only)	passes the GRL	passes the GRL
1	Electron Trigger	Muon Trigger
2	5 or more primary vertex tracks	5 or more primary vertex tracks
3	No <i>bad</i> jets and no LAr errors	No <i>bad</i> jets and no LAr errors
4	1 trigger matched electron	1 trigger matched muon
5	1 electron	0 electrons
6	0 muons	1 muons
7	1 <i>tight</i> trigger matched tag electron	1 <i>tight</i> trigger matched tag muon
8	$E_T^{\text{miss}} \geq 20$ GeV	$E_T^{\text{miss}} \geq 20$ GeV
9	$m_T \geq 50$ GeV	$m_T \geq 50$ GeV
	<i>Fill jet weight histograms with no tau requirement</i>	
10	1 tau	1 tau
	<i>Fill jet weight histograms</i>	

Table 5.6: Cut flow selection of  $W \rightarrow e\nu$  and  $W \rightarrow \mu\nu$  events used to measure the  $jet \rightarrow \tau$  fake rate.

Figures 5.29 and 5.30 show the  $m_T$  distributions, and the  $E_T^{\text{miss}}$  distributions after both the  $E_T^{\text{miss}}$  and  $m_T$  cuts. Both confirm the high purity of  $W$  events selected, and the low contamination from QCD and  $Z$  events. A small number of MC di-boson events also pass these cuts, where real taus are selected along with the tag lepton.

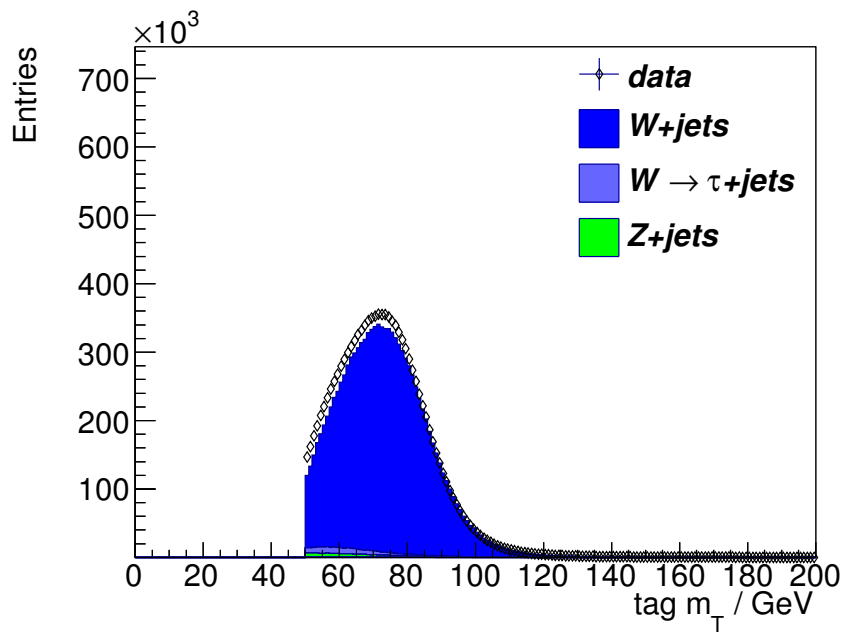
The jet distributions, before any tau selection has been applied, are well described by

the MC as shown in figures 5.31 and 5.32. However in events with a large number of jets or b-jets,  $t\bar{t}$  MC starts to dominate the distributions. These events are subtracted from data before the tau fake rate calculation.

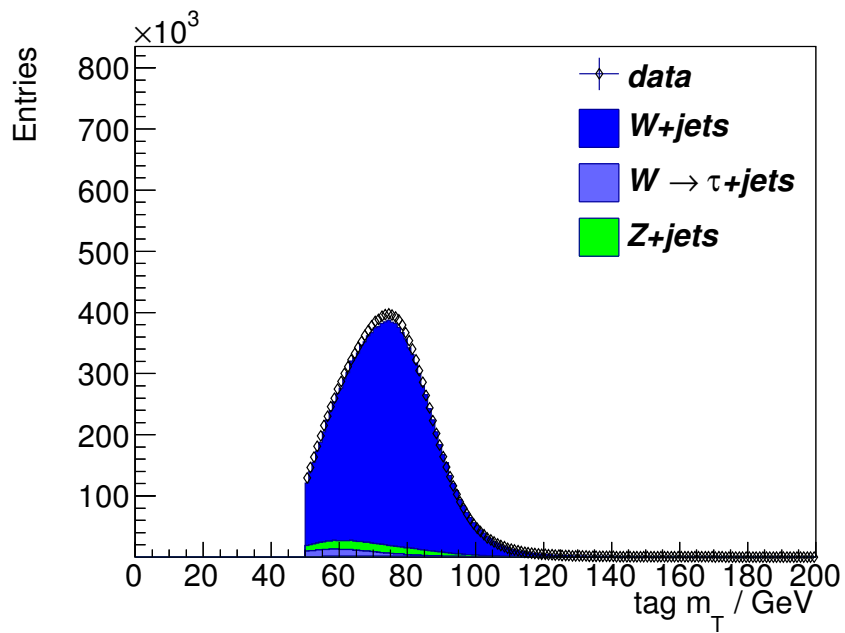
### 5.3.3 Tau fake rates measured in $W$ events

The numbers of jets before and after the hadronic tau cut are shown in figures 5.33 and 5.34. For events with a large number of jets, we see a large increase in the fraction of  $t\bar{t}$  events, especially for  $W \rightarrow \mu\nu + jets$  events. Also, by selecting events with a single lepton the sample is not independent of the  $t\bar{t}$  signal region. Because most events contain less than the 2 b-jets used in the final event selection this contamination is relatively small. In the electron channel 2.2% of the  $W$  events (with a reconstructed tau candidate) used to measure the tau fake rate have 2 b-jets. Similarly in the muon channel 2.0% have 2 b-jets. However, because the overlap exists the fake rates derived using this method are only used as a cross check to the fake rates derived in section 5.3.1 using  $Z$  events.

After subtracting di-boson contributions, which contain real hadronically decaying taus, the tau fake rates are calculated separately for each lepton trigger channel. The tau fake rates as a function of the number of jets in the event are shown in figure 5.35 separately for the electron and muon channels. The fake rate calculated by combining both channels is shown in figure 5.36.

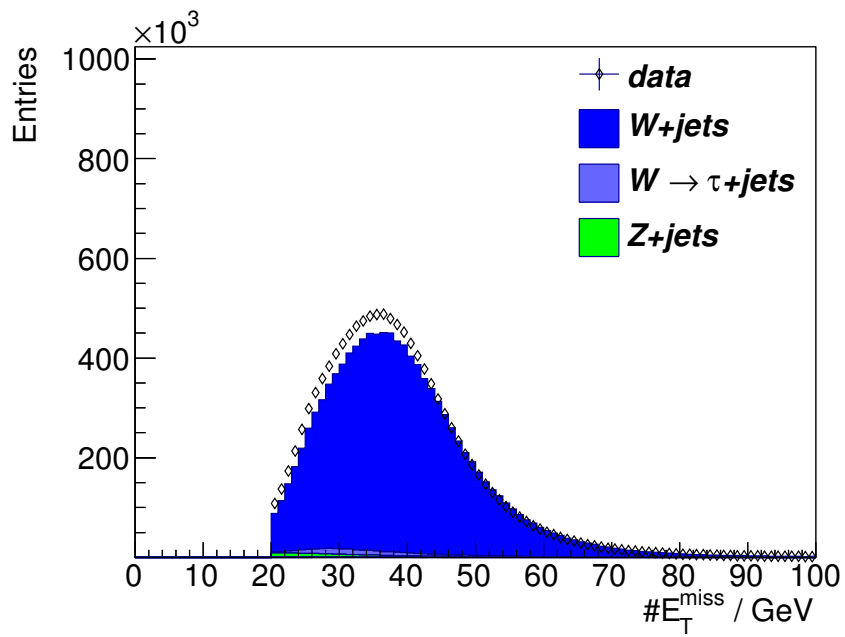


(a) electron channel

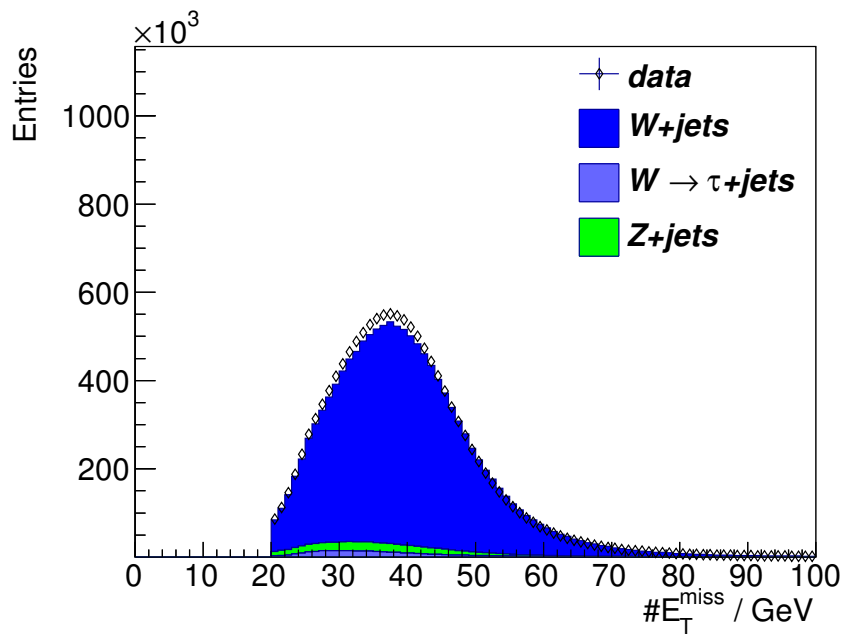


(b) muon channel

Figure 5.29: The  $m_T$  distribution in  $W \rightarrow e\nu$  (a)) and  $W \rightarrow \mu\nu$  (b)) events comparing data and MC.

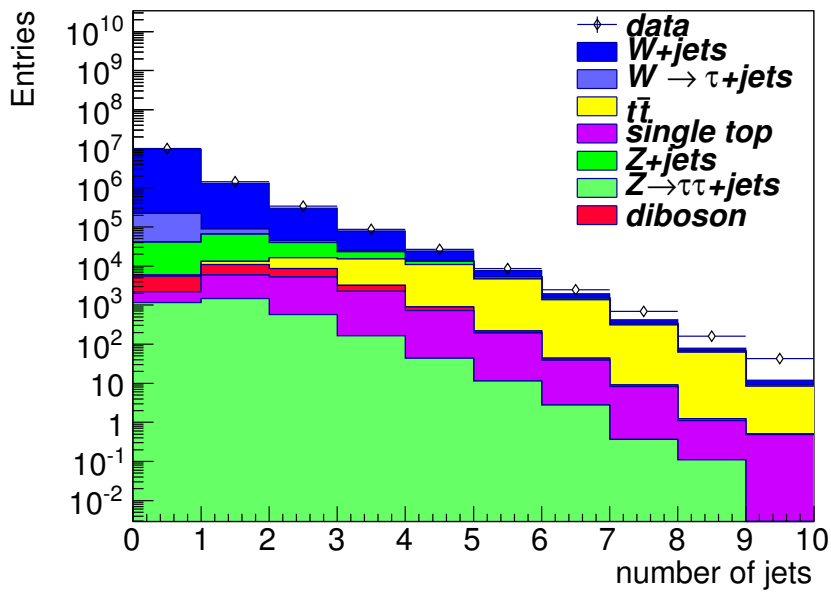


(a) electron channel

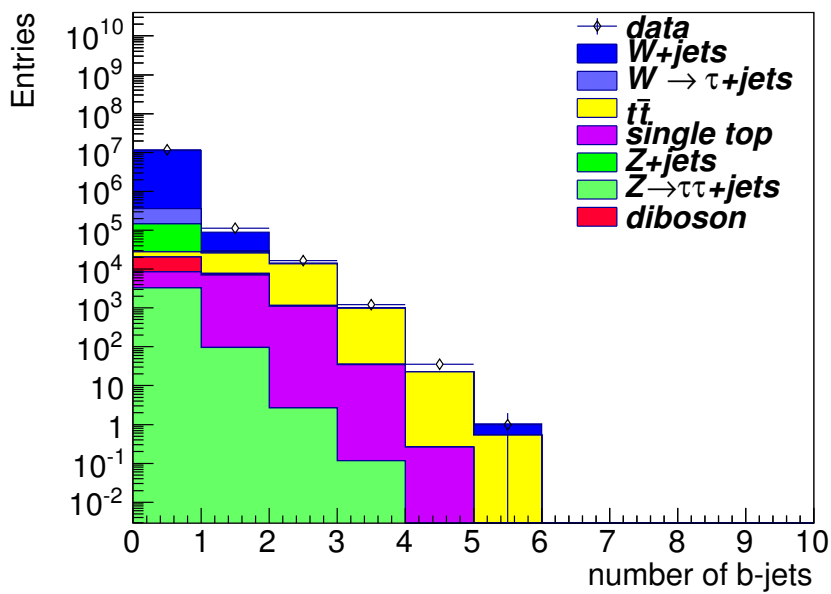


(b) muon channel

Figure 5.30: The  $E_T^{\text{miss}}$  distribution in  $W \rightarrow e\nu$  (a) and  $W \rightarrow \mu\nu$  (b) events comparing data and MC.

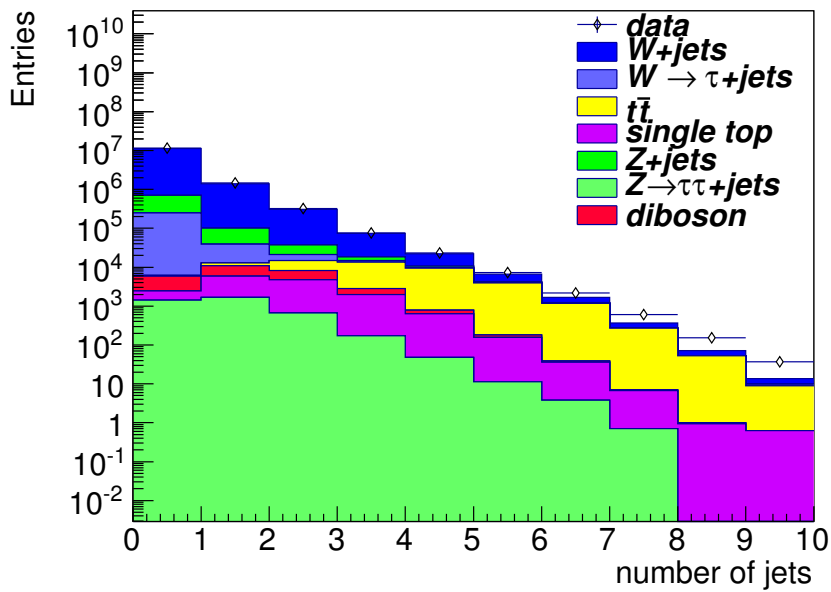


(a) electron channel

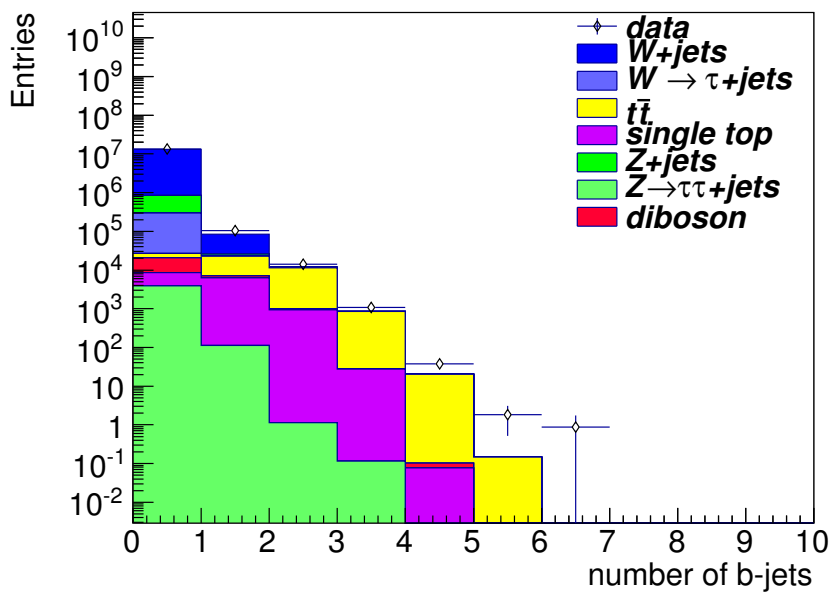


(b) electron channel

Figure 5.31: Jet and b-jet distributions in  $W \rightarrow e\nu$  events before any hadronic tau selection has been applied, comparing data and MC.

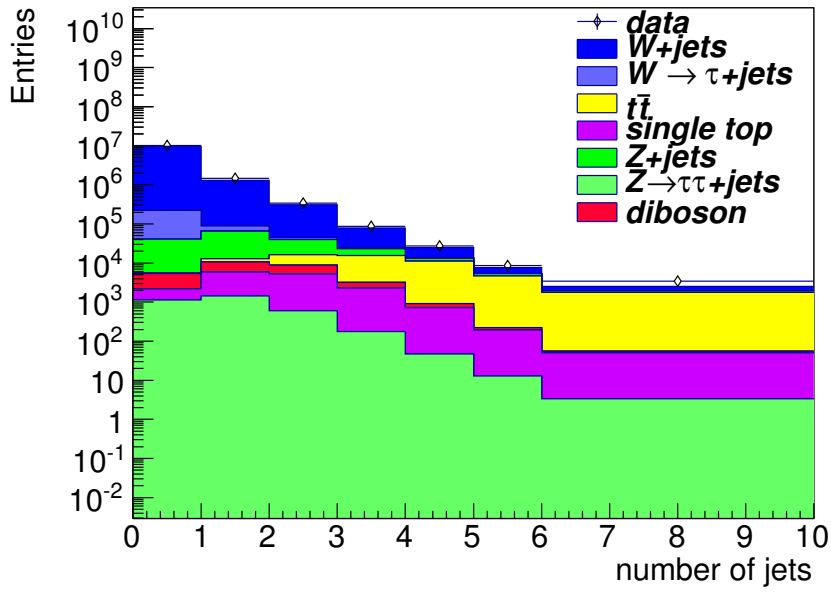


(a) muon channel

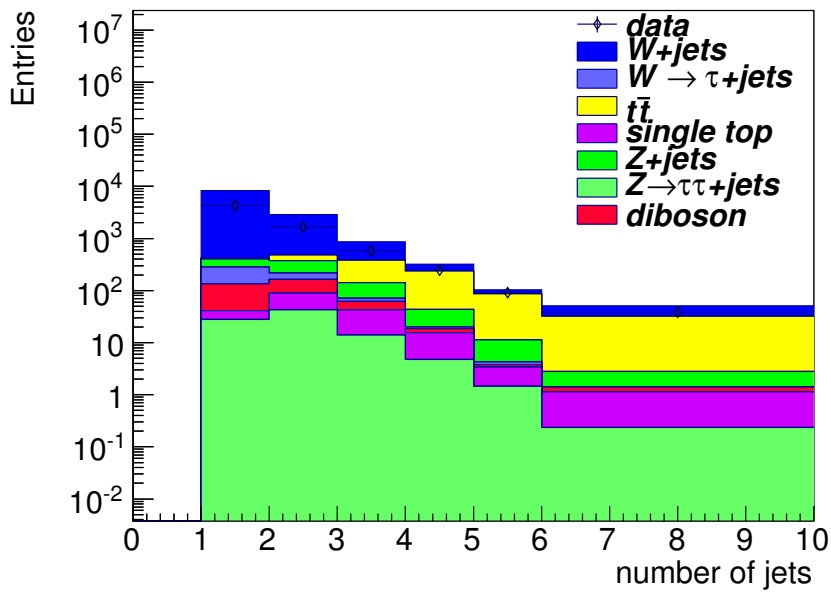


(b) muon channel

Figure 5.32: Jet and b-jet distributions in  $W \rightarrow \mu\nu$  events before any hadronic tau selection has been applied, comparing data and MC.

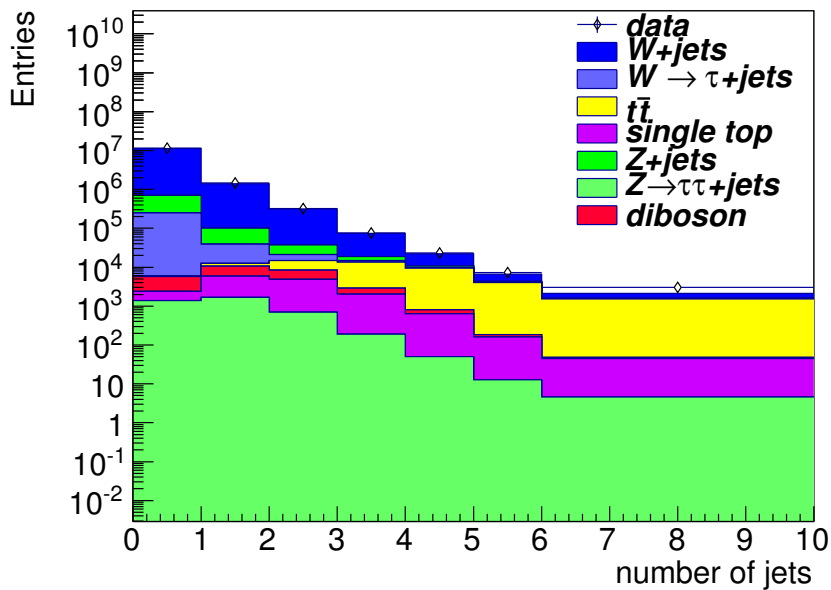


(a)  $W \rightarrow e\nu$  events with no  $\tau$  requirement

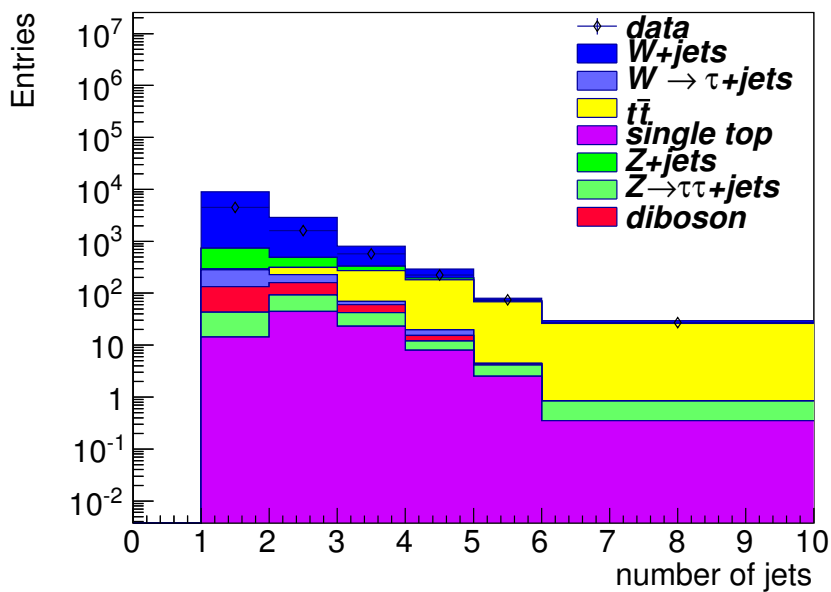


(b)  $W \rightarrow e\nu$  events with one  $\tau$

Figure 5.33: Total number of jets before (a) and after (b) a cut on the number of hadronic taus in  $W \rightarrow e + \text{jets}$  events comparing data and MC.

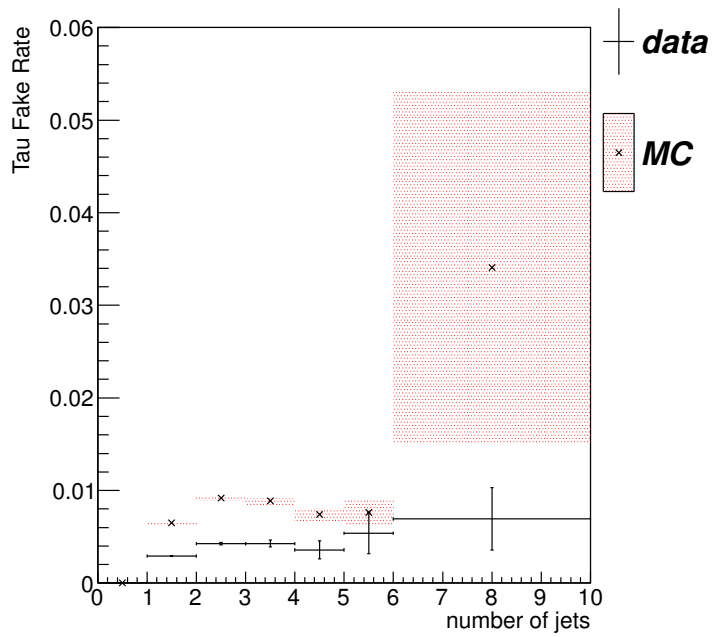


(a)  $W \rightarrow \mu\nu$  events with no  $\tau$  requirement

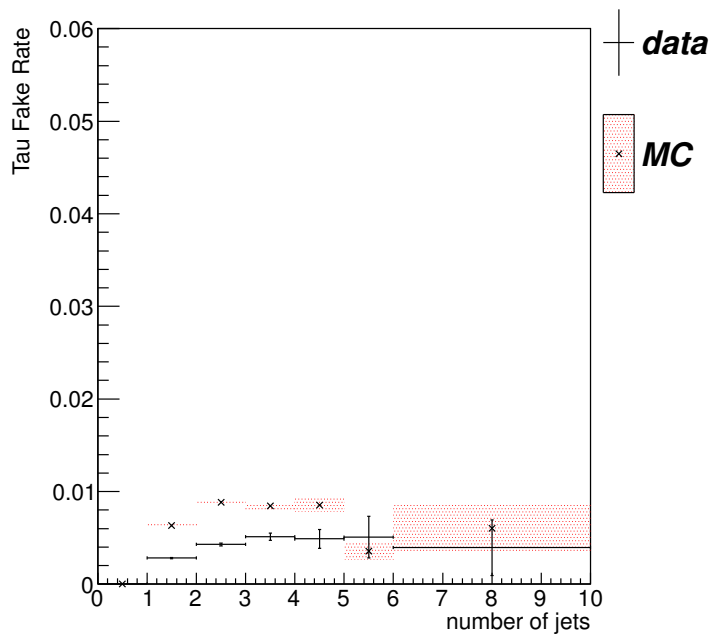


(b)  $W \rightarrow \mu\nu$  events with one  $\tau$

Figure 5.34: Total number of jets before (a) and after (b) a cut on the number of hadronic taus in  $W \rightarrow \mu + \text{jets}$  events comparing data and MC.



(a) electron channel



(b) muon channel

Figure 5.35: Tau fake rate as a function of number of jets in the event for electron channel (a) and muon channel (b) events comparing data and MC.

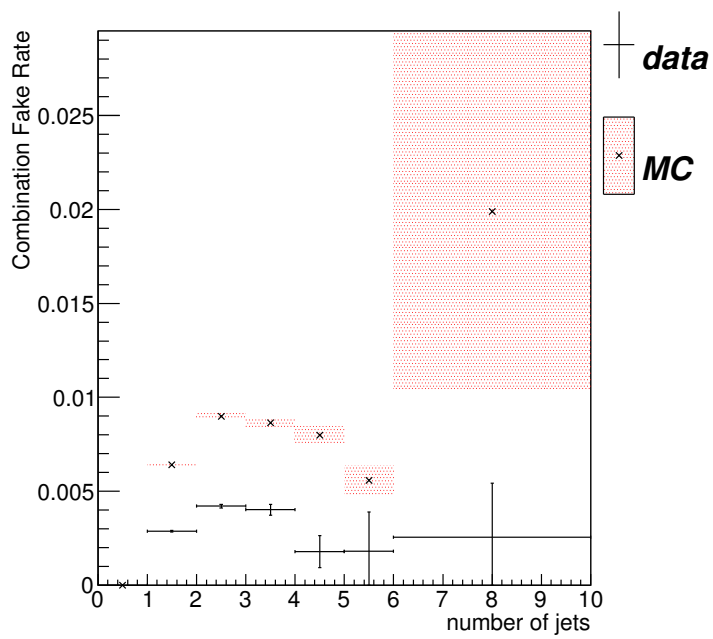


Figure 5.36: Tau fake rate as a function of number of jets in the event with the electron and muon channels combined comparing data and MC.

### 5.3.4 Tau fake rates comparison

Figure 5.37 shows the fake rates measured in  $Z$  and  $W$  events, where the fake rates measured in the electron and muon trigger channels have been combined (no charge separation is used here for the purposes of comparison). The measured fake rates are consistent within the statistical uncertainties in each bin, although a clear systematic shift towards lower tau fake rates can be seen in  $W$  events. By calculating the contribution of the tau fakes in the signal region, and by shifting the fake rates by the upper and lower limits of their statistical error, such a systematic difference is accounted for. Due to the large irreducible background from  $t\bar{t}$  events in the  $W$  sample, as seen in section 5.3.3, this fake rate is used only for this cross check.

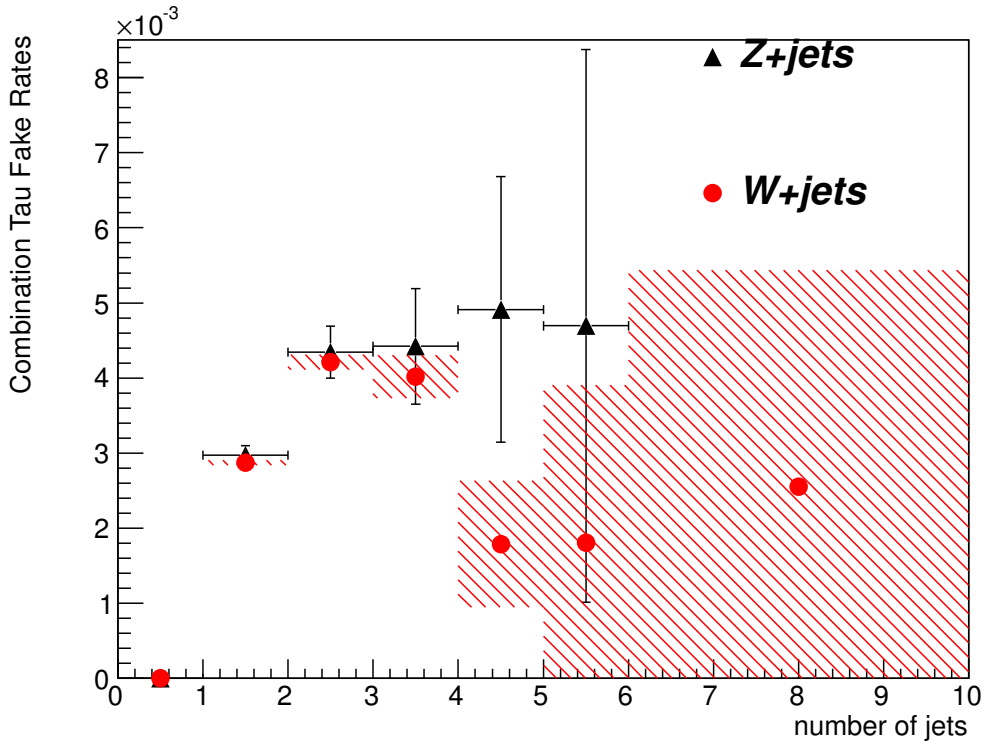


Figure 5.37: Tau fake rates measured using  $Z$  and  $W$  tagged events respectively. For each the electron and muon trigger channels have been combined for both samples.

The tau fake contributions to the signal region and to orthogonal regions are estimated using the fake rates shown in figure 5.28, treating the events with a positively

and negatively charged taus separately due to an approximate  $\sim 15\%$  difference in the tau fake rates.

## 5.4 Lepton and Tau Fake Yields in the Lepton Plus Tau Control Region

Using the  $t\bar{t}$  lepton plus jets selection outlined at the beginning of section 4.4 as a basis, a low  $E_T^{\text{miss}}$  region ( $E_T^{\text{miss}} \leq 40$  GeV) with no b-tag requirements is defined and used to validate the method of estimating the fake yields. The tau fake rate needs to be validated by ensuring that the predicted backgrounds, including the electron and muon fake rates, and signal match the data in this control region.

In section 5.1 the electron and muon fake rates are measured and a control region is used to validate the lepton fake rates in this  $t\bar{t}$  di-lepton control region. The same method is applied to the lepton plus tau control region. While validating both methods simultaneously is not ideal, the lepton fake rate yield is much lower than that from the tau fakes.

In section 5.3 the tau fake rate is measured as a function of the number of reconstructed jets, and equation 5.8 can be used to estimate the total number of fake taus in the signal region.

In order to estimate the yield of fake taus in  $t\bar{t}$  events, the tau fake rates are used with equation 5.9. The event selection outlined in section 5.3 requires that there are no reconstructed taus with an opposite sign to the trigger lepton, and that directly produced taus that have not been reconstructed are removed using MC. The numbers of positive and negative fake taus expected in the signal region for  $i$ -jets ( $N_{i\text{-jets}}^{\tau\text{fake}\pm}$ ) are calculated using:

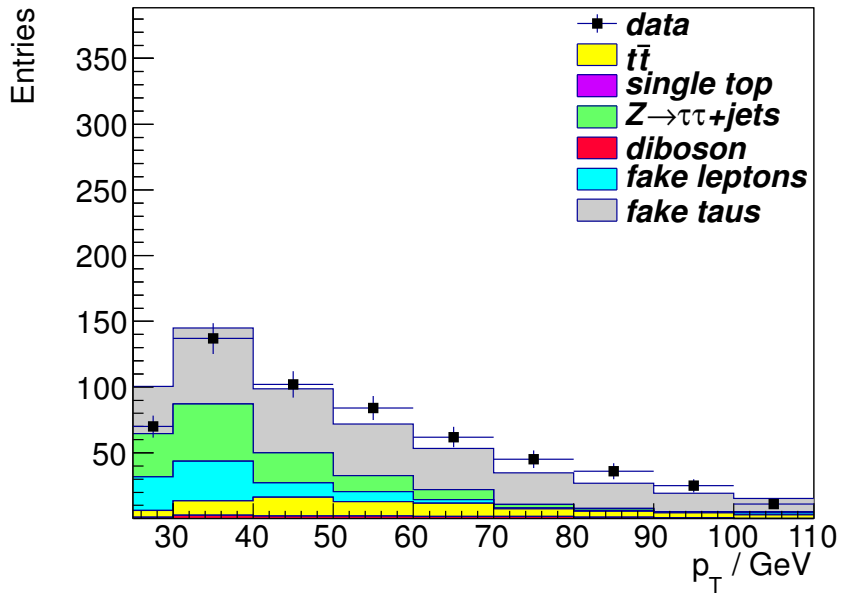
$$N_{i\text{-jets}}^{\tau\text{fake}\pm} = \frac{\epsilon_{i\text{-jets}}^{\tau\text{fake}\pm}}{1 - \epsilon_{i\text{-jets}}^{\tau\text{fake}\pm}} (N_{no\tau, i+1\text{-jets}}^{\text{data}} - N_{no\tau, i+1\text{-jets}}^{\text{MC real}\tau}). \quad (5.10)$$

where  $\epsilon_{i-jets}^{\tau^{\pm} fake}$  is the rate of events with  $i$ -jets to have a fake positive/negative tau. The number of events without a reconstructed tau and  $i + 1$ -jets in data is  $N_{no\tau, i+1-jets}^{data}$ , and  $N_{no\tau, i+1-jets}^{MC real\tau}$  in MC with real taus respectively.

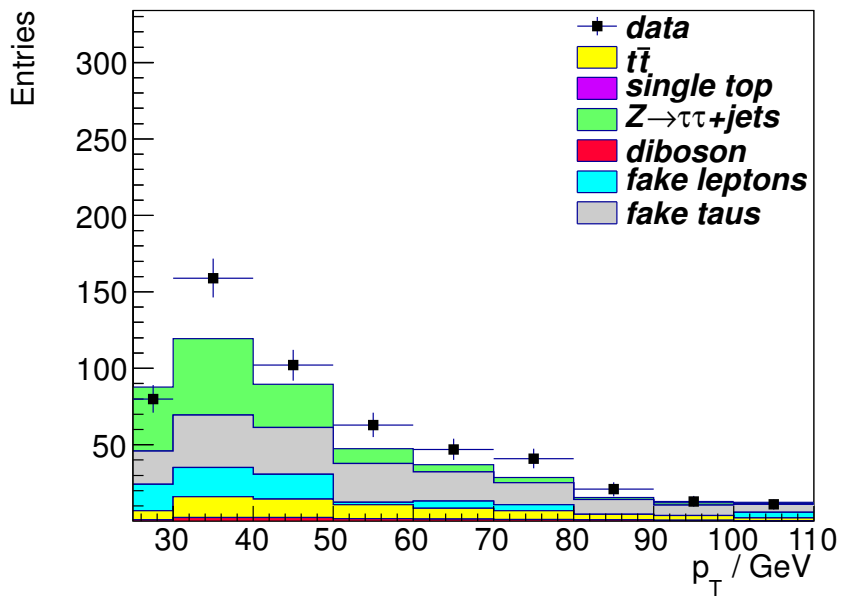
By weighting each event passing the cuts using equation 5.10, other event observables are preserved, with the exception of the tau kinematic properties. Backgrounds with a single lepton and three or more jets, such as leptonically decaying  $W + jets$  events, semi-leptonic  $t\bar{t}$  events, and s-channel and t-channel single top production contribute to this tau fake background, so this estimate replaces these MC background estimates.

The trigger lepton  $p_T$  distributions in the  $t\bar{t}$  control region are shown in figures 5.38. In these figures a systematic deficit is seen in the yields when the data driven tau fake rates are included, especially in the muon channel. Due to the large statistical errors in measuring the tau fake rates, there is a large systematic uncertainty on the tau fake rate, as calculated in section 6.4.1, which covers this discrepancy.

Figure 5.38 includes the estimated electron and muon fake rate, which produces a higher number of lepton fakes at low  $p_T$ , as expected for leptons produced in jet decay products. Note that, due to the way the lepton fake rate is calculated as described in section 5.1, when it is binned the statistics are lowered and the lepton fake rate can fluctuate below zero: where this is the case, the fake rate has been set to zero in that histogram bin for illustration purposes.



(a) electron  $p_T$



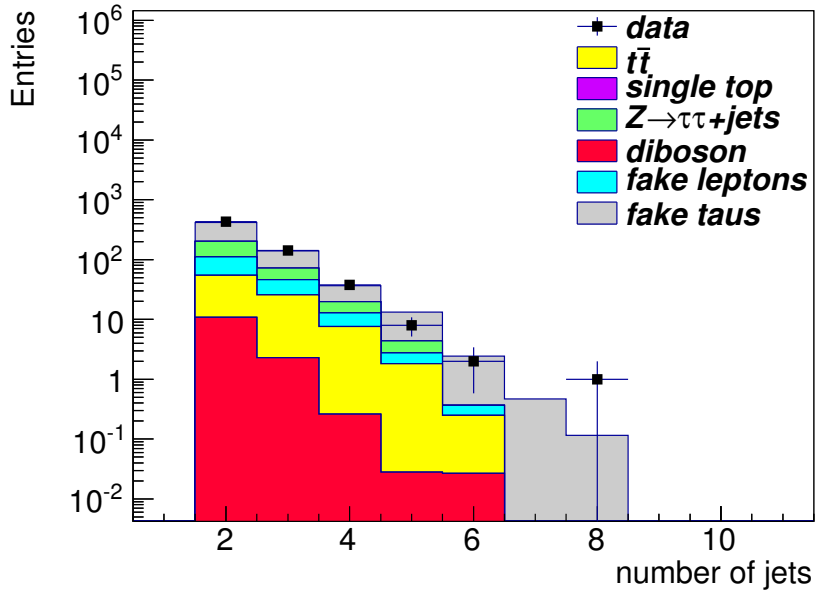
(b) muon  $p_T$

Figure 5.38: Lead lepton  $p_T$  for the electron channel (a) and muon channel (b) in the lepton plus tau control region, comparing data and the predicted background distributions.

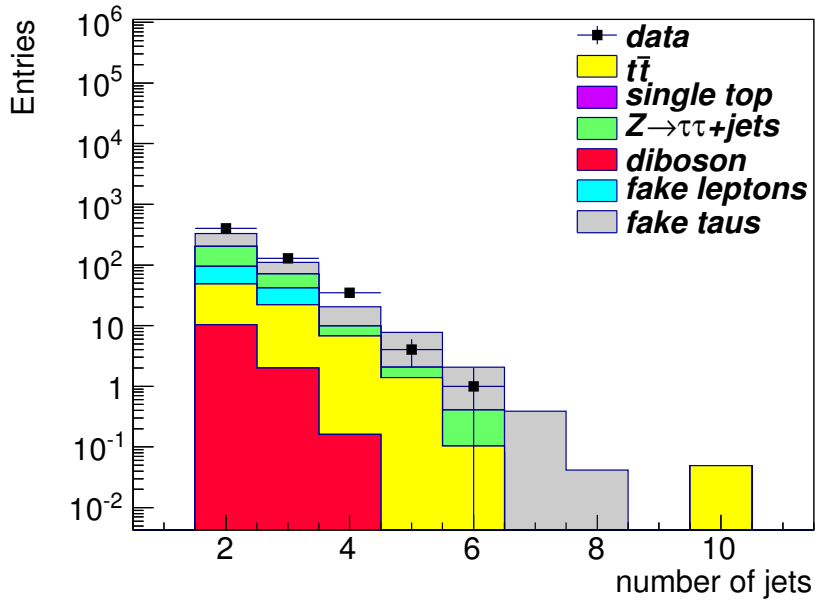
Figures 5.39 and 5.40 show the numbers of jets and b-jets in the lepton plus tau control region. There is good agreement in the electron channel for different numbers of jets and b-jets in the event.

In the muon there is a significant systematic deficit in the predict yield in the first three bins, though the distribution shapes are consistent in bins with high statistics. This deficit is around two standard deviations from data, when only considering the statistical uncertainty on data. Because  $t\bar{t}$  events have a large number of jets and b-jets, the ability of the tau fake rate estimate to describe these distributions gives some confidence in the method (at least in the electron channel), before any systematic uncertainty on the tau fake rate has been included.

Figure 5.41 shows the  $p_T$  distribution of the lead jet, in the lepton plus tau control region, and reproduces these distribution shapes, with the exception of the  $30 \text{ GeV} < p_T < 40 \text{ GeV}$  bin where the yield is significantly underestimated.

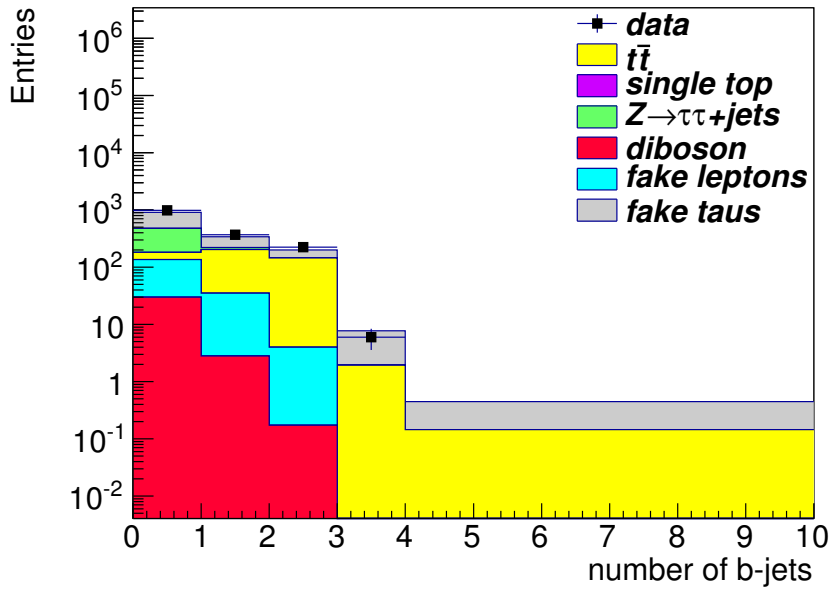


(a)  $e\tau$  channel

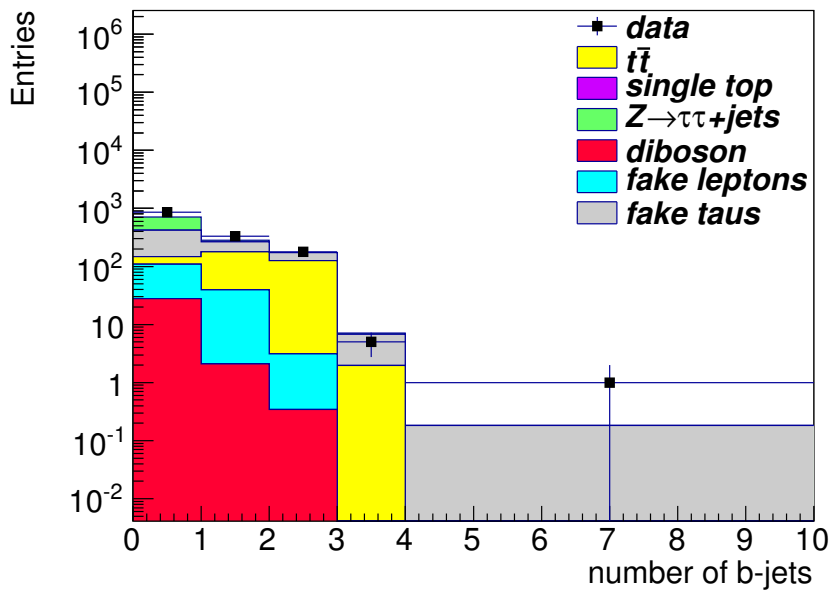


(b)  $\mu\tau$  channel

Figure 5.39: The number of jets in the electron and muon trigger channels in the lepton plus tau control region, comparing data and the predicted signal plus background distributions.



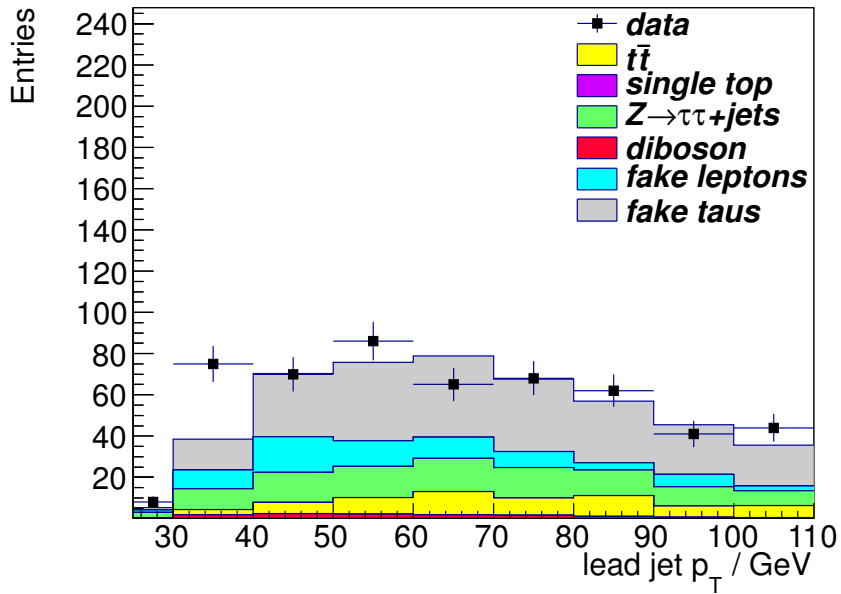
(a)  $e\tau$  channel



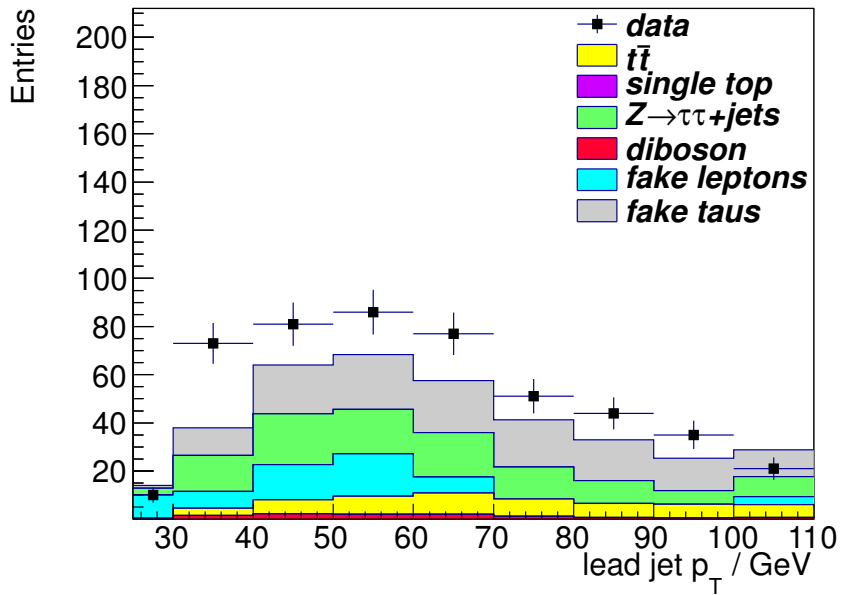
(b)  $\mu\tau$  channel

Figure 5.40: Number of b-jets in the electron and muon trigger channels in the lepton plus tau control region, comparing data and the predicted signal plus background distributions.

The contribution of the tau fakes is re-estimated by varying the tau fake rate measurements to their upper and lower statistical uncertainties. The  $\Sigma p_T$  and  $E_T^{\text{miss}}$  distributions are shown in figures 5.42 and 5.43 respectively and include estimates for the lepton and tau fake rates, with bands indicating the systematic shifts on the tau fake rates. Note this includes only the systematic shift in the tau fake rates, and not other systematic uncertainties, or statistical errors. The  $\mu\tau$  channel underestimates the predicted yield before other systematic uncertainties are included.

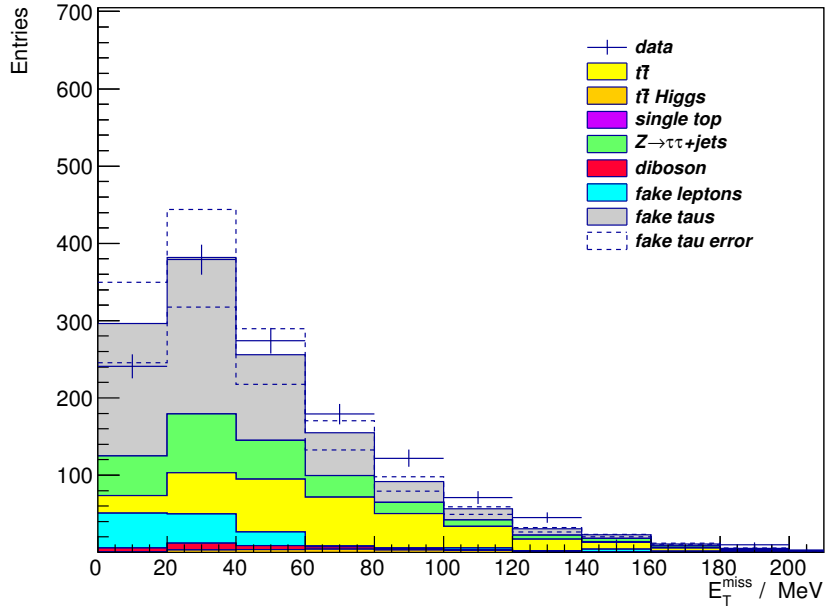


(a)  $e\tau$  channel

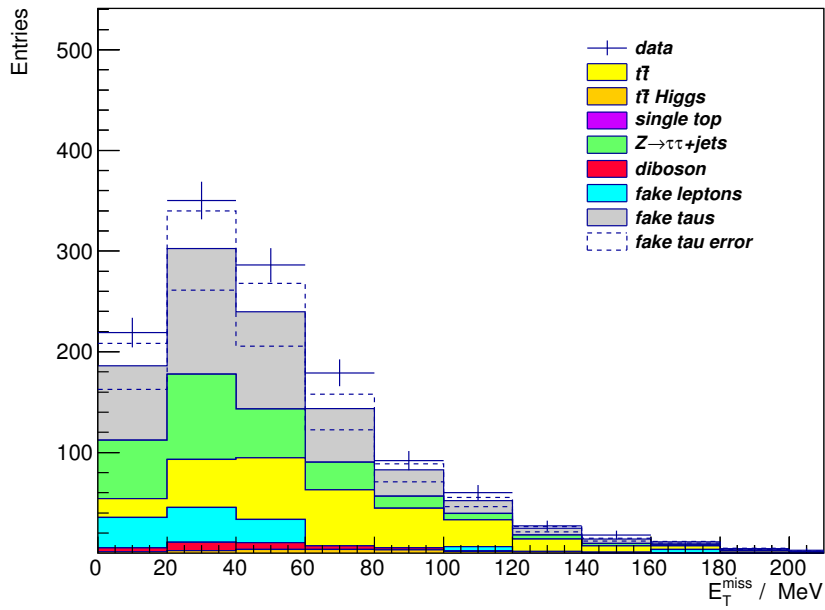


(b)  $\mu\tau$  channel

Figure 5.41: The lead jet  $p_T$  distributions for the electron and muon trigger channels in the lepton plus tau control region, comparing data and the predicted signal plus background distributions.

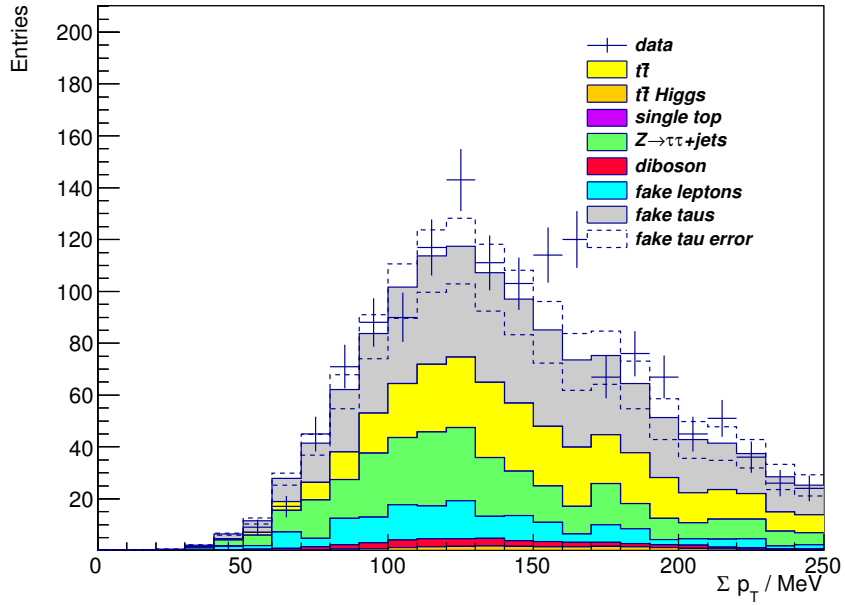


(a)  $e\tau$  channel

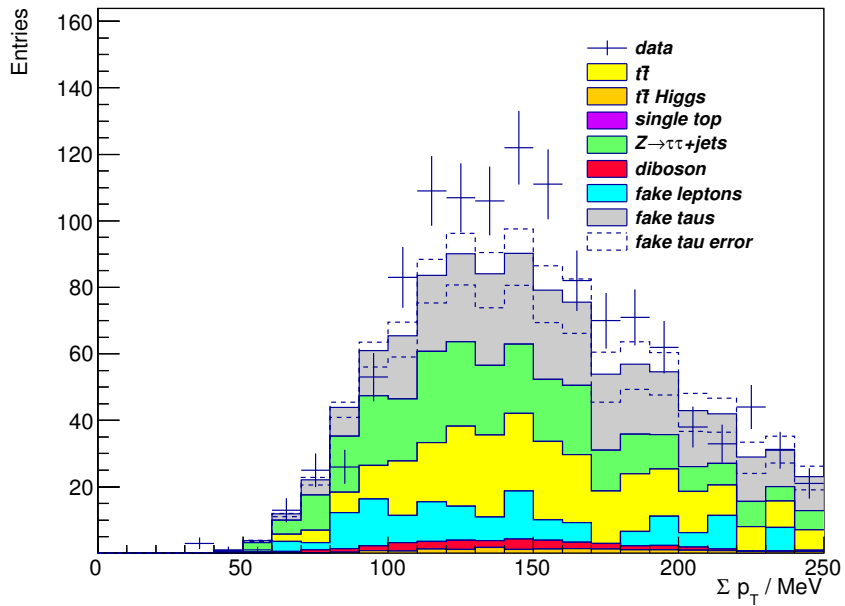


(b)  $\mu\tau$  channel

Figure 5.42: The  $E_T^{\text{miss}}$  distributions for the electron and muon trigger channels before any  $E_T^{\text{miss}}$  cut. A band indicates the effect of a systematic shift in the tau fake rate, but does not include other systematic errors.



(a)  $e\tau$  channel



(b)  $\mu\tau$  channel

Figure 5.43: The  $\Sigma p_T$  distributions for the electron and muon trigger channels before any  $E_T^{\text{miss}}$  cut. A band indicates the effect of a systematic shift in the tau fake rate, but does not include other systematic errors.

The yields from data and the predicted yields for signal and backgrounds for each  $t\bar{t}$  channel in the control region are shown in table 5.7. For the electron triggered channels agreement is within the statistical errors. The  $t\bar{t} \rightarrow \mu\tau$  channel has a predicted yield much lower than observed in data, but this does not include systematic uncertainties, including those on the lepton and tau fake backgrounds. The agreement in the electron channels gives confidence in the data driven methods of measuring the lepton and tau fake rates.

	$e\mu$	$\mu e$	$e\tau$	$\mu\tau$
$Z \rightarrow \tau\tau$	41.7	32.8	127	143
Di-boson	17.6	14.2	13.5	12.6
Lepton Fakes	62.1	47.2	82.7	64.3
Tau Fakes	0	0	310	183
Total Background	121	94.3	533	403
signal $t\bar{t}$	679	533	76.3	66.4
Signal + Background	800	628	609	469
Data	805	636	620	569

Table 5.7: Data yields and predicted signal and background yields for each  $t\bar{t}$  channel measured in a low  $E_T^{\text{miss}}$  region with no b-tag requirements.

## 5.5 Future Strategies for Measuring Fake Rates

The systematic deficit seen in section 5.4 in the estimate of the fake yields in the muon channel control region warrants further investigation if the muon triggered channels are to be integrated into the final result in possible future studies. With the increase in statistics in the 2012 data sample it may be possible to segment the fake rate measurements into b-jet bins and use the jet kinematics.

The large systematic uncertainties on the tau fake rate, which are estimated in section 6.4, warrant investigating alternative methods of estimating the tau fake rate which may have lower systematic uncertainties. In a study of the  $t\bar{t}$  lepton plus tau cross section performed by ATLAS using  $2.05\text{fb}^{-1}$  of data [123] an alternative method of estimating the tau fake rate was used. In calculating the cross sections,

similar cuts were used to those outlined in section 4.4 with a few notable differences. These included using events with 1 or more b-tagged jets. Importantly, the distributions used were of oppositely signed (OS) leptons with the same sign (SS) lepton distributions subtracted, (referred to as an OS-SS distribution). This utilises the observation that the gluon contribution to the tau fake rate will be symmetric in both of these event types. Additionally, the contribution from QCD events will also be symmetric. It is expected that  $b$  and  $\bar{b}$  quarks in top events will fake taus equally, and the production rate of single  $b$  quarks in proton-proton collisions is very low. Subtracting same sign event distributions from opposite sign distributions leaves only light quark distributions that significantly contribute to the tau fake rate. Fitting templates for real taus, and fake taus from light quarks, the fake rate for the OS-SS distribution was estimated. The uncertainty on the fake contribution using this method was estimated to be  $\sim 30\%$  from QCD processes (before these were subtracted), and the uncertainty on the light quark contribution was of order  $\sim 5\%$  when summing the contributions from one and three prong taus in quadrature [123]. Using a similar definition for the fake rates as used in section 5.3, in a sample of  $t\bar{t}$  events populated by real taus and fake taus from light quarks, a matrix method was also used as a cross-check in [123], which was in agreement with the background estimate using the template method.

## 5.6 Summary of the Fake Rate Measurements

In section 5.1.2 the real electron and muon efficiencies were measured using  $Z$  tag and probe events as a function of different event observables. The measured efficiencies were found to be compatible with similar efficiency measurements performed in ATLAS [22, 146]. In section 5.1.3 events with a single lepton were selected, cutting out  $W$  events to exclude leptons produced directly from a hard interaction by selecting a low  $m_T$  and low  $E_T^{\text{miss}}$  region. The lepton fake rates were measured in a QCD enriched region as a function of many of the same observables as the lepton efficiencies, also including a dependence on the  $\Delta R$  to the nearest jet in the event to take account

of fake leptons produced in hadronic decay products of hadronic jets.

Using the matrix method described in section 5.1.1, the number of fake leptons was estimated in a region orthogonal to the signal region, with  $E_T^{\text{miss}} \leq 40$  GeV and no b-tag requirements, and found to be compatible with the distributions observed in data in  $e\mu$  and  $\mu e$  events. The lepton fake rates for  $e\tau$  and  $\mu\tau$  events are shown in section 5.4, and also include the estimate for the number of tau fakes.

The yields in the control region, and the predicted contributions from signal and backgrounds, show good agreement in the  $e\mu$ ,  $\mu e$  and  $e\tau$  channels. In the  $\mu\tau$  channel, before considering systematic effects, there is a deficit in the predicted signal plus background yield, though the re-production of the distribution shapes gives confidence that the methods are reasonable.

In section 5.3 a method for estimating the tau fake rate as a function of the number of hadronic objects in the event was outlined. Two independent samples of  $W$  and  $Z$  events were used to probe the  $jet \rightarrow \tau$  fake rate; the two methods yielded comparable fake rates despite different topologies. The tau fake rate estimated using  $W$  events was only used as a cross-check (due to the high proportion of  $t\bar{t}$  events with a higher number of jets). A small systematic difference was observed that was the same order as the statistical uncertainties on the measured fake rates, see section 5.3.4. The  $jet \rightarrow \tau$  fake rate was measured in section 5.3.1 as function of the number of jets in the event separately for events where a jet is reconstructed as a positively or negatively charged tau, combining events from  $Z \rightarrow ee$  and  $Z \rightarrow \mu\mu$  to decrease statistical errors for large numbers of jets.

Using these fake rates, equation 5.10 was used to estimate the number of tau fakes in a region orthogonal to the signal region in  $e\tau$  and  $\mu\tau$  events, with  $E_T^{\text{miss}} \leq 40$  GeV and no b-tag requirements.

The estimate for the number of signal and background events, including the tau fake rate, matched that of data in  $e\tau$  events and re-produced the shapes for several observables used in selecting the  $t\bar{t}$  events in the signal region. Including an error

band representing a systematic increase and decrease of the tau fake rate within its measured statistical errors it can be seen that the signal and backgrounds for  $e\tau$  events describe the data well. The  $\mu\tau$  distribution shapes of the expected signal  $t\bar{t}$  events and background are also well re-produced but the overall yield is lower than in the data. However some important systematic uncertainties, which are discussed in the final chapter, were not included. Possible improvements to the fake rate estimates were briefly discussed in section 5.5.

# Chapter 6

## Top Candidates, Cross sections and Their Ratios

The  $t\bar{t}$  event selection is outlined in chapter 4, in section 6.2 the signal  $t\bar{t}$  and background estimates are validated using a control region, and the candidate  $t\bar{t}$  events and their yields are presented in the signal region in section 6.2.

The efficiency measurement, cross sections and cross section ratios are presented in section 6.3, and their systematic uncertainties are explained and presented in section 6.4. The results from the muon triggered channels are used as a cross-check of the measurements in the electron channel, as they are not statistically independent.

The cross sections are presented only to validate the  $t\bar{t}$  selection and fake rate estimates (and should not be used elsewhere), as some systematic uncertainties, notably those from uncertainties in the PDFs used to generate the  $t\bar{t}$  MC samples, have not been included as they do not affect the cross section ratio. Extensions to the analysis are discussed in section 6.6 and the results are summarised in section 6.7.

## 6.1 Control Region for $t\bar{t}$ Events

A control region, first used in sections 6.4.1 and 5.4, was defined using the same cuts in tables 4.1 4.2 but without any b-tag requirements and reversing the  $E_T^{\text{miss}}$  cut. The selection of events in this control region is presented in section 6.1.1, and the events selected and their yields are presented in sections 6.1.2 and 6.1.3 respectively. Systematic uncertainties are not included at this point and are only calculated in the signal region.

### 6.1.1 Control Region Event Selection

Figure 6.1 shows the b-jet multiplicity distributions for  $t\bar{t}$  events selected without any b-jet requirements, and before any  $E_T^{\text{miss}}$  and  $\Sigma p_T$  cuts. The signal plus background estimates, including the lepton and tau fake rates, match the expected b-tagged jet content of the events well, despite the tau fake rate having no explicit dependence on quark flavour.

Figure 6.2 shows the  $\Sigma p_T$  distribution before any  $E_T^{\text{miss}}$  cut, at the same point in the cut flow as figure 6.1. There is good agreement between distribution shapes in data and the predicted signal plus backgrounds in all channels, except for a discrepancy in the  $\mu\tau$  channel. In the  $\Sigma p_T$  distribution in the range 100–160 GeV the predicted signal and background yield is significantly below that observed in data (when only considering statistical uncertainties).

Figure 6.3 shows the  $E_T^{\text{miss}}$  distribution with  $\Sigma p_T > 100$  GeV with good agreement in the distribution shapes. In the muon plus hadronic tau channel there is a systematic difference in the predicted yield from signal and background (which was accentuated with the  $\Sigma p_T$  cut described above). In section 5.4 the systematic uncertainty from the tau fake rate estimate in the control region was calculated and was shown to largely cover this systematic difference.

Note that, due to the way the lepton fake rate is calculated as described in section 5, when it is binned the statistics are lowered and the lepton fake rate can fluctuate below zero: where this is the case, the fake rate has been set to zero in that histogram bin for illustration purposes.

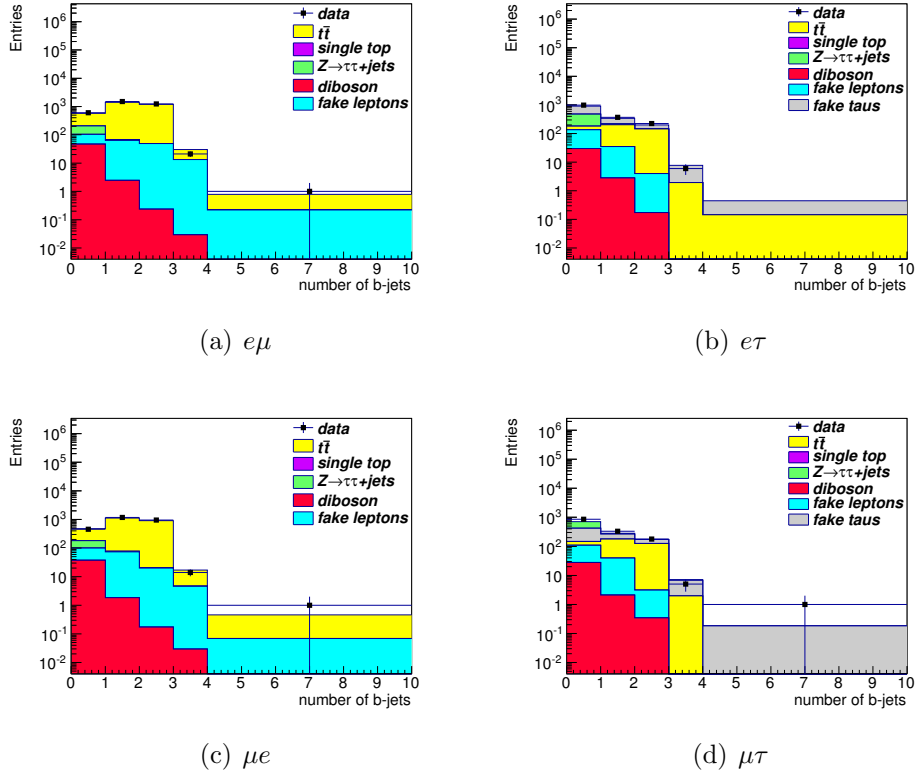
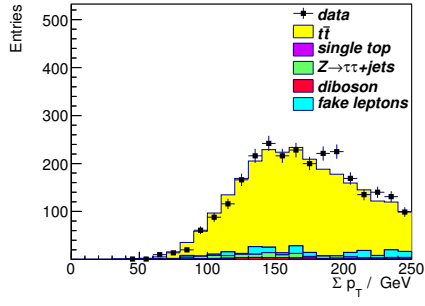
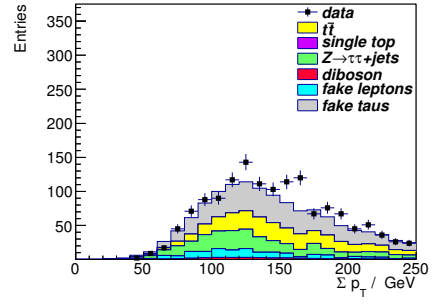


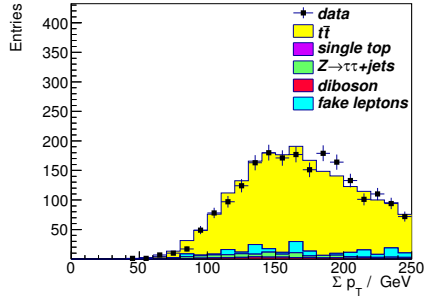
Figure 6.1: Number of b-jets in the control region for the electron triggered channels ( $e\mu$  (a),  $e\tau$  (b)) and the muon triggered channels ( $\mu e$  (c),  $\mu\tau$  (d)) before any cut on  $\Sigma p_T$  or  $E_T^{\text{miss}}$ . The di-lepton channel figures (a) and (b) were previously seen in figure 5.17, and the lepton plus channel figures (c) and (d) are repeated from 5.40. They depicted again for comparison purposes.



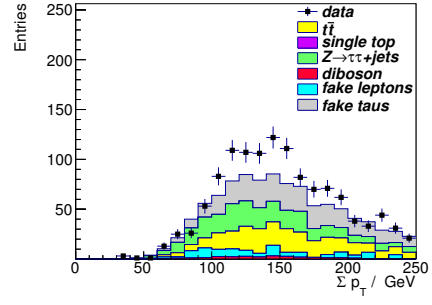
(a)  $e\mu$



(b)  $e\tau$

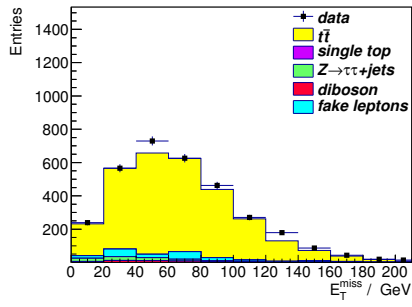


(c)  $\mu e$

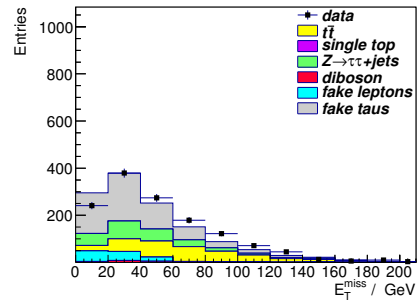


(d)  $\mu\tau$

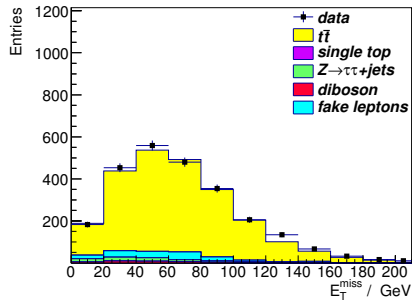
Figure 6.2: The  $\Sigma p_T$  of all tracks in the control region for the electron triggered channels ( $e\mu$  a),  $e\tau$  b)) and the muon triggered channels ( $\mu e$  c),  $\mu\tau$  d) before any cut on  $\Sigma p_T$  or  $E_T^{\text{miss}}$ . The lepton plus channel figures (c) and (d) are repeated from 5.43. They depicted again for comparison purposes.



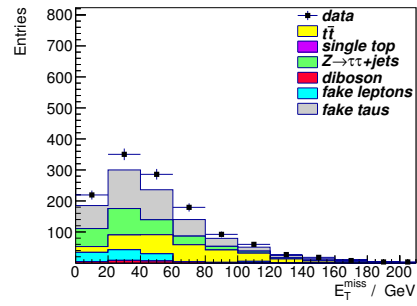
(a)  $e\mu$



(b)  $e\tau$



(c)  $\mu e$



(d)  $\mu\tau$

Figure 6.3: The  $E_T^{\text{miss}}$  distributions in the control region for the electron triggered channels ( $e\mu$  a),  $e\tau$  b)) and the muon triggered channels ( $\mu e$  c),  $\mu\tau$  d) after the  $\Sigma p_T$  cut. The lepton plus channel figures (c) and (d) are repeated from 5.42. They depicted again for comparison purposes.

## 6.1.2 Selected Event in a $t\bar{t}$ Control Region

The control region is orthogonal to the signal region (see the cut flow tables 4.1 and 4.2), with the  $E_T^{\text{miss}}$  cut reversed and without any b-jet requirements. Using these selected events, figure 6.4 shows the lepton  $p_T$  distributions and figure 6.5 shows the number of selected jets. The electron triggered channels show good agreement between data and the predicted signal and backgrounds, before any systematic uncertainty on the tau fake background has been included. In the muon triggered channels there is some agreement between data and the signal plus background distribution shapes in the muon channels but the difference between the yields is significant. Before considering the systematic uncertainty, the yields differ by greater than two standard deviations.

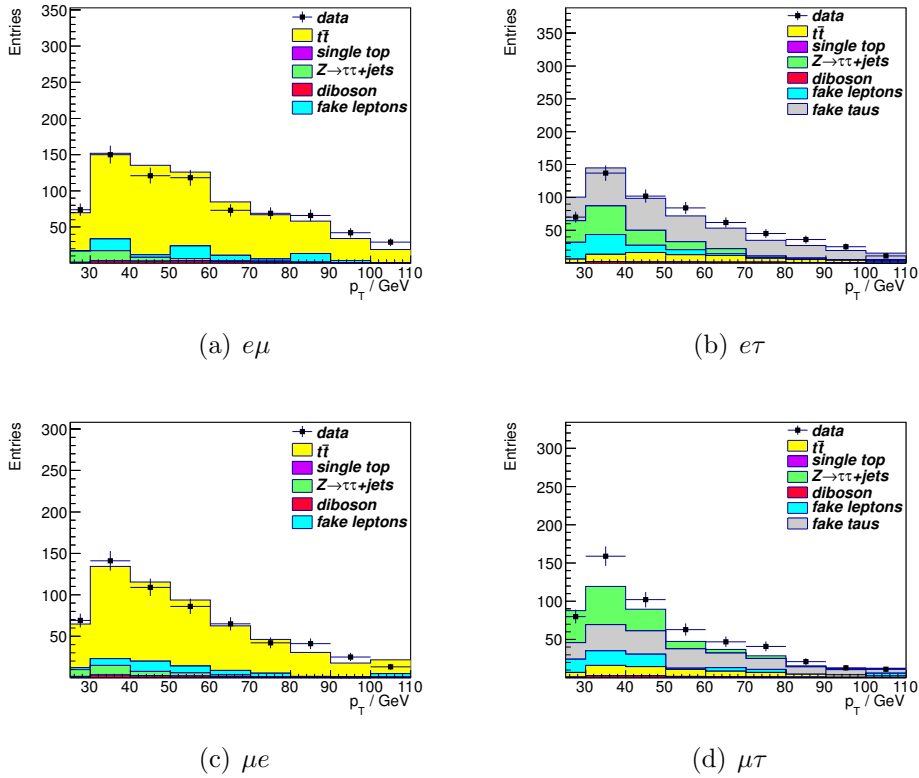


Figure 6.4: The  $p_T$  of the triggered electron (a)) and muon (b)) in the low  $E_T^{\text{miss}}$  region with no b-jet requirements.

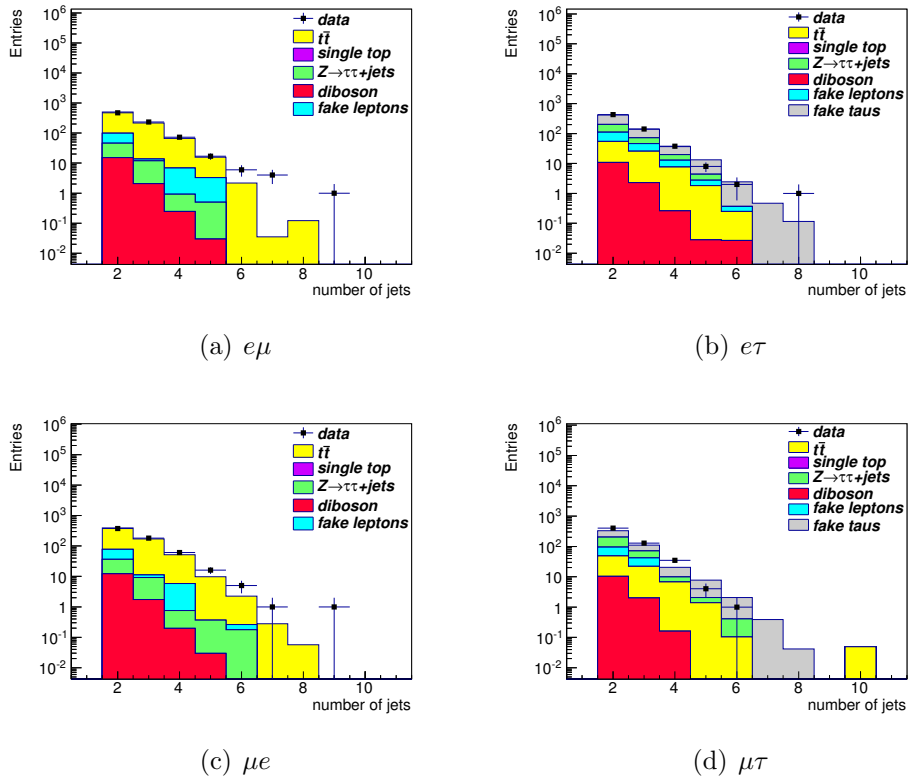
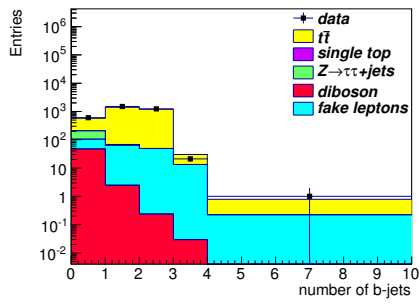
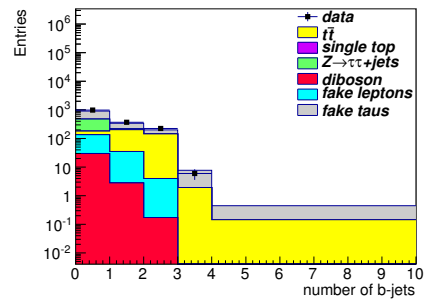


Figure 6.5: The number of jets in the events for electron (a)) and muon (b)) triggered events in the low  $E_T^{\text{miss}}$  region with no b-jet requirements.

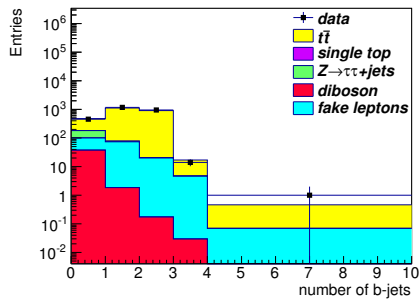
Figure 6.6 shows the b-jet multiplicity distribution in the control region. While the signal region only includes events with two b-jets, it is necessary to show that the fake rate estimates and the MC backgrounds account for any dependence on the numbers of reconstructed b-jets in an event. There is good agreement in all the  $t\bar{t}$  channels, the systematic excess can be accounted for by the difference already observed in data in the  $\mu\tau$  channel.



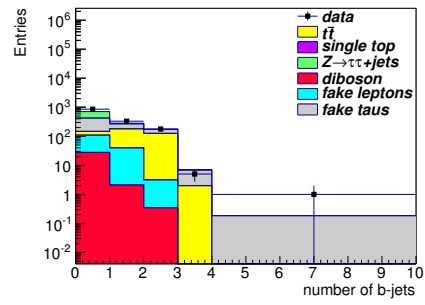
(a)  $e\mu$



(b)  $e\tau$



(c)  $\mu e$



(d)  $\mu\tau$

Figure 6.6: The number of b-jets in the events for electron (a) and muon (b)) triggered events in the low  $E_T^{\text{miss}}$  region.

### 6.1.3 Control Region Yields

In sections 5.1 and 5.3 a region orthogonal to the signal region defined in section 4.4 was chosen that has a reversed  $E_T^{\text{miss}}$  cut and has no b-tag requirements applied to the event selection. Table 5.7 showed the predicted yields for signal and all background events and those observed in data in this region. The background yield consists of  $Z \rightarrow \tau\tau$  and di-boson MC events, the predicted contributions from fake leptons, and the contributions to the  $e\tau$  and  $\mu\tau$  channels from fake hadronic taus. The fake lepton and tau predictions are used in place of  $t\bar{t}$  MC with incorrectly reconstructed final states, single top MC, and  $W + jets$  MC as explained more fully in sections 5.1 and 5.3. The signal  $t\bar{t}$  MC events are those that have been filtered to include only events where the final state leptons have been correctly reconstructed, see section 4.6.2 for more details.

In the electron triggered channels and the  $\mu e$  channel the predicted yields from signal and background are consistent within  $\sim 1\sigma$  of the observed yield in data. A low yield is predicted for signal plus background compared to data in the  $\mu\tau$  channel as observed in section 6.1.2 (partly exacerbated by the  $\Sigma p_T$  cut which selected a less well described region). The  $\mu\tau$  channel was shown in section 5.3 to match the other cut variable shapes. In section 5.4 the systematic uncertainty from the tau fake rate was considered which covers this deficit. While only the electron triggered channels are quoted in the final measurement, any extensions to this analysis which include the muon triggered channels will need to explain or compensate for this difference in the  $e\tau$  and  $\mu\tau$  channels.

## 6.2 Signal Region Event Selection

Events are selected using the cuts listed in sections 4.1 and 4.2, where 2 b-jets are selected. Plots of the  $\Sigma p_T$  distributions in the signal region are shown in figures 6.7 before their respective cuts. The shapes and normalisation of the predicted signal

plus background show good agreement with data before any systematic uncertainties are included.

Plots of the  $E_T^{\text{miss}}$  distributions in the signal region are shown in figure 6.8, which show good agreement in the distribution shapes and yields, with the exception of the  $40 \text{ GeV} \leq E_T^{\text{miss}} < 60 \text{ GeV}$  bin where there is a discrepancy of  $\sim 2\sigma$  between data the signal plus background estimate in all channels except the  $\mu\tau$  channel, though because the same bin in the control region did not have this discrepancy, it seems likely this is a statistical fluctuation.

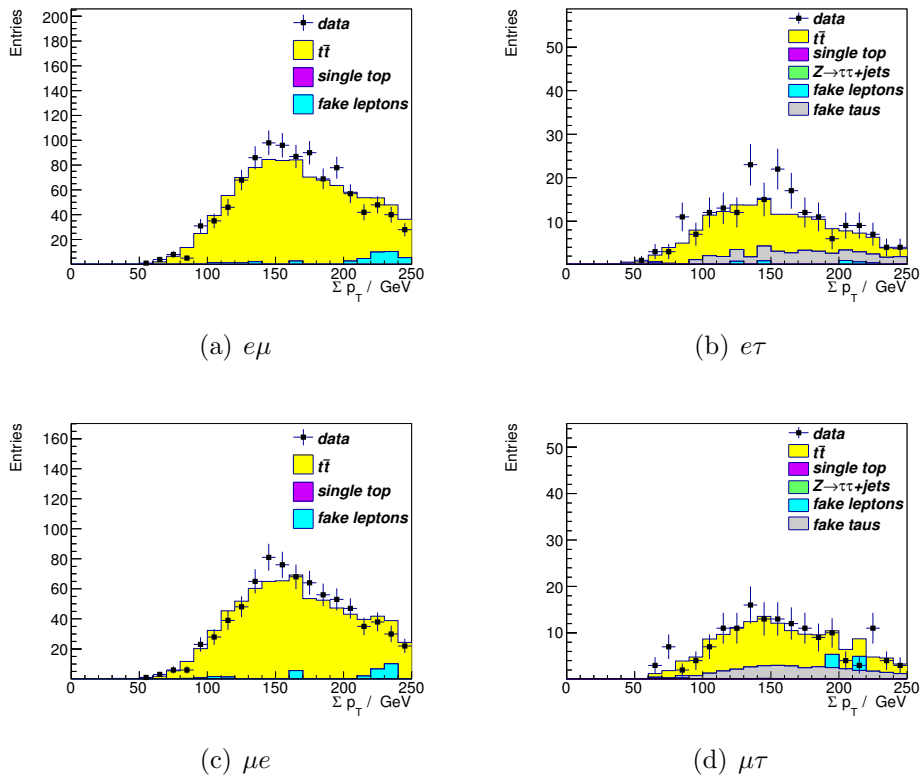
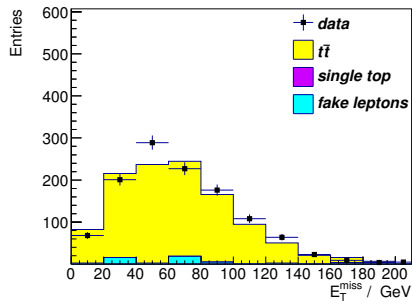
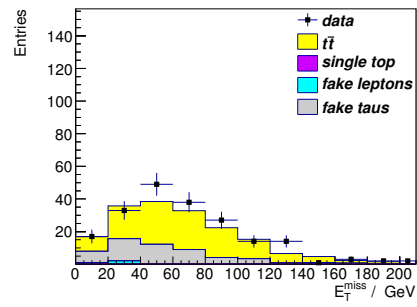


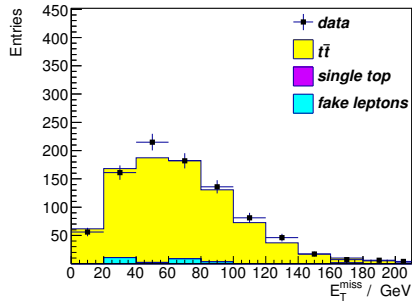
Figure 6.7: The  $\Sigma p_T$  of all tracks in the signal region for the electron triggered channels ( $e\mu$  a),  $e\tau$  b)) and the muon triggered channels ( $\mu e$  lower left,  $\mu\tau$  lower right) before any cut on  $\Sigma p_T$  or  $E_T^{\text{miss}}$ .



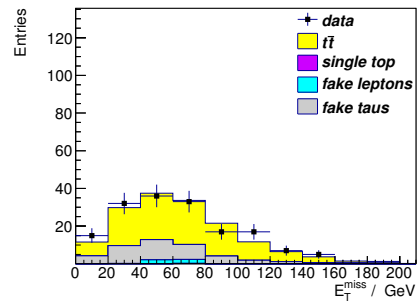
(a)  $e\mu$



(b)  $e\tau$



(c)  $\mu e$



(d)  $\mu\tau$

Figure 6.8: The  $E_T^{\text{miss}}$  of all tracks in the signal region for the electron triggered channels ( $e\mu$  a),  $e\tau$  b)) and the muon triggered channels ( $\mu e$  c),  $\mu\tau$  d) before the  $E_T^{\text{miss}}$  cut.

Selecting events with two b-jets in the event gives a high purity of signal  $t\bar{t}$  events, before the final cuts of the event selection are applied, and the data driven fake rates have low yields in the signal region minimising their systematic uncertainty on the yield. Importantly the signal and background shapes show reasonable agreement where the signal region cuts are applied.

### 6.2.1 Signal Region Yield

The yields observed in data and the predicted  $t\bar{t}$  signal plus background yields are shown in table 6.1. Using the truth classification described in section 4.6.2 the number of signal  $t\bar{t}$  events in both the  $e\mu$  and  $\mu e$  channel is estimated to be 622. In the di-lepton channels and  $e\tau$  channels a  $2\sigma$  excess is observed when only considering statistical uncertainties on data, though in the  $\mu\tau$  channel good agreement is observed. In the control region a lower yield was observed in the  $\mu\tau$  channel compared to the other channels as shown in table 5.7, which is consistent with that observed in the signal region. This indicates there may be a general systematic shift in all the signal channels. However the systematic uncertainties discussed in section 6.4.1 have not been included, including large systematic uncertainties from the background estimates and systematic uncertainties estimated using the samples discussed in 6.4.1.1 which affect  $t\bar{t}$  production and decay.

In the  $e\tau$  channel the estimated lepton fake yield has fluctuated below zero due to limited statistics and so the lepton fake rate is set to zero in this channel. In the di-lepton channels the selection has a high purity of  $t\bar{t}$  events, with the dominant background coming from fake leptons. In the lepton plus tau channels the dominant background is from fake taus.

	$e\mu$	$\mu e$	$e\tau$	$\mu\tau$
$Z \rightarrow \tau\tau$	0	0	0.2	0.3
Di-boson	0.1	0.07	0.05	0.02
Lepton Fakes	30.1	11.7	1.6	4.8
Tau Fakes	0	0	28.7	26.0
Total Background	30.2	11.8	30.6	31.1
Signal $t\bar{t}$	813	635	93.6	85.5
Signal + Background	843	647	124	117
Data	913	702	150	116

Table 6.1: Data yields and predicted signal and background yields for each  $t\bar{t}$  channel in the signal region with 2 b-tagged jets and  $E_T^{\text{miss}} > 40$  GeV.

### 6.2.2 Selected $t\bar{t}$ Events

The number of jets in selected events is shown in figure 6.9 and show good agreement between data and the signal plus background estimates. The  $p_T$  of the triggering lepton is shown in figure 6.10. The shapes of the distributions observed in data are well reproduced in the di-lepton channels in the high  $p_T$  region: however an excess is observed in data in the lowest two  $p_T$  bins, which was not observed in the control region. In the lepton plus tau distributions no significant deviations are seen between data and the predicted signal plus background distributions.

Figure 6.11 shows the  $E_T$  of the highest  $E_T$  jet in the event, and figure 6.12 shows the  $\Sigma E_T$  of all selected objects in the event. While no cut has been applied to these variables, the distribution shapes observed in data in the di-lepton channels some agreement, with the notable exception of the 70 – 80 GeV bin in the lead jet  $E_T$  distribution. The  $\mu\tau$  channel lead jet  $E_T$  distribution seems well described though is limited by low statistics. The  $e\tau$  channel distributions are not well described.

## 6.3 Cross section and Ratio Measurements

In section 6.2 the  $t\bar{t}$  di-lepton and lepton plus tau events were selected in data and the yields were presented. The yields in data and the estimated signal plus

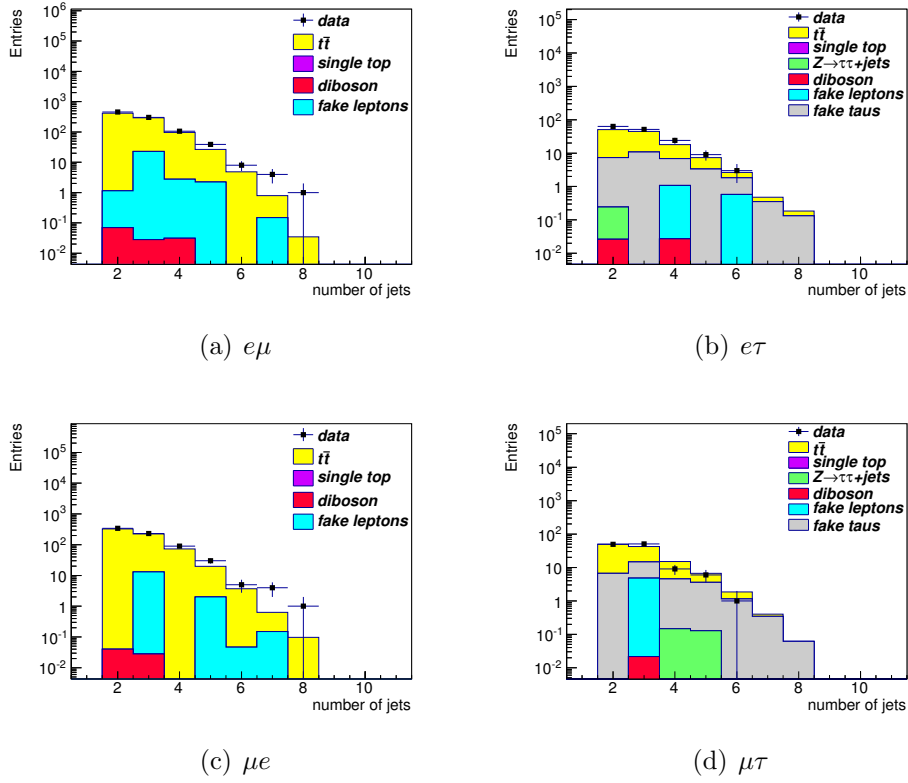


Figure 6.9: The number of jets in the events for electron (a)) and muon (b)) triggered events in the signal region.

background yields are used to estimate the  $t\bar{t}$  cross sections for the di-lepton channel with one final state electron and one final state muon for both trigger streams ( $\sigma^{e\mu}$  and  $\sigma^{\mu e}$ ), and the single lepton plus hadronic tau channels ( $\sigma^{e\tau}$  and  $\sigma^{\mu\tau}$ ). Several systematic uncertainties which cancel in the cross-section ratio are not considered in this analysis so the cross sections are presented here only to validate the cross section ratios estimates ( $\mathcal{R}_{\tau e}$  and  $\mathcal{R}_{\tau\mu}$ ).

Equation 3.8 is used to estimate the partial  $t\bar{t}$  cross sections. In section 6.3.2  $t\bar{t}$  MC is used to predict the combined selection and acceptance efficiency for each  $t\bar{t}$  channel including the detector acceptance, the simulated trigger efficiency, and the efficiency of the cut flow. In section 6.4 the systematic tools and methods used to estimate the systematic uncertainty on the cross sections (excluding systematic uncertainties which exactly cancel) and cross section ratios are explained. Finally, possible extensions to the analysis are explored in section 6.6.

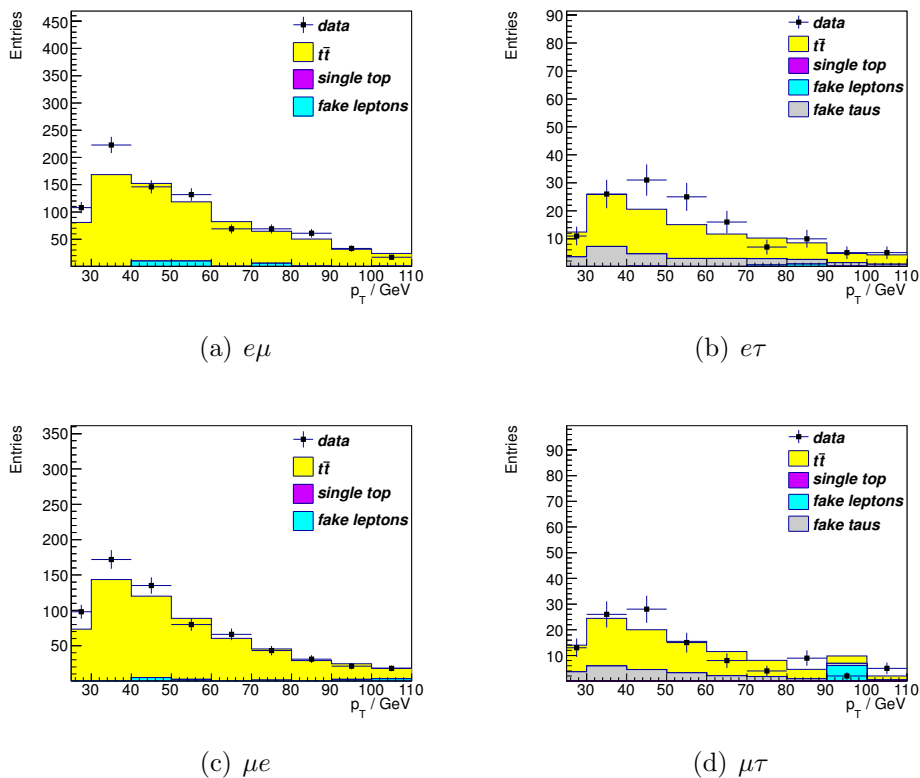


Figure 6.10: The  $p_T$  of the triggered electron (a) and muon (b) in the signal region.

### 6.3.1 Cross Sections

The  $t\bar{t}$  production cross section is discussed in section 3.5.1 including the effects on the cross section branching fractions from the incoming partons' PDFs, the strong coupling, the assumption of lepton universality in electro-weak couplings, and from their dependence of the lepton masses. Experimentally no distinction is made between electrons and muons produced directly from the decay of the  $W$  (produced from the decay of a top) and those from the leptonic decay of a tau. The cross sections and cross section ratios are inclusive of electrons and muons from tau decays. Using the top cross sections measured in the ATLAS detector, and the previously measured values of the branching ratios, the expected cross sections are listed in table 4.3.

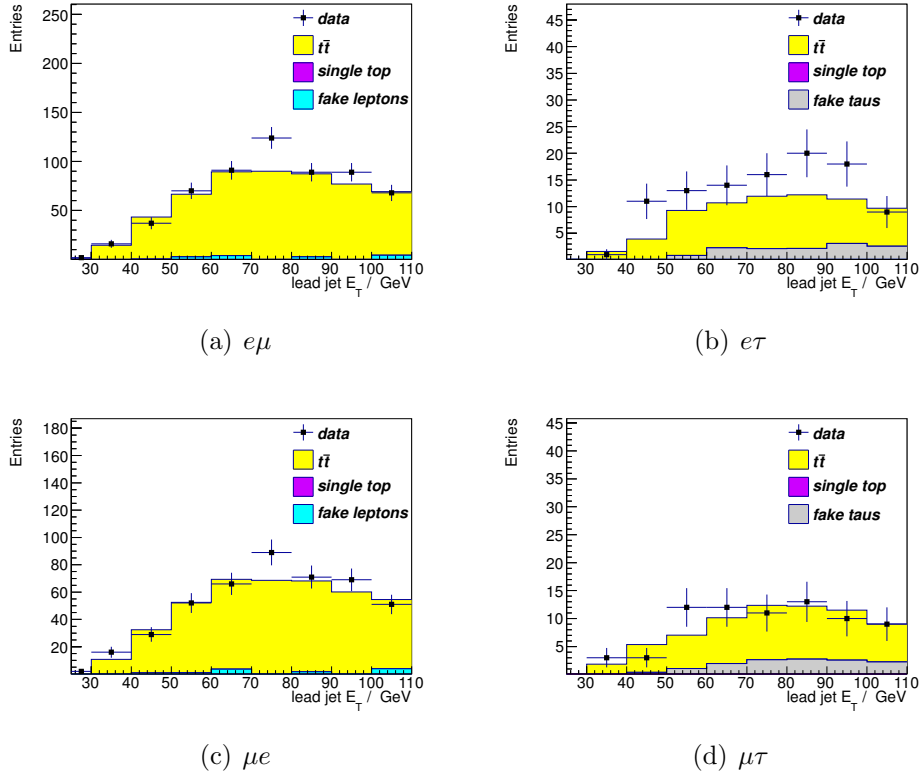


Figure 6.11: The  $E_T$  of the lead jet for the electron (a) and muon (b) triggered events in the signal region.

### 6.3.2 Top Signal Efficiency Measurement using MC

By filtering MC signal  $t\bar{t}$  events by their final state lepton truth content we can estimate the efficiency expected for the signal region. In section 4.6.2 the method for classifying and filtering each  $t\bar{t}$  event at truth level is explained. By using MC, the kinematic acceptance is folded into the overall cut efficiency measurement. Tables 6.2 and 6.3 list the efficiencies of each cut individually and the total efficiency and acceptance used to calculate the cross sections and cross section ratios. The systematic uncertainties from modelling of  $t\bar{t}$  events, which will affect the calculated efficiencies, are discussed in section 6.4.1.1. Note that the di-lepton efficiency measurements are not orthogonal by construction, with no veto on a muon trigger in the electron trigger stream and vice-versa for the muon trigger stream.

One difference between the di-lepton and lepton plus tau  $t\bar{t}$  event topologies are the

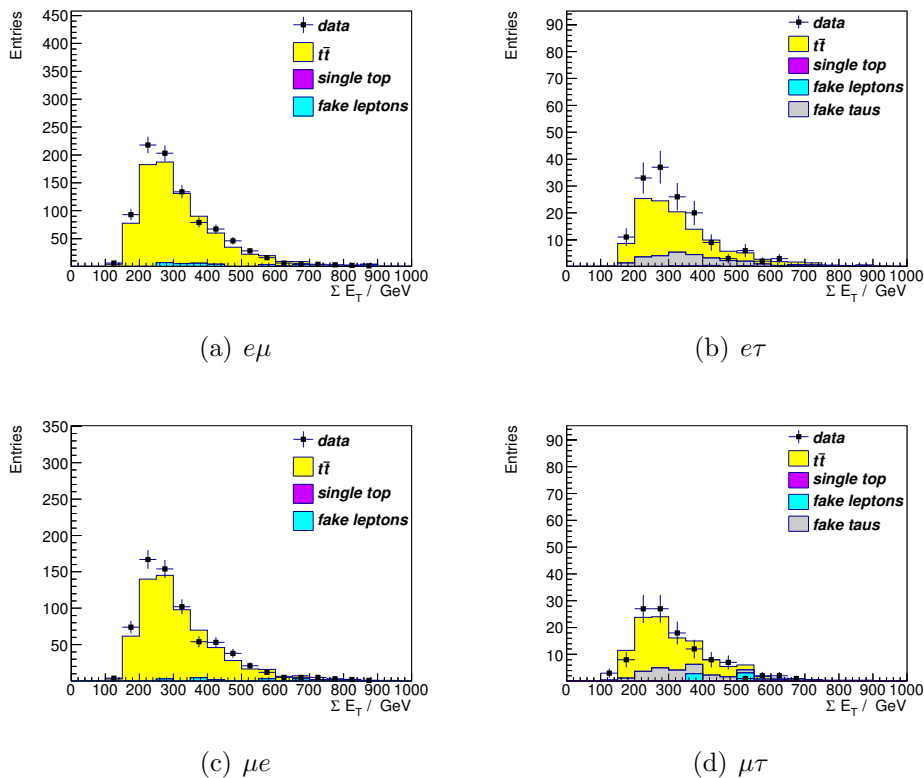


Figure 6.12: The  $\Sigma E_T$  of all selected objects for the electron (a)) and muon (b)) triggered events in the signal region.

non-triggering leptons, particularly the MC simulation of hadronically decaying tau leptons which affects the calculated  $t\bar{t}$  selection efficiencies which do not cancel in the cross section ratios. The tau BDT variable was trained using MC events for real taus and validated with data which showed that hadronic tau decay is well described by MC (see section 4.1.5 for more details on tau reconstruction). A tau identification systematic uncertainty on the yields was measured in a similar analysis and was reported to be  $\sim 3\%$  [1], which is much smaller than the dominant systematic uncertainties evaluated in section 6.4. Tools to estimate the systematic uncertainty on the tau efficiency in MC were not available for the software release used in this analysis: this would need to be included in any future extensions of this analysis.

The trigger efficiencies are expected to almost cancel in the cross section ratio measurements because of the similar event topologies in di-lepton, and lepton plus tau  $t\bar{t}$  events. However, only samples of data and MC with at least one loose lepton in

them were used (known as lepton skimmed samples) in any of the analyses presented here. Therefore, it is not possible to simply compare triggering efficiencies as they are biased towards events that already include one pre-selected lepton.

The product of the lepton skim efficiency, lepton trigger efficiency, and the trigger matched lepton efficiency defines a combined trigger and lepton selection efficiency that can be compared between the di-lepton and lepton plus tau channels. These combined efficiencies measured in MC are  $\epsilon_{e\mu} = 0.363$  and  $\epsilon_{e\tau} = 0.361$  in the electron triggered channels, and  $\epsilon_{\mu e} = 0.305$  and  $\epsilon_{\mu\tau} = 0.302$  in the muon triggered channels. These combined efficiencies for each lepton trigger agree within  $\sim 1\%$  and so as expected will have a very small effect on the cross section ratios. The remaining di-lepton and lepton plus tau cut efficiencies are consistent.

Cut	$t\bar{t}$ Cut Efficiencies	
	$\epsilon^{e\mu}$	$\epsilon^{\mu e}$
Lepton Skim	0.90	0.90
Lepton Trigger	0.62	0.64
PV	1.00	1.00
$N^{bad-jets}$	1.00	1.00
1 trigger matched $e/\mu$	0.65	0.53
$N^{jets} \geq 2$	0.78	0.84
$N^{b-jets} = 2$	0.39	0.36
1 $\mu/e$	0.40	0.38
0 $\tau$	1.00	1.00
oppositely charged leptons	1.00	1.00
$\Sigma p_T > 100$ GeV	0.96	0.96
$E_T^{miss} > 40$ GeV	0.74	0.74
Total signal efficiency	0.032	0.025

Table 6.2: Signal  $t\bar{t}$  efficiencies, relative to the previous cut, measured using MC inclusive of the detector acceptance for leptons, hadronic taus and jets.

## 6.4 Systematic Uncertainties

In section 4.1 the reconstruction of electrons, muons, jets, b-jets, hadronic taus, and the event  $E_T^{miss}$  are described. To validate each object reconstruction routine

Cut	$t\bar{t}$ Cut Efficiencies	
	$\epsilon^{e\tau}$	$\epsilon^{\mu\tau}$
Lepton Skim	0.58	0.78
Lepton Trigger	0.84	0.73
PV	1.00	1.00
$N^{bad-jets}$	1	1
1 trigger matched $e/\mu$	0.74	0.53
$N^{jets} \geq 2$	0.85	0.85
$N^{b-jets} = 2$	0.37	0.37
$0\mu/e$	1.00	1.00
1 $\tau$	0.089	0.094
oppositely charged leptons	0.99	0.99
$\Sigma p_T > 100$ GeV	0.87	0.92
$E_T^{miss} > 40$ GeV	0.76	0.76
Total signal efficiency	0.0067	0.0062

Table 6.3: Signal  $t\bar{t}$  efficiencies, relative to the previous cut, measured using MC inclusive of the detector acceptance for leptons, hadronic taus and jets.

samples of data and MC are compared, and various scale factors are applied to correct either MC simulations or data. Uncertainties in the scales necessarily have statistical errors associated with them which can lead to a systematic shift in the reconstructed objects properties. Tools to apply these systematic shifts to objects are provided by the relevant ATLAS analysis groups and are described below.

In sections 5.1 and 5.3 the methods for estimating the lepton and tau fake rates are described. The measurements of the electron and muon fake rates and efficiencies, and the tau fake rates include statistical errors.

Each lepton efficiency and fake rate used to calculate an event weight is shifted up and down by one standard deviation. The error on the predicted lepton fake rate yield is estimated by repeating the analysis and increasing each of the two real efficiencies and fake rates by the systematic uncertainties listed in table 5.2 and 5.4. Half the difference between the cross sections and cross section ratios are taken as the systematic uncertainties due to the fake rate estimates. Further discussion and analysis of the lepton fake rate estimate in the control and signal regions is found in sections 6.1 and 6.2, including distributions after all the di-lepton control region

event selection has been applied.

For most of the individual systematic uncertainties ( $\sigma^{syst}$ ) half the difference of the cross sections or cross section ratio (both represented by  $X$ ), shifted up and down ( $X_{up}^{syst}$  and  $X_{down}^{syst}$  respectively) by each systematic tool, from their nominal values ( $X_{nom}$ ) is taken as one standard deviation:

$$\pm\sigma^{syst} = (|X_{up}^{syst} - X_{nom}| + |X_{down}^{syst} - X_{nom}|)/2. \quad (6.1)$$

Where the systematic uncertainty is obtained by turning off a tool, the difference from the nominal value is taken as as one standard deviation:

$$\pm\sigma^{syst} = |X_{off} - X_{nom}|. \quad (6.2)$$

Theoretical uncertainties are included due to incomplete knowledge of SM parameters, and the theoretical difficulties of simulating non-perturbative physics. Where model parameters have been varied between two extremes, the full difference is taken as one standard deviation ( $\pm\sigma^{syst} = |X_{up}^{syst} - X_{down}^{syst}|$ ) due to this parameter.

Several systematic effects which only affect  $t\bar{t}$  production and not the branching fractions have not been included, including PDF systematic uncertainties and variation of the top mass. While using the cross sections to calculate the cross section ratios is appropriate, they should not be used elsewhere or taken as a definitive measurements for this reason.

A systematic uncertainty on the integrated luminosity during 2011 proton-proton collisions at  $\sqrt{s} = 7$  TeV was calculated to be 1.8% in [4]. This is evaluated as a separate systematic uncertainty on the cross sections, though these cancel in the calculation of the cross section ratio.

### 6.4.1 Systematic Tools

The energy scale of electrons is measured using  $Z \rightarrow e^+e^-$  events in data and by ensuring that that invariant mass peak measured in data matches that measured using MC, as explained in 4.1.1. Re-applying each scaling correction with the statistical errors added and subtracted, yields a systematic shift up and down respectively in the energy and  $p_T$  of the electrons [102,147]. The systematic uncertainty is symmetrised by taking the sum of half of the difference using these shifts from the nominal value as  $\pm 1\sigma$ .

The difference between simulated and measured electron energy resolution is corrected by smearing MC electrons with  $p_T > 7$  GeV, by applying a Gaussian shift to the electron energy and  $p_T$  to match the energy resolution measured in data as explain in section 4.1.1. A tool provided by an ATLAS performance group re-applied this Gaussian smearing and added or subtracted the statistical errors of the measured energy resolution to give a systematic shift up and down respectively (as described in [102]). The systematic uncertainty is symmetrised by taking the sum of half of the difference using these shifts from the nominal value as  $\pm 1\sigma$ .

The muon smearing factors are applied by default, using a standard software tool, to all ID and MS MC muons, separately, before any object pre-selection (as described in section 4.1.2). Shifting each smearing factor up and down by one standard deviation for both ID and MS muons respectively, the sum of half of the difference using these shifts from the nominal value as  $\pm 1\sigma$ .

The  $p_T$  values of all MC muons are scaled to match those in data concurrently with muon  $p_T$  resolution smearing. In this analysis the systematic uncertainty for the muon momentum scaling is obtained by turning this scaling off: the full difference between between the analysis results measured with the tool off and the nominal values are taken as  $\pm 1\sigma$ .

The EM scale and JES are measured as a function of the jet kinematic properties, and the physics environment as described in section 4.1.3, where several methods

of estimating the systematic uncertainty on the JES were discussed as measured in [106,107]. A tool was provided which shifted the JES applied to each jet to the upper and lower bounds of the uncertainty on the JES in MC. The sum of half of the difference using these shifts from the nominal value as  $\pm 1\sigma$ .

There is good agreement between the JER measured in data and MC, as described in section 4.1.3.2, and no additional  $p_T$  smearing is applied to MC. The error on the JER, measured in data using di-jet  $p_T$  balancing (see [111,112]), is added and subtracted using a standard software tool to the JER of MC. The sum of half of the difference using these shifts from the nominal value as  $\pm 1\sigma$ .

The JRE is well modelled in MC and no corrections are necessary. However for large numbers of jets the low statistics means the JRE could not be accurately measured, see section 4.1.3.3. The error on the measured efficiencies is included in the MC by randomly dropping jets from the event using a standard software tool to simulate an increase in the jet in-efficiency (see [113]). The full difference between the analysis results obtained by applying this systematic prescription, and the nominal value, is taken as  $\pm 1\sigma$ .

The construction of each event's  $E_T^{\text{miss}}$  uses all of the pre-selected objects as described in section 4.1.6. All changes to the pre-selected objects from applying the systematic tools described above are used in a re-calculation of each event's  $E_T^{\text{miss}}$ .

The method for estimating the lepton fake rate assigns a weight to each selected event as described in section 5.1. The efficiency (fake rate) for an individual lepton in an event is taken from the lepton  $p_T$  (lead jet  $p_T$ ) distributions in figures 5.2 and 5.3 (5.14 and 5.15). These are then used to calculate the event weight (using equation 5.3).

Four systematic uncertainties are separately calculated for the electron efficiency, muon efficiency, electron fake rate, and muon fake rate respectively. By adding or subtracting one standard deviation in the uncertainty to each efficiency or fake rate used to calculate the weighted efficiencies (or weighted fake rate), the event weight is

consequently increased or decreased. For the real lepton efficiencies this uncertainty is the statistical uncertainty on the efficiency. For the electron (muon) fake rate the fake rate as a function of the lepton  $\eta$  ( $N_{jets}$ ) are used to estimate the systematic uncertainty as described in section 5.1. These systematic uncertainties are listed in table 5.4. For each of these four systematic uncertainties, the sum of half of the difference using these shifts from the nominal value is taken as  $\pm 1\sigma$ . Because all the efficiencies (or fake rates) used to estimate the weighted efficiency for each lepton in an event are increased or decreased at the same time, the systematic uncertainty is conservative.

The method for estimating the number of fake taus in the signal  $t\bar{t}$  region uses the tau fake rates, measured in section 5.3.1, to calculate a weight for each event using equation 5.9. In section 5.3.4 a lower fake rate was measured in  $W$  events compared to that measured in  $Z$  events. To estimate the systematic uncertainty on the tau fake rate, including this systematic difference, the tau fake rate used to calculate the weight for each event is increased and decreased by one standard deviation in its statistical uncertainty. This results in an increased and decreased event weight, and an increase and decrease in the estimate of the number of fake taus in the signal  $t\bar{t}$  region. The sum of half of the difference using these shifts from the nominal value as  $\pm 1\sigma$ .

#### 6.4.1.1 Systematic Uncertainties from $t\bar{t}$ Modelling

Several  $t\bar{t}$  samples used to estimate the systematic uncertainty were described in section . The method for combining these is that recommended by the ATLAS top group [55, 82].

Two comparisons are made between different MC generators and different programs that model parton hadronisation, which are used to create alternative  $t\bar{t}$  MC samples. The samples used are discussed in section 4.6). The comparisons were made between different MC generators used to make alternative  $t\bar{t}$  samples: the nomi-

nal MC@NLO generator was compared to samples of  $t\bar{t}$  events generated using ALPGEN and POWHEG.

Both generators used the CTEQ6.6 PDF schemes and HERWIG for the parton shower model. The full differences in the cross sections and cross section ratios are evaluated and the average comparisons is taken as  $\pm 1\sigma$ , and is referred to as the generator systematic uncertainty. These comparisons take account of differing amounts of ISR/FSR and different re-normalisation schemes and therefore no separate systematic uncertainties were needed to take these into account.

The systematic uncertainty on the parton shower is evaluated by comparing two samples (both generated using POWHEG) using PYTHIA 6 or HERWIG to make  $t\bar{t}$  samples with differing parton shower models and fragmentation schemes.

In section 3.3 confinement, colour reconnection and the underlying event are briefly discussed. Confinement means all final state hadrons and the overall  $t\bar{t}$  system and must be colour neutral, including hadrons formed from b-quarks produced from the decay of high  $p_T$  top quarks. Gluon exchange ensures this is the case, but such interactions are non-perturbative in nature and difficult to model. Using two  $t\bar{t}$  MC samples using PYTHIA tunes with different levels of colour reconnection, the difference between the analysis results is taken as  $\pm 1\sigma$  [140]. Using similar PYTHIA tunes, where instead the underlying event parameters have been varied, the systematic uncertainty from the underlying event is assessed in the same way [140].

## 6.4.2 Measuring the Systematic Uncertainties on the Partial Cross-Sections

In each channel only the average absolute systematic uncertainties due to the MC generator, listed in table 6.4, are used as in other ATLAS top studies [82]. The cross sections and the absolute systematic uncertainties are listed in table 6.5. The total systematic uncertainty is obtained by adding the uncertainties in quadrature sum,

and assumes that there is minimal correlation between them. The cross sections are calculated using the yields in table 6.1, and the efficiencies in tables 6.2 and 6.3 with equation 3.8, and using the integrated luminosity  $4713.11 \text{ pb}^{-1}$  (defined by the GRL described in section 4.4.1). The systematic shifts are calculated using the prescriptions described in section 6.4.

The total systematic uncertainty for each channel is dominated by the systematic uncertainties on the tau fake rate, the generator uncertainties, and the parton shower uncertainties. The systematic uncertainties from colour reconnection and the underlying event also have significant contributions in some channels. Of the systematic uncertainties from particle identification and reconstruction, the JES and JRE uncertainties are the largest but they do not contribute significantly to the cross section uncertainties.

	$t\bar{t}$ Channel			
	$e\mu$	$\mu e$	$e\tau$	$\mu\tau$
Cross section	5.89	5.89	3.80	2.97
POWHEG	0.3	0.39	0.4	0.46
ALPGEN	1.1	1.1	0.33	0.27
Average Generator Uncertainty	0.71	0.76	0.34	0.38

Table 6.4: The calculated cross-sections, and the POWHEG systematic uncertainty from the comparison between an MC@NLO and a POWHEG  $t\bar{t}$  samples, the ALPGEN systematic uncertainty from the comparison between an MC@NLO and a ALPGEN  $t\bar{t}$  samples. The average generator systematic uncertainty is included in the total systematic uncertainty. All uncertainties are absolute.

In section 3.5.1 the latest public results for  $t\bar{t}$  production cross sections at  $\sqrt{s} = 7 \text{ TeV}$  in proton-proton collisions from the ATLAS and the CMS collaborations were given. The partial cross sections in the di-lepton and lepton plus tau channels are calculated in table 6.6 using the statistically independent  $t\bar{t}$  cross section result from the CMS collaboration, and the world average  $W$  and tau branching fractions inferred from the PDG ( $B^{PDG}$ ) [9] in equations 3.11 and 3.12. The partial cross sections are presented in table 6.6 are consistent with the cross sections predicted using the CMS result, within statistical and systematic uncertainties. It is therefore reasonable to use them to calculate the cross section ratio measurements.

	$t\bar{t}$ Channel			
	$e\mu$	$\mu e$	$e\tau$	$\mu\tau$
Cross section	5.88	5.89	3.76	2.91
Electron smear	0.0014	0.0024	0.009	0
Electron scale	9.3e-05	0.00058	0	0
MS muon smear	0.00036	0.0011	0	0
ID muon smear	0.00018	0.001	0	0.00093
Muon scale	0.0041	0.0052	5.9e-05	0.0015
JER	0.026	0.028	0.013	0.022
JRE smear	0.089	0.089	0.084	0.044
JES	0.16	0.15	0.086	0.099
Real $e$ eff.	0.0061	0.0061	0.0048	0
Real $\mu$ eff.	0.011	0.011	0	0.0068
Fake $e$ rate	0.0054	0.003	0.049	0.03
Fake $\mu$ rate	0.049	0.0098	0.049	0.11
Tau fake	0	0	0.4	0.38
Colour reconnection	0.06	0.082	0.37	0.21
Underlying event	0.01	0.052	0.17	0.041
Parton Shower	0.84	0.85	0.61	0.27
Generator	0.71	0.76	0.34	0.38
Total Systematic Uncertainty	1.1	1.2	0.91	0.65
Luminosity Uncertainty	+0.11 -0.10	+0.11 -0.10	$\pm 0.07$	$\pm 0.05$
Statistical Uncertainty	+0.22 -0.22	+0.25 -0.25	+0.61 -0.56	+0.56 -0.51

Table 6.5: The calculated cross-sections, their respective individual systematic uncertainties, the statistical uncertainty, the total systematic uncertainty, and the luminosity uncertainty. All uncertainties are absolute.

## 6.5 Top Cross Section Ratio Measurement

Calculating the ratios using equation 3.8, the same procedure is used as described in section 6.4.1 to calculate the systematic shifts. Where a systematic prescription shifts a parameter in one direction, this is applied to both the numerator and denominator of the cross section ratio simultaneously. Many systematic effects should naturally cancel as they are expected to apply equally to the numerator and denominator in the ratio, but they are not artificially forced to do so. Table 6.7 gives the systematic uncertainties and the total systematic uncertainty calculated as the quadrature sum of these.

	$t\bar{t}$ Channel			
	$e\mu$	$\mu e$	$e\tau$	$\mu\tau$
$\sigma_{CMS}^{t\bar{t}} \cdot B^{PDG}$	5.3	5.3	3.0	3.0
Cross section	5.88	5.89	3.76	2.91
Statistical Uncertainty	$\pm 0.22$	$\pm 0.25$	$^{+0.61}_{-0.56}$	$^{+0.56}_{-0.51}$
Total Systematic Uncertainty	1.1	1.2	0.91	0.65
Luminosity Uncertainty	$^{+0.11}_{-0.10}$	$^{+0.11}_{-0.10}$	$\pm 0.07$	$\pm 0.05$

Table 6.6: Comparison of the partial cross sections predicted using the CMS  $t\bar{t}$  production cross section result [56] and the branching ratios inferred from the PDG, with the calculated cross-sections.

Excluding the uncertainty on the tau fake rate, most systematic uncertainties cancel partially in cross section ratios. The JES is the largest systematic uncertainty from object ID and reconstruction that contributes significantly to the total systematic uncertainty. The tau fake rate systematic uncertainties are large, and comparable in size to the generator and parton shower uncertainties. The JER systematic uncertainty also have smaller, but significant, contributions to the final systematic uncertainty calculation.

The cross section ratios measured in data are presented in table 6.8 together with the cross section ratios inferred from the PDG values and those found in  $t\bar{t}$  MC events. Both ratios ( $\mathcal{R}_{e\tau}$  and  $\mathcal{R}_{\mu\tau}$ ) are consistent with those predicted for the SM, within statistical and systematic uncertainties.

An initial estimate of the cross section ratios including a charged Higgs signal was given in table 3.6 which did not account for the difference in reconstruction efficiency between  $t\bar{t}$  events with and without a charged Higgs boson. Using a charged Higgs MC sample scaled to different  $t \rightarrow H$  branching fractions the cross section ratios have been re-calculated in table 6.9. The uncertainties shown in this table are from the statistical uncertainties on the charged Higgs events only. Because there were no similar samples to those available for the  $t\bar{t}$  MC, the MC modelling systematic uncertainties could not be recalculated for these samples. At present the systematic uncertainties in table 6.8 would dominate any charged Higgs like signal.

Data Ratio	$\mathcal{R}_{e\tau}$	$\mathcal{R}_{\mu\tau}$
	0.65	0.5
Systematic		
Electron smear	0.0015	0.00021
Electron scale	1e-05	5e-05
MS muon smear	3.9e-05	9.7e-05
ID muon smear	2e-05	7.5e-05
Muon scale	0.00046	0.00019
JER	0.00064	0.0014
JRE smear	0.0045	8.3e-05
JES	0.015	0.0058
Real $e$ eff.	0.00014	0.00039
Real $\mu$ eff.	0.00085	0.00017
Fake $e$ rate	0.00018	4.4e-05
Fake $\mu$ rate	8.2e-05	0.00013
Tau fake rate	0.068	0.064
Colour reconnection	0.055	0.024
Underlying event	0.03	0.0011
Parton shower	0.019	0.022
Generator	0.15	0.12
Total Systematic Uncertainty	0.18	0.15
Statistical Uncertainty	+0.12 -0.10	+0.11 -0.09

Table 6.7: The calculated ratios, their respective individual systematic uncertainties, the total statistical uncertainty, and the statistical uncertainty. All uncertainties are absolute.

The cross section ratios measured in data are divided by those inferred from the PDG branching fractions of the  $W$  and the hadronic tau branching fraction. These are given in table 6.10 along with statistical and systematic uncertainties on this value and are consistent with the SM expectation of unity. Because the systematic and statistical uncertainties are large, only very large deviations from lepton universality could be excluded. To increase the sensitivity to smaller deviations from lepton universality, a larger sample of data would be needed in future measurements.

	$\mathcal{R}_{e\tau}$	$\mathcal{R}_{\mu\tau}$
MC Ratio	0.54	0.54
PDG Ratio	0.57	0.56
Data Ratio	0.65	0.5
Statistical Uncertainty	+0.12 -0.10	+0.11 -0.09
Total Systematic Uncertainty	0.18	0.15

Table 6.8: The calculated ratios compared to those calculated from MC and PDG branching fractions. All uncertainties are absolute.

$B(t \rightarrow H^\pm)$	$t\bar{t} \rightarrow e\tau/t\bar{t} \rightarrow e\mu$	$t\bar{t} \rightarrow \mu\tau/t\bar{t} \rightarrow \mu\mu$
0	$0.54 \pm 0$	$0.54 \pm 0$
0.05	$0.57 \pm 3.7\text{e-}05$	$0.57 \pm 4\text{e-}05$
0.1	$0.59 \pm 7.5\text{e-}05$	$0.6 \pm 8.1\text{e-}05$
0.15	$0.62 \pm 0.00011$	$0.63 \pm 0.00012$
0.2	$0.64 \pm 0.00016$	$0.66 \pm 0.00017$

Table 6.9: Partial cross section ratio estimates using the charged Higgs MC with branching fractions given in the table. Because the MC is treated like  $t\bar{t}$  signal MC, this takes into account the difference between the charged Higgs and top reconstruction efficiencies. The  $t\bar{t}$  branching fractions were reduced to ensure the total branching fraction was unity in each case. The uncertainties only include the MC statistical errors.

## 6.6 Future Analysis Extensions

Including the total recorded integrated luminosity from the 2012 dataset,  $21.7 \text{ fb}^{-1}$  of integrated luminosity was delivered to ATLAS in 2012 [148], will increase the available statistics and reduce the statistical uncertainty. The conditions in 2012 were significantly different, with a centre of mass energy of  $\sqrt{s} = 8 \text{ TeV}$ , while the 2011 dataset used here had a centre of mass energy of  $\sqrt{s} = 7 \text{ TeV}$ . This means that the triggers were adjusted, the pileup increased, and the detector conditions changed. Including additional data would involve re-evaluating all the lepton and tau fake rates, and changing cuts to accommodate the change in trigger plateaus.

An alternative method for estimating the fake rate in the lepton plus tau channel was used in another ATLAS analysis [123] as explained in section 5.5, where the same sign events in data are subtracted to leave only fake events from the mis-reconstruction

$\mathcal{R}_{e\tau}^{Data}/\mathcal{R}_{e\tau}^{PDG}$	$\mathcal{R}_{\mu\tau}^{Data}/\mathcal{R}_{\mu\tau}^{PDG}$
$1.1_{-0.17}^{+0.21}(stat.) \pm 0.31(syst.)$	$0.88_{-0.16}^{+0.19}(stat.) \pm 0.26(syst.)$

Table 6.10: The ratio of the measured cross-section ratios to values inferred from the PDG calculated in section 3.5.2 (see [9] ).

of light quarks. The number of fake events is found by fitting templates for real and fake hadronic taus to data, and as a cross-check the matrix method is additionally used to estimate the tau fake rate using a similar definition to that used in section 5.3. These methods may well have smaller systematic uncertainties on the final cross section ratio measurements

The efficiency for real taus is simulated in MC, and this is relied upon in this analysis. An alternative method would select  $Z \rightarrow \tau\tau$  events in data, where one tau decayed leptonically and the other hadronically. By selecting electron-jet pairs that have an invariant mass close to the  $Z$ , the jet can be used to probe how frequently it is reconstructed as a hadronic tau lepton. However, this measurement would be complicated by contamination from  $Z \rightarrow e^+e^-$  events where one electron is incorrectly identified as a jet, and hadronically decaying  $Z$ s where one jet is reconstructed as a tau. Differences in the  $E_T^{\text{miss}}$  distributions and other event distributions for these events could allow these backgrounds to be accounted for, relying on the correct simulation of  $E_T^{\text{miss}}$  distributions instead of on the MC simulation of hadronic tau decays. This may allow the efficiency of hadronically decaying taus to be measured in data, and the estimate for the small systematic uncertainty expected from tau identification (see 6.3.2).

As discussed in section 6.3.2 no tools were available for the software release used in this analysis for estimating the tau reconstruction systematic uncertainties, and future measurements should include these additional systematic uncertainties.

In section 4.7 alternative techniques for separating signal events from background were discussed, including the use of machine learning algorithms such as BDTs. While a fuller understanding of some of the systematic uncertainties would be necessary, it

would be prudent to investigate these to improve the sensitivity to lepton universality violations in  $t\bar{t}$  events in any possible future extension to this analysis.

An alternative measurement, which has not been conducted to date using ATLAS data, is a measurement of  $W$  hadronic and leptonic branching ratios for which small deviations from lepton universality have been observed in previous experiments (see section 3.5.2). Such an analysis would be statistically independent to that detailed in this thesis and would provide a complementary measurement of lepton universality in charged weak decays from a direct measurement of the ratio of charged weak decay coupling constants to leptons.

## 6.7 Summary of Results

In chapter 4 the object reconstruction, pre-selection, and overlap removal were outlined. The selection criteria for  $t\bar{t}$  events with one final state electron and one final state muon, and  $t\bar{t}$  events with one triggering electron or muon, and one hadronically decaying tau, were outlined. These also formed the basis for cuts to select events for measuring the fake rates for electrons, muons and taus as discussed in section 5.1 and 5.3. These were used in sections 6.4.1 and 5.4 to estimate the yields in a region orthogonal to the signal region with no b-tag requirements and a reverse  $E_T^{\text{miss}}$  requirement. Reasonable agreement was found in the yields produced and for the variables used in the selection of top events, before any systematic uncertainties were included.

In section 6.2.1 the yields were used to calculate the  $t\bar{t}$  cross sections for di-lepton events with one final state electron and one final state muon, and for events with a final state electron or muon and a final state hadronically decaying tau. The efficiencies were measured using MC as explained in section 6.3.2. The triggering efficiencies were shown to cancel as expected as a check before using them to calculate the cross section ratios.

The tools and methods used to estimate the systematic uncertainties were explained in section 6.4, and the uncertainties from each source were added in quadrature to give the total systematic uncertainties on the cross sections and cross section ratios respectively. One of the dominant systematic uncertainties of the ratio measurement is the uncertainty on the tau fake rate estimate. As shown in section 6.5, the current measurement would not be sensitive to non SM process such as a charged Higgs signal without reducing the systematic uncertainties.

In section 6.5 the cross section ratios of  $t\bar{t}$  events with a final state electron and a final state hadronic tau, to events with a final state electron and muon, was measured to be  $\mathcal{R}_{e\tau} = 0.65_{-0.10}^{+0.12}(stat.) \pm 0.18(syst.)$  which is consistent with the values calculated from the PDG and the principle of lepton universality. The ratio of  $\mathcal{R}_{e\tau}$  measured in data, to the value inferred from PDG, was measured to be  $\mathcal{R}_{e\tau}^{Data} / \mathcal{R}_{e\tau}^{PDG} = 1.1_{-0.17}^{+0.21}(stat.) \pm 0.31(syst.)$  which is consistent with the SM expectation of unity.

# Bibliography

- [1] A. Collaboration, *Measurement of the top quark pair cross section with ATLAS in pp collisions at  $\sqrt{s} = 7$  TeV using final states with an electron or a muon and a hadronically decaying  $\tau$  lepton*, Phys.Lett. **B717** (2012) 89–108, arXiv:1205.2067 [hep-ex].
- [2] The ATLAS Collaboration, *The ATLAS Collaboration, Search for charged Higgs bosons through the violation of lepton universality in  $t\bar{t}$  events using pp collision data at  $\sqrt{s} = 7$  TeV with the ATLAS experiment*, Journal of High Energy Physics **2013** (2013) no. 3, 1–36. <http://dx.doi.org/10.1007/JHEP03%282013%29076>.
- [3] A. M. Lombardi et al., *CERN LINAC UPGRADE ACTIVITIES*, LINAC. 2008.
- [4] The ATLAS Collaboration, *Improved luminosity determination in pp collisions at  $\sqrt{s} = 7$  TeV using the ATLAS detector at the LHC*, Eur.Phys.J. **C73** (2013) 2518, arXiv:1302.4393 [hep-ex].
- [5] AC Team, *The four main LHC experiments*, Jun, 1999.
- [6] The ATLAS Collaboration, *ATLAS detector and physics performance: Technical Design Report, 1*. Technical Design Report ATLAS. CERN, Geneva, 1999.
- [7] The ATLAS Collaboration, *Observation of a new particle in the search for the Standard Model Higgs boson with the ATLAS detector at the LHC*, Physics Letters B **716** (2012) no. 1, 1 – 29. <http://www.sciencedirect.com/science/article/pii/S037026931200857X>.
- [8] The CMS Collaboration, S. Chatrchyan et al., *Observation of a new boson at a mass of 125 GeV with the {CMS} experiment at the {LHC}*, Physics Letters B **716** (2012) no. 1, 30 – 61. <http://www.sciencedirect.com/science/article/pii/S0370269312008581>.
- [9] K. Nakamura and the Particle Data Group, *Review of Particle Physics*, Journal of Physics G: Nuclear and Particle Physics **37** (2010) no. 7A, 075021. <http://pdg.lbl.gov/2011/download/rpp-2010-booklet.pdf>. and 2011 partial update for the 2012 edition.

- [10] J. Pequenaó, *Computer generated image of the whole ATLAS detector*, Mar, 2008.
- [11] The ATLAS Collaboration, *The ATLAS Experiment at the CERN Large Hadron Collider*, Journal of Instrumentation **3** (2008) no. 08, S08003.
- [12] The ATLAS Collaboration, *Studies of the performance of the ATLAS detector using cosmic-ray muons*, European Physical Journal C **71** (2011) 1593, arXiv:1011.6665.
- [13] The ATLAS Collaboration, *Mapping the material in the ATLAS Inner Detector using secondary hadronic interactions in 7 TeV collisions*, Tech. Rep. ATLAS-CONF-2010-058, CERN, Geneva, Jul, 2010.
- [14] C. Leroy and P.-G. Rancoita, *Principles of radiation interaction in matter and detection; 2nd ed.* World Scientific, Singapore, 2009.
- [15] A. L. Schorlemmer, *Monitoring radiation damage in the ATLAS Pixel Detector*, Journal of Instrumentation **8** (2013) no. 01, C01045. <http://stacks.iop.org/1748-0221/8/i=01/a=C01045>.
- [16] The ATLAS Collaboration, *Public Pixel Tracker Plots for Collision Data*, <https://twiki.cern.ch/twiki/bin/view/AtlasPublic/PixelPublicResul>, may, 2012.
- [17] The ATLAS Collaboration, *dE/dx measurement in the ATLAS Pixel Detector and its use for particle identification*, Tech. Rep. ATLAS-CONF-2011-016, CERN, Geneva, Mar, 2011.
- [18] S. McMahon, *Approved SCT Plots*, <https://twiki.cern.ch/twiki/bin/view/AtlasPublic/ApprovedPlotsSCT>, apr, 2012.
- [19] The ATLAS Collaboration, *Performance of the ATLAS Inner Detector Track and Vertex Reconstruction in the High Pile-Up LHC Environment*, Tech. Rep. ATLAS-CONF-2012-042, CERN, Geneva, Mar, 2012.
- [20] The ATLAS Collaboration, *Jet energy measurement with the ATLAS detector in proton-proton collisions at  $\sqrt{s} = 7$  TeV*, The European Physical Journal C **73** (2013) 1–118. <http://dx.doi.org/10.1140-s10052-013-2304-2>.
- [21] The ATLAS Collaboration, *The ATLAS Experiment at the CERN Large Hadron Collider*, JINST **3** (2008) S08003.
- [22] The ATLAS Collaboration, *Electron performance measurements with the ATLAS detector using the 2010 LHC proton-proton collision data*, Eur.Phys.J. **C72** (2012) 1909, arXiv:1110.3174 [hep-ex].
- [23] The ATLAS Collaboration, *ATLAS liquid-argon calorimeter: Technical Design Report*. Technical Design Report ATLAS. CERN, Geneva, 1996.

- [24] I. Wingerter, *Public Liquid Argon Calorimeter Plots for 7 TeV Collision Data (2010, 2011 and 2012)*, <https://twiki.cern.ch/twiki/bin/view/AtlasPublic/LArCaloPublicResults2010>, may, 2010.
- [25] The ATLAS Collaboration, *Readiness of the ATLAS Tile Calorimeter for LHC collisions*, The European Physical Journal C - Particles and Fields **70** (2010) 1193–1236. <http://dx.doi.org/10.1140-s10052-010-1508-y>. 10.1140-s10052-010-1508-y.
- [26] B. Demirköz, *Construction and Performance of the ATLAS SCT Barrels and Cosmic Tests*. University of Oxford, 2007. <http://books.google.co.uk/books?id=aveSPAAACAAJ>.
- [27] The ATLAS Collaboration, R. Achenbach et al., *The ATLAS Level-1 Calorimeter Trigger*, Journal of Instrumentation **3** (2008) no. 03, P03001. <http://stacks.iop.org/1748-0221/3/i=03/a=P03001>.
- [28] The ATLAS Collaboration, T. F-Martin et al., *Event reconstruction algorithms for the ATLAS trigger*, Journal of Physics: Conference Series **119** (2008) no. 2, 022022. <http://stacks.iop.org/1742-6596/119/i=2/a=022022>.
- [29] The ATLAS Collaboration, *Expected performance of the ATLAS experiment: detector, trigger and physics*. CERN, Geneva, 2009.
- [30] The ATLAS Collaboration, *Performance of the ATLAS Electron and Photon Trigger in p-p Collisions at  $\sqrt{s} = 7$  TeV in 2011*, Tech. Rep. ATLAS-CONF-2012-048, CERN, Geneva, May, 2012.
- [31] The ATLAS Collaboration, *Performance of the Electron and Photon Trigger in p-p Collisions at  $\sqrt{s} = 7$  TeV*, Tech. Rep. ATLAS-CONF-2011-114, CERN, Geneva, Aug, 2011.
- [32] The ATLAS Collaboration, *Performance of the ATLAS muon trigger in 2011*, Tech. Rep. ATLAS-CONF-2012-099, CERN, Geneva, Jul, 2012.
- [33] The ATLAS Collaboration, *Performance of the ATLAS Trigger System in 2010*, Eur.Phys.J. **C72** (2012) 1849, [arXiv:1110.1530](https://arxiv.org/abs/1110.1530) [hep-ex].
- [34] J. G. W. J. Murray, G. Birch et al., *Proceedings of the School for Experimental High Energy Physics Student*, Tech. Rep. RAL-TR-2010-010, STFC, Sept, 2009.
- [35] CKMfitter Group, J. Charles et al., *CP violation and the CKM matrix: Assessing the impact of the asymmetric B factories*, Eur.Phys.J. **C41** (2005) 1–131, [arXiv:hep-ph/0406184](https://arxiv.org/abs/hep-ph/0406184) [hep-ph].
- [36] G. Fogli, E. Lisi, A. Marrone, D. Montanino, A. Palazzo, et al., *Global analysis of neutrino masses, mixings and phases: entering the era of leptonic CP violation searches*, Phys.Rev. **D86** (2012) 013012, [arXiv:1205.5254](https://arxiv.org/abs/1205.5254) [hep-ph].

- [37] M. Dupuis, J. P. Ryan, and S. Speziale, *Discrete gravity models and Loop Quantum Gravity: a short review*, SIGMA **8** (2012) 052, arXiv:1204.5394 [gr-qc].
- [38] X. Calmet, *A Review of Quantum Gravity at the Large Hadron Collider*, Mod.Phys.Lett. **A25** (2010) 1553–1579, arXiv:1005.1805 [hep-ph].
- [39] S. Petcov, *The Nature of Massive Neutrinos*, Adv.High Energy Phys. **2013** (2013) 852987, arXiv:1303.5819 [hep-ph].
- [40] NASA/WMAP Science Team, *What is the Inflation Theory?*, map.gsfc.nasa.gov/universe/bb\_cosmo\_infl.html, apr, 2010.
- [41] N. Jarosik, C. Bennett, J. Dunkley, B. Gold, M. Greason, et al., *Seven-Year Wilkinson Microwave Anisotropy Probe (WMAP) Observations: Sky Maps, Systematic Errors, and Basic Results*, Astrophys.J.Suppl. **192** (2011) 14, arXiv:1001.4744 [astro-ph.CO].
- [42] B. Martin and G. Shaw, *Particle Physics Second Edition*. Wiley and Sons Ltd., 1997.
- [43] J. Goldstone, A. Salam, and S. Weinberg, *Broken Symmetries*, Phys.Rev. **127** (1962) 965–970.
- [44] S. Weinberg, *Effects of a neutral intermediate boson in semileptonic processes*, Phys.Rev. **D5** (1972) 1412–1417.
- [45] B. Martin and G. Shaw., *Particle Physics*. The Manchester Physics Series. Wiley, 2002.
- [46] G. Ingelman, R. Pasechnik, J. Rathsman, and D. Werder, *Diffractional  $W^\pm$  production at hadron colliders as a test of colour singlet exchange mechanisms*, Phys.Rev. **D87** (2013) no. 9, 094017, arXiv:1210.5976 [hep-ph].
- [47] C. Marquet, C. Royon, M. Saimpert, and D. Werder, *Probing the Pomeron structure using dijets and  $\gamma$ +jet events at the LHC*, Phys.Rev. **D88** (2013) no. 7, 074029, arXiv:1306.4901 [hep-ph].
- [48] C. B. Mariotto and V. P. Goncalves, *Diffractional photon production at the LHC*, Phys. Rev. D **88** (2013) 074023. <http://link.aps.org/doi/10.1103/PhysRevD.88.074023>.
- [49] M. Bahr, J. M. Butterworth, S. Gieseke, and M. H. Seymour, *Soft interactions in Herwig++*, arXiv:0905.4671 [hep-ph].
- [50] M. Bahr, S. Gieseke, M. Gigg, D. Grellscheid, K. Hamilton, et al., *Herwig++ Physics and Manual*, Eur.Phys.J. **C58** (2008) 639–707, arXiv:0803.0883 [hep-ph].

- [51] G. 't Hooft and M. Veltman, *Regularization and renormalization of gauge fields*, Nuclear Physics B **44** (1972) no. 1, 189–213.
- [52] B. S. Acharya et al., *Monte Carlo generators for top quark physics at the LHC*, Nuovo Cim. **B123** (2008) 415–420, [arXiv:0804.4122 \[hep-ph\]](#).
- [53] M. Czakon, M. L. Mangano, A. Mitov, and J. Rojo, *Constraints on the gluon PDF from top quark pair production at hadron colliders*, JHEP **1307** (2013) 167, [arXiv:1303.7215 \[hep-ph\]](#).
- [54] W. Beenakker, F. A. Berends, E. Argyres, D. Y. Bardin, A. Denner, et al., *WW cross-sections and distributions*, [arXiv:hep-ph/9602351 \[hep-ph\]](#).
- [55] The ATLAS Collaboration, *Statistical combination of top quark pair production cross-section measurements using dilepton, single-lepton, and all-hadronic final states at  $s = 7$  TeV with the ATLAS detector*, Tech. Rep. ATLAS-CONF-2012-024, CERN, Geneva, Mar, 2012.
- [56] The CMS Collaboration, *Combination of top pair production cross section measurements*, Tech. Rep. CMS-PAS-TOP-11-024, CERN, Geneva, 2011.
- [57] M. Aliev, H. Lacker, U. Langenfeld, S. Moch, P. Uwer, et al., *HATHOR: HAdronic Top and Heavy quarks crOss section calculator*, Comput.Phys.Commun. **182** (2011) 1034–1046, [arXiv:1007.1327 \[hep-ph\]](#).
- [58] N. Kidonakis, *Next-to-next-to-leading soft-gluon corrections for the top quark cross section and transverse momentum distribution*, Phys. Rev. D **82** (2010) 114030. <http://link.aps.org/doi/10.1103/PhysRevD.82.114030>.
- [59] U. Langenfeld, S. Moch, and P. Uwer, *Measuring the running top-quark mass*, Phys. Rev. D **80** (2009) 054009. <http://link.aps.org/doi/10.1103/PhysRevD.80.054009>.
- [60] V. Ahrens, A. Ferroglia, M. Neubert, B. D. Pecjak, and L. L. Yang, *Precision predictions for the  $t+t(\bar{t})$  production cross section at hadron colliders*, Phys.Lett. **B703** (2011) 135–141, [arXiv:1105.5824 \[hep-ph\]](#).
- [61] F. Mandl and G. Shaw., *Quantum Field Theory*. The Manchester Physics Series. Wiley, 1984.
- [62] CLEO Collaboration, I. Danko and C. Collaboration, *Test of lepton universality and search for lepton flavor violation in Upsilon(1S,2S,3S) decays at CLEO*, AIP Conference Proceedings **842** (2006) no. 1, 699–701. <http://link.aip.org/link/?APC/842/699/1>.
- [63] BaBar Collaboration, P. del Amo Sanchez et al., *Test of lepton universality in Upsilon(1S) decays at BaBar*, Phys.Rev.Lett. **104** (2010) 191801, [arXiv:1002.4358 \[hep-ex\]](#).

- [64] The KLOE Collaboration, F. Ambrosino et al., — *V<sub>us</sub> — and lepton universality from kaon decays with the KLOE detector*, Journal of High Energy Physics **2008** (2008) no. 04, 059.  
<http://stacks.iop.org/1126-6708/2008/i=04/a=059>.
- [65] E. Goudzovski, *Lepton flavour universality test at the {CERN} {NA62} experiment*, Nuclear Physics B - Proceedings Supplements **210211** (2011) no. 0, 163 – 168. <http://www.sciencedirect.com/science/article/pii/S0920563210005025>.  
Proceedings of the 9th International Conference on Beauty, Charm and Hyperons in Hadronic Interactions.
- [66] A. Lusiani, *Experimental Review on Lepton Universality and Lepton Flavour Violation tests at the B-factories*, PoS **KAON** (2008) 054,  
[arXiv:0709.1599](https://arxiv.org/abs/0709.1599) [hep-ex].
- [67] BaBar Collaboration, B. Aubert et al., *Measurements of Charged Current Lepton Universality and |V<sub>us</sub>| using Tau Lepton Decays to e<sup>-</sup>ν<sub>e</sub>ν̄<sub>τ</sub>, μ<sup>-</sup>ν̄<sub>μ</sub>ν<sub>τ</sub>, π<sup>-</sup>ν<sub>τ</sub> and K<sup>-</sup>ν<sub>τ</sub>*, Phys.Rev.Lett. **105** (2010) 051602, [arXiv:0912.0242](https://arxiv.org/abs/0912.0242) [hep-ex].
- [68] ALEPH Collaboration, DELPHI Collaboration, L3 Collaboration, OPAL Collaboration, LEP Electroweak Working Group, J. Alcaraz et al., *A Combination of preliminary electroweak measurements and constraints on the standard model*, [arXiv:hep-ex/0612034](https://arxiv.org/abs/hep-ex/0612034) [hep-ex].
- [69] The ATLAS Collaboration, *Measurement of the W to τν Cross Section in pp Collisions at √s = 7 TeV with the ATLAS experiment*, Phys.Lett. **B706** (2012) 276–294, [arXiv:1108.4101](https://arxiv.org/abs/1108.4101) [hep-ex].
- [70] F.-P. Schilling, *Top Quark Physics at the LHC: A Review of the First Two Years*, Int.J.Mod.Phys. **A27** (2012) 1230016, [arXiv:1206.4484](https://arxiv.org/abs/1206.4484) [hep-ex].
- [71] Tevatron Electroweak Working Group, CDF Collaboration, D0 Collaboration, *Combination of CDF and D0 results on the mass of the top quark using up to 5.8 fb<sup>-1</sup> of data*, [arXiv:1107.5255](https://arxiv.org/abs/1107.5255) [hep-ex].
- [72] W. Bernreuther, *Top-quark physics at the LHC*, Journal of Physics G: Nuclear and Particle Physics **35** (2008) no. 8, 083001.  
<http://stacks.iop.org/0954-3899/35/i=8/a=083001>.
- [73] CDF Collaboration, *Direct Top-Quark Width Measurement at CDF*, Phys. Rev. Lett. **105** (2010) 232003.  
<http://link.aps.org/doi/10.1103/PhysRevLett.105.232003>.
- [74] The D0 Collaboration, *Determination of the Width of the Top Quark*, Phys. Rev. Lett. **106** (2011) 022001.  
<http://link.aps.org/doi/10.1103/PhysRevLett.106.022001>.

- [75] I. Bigi, Y. Dokshitzer, V. Khoze, J. Khn, and P. Zerwas, *Production and decay properties of ultra-heavy quarks*, Physics Letters B **181** (1986) no. 12, 157 – 163. <http://www.sciencedirect.com/science/article/pii/037026938691275X>.
- [76] M. Beneke, I. Efthymiopoulos, M. L. Mangano, J. Womersley, A. Ahmadov, et al., *Top quark physics*, arXiv:hep-ph/0003033 [hep-ph].
- [77] CDF Collaboration, T. Aaltonen et al., *Exclusion of an Exotic Top Quark with  $-4/3$  Electric Charge Using Soft Lepton Tagging*, Phys.Rev.Lett. **105** (2010) 101801, arXiv:1006.4597 [hep-ex].
- [78] The ATLAS Collaboration, *Measurement of the top quark charge in pp collisions at  $\sqrt{s} = 7$  TeV in the ATLAS experiment.*, Tech. Rep. ATLAS-CONF-2011-141, CERN, Geneva, Sep, 2011.
- [79] The CMS Collaboration, *Constraints on the Top-Quark Charge from Top-Pair Events*, Tech. Rep. CMS-PAS-TOP-11-031, CERN, Geneva, 2012.
- [80] The ATLAS Collaboration, *Measurement of the top quark charge in pp collisions at  $\sqrt{s} = 7$  TeV with the ATLAS detector*, arXiv:1307.4568 [hep-ex].
- [81] D0 Collaboration, V. M. Abazov et al., *Evidence for spin correlation in  $t\bar{t}$  production*, Phys.Rev.Lett. **108** (2012) 032004, arXiv:1110.4194 [hep-ex].
- [82] The ATLAS Collaboration, *Observation of Spin Correlation in  $t\bar{t}$  Events from pp Collisions at  $\sqrt{s} = 7$  TeV Using the ATLAS Detector*, Phys. Rev. Lett. **108** (2012) 212001. <http://link.aps.org/doi/10.1103/PhysRevLett.108.212001>.
- [83] D0 Collaboration, V. Abazov et al., *Precision measurement of the ratio  $B(t \rightarrow Wb)/B(t \rightarrow Wq)$  and Extraction of  $V_{tb}$* , Phys.Rev.Lett. **107** (2011) 121802, arXiv:1106.5436 [hep-ex].
- [84] CDF Collaboration, T. Aaltonen et al., *Evidence for a Mass Dependent Forward-Backward Asymmetry in Top Quark Pair Production*, Phys.Rev. **D83** (2011) 112003, arXiv:1101.0034 [hep-ex].
- [85] D0 Collaboration, V. M. Abazov et al., *Forward-backward asymmetry in top quark-antiquark production*, Phys.Rev. **D84** (2011) 112005, arXiv:1107.4995 [hep-ex].
- [86] The ATLAS Collaboration, *Measurement of the charge asymmetry in top quark pair production in pp collisions at  $\sqrt{s} = 7$  TeV using the ATLAS detector*, Eur.Phys.J. **C72** (2012) 2039, arXiv:1203.4211 [hep-ex].
- [87] The CMS Collaboration, *Measurement of the charge asymmetry in top quark pair production with the CMS experiment*, Tech. Rep. CMS-PAS-TOP-10-010, CERN, Geneva, 2011.

- [88] T. Sjöstrand, S. Mrenna, and P. Skands, *PYTHIA 6.4 physics and manual*, Journal of High Energy Physics **2006** (2006) no. 05, 026. <http://stacks.iop.org/1126-6708/2006/i=05/a=026>.
- [89] Z. Was and P. Golonka, *TAUOLA as tau Monte Carlo for future applications*, Nucl.Phys.Proc.Suppl. **144** (2005) 88–94, [arXiv:hep-ph/0411377](https://arxiv.org/abs/hep-ph/0411377) [hep-ph].
- [90] CDF Collaboration, T. Aaltonen et al., *First Observation of Electroweak Single Top Quark Production*, Phys.Rev.Lett. **103** (2009) 092002, [arXiv:0903.0885](https://arxiv.org/abs/0903.0885) [hep-ex].
- [91] D0 Collaboration, V. Abazov et al., *Observation of Single Top Quark Production*, Phys.Rev.Lett. **103** (2009) 092001, [arXiv:0903.0850](https://arxiv.org/abs/0903.0850) [hep-ex].
- [92] The ATLAS Collaboration, *Measurement of the top quark pair production cross-section with ATLAS in the single lepton channel*, Phys.Lett. **B711** (2012) 244–263, [arXiv:1201.1889](https://arxiv.org/abs/1201.1889) [hep-ex].
- [93] The CMS Collaboration, S. Chatrchyan et al., *Measurement of the single-top-quark  $t$ -channel cross section in  $pp$  collisions at  $\sqrt{s} = 7$  TeV*, JHEP **1212** (2012) 035, [arXiv:1209.4533](https://arxiv.org/abs/1209.4533) [hep-ex].
- [94] The ATLAS Collaboration, *Evidence for the spin-0 nature of the Higgs boson using ATLAS data*, [arXiv:1307.1432](https://arxiv.org/abs/1307.1432) [hep-ex].
- [95] S. Weinberg, *The quantum theory of fields. Vol. 3: Supersymmetry*. 2000. <http://www.slac.stanford.edu/spires/find/hep/www?key=4384008>. Cambridge, UK: Univ. Pr. (2000) 419 p.
- [96] The ATLAS Collaboration, *Mass reach of ATLAS searches for Supersymmetry.*, [https://twiki.cern.ch/twiki/pub/AtlasPublic/CombinedSummaryPlots/AtlasSearchesSUSY\\_EPS2013.pdf](https://twiki.cern.ch/twiki/pub/AtlasPublic/CombinedSummaryPlots/AtlasSearchesSUSY_EPS2013.pdf), May, 2013.
- [97] The CMS Collaboration, *Summary of CMS SUSY Results\* in SMS framework.*, [https://twiki.cern.ch/twiki/pub/CMSPublic/SUSYSMSummaryPlots8TeV/barplot\\_blue\\_orange\\_EPSHEP2013.pdf](https://twiki.cern.ch/twiki/pub/CMSPublic/SUSYSMSummaryPlots8TeV/barplot_blue_orange_EPSHEP2013.pdf), May, 2013.
- [98] G. Altarelli, *The SM and SUSY after the 2011 LHC results*, [arXiv:1206.1476](https://arxiv.org/abs/1206.1476) [hep-ph].
- [99] J. Kretzschmar, *EfficiencyMeasurements*, [https://twiki.cern.ch/twiki/bin/viewauth/AtlasProtected/EnergyScaleResolutionRecommendations#2012\\_Moriond\\_Recommendations\\_2012](https://twiki.cern.ch/twiki/bin/viewauth/AtlasProtected/EnergyScaleResolutionRecommendations#2012_Moriond_Recommendations_2012), apr, 2012.
- [100] L. Fayard and J. Kretzschmar, *Electron efficiency measurement updates for the winter conferences*, <https://indico.cern.ch/getFile.py/access?contribId=6&sessionId=0&resId=0&materialId=slides&confId=163453>, feb, 2012.

- [101] L. Fayard and J. Kretzschmar, *Follow-up of electron efficiency recommendations with rel. 17*, <https://indico.cern.ch/getFile.py/access?contribId=7&resId=0&materialId=slides&confId=163455>, jan, 2012.
- [102] F. Hubaut, *EnergyScaleResolutionRecommendations*, [https://twiki.cern.ch/twiki/bin/viewauth/AtlasProtected/EnergyScaleResolutionRecommendations#2012\\_Moriond\\_Recommendations\\_2012](https://twiki.cern.ch/twiki/bin/viewauth/AtlasProtected/EnergyScaleResolutionRecommendations#2012_Moriond_Recommendations_2012), feb, 2012.
- [103] The ATLAS Collaboration, *Determination of the muon reconstruction efficiency in ATLAS at the Z resonance in proton-proton collisions at  $\sqrt{s}=7$  TeV*, Tech. Rep. ATLAS-CONF-2011-008, CERN, Geneva, Feb, 2011.
- [104] The ATLAS Collaboration, *Muon Momentum Resolution in First Pass Reconstruction of pp Collision Data Recorded by ATLAS in 2010*, Tech. Rep. ATLAS-CONF-2011-046, CERN, Geneva, Mar, 2011.
- [105] M. Cacciari, G. P. Salam, and G. Soyez, *The anti- $k_{\perp}$  jet clustering algorithm*, Journal of High Energy Physics **2008** (2008) no. 04, 063. <http://stacks.iop.org/1126-6708/2008/i=04/a=063>.
- [106] The ATLAS Collaboration, *Close-by Jet Effects on Jet Energy Scale Calibration in pp Collisions at  $\sqrt{s}=7$  TeV with the ATLAS Detector*, Tech. Rep. ATLAS-CONF-2011-062, CERN, Geneva, Apr, 2011.
- [107] S. Adomeit, *MultijetJESUncertaintyProvider for Top*, <https://twiki.cern.ch/twiki/bin/viewauth/AtlasProtected/MultijetJESUncertaintyProviderTop>, jan, 2012.
- [108] The ATLAS Collaboration, *Measurement of the top quark pair production cross-section with ATLAS in the single lepton channel*. [oai:cds.cern.ch:1415176](http://oai.cds.cern.ch:1415176), Tech. Rep. arXiv:1201.1889. CERN-PH-EP-2011-201, CERN, Geneva, Jan, 2012. submitted to Physics Letter B.
- [109] The ATLAS Collaboration, *Measurement of inclusive jet and dijet cross sections in proton-proton collisions at 7 TeV centre-of-mass energy with the ATLAS detector*, The European Physical Journal C - Particles and Fields **71** (2011) 1–59. <http://dx.doi.org/10.1140-s10052-010-1512-2>. 10.1140-s10052-010-1512-2.
- [110] The ATLAS Collaboration, *Measurement of the top quark-pair production cross section with ATLAS in pp collisions at  $\sqrt{s}=7$  TeV*, The European Physical Journal C - Particles and Fields **71** (2011) 1–36. <http://dx.doi.org/10.1140-s10052-011-1577-6>. 10.1140-s10052-011-1577-6.

- [111] S. Sacerdoti, *Update on the Jet Resolution Results in Release 17*, <https://indico.cern.ch/conferenceDisplay.py?confId=176491>, feb, 2012.
- [112] The ATLAS Collaboration, *Jet energy resolution in proton-proton collisions at  $\sqrt{s} = 7$  TeV recorded in 2010 with the ATLAS detector*, The European Physical Journal C **73** (2013) no. 3, 1–27.  
<http://dx.doi.org/10.1140/epjc/s10052-013-2306-0>.
- [113] G. Nabil, *Top Jet Reconstruction Efficiency*, <https://twiki.cern.ch/twiki/bin/viewauth/AtlasProtected/TopJetReconstructionEfficiency>, mar, 2013.
- [114] ATLAS Collaboration, *Performance of the ATLAS Secondary Vertex b-tagging Algorithm in 7 TeV Collision Data*, Tech. Rep. ATLAS-CONF-2010-042, CERN, Geneva, Jul, 2010.
- [115] The ATLAS Collaboration, G. Piacquadio and C. Weiser, *A new inclusive secondary vertex algorithm for b-jet tagging in ATLAS*, Journal of Physics: Conference Series **119** (2008) no. 3, 032032.  
<http://stacks.iop.org/1742-6596/119/i=3/a=032032>.
- [116] The ATLAS Collaboration, *Commissioning of the ATLAS high-performance b-tagging algorithms in the 7 TeV collision data*, Tech. Rep. ATLAS-CONF-2011-102, CERN, Geneva, Jul, 2011.
- [117] The ATLAS Collaboration, M. zur Nedden et al., *Measuring the b-tag efficiency in a top-pair sample with  $4.7 \text{ fb}^{-1}$  of data from the ATLAS detector*, Tech. Rep. ATLAS-COM-CONF-2012-089, CERN, Geneva, May, 2012.
- [118] The ATLAS Collaboration, *Measurement of the Mistag Rate with  $5 \text{ fb}^{-1}$  of Data Collected by the ATLAS Detector*, Tech. Rep. ATLAS-CONF-2012-040, CERN, Geneva, Mar, 2012.
- [119] The ATLAS Collaboration, *Measurement of the b-tag Efficiency in a Sample of Jets Containing Muons with  $5 \text{ fb}^{-1}$  of Data from the ATLAS Detector*, Tech. Rep. ATLAS-CONF-2012-043, CERN, Geneva, Mar, 2012.
- [120] The ATLAS Collaboration, *Performance of the Reconstruction and Identification of Hadronic Tau Decays with ATLAS*, Tech. Rep. ATLAS-CONF-2011-152, CERN, Geneva, Nov, 2011.
- [121] J. Keller, *Tau-Muon Veto*, <https://indico.cern.ch/event/125875/contribution/6/material/slides/0.pdf>, oct, 2011.
- [122] J. Keller, *Tau-Muon Veto*, <https://indico.cern.ch/getFile.py/access?contribId=14&resId=0&materialId=slides&confId=159518>, oct, 2011.

- [123] ATLAS Collaboration, *Measurement of the top quark pair cross section with ATLAS in pp collisions at using final states with an electron or a muon and a hadronically decaying lepton*, Physics Letters B **717** (2012) no. 13, 89 – 108. <http://www.sciencedirect.com/science/article/pii/S0370269312009793>.
- [124] The ATLAS Collaboration, *Performance of missing transverse momentum reconstruction in proton-proton collisions at  $\sqrt{s} = 7\text{TeV}$  with ATLAS*, The European Physical Journal C - Particles and Fields **72** (2012) 1–35. <http://dx.doi.org/10.1140-s10052-011-1844-6>. 10.1140-s10052-011-1844-6.
- [125] K. Venkatesh, *Description of the Top Missing ET (MET\_RefFinal\_em\_tightpp)*, [https://twiki.cern.ch/twiki/bin/viewauth/AtlasProtected/TopETmissLiaisonMoriond12#Description\\_of\\_the\\_Top\\_Missing\\_E](https://twiki.cern.ch/twiki/bin/viewauth/AtlasProtected/TopETmissLiaisonMoriond12#Description_of_the_Top_Missing_E), feb, 2012.
- [126] The ATLAS Collaboration, *Data-Quality Requirements and Event Cleaning for Jets and Missing Transverse Energy Reconstruction with the ATLAS Detector in Proton-Proton Collisions at a Center-of-Mass Energy of  $\sqrt{s} = 7\text{ TeV}$* , Tech. Rep. ATLAS-CONF-2010-038, CERN, Geneva, Jul, 2010.
- [127] S. Frixione and B. R. Webber, *Matching NLO QCD computations and parton shower simulations*, Journal of High Energy Physics **2002** (2002) no. 06, 029. <http://stacks.iop.org/1126-6708/2002/i=06/a=029>.
- [128] S. Frixione, E. Laenen, P. Motylinski, and B. R. Webber, *Single-top production in MC@NLO*, Journal of High Energy Physics **2006** (2006) no. 03, 092. <http://stacks.iop.org/1126-6708/2006/i=03/a=092>.
- [129] S. Frixione, P. Nason, and B. R. Webber, *Matching NLO QCD and parton showers in heavy flavour production*, Journal of High Energy Physics **2003** (2003) no. 08, 007. <http://stacks.iop.org/1126-6708/2003/i=08/a=007>.
- [130] P. M. Nadolsky et al., *Implications of CTEQ global analysis for collider observables*, . <http://link.aps.org/doi/10.1103/PhysRevD.78.013004>.
- [131] M. Aliev, H. Lacker, U. Langenfeld, S. Moch, P. Uwer, and M. Wiedermann, *HATHOR HAdronic Top and Heavy quarks crOss section calculatoR*, Computer Physics Communications **182** (2011) no. 4, 1034 – 1046. <http://www.sciencedirect.com/science/article/pii/S0010465510005333>.
- [132] M. L. Mangano, F. Piccinini, A. D. Polosa, M. Moretti, and R. Pittau, *ALPGEN, a generator for hard multiparton processes in hadronic collisions*, Journal of High Energy Physics **2003** (2003) no. 07, 001. <http://stacks.iop.org/1126-6708/2003/i=07/a=001>.

- [133] J. Pumplin, D. R. Stump, J. Huston, H.-L. Lai, P. Nadolsky, and W.-K. Tung, *New Generation of Parton Distributions with Uncertainties from Global QCD Analysis*, Journal of High Energy Physics **2002** (2002) no. 07, 012. <http://stacks.iop.org/1126-6708/2002/i=07/a=012>.
- [134] G. Corcella, I. G. Knowles, G. Marchesini, S. Moretti, K. Odagiri, P. Richardson, M. H. Seymour, and B. R. Webber, *HERWIG 6: an event generator for hadron emission reactions with interfering gluons (including supersymmetric processes)*, Journal of High Energy Physics **2001** (2001) no. 01, 010. <http://stacks.iop.org/1126-6708/2001/i=01/a=010>.
- [135] G. Corcella, I. Knowles, G. Marchesini, S. Moretti, K. Odagiri, et al., *HERWIG 6.5 release note*, arXiv:hep-ph/0210213 [hep-ph].
- [136] J. M. Butterworth, J. R. Forshaw, and M. H. Seymour, *Multiparton Interactions in Photoproduction at HERA*, Z.PHYS.C **72** (1996) 637. doi:10.1007/s002880050286.
- [137] The ATLAS Collaboration, *ATLAS tunes of PYTHIA 6 and Pythia 8 for MC11*, Tech. Rep. ATL-PHYS-PUB-2011-009, CERN, Geneva, Jul, 2011.
- [138] S. Agostinelli et al., *Geant4a simulation toolkit*, Nuclear Instruments and Methods in Physics Research Section A: Accelerators, Spectrometers, Detectors and Associated Equipment **506** (2003) no. 3, 250 – 303. <http://www.sciencedirect.com/science/article/pii/S0168900203013688>.
- [139] S. Frixione, P. Nason, and C. Oleari, *Matching NLO QCD computations with Parton Shower simulations: the POWHEG method*, JHEP **0711** (2007) 070, arXiv:0709.2092 [hep-ph].
- [140] P. Z. Skands, *Tuning Monte Carlo Generators: The Perugia Tunes*, Phys.Rev. **D82** (2010) 074018, arXiv:1005.3457 [hep-ph].
- [141] P. C. Bhat, *Multivariate Analysis Methods in Particle Physics*, Annual Review of Nuclear and Particle Science **61** (2011) no. 1, 281–309. <http://www.annualreviews.org/doi/abs/10.1146/annurev.nucl.012809.104427>.
- [142] ATLAS Collaboration, G. Aad et al., *Measurement of the  $t\bar{t}$  production cross section in the  $\tau$ +jets channel using the ATLAS detector*, Eur.Phys.J. **C73** (2013) 2328, arXiv:1211.7205 [hep-ex].
- [143] ATLAS Collaboration, G. Aad et al., *Measurement of the low-mass Drell-Yan differential cross section at  $\sqrt{s}=7$  TeV using the ATLAS detector*, arXiv:1404.1212 [hep-ex].
- [144] ATLAS Collaboration, G. Aad et al., *Measurement of the  $WW$  cross section in  $\sqrt{s} = 7$  TeV  $pp$  collisions with the ATLAS detector and limits on anomalous gauge couplings*, Phys.Lett. **B712** (2012) 289–308, arXiv:1203.6232 [hep-ex].

- [145] ATLAS Collaboration, G. Aad et al., *Measurement of the transverse momentum distribution of  $Z/\gamma^*$  bosons in proton-proton collisions at  $\sqrt{s} = 7$  TeV with the ATLAS detector*, Phys.Lett. **B705** (2011) 415–434, arXiv:1107.2381 [hep-ex].
- [146] The ATLAS Collaboration, *Muon reconstruction efficiency in reprocessed 2010 LHC proton-proton collision data recorded with the ATLAS detector*, Tech. Rep. ATLAS-CONF-2011-063, CERN, Geneva, Apr, 2011.
- [147] *Egamma Calibration Meeting*, <https://indico.cern.ch/conferenceDisplay.py?confId=168562>, feb, 2012.
- [148] The ATLAS Collaboration, *ATLAS Online Luminosity*, ATLAS Online Luminosity, 2013.